

# **Assessment and Compensation of Dynamic Instabilities in Voltage Source Converters Connected to Weak AC Grids and Microgrids**

by  
**Saeed Rezaee**

M.Sc., Shiraz University, 2012  
B.Sc., University of Tehran, 2009

Thesis Submitted in Partial Fulfillment of the  
Requirements for the Degree of  
Doctor of Philosophy

in the  
School of Mechatronic Systems Engineering  
Faculty of Applied Sciences

© Saeed Rezaee 2022  
SIMON FRASER UNIVERSITY  
Summer 2022

## Declaration of Committee

**Name:** Saeed Rezaee

**Degree:** Doctor of Philosophy

**Title:** **Assessment and Compensation of Dynamic Instabilities in Voltage Source Converters Connected to Weak AC Grids and Microgrids**

**Committee:** **Chair: Krishna Vijayaraghavan**  
Associate Professor, Mechatronic Systems Engineering

**Mehrdad Moallem**  
Co-Supervisor  
Professor, Mechatronic Systems Engineering

**Jiacheng (Jason) Wang**  
Co-Supervisor  
Associate Professor, Mechatronic Systems Engineering

**Amr Radwan**  
Committee Member  
Assistant Professor, College of Science and Engineering  
Western Washington University

**Mariana Resener**  
Examiner  
Assistant Professor, Sustainable Energy Engineering

**Carl Ngai Man Ho**  
External Examiner  
Professor, Electrical and Computer Engineering  
University of Manitoba

## Abstract

This thesis addresses the integration of three-phase dc/ac voltage source converter (VSC)-interfaced dc sources and loads into the three-phase ac grids or microgrids under very weak conditions. VSCs are the dominant topologies in high-power electronics due to their excellent performance and their common control method is voltage-oriented control (VOC). Motivated by the VSC industrial popularity on one hand and the issues yielding from dynamic interactions between the VOC-based VSC and the weak grid (WG) or weak microgrid (WMG) impedances, four situations are considered: VSC connected to a very weak grid (VSC-WG) in the inversion mode; VSC-WG in the rectification mode; passive load (PL) connected to a very weak microgrid (PL-WMG); and VSC connected to very weak microgrid (VSC-WMG). The dynamic model of the VSC-WG system is derived in the direct-quadrature reference frame ( $dq$ -RF) which serves as the basis for the study. Using the VSC-WG dynamics, the small-signal model of the system is developed in the standard state-space form which makes it possible to obtain the eigenvalue spectrum of the system. Using the eigenvalue analysis, the small-signal stability of the system is investigated under different operating points, grid impedance values, and control parameters variations. It is found that complex unstable modes are present in the eigenvalue spectrum of the system under the nominal conditions of the VSC-WG in both inversion and rectification modes as well as WMG in islanded mode. Linear active compensators are proposed that utilize the VSC output variables as inputs and integrate them into the primary control system of the VSC without adding extra measurement sensors or interfering with the VSC original control design. Moreover, these active compensation methods are lossless and do not change the VSC steady-state values. The design of the compensators is provided in detail using the state-space approach. It is shown that with proper design of the linear compensators, the instabilities are completely resolved under nominal conditions and the system dynamic performance under different conditions is improved. Computer simulations and real-time simulation (using hardware-in-the-loop platform) results are provided to verify the proposed methods and validate the theoretical findings.

**Keywords:** Active Compensation; Dynamic Interaction; Small-Signal Stability; Voltage Source Converter; Weak Grid; Weak Microgrid.

## **Acknowledgements**

I would like to express my deepest gratitude towards my supervisors, Prof. Mehrdad Moallem, Dr. Jason Wang, and Dr. Amr Radwan, for their consistent guidance and excellent technical assistance during this research. I am greatly indebted to their encouragement and moral support during past years.

I would like to extend a special thank to the members of the examining committee, Prof. Carl Ho and Dr. Mariana Resener, for taking the time to review the thesis and offer me valuable feedback, as well as Dr. Krishna Vijayaraghavan for chairing my defense session. I wish to thank my fellow graduate students in the School of Mechatronic Systems engineering for their moral support during my time at SFU and creating a nice working environment in the lab.

# Table of Contents

Declaration of Committee .....	ii
Abstract .....	iii
Acknowledgements .....	iv
Table of Contents .....	v
List of Tables .....	ix
List of Figures .....	x
List of Acronyms .....	xvi
<b>Chapter 1. Introduction .....</b>	<b>1</b>
1.1. Motivation for the Research .....	1
1.2. Background and Overview of the Present State of the Technology .....	3
1.2.1. Three-phase Voltage Source Converters .....	3
1.2.2. Stability Study of AC Power Grids with Presence of Power Electronic Converters .....	6
1.2.3. Small-Signal Model of VSC for Stability Study .....	7
1.2.4. Dynamic interaction between VSC control, ac filter, and grid impedance .....	8
1.3. Summary of Contributions and Outline of the Dissertation .....	11
1.3.1. Chapter 2: Dynamic Model of VSC-WG and Control Design .....	12
1.3.2. Chapter 3: Small-Signal Analysis and Stability Improvements of VSC-WG in Inversion Mode .....	12
1.3.3. Chapter 4: Small-Signal Analysis and Stability Improvements of VSC-WG in Rectification Mode .....	13
1.3.4. Chapter 5: Dynamic Modeling and Stability Analysis of Converter-Based AC Microgrids .....	13
1.3.5. Dynamic Modeling and Stability Improvements of Weak AC Microgrid Systems .....	14
1.3.6. Chapter 7: Conclusions and Suggestions for Future Works .....	14
<b>Chapter 2. Dynamic Model of VSC-WG and Control Design .....</b>	<b>15</b>
2.1. VSC-WG Dynamic Model .....	15
2.1.1. Power Circuit .....	16
2.1.2. Current Control .....	17
2.1.3. DC-Link Voltage Control .....	18
2.1.4. Phase-Locked Loop .....	19
2.1.5. AC Voltage Control .....	20
Detailed Model of PCC Voltage Dynamics .....	20
Simplified Model of PCC Voltage Dynamics .....	22
2.2. Control Design .....	23
2.3. Simulation Results .....	24
2.4. Conclusion .....	26
<b>Chapter 3. Small-Signal Analysis and Stability Improvements of VSC-WG in Inversion Mode .....</b>	<b>28</b>

3.1.	Introduction.....	28
3.2.	Stability Assessment of Uncompensated System .....	31
3.2.1.	Participation Analysis .....	31
3.2.2.	Sensitivity Analysis.....	32
	Influence of the VSC Power Level.....	32
	Influence of the LC Filter Damping .....	33
	Influence of the PLL Controller .....	33
	Influence of the DC-Link Voltage Controller .....	34
	Influence of the AC Voltage Controller .....	34
3.3.	Suggested Active Compensation.....	35
3.3.1.	Small-Signal Model of Actively Compensated System.....	36
3.3.2.	Active Compensator Design .....	36
3.3.3.	Stability Assessment of Compensated System .....	37
3.4.	Simulation Results.....	38
3.4.1.	Influence of AC Voltage Control .....	38
3.4.2.	Influence of Power Level .....	39
3.4.3.	Influence of Grid Angle Variation .....	40
3.4.4.	Influence of Grid Impedance Variation .....	41
3.4.5.	Dynamic Interactions with VSC Primary Controllers .....	42
3.5.	Real-Time Verification .....	43
3.6.	Conclusion.....	45
<b>Chapter 4.</b>	<b>Small-Signal Analysis and Stability Improvements of VSC-WG in Rectification Mode .....</b>	<b>46</b>
4.1.	Introduction.....	46
4.2.	Dynamic Model of VSC-WG System.....	49
4.2.1.	Power Circuit.....	51
4.2.2.	VOC System .....	51
4.2.3.	Control Design .....	52
4.3.	Power-Angle Limitation at Low SCR Level.....	53
4.4.	Stability Assessment of Uncompensated System .....	54
4.4.1.	Modal Analysis.....	54
4.4.2.	Sensitivity Analysis.....	55
	Influence of VSC Power Level.....	55
	Influence of Passive Damping .....	56
	Influence of PLL.....	57
	Influence of DC Voltage Control.....	57
	Influence of AC Voltage Control .....	58
4.5.	Proposed Dual Active Compensation .....	59
4.5.1.	Linear Model of Compensated System.....	60
4.5.2.	Design of Dual Active Compensators .....	61
4.5.3.	Stability Assessment of Compensated System .....	62
4.6.	Simulation Results.....	64
4.6.1.	Response to Active Power Step-Up .....	64
4.6.2.	Response to Grid Angle Change .....	65

4.6.3.	Response to Grid Impedance Variation .....	66
4.6.4.	Dynamic Interactions with VSC Primary Controllers .....	67
4.7.	Real-Time Verification .....	68
4.8.	Conclusion.....	72
<b>Chapter 5. Dynamic Modeling and Stability Analysis of Converter-Based AC Microgrids.....</b>		<b>73</b>
5.1.	Introduction.....	73
5.2.	Small-Signal Dynamic Modeling of AC Microgrid .....	75
5.2.1.	Multiple Reference Frames and Dynamical Transform .....	75
5.2.2.	Dynamic Model of VSI.....	77
Power Circuit .....	79	
Power Sharing Control .....	79	
Voltage and Current Control.....	80	
State-Space Model of VSI .....	81	
5.2.3.	The Dynamic Model of VSR .....	81
Power Circuit .....	81	
PLL .....	82	
Voltage and Current Control.....	83	
State-Space Model of VSR.....	83	
5.2.4.	Dynamic Model of PL .....	84
5.2.5.	Dynamic Model of Network Line.....	85
5.2.6.	State-Space Model of AC Microgrid .....	86
5.3.	Small-signal Stability Analysis .....	86
5.3.1.	Case I: Microgrid with Three PLs .....	86
5.3.2.	Case II: Microgrid with Two PLs and an AEL.....	87
5.3.3.	Participation Factor Analysis .....	88
5.3.4.	Sensitivity Analysis.....	89
5.4.	Time-Domain Simulation Results.....	90
5.5.	Conclusion.....	92
<b>Chapter 6. Dynamic Modeling and Stability Improvements of Weak AC Microgrid Systems .....</b>		<b>93</b>
6.1.	Introduction.....	93
6.2.	Weak AC Microgrid Structure .....	94
6.3.	Definition of Short-Circuit Ratio in Weak AC Microgrid Systems .....	95
6.4.	Weak Microgrid Dynamics .....	96
6.4.1.	Dynamic Model of VSI.....	97
6.4.2.	Dynamic Model of VSR .....	97
6.4.3.	Dynamic Model of PL .....	98
6.4.4.	Weak Microgrid State-Space Model .....	99
6.5.	Static Capability of Weak AC Microgrid .....	99
6.6.	Small-Signal Stability of Weak AC Microgrid.....	101
6.6.1.	Case 1: PL-WMG System .....	101
Influence of Power Level .....	101	
Influence of Impedance Ratio.....	102	

	Influence of Short Circuit Ratio.....	103
	Participation Factor of Dominant Modes .....	104
	Sensitivity Analysis of Control Parameters.....	105
6.6.2.	Case II: VSC-WMG System .....	106
	Influence of Power Level .....	106
	Influence of Impedance Ratio.....	107
	Influence of Short Circuit Ratio.....	107
	Participation Factor of Dominant Modes .....	108
	Sensitivity Analysis of Control Parameters.....	109
6.7.	Active Compensation of PL-WMG System.....	111
6.7.1.	Compensation Design.....	111
	Analysis of Active Compensation .....	112
6.8.	Active Compensation of VSC-WMG System.....	113
6.8.1.	Compensation Design.....	113
6.8.2.	Analysis of Active Compensation .....	115
6.9.	Time-Domain Simulation Results.....	116
6.9.1.	PL-WMG System Responses.....	116
6.9.2.	VSC-WMG System Responses.....	118
6.10.	Conclusion.....	122
<b>Chapter 7.</b>	<b>Summary, Conclusions, and Suggestions for Future Work.....</b>	<b>124</b>
7.1.	Summary and Conclusion.....	124
7.2.	Suggestions for Future Research .....	125
7.2.1.	Other Load Configurations .....	125
7.2.2.	Impedance-based modeling .....	125
7.2.3.	Robust Control Design .....	126
<b>References</b>	<b>.....</b>	<b>127</b>
<b>Appendix A.</b>	<b>State Matrices of VSC-WG System in Inversion Mode .....</b>	<b>136</b>
<b>Appendix B.</b>	<b>State Matrices of VSC-WG System in Rectification Mode .....</b>	<b>137</b>
<b>Appendix C.</b>	<b>State Matrices of AC Microgrid System .....</b>	<b>138</b>
	VSI state-space matrices.....	138
	VSR state-space matrices .....	139
	RL-Type PLs state-space matrices .....	140
	Network lines state-space matrices.....	141
	Microgrid state-space matrices .....	142
<b>Appendix D.</b>	<b>State Matrices of Weak AC Microgrid.....</b>	<b>144</b>
	RC-Type PL state-space matrices .....	144
	Weak microgrid state-space matrices .....	144

## List of Tables

Table 2-1 Parameters of VSC-WG System .....	24
Table 3-1 Participation Factor of the VSC-WG States in the Dominant Modes .....	32
Table 3-2 Active Compensator Parameters .....	38
Table 4-1 Parameters of VSC-WG System .....	50
Table 4-2 Participation Factor of the States in the Dominant Modes .....	55
Table 5-1 Parameters of AC Microgrid System.....	78
Table 5-2 Participation Factors of AC Microgrid State Variables on Dominant Modes ..	88
Table 6-1 Parameters of WMG System .....	100
Table 6-2 Participation factor of PL-WMG variables on dominant modes at $SCR^{mg} = 1.6$ , impedance ratio equal to 1.5, and under nominal loading power condition. .....	103
Table 6-3 Participation factor of VSC-WMG variables on dominant modes at $SCR^{mg} =$ 1.6, impedance ratio equal to 1.5, and under nominal loading power condition.....	108

## List of Figures

Figure 1.1: Two-level three-phase VSC topology. ....	3
Figure 1.2: DC source or dc load interfaced to the WG by a VSC.....	4
Figure 1.3: VSC controlled as an AEL. ....	9
Figure 2.1: VSC-WG system. (a) VSC with LC filter connected to the utility grid through a step-up transformer and the grid impedance. (b) VSC control loops....	16
Figure 2.2: Block diagram of the CC loops. ....	17
Figure 2.3: Block diagram of the DVC control loop. (a) Large-signal model. (b) Small-signal model.....	18
Figure 2.4: Block diagram of the PLL control loop. (a) Large-signal model. (b) Small-signal model.....	19
Figure 2.5: Block diagram of the AVC loop.....	22
Figure 2.6: Dynamic response of the PCC voltage to 1 percent step variation in the voltage reference at $t = 0.5$ s under $P_{ac} = 0.84$ pu. (a) Slow PLL with a bandwidth of 3.2 Hz. (b) Fast PLL with a bandwidth of 25 Hz.....	26
Figure 3.1: Spectrum of the dominant eigenvalues corresponding to $\mathbf{A}_{uc}$ when $P_{ac}$ changes between 0.35 to 1 pu. ....	32
Figure 3.2: Spectrum of the dominant eigenvalues corresponding to $\mathbf{A}_{uc}$ when $r_d$ changes between 0.4 to 0.6 $\Omega$ under $P_{ac} = 1$ pu condition. ....	33
Figure 3.3: Spectrum of the dominant eigenvalues corresponding to $\mathbf{A}_{uc}$ when $(K_{p\omega}, K_{i\omega})$ change by a gain of 0.1 to 1 under $P_{ac} = 1$ pu condition. ....	33
Figure 3.4: Spectrum of the dominant eigenvalues corresponding to $\mathbf{A}_{uc}$ when $(K_{pdc}, K_{idc})$ change by a gain of 0.28 to 1.23 under $P_{ac} = 1$ pu condition. ....	34
Figure 3.5: Spectrum of the dominant eigenvalues corresponding to $\mathbf{A}_{uc}$ when $(K_{pv}, K_{iv})$ change by a gain of: (a) 0.08 to 1.05 and (b) 0.98 to 1.05 under $P_{ac} = 1$ pu. ....	35
Figure 3.6: Block diagram of the AVC loop with active compensation. ....	36
Figure 3.7: Spectrum of the dominant eigenvalues corresponding to $\mathbf{A}_{cp}$ when $K_{cp}$ changes by a gain of 0.3 to 3 for $\omega_{cp} = (15, 20, 25)$ rad/s under $P_{ac} = 1$ pu. ....	37
Figure 3.8: Spectrum of the dominant eigenvalues corresponding to $\mathbf{A}_{cp}$ when $P_{ac}$ changes from 0.35 pu to 1 pu.....	37

Figure 3.9: Dynamic response of the actively compensated PCC voltage to 1 percent step variation in the voltage reference at $t = 0.5$ s under $P_{ac} = 0.84$ pu and fast PLL bandwidth of 25 Hz.....	38
Figure 3.10: Dynamic response of the active power following a step variation in the active power at $t = 0.5$ s at different power levels. ....	39
Figure 3.11: Transient responses of the VSC following a $70^\circ$ step change in the phase angle of the grid voltage at $t = 1$ s and $P_{ac} = 0.85$ pu.....	40
Figure 3.12: Transient responses of the compensated VSC following a $20^\circ$ step change in the phase angle of the grid voltage at $t = 1$ s and $P_{ac} = 1$ pu. ....	40
Figure 3.13: Transient responses of the compensated VSC at $P_{ac} = 1$ pu when $Z_g$ linearly increases at $t = 0.25$ s from one-third of the nominal value to the full value in the 0.3 and 1 s corresponding to fast and slow rates, respectively. ....	41
Figure 3.14: Dynamic response of the VSC control loops to a step variation in the reference input at $t = 0.5$ s and $P_{ac} = 0.75$ pu. (a) Response of $\omega_{vsc}$ following a 1 Hz step in the grid frequency. (b) Response of $i_{fd}$ following a step in the current reference ( $d$ -axis) from 0.75 pu to 0.8 pu. (c) Response of $v_o$ (magnitude) following a 5% step in the voltage reference. ....	42
Figure 3.15: VSC-WG experiment platform. ....	43
Figure 3.16: Voltages and current responses of the VSC during start-up transients and staircase changes in $P_{dc}$ . (a) Response of $v_o$ (phase a), $i_o$ (phase a), and $\Delta v_{dc}$ . (b) Zoomed view of $v_o$ and $i_o$ . ....	44
Figure 3.17: VSC Active power, phase angle difference, and compensation signal responses during start-up transients and staircase changes in $P_{dc}$ . ....	44
Figure 4.1: VSC-WG system. (a) VSC with LC filter connected to the utility grid through a step-down transformer and the grid impedance. (b) VSC control loops. ....	50
Figure 4.2: Active electronic load connected to the WG through an equivalent series impedance. ....	53
Figure 4.3 Spectrum of the dominant eigenvalues when $P_{ac}$ changes between 0.82 to 1 pu in the (a) rectification mode and (b) inversion mode. ....	56
Figure 4.4: Spectrum of the dominant eigenvalues at $P_{ac} = 1$ pu when $r_d$ changes between 0 to 1 $\Omega$ . ....	57
Figure 4.5: Spectrum of the dominant eigenvalues at $P_{ac} = 1$ pu when $(K_{p\omega}, K_{i\omega})$ change by a gain of 0.1 to 1. ....	57
Figure 4.6: Spectrum of the dominant eigenvalues at $P_{ac} = 1$ pu when $(K_{pdc}, K_{idc})$ change by a gain of 0.5 to 1. ....	58

Figure 4.7: Spectrum of the dominant eigenvalues considering the active compensation at $P_{ac} = 1$ pu when $(K_{pv}, K_{iv})$ change by a gain of 0.08 to 1.....	59
Figure 4.8: Block diagram of the AVC loop with active compensation. ....	59
Figure 4.9: Block diagram of the DVC control loop with active compensation.....	59
Figure 4.10: Spectrum of the dominant eigenvalues with DAC at $P_{ac} = 1$ pu and $SCR = 1.18$ . (a) $K_{cpd}$ varies from 0 to 5 and $K_{cpq} = 0$ at $\omega_{cpd} = (300, 600, 900)$ rad/s. (b) $K_{cpq}$ varies from 0 to 400 at $\omega_{cpq} = (5, 10, 15)$ rad/s, $K_{cpd} = 3.5$ , and $\omega_{cpd} = 600$ rad/s. ....	61
Figure 4.11: Spectrum of the dominant eigenvalues with DAC when $P_{ac}$ changes from 0.85 pu to 1 pu. ....	63
Figure 4.12: Spectrum of the dominant eigenvalues (a) without DAC. (b) with DAC when $SCR$ changes from 1.5 to 1.1 ( $= SCR^c$ ). ....	63
Figure 4.13: Dynamic response of the active power following a step variation in the active power at $t = 0.1$ s at different power levels in the rectification mode.....	64
Figure 4.14: Transient responses of the VSC-WG with DAC scheme at $P_{ac} = 0.85$ pu during $10^\circ$ step changes in the phase angle of the grid voltage. (a) active power response. (b) angle difference response.....	65
Figure 4.15: Transient responses of the VSC-WG with DAC scheme at $P_{ac} = 1$ pu when $Z_g$ linearly increases at slow (0.33 s period) and fast rates (1s period). (a) reactive power response. (b) angle difference response. ....	66
Figure 4.16: Dynamic responses of the VSC control loops subject to a step in the reference inputs at $t = 0.5$ s and $P_{ac} = 0.85$ pu. (a) frequency response following a 1 Hz grid frequency step. (b) $d$ channel current response $i_{fd}$ following a 5% in the current reference. (c) voltage response following a 5% step in the ac voltage reference. (d) dc voltage response following a 1% step in the dc voltage reference. ....	67
Figure 4.17: VSC-WG FPGA-based experimental set-up. ....	68
Figure 4.18: Measurement of the VSC-WG responses (DAC disabled) during start-up transients and step-ups in the dc power. ....	69
Figure 4.19: Measurement of the VSC-WG responses (DAC enabled) during start-up transients and step-ups in the dc current. (a) VSC output voltage/current (phase $a$ ) and dc-side voltage error. (b) zoomed view of the VSC responses in the steady state.....	70
Figure 4.20: The VSC-WG responses (DAC enabled) during start-up transients and step-ups in the dc current (continued). (a) active power. (b) phase angle difference. (c) DAC compensation signals.....	71
Figure 5.1: Single-line diagram of the ac microgrid with $VSI_{1-3}$ , $PL_{1,3}$ at nodes 1 and 3, and a selector switch $ST$ to switch between $PL_2$ and $AEL$ at node 2. ....	75
Figure 5.2: RF transformation.....	76

Figure 5.3: VSI with cascaded control loops, LC filter, and interface inductance interfacing DG source.....	78
Figure 5.4: VSR with cascaded control loops, LC filter, and interface inductance interfacing dc load to the ac microgrid. ....	82
Figure 5.5: (a) PL interfaced directly to the AC microgrid, (b) Network line connecting $i^{\text{th}}$ and $j^{\text{th}}$ nodes of the ac microgrid.....	84
Figure 5.6: Eigenvalue spectrum of the ac microgrid when ST is at (a) position 1; (b) position 2 and $P_{dc} = 15$ kW; (c) position 2 and $P_{dc}$ is varied from 15 kW to 25 kW (only the eigenvalues with $\text{Re}\{\lambda\} \geq -400$ are shown).....	87
Figure 5.7: Progress of the dominant eigenvalue of the ac microgrid as a function of (a) $9.4 \times 10^{-6} \leq n \leq 1.8 \times 10^{-3}$ ; (b) $1.3 \times 10^{-4} \leq n \leq 1.9 \times 10^{-2}$ ; (c) $1 \times 10^{-4} \leq L_f^{vsr} \leq 1 \times 10^{-3}$ ; (d) $0.5 \leq K_{pv}^{vsr} \leq 6$ .....	89
Figure 5.8: Active power of VSI <sub>1-3</sub> with step changes in the PL at node 2.....	90
Figure 5.9: Active power of VSI <sub>1-3</sub> with step changes in the AEL at node 2. ....	91
Figure 5.10: DC-Side voltage of VSR with step changes in the AEL at node 2. ....	91
Figure 6.1: Single-line diagram of an islanded ac microgrid with a network of high-impedance lines that hosts two converter-interfaced sources, an AEL, and a PL. ....	94
Figure 6.2: Thevenin equivalent circuit of the WMG. ....	96
Figure 6.3: Single-line diagram of the WMG. ....	100
Figure 6.4: Spectrum of the dominant eigenvalues of PL-WMG when $P_{pl}$ changes between 0.42 to 1 pu at $SCR^{mg} = 1.6$ and the impedance ratio is equal to 9.....	102
Figure 6.5: Spectrum of the dominant eigenvalues of PL-WMG when impedance ratio changes between 0.2 to 19 at the nominal loading power and $SCR^{mg} = 1.6$ .....	102
Figure 6.6: Spectrum of the dominant eigenvalues of PL-WMG at the nominal loading power when $SCR^{mg}$ changes between 1.13 to 10 and the impedance ratio is equal to 9.....	103
Figure 6.7: Spectrum of the dominant eigenvalues of PL-WMG when $m_{1-2}$ vary between 0–1.5 times the nominal values at the nominal power, $SCR^{mg} = 1.6$ , and the impedance ratio is equal to 9.....	104
Figure 6.8: Spectrum of the dominant eigenvalues of PL-WMG when $n_{1-2}$ vary 0–1.5 times the nominal values at the nominal power, $SCR^{mg} = 1.6$ , and the impedance ratio is equal to 9.....	105
Figure 6.9: Spectrums of the dominant eigenvalues of PL-WMG when $(K_{pv1}^{vsi}, K_{iv1}^{vsi})$ and $(K_{pv2}^{vsi}, K_{iv2}^{vsi})$ vary between 0.1–1.6 times the nominal values at the nominal power, $SCR^{mg} = \{1.6, 2\}$ , and the impedance ratio is equal to 9. ....	106

Figure 6.10: Spectrums of the dominant eigenvalues of VSC-WMG when $P_{vsr}$ changes between 0.42 to 1 pu, $SCR^{mg} = 1.6$ , and the impedance ratio is equal to 9. ....	106
Figure 6.11: Spectrum of the dominant eigenvalues of VSC-WMG at the nominal loading power when impedance ratio changes between 0.2 to 19 at $SCR^{mg} = 1.6$ . ....	107
Figure 6.12: Spectrum of the dominant eigenvalues of VSC-WMG at the nominal loading power when $SCR^{mg}$ changes between 1.15 to 10 and the impedance ratio equal to 9. ....	108
Figure 6.13: Spectrum of the dominant eigenvalues of VSC-WMG when $m_{1-2}$ vary between 0–1.5 times the nominal values at the nominal power, $SCR^{mg} = 1.6$ , and the impedance ratio equal to 9. ....	109
Figure 6.14: Spectrum of the dominant eigenvalues of VSC-WMG when $n_{1-2}$ vary 0–1.5 times the nominal values at the nominal power, $SCR^{mg} = 1.6$ , and the impedance ratio equal to 9. ....	110
Figure 6.15: Spectrum of the dominant eigenvalues of VSC-WMG when $(K_{pv1}^{vsi}, K_{iv1}^{vsi})$ and $(K_{pv2}^{vsi}, K_{iv2}^{vsi})$ vary between 0.1–1.6 times the nominal values at the nominal power, $SCR^{mg} = 1.6$ , and the impedance ratio equal to 9. ....	110
Figure 6.16: Spectrum of the dominant eigenvalues of VSC-WMG when $(K_{pdc}^{vsr}, K_{idc}^{vsr})$ vary between 0.6–1 times of the nominal values at the nominal power, $SCR^{mg} = 1.6$ , and the impedance ratio equal to 9. ....	110
Figure 6.17: Spectrums of the dominant eigenvalues of compensated PL-WMG system at the nominal power, $SCR^{mg} = 1.6$ , and impedance ratio equal to 9. (a) $m_{d1}$ changes between $0-15 \times 10^{-7}$ and $n_{d1} = 0$ . (b) $n_{d1}$ changes from $0-15 \times 10^{-6}$ and $m_{d1} = 0$ . ....	112
Figure 6.18: Spectrums of the dominant eigenvalues of uncompensated PL-WMG system (in red) versus compensated PL-WMG system assuming $m_{d1} = 8 \times 10^{-7}$ and $n_{d1} = 0 \times 10^{-7}$ (in blue) subjected to variations of (a) $P_{pl}$ between 0.42 to 1 pu at $SCR^{mg} = 1.6$ and impedance ratio equal to 9, (b) impedance ratio between 0.2 to 19 at the nominal loading power and $SCR^{mg} = 1.6$ , (c) $SCR^{mg}$ value between 1.13–10 at the nominal loading power and impedance ratio equal to 9. ....	112
Figure 6.19: Spectrums of the dominant eigenvalues of compensated VSC-WMG system at the nominal power, $SCR^{mg} = 1.6$ , and impedance ratio equal to 9. (a) $0 \leq m_{d1} \leq 5 \times 10^{-7}$ , $n_{d1} = 0$ , and $K_{cpd} = 0$ . (b) $m_{d1} = 0$ , $0 \leq n_{d1} \leq 2 \times 10^{-6}$ and $K_{cpd} = 0$ . (c) $m_{d1} = 5 \times 10^{-7}$ , $n_{d1} = 0$ , $0 \leq K_{cpd} \leq 15$ , $\omega_{cpd} = \{150, 300, 450\}$ rad/s, and $\zeta = 0.9$ . ....	114
Figure 6.20: Spectrums of the dominant eigenvalues of uncompensated VSC-WMG system (in red) versus compensated VSC-WMG system assuming $m_{d1} = 5 \times 10^{-7}$ and $n_{d1} = 0 \times 10^{-7}$ (in blue) subjected to variations of (a) $P_{vsr}$ between 0.42 to 1 pu at $SCR^{mg} = 1.6$ and impedance ratio equal to 9, (b)	

	impedance ratio between 0.2 to 19 at the nominal loading power and $SCR^{mg} = 1.6$ , (c) $SCR^{mg}$ between 1.42–10 at the nominal loading power and impedance ratio equal to 9. ....	115
Figure 6.21:	Responses of PL-WMG system with and without active compensation with $m_{1-2}$ initially set at one-tenth of the original values and stepped to the designated values at $t = 2$ s under the nominal loading power condition at $SCR^{mg} = 1.6$ and impedance ratio equal to 9. (a) active power of VSI <sub>1-2</sub> and PL (in blue, red, and black respectively). (b) VSI <sub>2</sub> frequency. (c) VSI <sub>2</sub> voltage angle.....	116
Figure 6.22:	Responses of PL-WMG system during start-up transient and staircase changes in $P_{pl}$ . (a)–(d) with active compensation. (e)–(h) without active compensation.....	117
Figure 6.23:	Responses of VSC-WMG system with and without active compensation with $m_{1-2}$ initially set at one-tenth of the original values and stepped to the designated values at $t = 2$ s under 0.5 pu loading power condition at $SCR^{mg} = 1.6$ and impedance ratio equal to 9. (a) active power of VSI <sub>1-2</sub> and AEL (in blue, red, and black respectively). (b) VSI <sub>2</sub> frequency. (c) VSI <sub>2</sub> voltage angle.....	119
Figure 6.24:	Responses of VSC-WMG system with and without mid-frequency active compensation while low-frequency compensation is enabled subject to step change of 0.69–0.74 times pu power in $P_{vsr}$ at $t = 2$ s, $SCR^{mg} = 1.6$ , and impedance ratio equal to 9. (a) active power of VSI <sub>1-2</sub> and AEL. (b) zoomed view of active power responses. (c) VSR dc-link voltage. ....	119
Figure 6.25:	Responses of VSC-WMG system during start-up transient and staircase changes in $P_{dc}$ . (a)–(e) with active compensation. (f)–(j) without active compensation.....	121

## List of Acronyms

AC	Alternating current
AEL	Active electronic load
AVC	AC voltage control
BPF	Band-pass filter
CC	Current control
DC	Direct current
DG	Distributed generation
$dq$	Direct-quadrature
DVC	DC voltage control
HIL	Hardware-in-the-loop
HVDC	High-voltage direct current
LHP	Left-half plane
LPF	Low-pass filter
LTI	Linear time-invariant
NIR	Negative incremental resistance
PF	Participation factor
PCC	Point of common coupling
PEC	Power electronic converter
PI	Proportional-and-integral
PL	Passive load
PLL	Phase-locked loop
pu	Per-unit
PSC	Power synchronization control
PWM	Pulse-width modulation
RES	Renewable energy sources
RHP	Right-half plane
RF	Reference frame
SCR	Short-circuit ratio
SG	Stiff grid

SISO	Single-input-single-output
STATCOM	Static compensator
VOC	Voltage-oriented control
VSC	Voltage source converter
VSI	Voltage source inverter
VSR	Voltage source rectifier
VWG	Very weak grid
WG	Weak grid
WMG	Weak microgrid

# Chapter 1.

## Introduction

### 1.1. Motivation for the Research

The importance of alternating current (AC) power grids in the primary infrastructure of today's societies is undeniable. Although it is more than a century since the first power systems were developed, they are still growing in size and complexity. This expansion is happening in both demand and structure (interconnections) parts. Power systems of today are essentially interconnected systems. Therefore, they are subjected to large disturbances that can impose security issues [1]. Moreover, the aging infrastructure in the transmission and distribution sectors can challenge the system reliability and impose security issues [2]. Three main technologies that are developed to mitigate these issues are: distributed generations (DGs), voltage source converters (VSC), and wide-area measurement systems [1].

In addition to the growth of energy demand, environmental and economic problems related to fossil fuels; growing needs for a highly reliable electrical energy for critical loads; and economic incentives rising from electricity market are among the reasons behind the adoption of DGs in power systems [3]–[6]. DG units often utilize clean energy storage units, e.g., fuel cells, and renewable energy sources (RESs) such as hydro, wind, and solar energy. Considered as the generation at the distribution level, DG units can provide clean energy for dispersed locations and remote areas [5], [6]. In summary, the adoption of DGs in the electrical grid can increase the service reliability, improves local power quality, and reduces the need for future generation expansion or grid reinforcement [7], while more studies should be done to analyse their effect on the reliability indices of power grids.

To interface most DG systems to the ac grids, power electronic converters (PEC) are used [1], [5], [6]. VSC is the dominant family of power electronic converters for many forms of DGs, such as solar and wind power systems; high-voltage direct current (HVDC) transmission systems; motor drive applications; and modern loads such as energy storage systems, data centers, and electric vehicles [8]–[10]. Therefore, while

high-power VSCs are traditionally used for applications like HVDC transmission systems and static VAR compensators, their applications in different parts of modern power systems including generation and distribution are reported [8].

On the system level, the development of new operational concepts called active grids, i.e., smart grids<sup>1</sup> and microgrids<sup>2</sup>, as opposed to the traditional passive grids where the power is unidirectional, shows the growing importance of power electronics role, particularly VSCs, in power systems [2], [8], [11]. Therefore, the conventional power grids are gradually transforming into converter-dominated networks [10].

Dynamic interaction between tightly regulated interfacing PECs and the rest of the grid may adversely influence the overall stability even if the converter is inherently functional and stable [10]. In particular, in weak grids (WGs), where the short circuit level of the grid is low with respect to the nominal dc power of the interface converter, the dynamic interaction between the PEC and the grid impedance can induce instability. With the high penetration of DGs, the modern grids tend to be weaker than before [12].

Several studies have addressed the instability issues when VSCs are connected to WGs, called VSC-WG systems hereafter. While most of the related literature is about the inversion mode of operation and how to improve the system performance or stability by modifying the VSC control design or adjusting the parameters design [12]–[14], few works have considered the rectification mode [15]. Moreover, as will be discussed in the next sections, there is still a need for an effective, yet simple, method to mitigate instability issues when the VSC is connected to a very weak grid (VWG).

On the other hand, the idea of weak microgrids (WMGs) and the interaction dynamics between the PEC-interfaced modules and microgrids with large effective impedances is not studied in the existing literature. These potential problems are the sources of motivation that initiated this thesis and the attempts that are done accordingly to improve the stability of WG and WMG as reflected in the following chapters.

---

<sup>1</sup> Smart grid is defined as a network that can intelligently integrate the actions of all users connected to it to efficiently deliver sustainable, economic and secure electricity supplies [2].

<sup>2</sup> Microgrid is an integration platform for supply-side distributed energy resources and demand resources (controllable loads) located in a local low-voltage distribution grid [2].

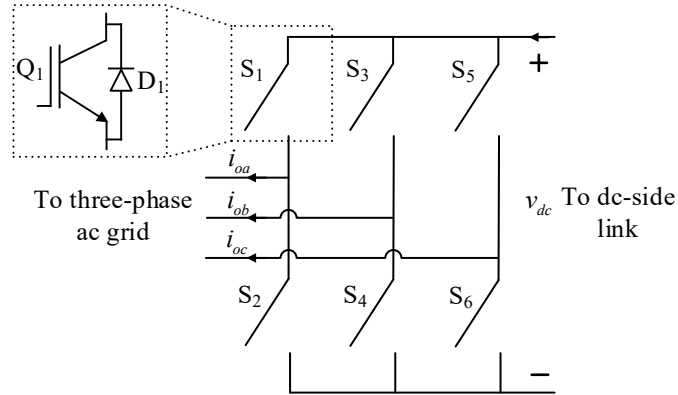


Figure 1.1: Two-level three-phase VSC topology.

## 1.2. Background and Overview of the Present State of the Technology

### 1.2.1. Three-phase Voltage Source Converters

Three-phase VSCs are the state-of-the-art technology to interface DGs, dc loads, and dc grids into the power grid due to the high-frequency switching capability which results in reduced harmonic content, excellent dynamics, and the ability to regulate bidirectional active and reactive powers independently [4]–[8]. Figure 1.1 shows a two-level VSC<sup>3</sup> which incorporates six bidirectional switches  $S_1$ – $S_6$  to convert dc power to ac power and vice versa. Operation of switches in one leg, e.g.,  $S_1$  and  $S_2$  in the first leg of the VSC in Figure 1.1, are complementary. The three-phase VSC is essentially a combination of three half-bridge legs, with the commanding signals forming a three-phase balanced set in the steady state [5]. The zoomed display of  $S_1$  is shown in Figure 1.1. As shown, each switch of the VSC is a fully controllable unidirectional switch such as IGBT or MOSFET<sup>4</sup> with an antiparallel diode that offers reverse conducting capability [5].

Figure 1.2(a) shows a VSC (symbolically shown as a box) cascaded with an  $LC$  filter which, in turn, is connected to the point of common coupling (PCC) where the VSC

<sup>3</sup> Since the focus of this thesis is not on the VSC topology but on the VSC external dynamics and its interaction with the rest of grids, the two-level VSC topology is selected to be studied in the following chapters. Thus, the VSC term refers to two-level topology throughout this thesis, but the control-based developments shall be conceptually applicable to other types VSC family.

<sup>4</sup> Insulated-Gate bipolar transistor (IGBT) and metal-oxide-semiconductor field-effect transistor (MOSFET).

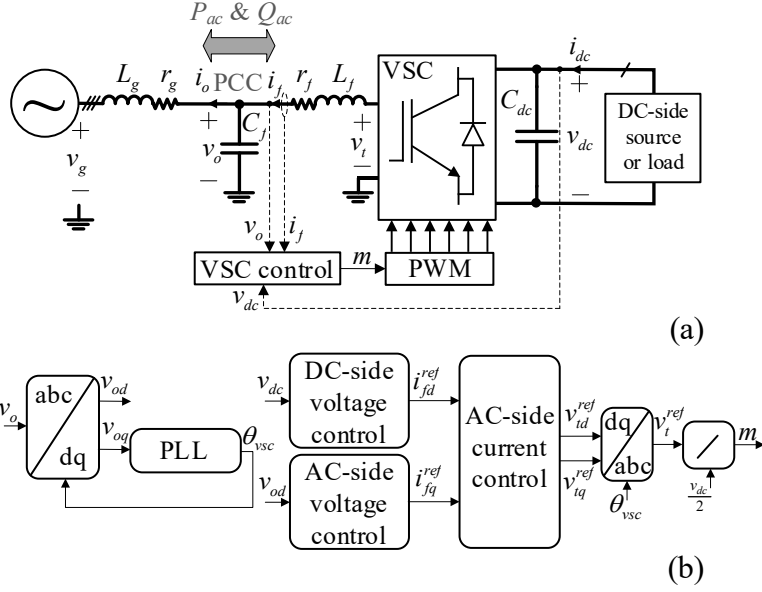


Figure 1.2: DC source or dc load interfaced to the WG by a VSC.

and the ac system are interfaced. The VSC is interfacing a dc grid or load on the dc-side to the ac grid. There is a filter capacitor at the dc-side that filters out the ripples and smooths the dc voltage. As shown in the figure, the electrical grid is modeled as an ideal voltage source with voltage  $v_g$  and an equivalent series impedance with parameters  $L_g$  and  $r_g$ . The VSC can exchange active power and reactive power with the WG depending on the mode of operation.

Switching PECs including VSCs are nonlinear devices. The switching models can accurately capture the dynamics and steady-state behavior of the converter [8]. However, besides the fact that simulating the converter-dominant systems using the detailed switching models of the VSCs is excessively long especially when there is a large number of converters and different dynamic scenarios are involved, these models do not give enough analytical insight into the input-output relationship of the converters [16]. Therefore, the averaging technique is introduced to remove the high-frequency components of the switching functions from the VSC dynamic equation and provide an average model of the VSC which can be conveniently used in designing a linear controller for the VSC [8]. Based on the developed VSC average model, the relationship between the dc-side average voltage  $v_{dc}$  and the VSC terminal phase voltage  $v_t$  is presented by

$$\langle v_t \rangle_{T_s} = \frac{1}{2} m \langle v_{dc} \rangle_{T_s} \quad (1-1)$$

where  $\langle \cdot \rangle_{T_s}$  denotes the average of a variable over one switching cycle  $T_s$  and  $m$  is the modulation index which is the control input in the linear closed-loop control model of the VSC. For brevity, the averaging angle brackets are dropped from all VSC averaged variables in the rest of the thesis.

The control system of the VSC is shown schematically in Figure 1.2(b). The control system is the conventional linear voltage-oriented control (VOC) which is a type of current control (CC)<sup>5</sup> where the VSC combined with the ac-side filter inductance is regulated as a controlled current source in the voltage-oriented coordination [17]. In this method, phase variables, which are initially in  $abc$  reference frame ( $abc$ -RF), are transformed into synchronously rotating (with the voltage phasor) direct-quadrature RF ( $dq$ -RF) before the control process [5], [6]. A closed-loop mechanism named phase-locked loop (PLL) is used to track the phase angle of the VSC output voltage  $v_o$  and generate the required angle for the RF transformation. In grid-connected applications, in addition to exchanging the active power with the ac grid, the VSC is usually responsible for either injecting the reactive power or regulating the PCC voltage magnitude. When connected to the WG, the latter application is more common [18], [19]. AC voltage control (AVC) is implemented as the outer control loop to regulate the output voltage (at the PCC ac bus) at the nominal value since the grid is assumed to be nonstiff [8], [12], [18]–[22]. Moreover, dc voltage control (DVC) is used to regulate the dc voltage  $v_{dc}$  if required.

In the innermost part of the VOC method, CC loops are used to regulate the  $L$  filter current components in  $dq$ -RF through issuing the reference signals, denoted by  $m$  in Figure 1.2(b), for the modulation block. The conventional sinusoidal pulse-width modulation (PWM) technique is used to command the VSC switches [8] where  $m$  is used as the input. Further discussion about other PWM techniques and control methods of VSC controllers including the nonlinear class of controllers are presented in [23].

---

<sup>5</sup> Also known as the current-mode control [8].

### 1.2.2. Stability Study of AC Power Grids with Presence of Power Electronic Converters

Stationary phasors were introduced more than a century ago to facilitate the computation and analysis of the power system when in stationary operation, i.e., steady state, [24]. While the stationary phasors are extensively useful in the steady-state condition, they do not seem to be useful tools, by definition, when studying the power system involves dynamics or transients. Traditionally, there are three common stability problems in power systems: static (steady-state) stability, dynamic stability and transient stability [25], [26]. While the first category involves small disturbances or perturbations in the power system variables, the latter two relate to larger perturbations or fault occurrence in the power system. Therefore, the assumption of stationarity can be relaxed to an approximation, under the so called quasistationary theory, which allows slow variations in the voltages, current, and powers such that the classic phasors could be retrieved [16], [24].

The introduction of quasistationary phasors facilitates small-signal stability study of the power system, especially in the transmission level where the synchronous machines with slow dynamics dominate the rest of the system. As an example, the well-known rotor angle stability problem of the power system can be studied by linearizing the well-known steady-state expression of active power. This is justified because of the low-frequency nature of the rotor angle oscillations<sup>6</sup> (typically slower than 0.5 or one-third Hz [24]). Therefore, the electromechanical or low-frequency scale stability study of power system is developed upon the quasistationary phasors

Due to the physical inertia in the synchronous generators, there is a natural coupling between the generator operating frequency and output active power [27]. However, in PECs, this natural coupling does not exist. Hence, to maintain stability, especially in microgrids, the PEC control system needs to be designed with attention to overall system stability concerns. Moreover, with the advancement in power electronics, modern PECs with high switching frequencies are introduced. This allows for the voltage and current control design of medium to high-frequency bandwidths range; typically

---

<sup>6</sup> In technical literature, these oscillations are referred to as swings and the differential equation describing the synchronous generator dynamics is known as swing equation [1].

around 0.5-1.5 kHz<sup>7</sup> [7], [28]. With the growing adoption of renewable energies and proliferation of PECs in modern grids and microgrids, the lack of physical inertia appears to be problematic in PEC-dominated grids [10], [27]. Therefore, studying the stability of such converter-dominated systems becomes more important than before.

With the inherent fast dynamics of modern PECs, the corresponding dynamic modes of the instabilities (or undesired oscillations) disperse from low- to medium-frequency range particularly in WG systems [28], [30]–[32]. A few works have studied stability of converter-dominated ac systems using quasistationary theory where the dynamics of voltage and current controls are ignored, i.e., reduced-order modeling is applied, [27], [33], [34]. While these models can significantly enhance the computational speed, however, their lack of accuracy can lead to completely wrong conclusions about the system dynamics and stability when the effect of medium-frequency or higher dynamics are involved [33]. Overall, the quasistationary theory does not appear to be a proper means to study the dynamics and stability of converter-dominated ac systems.

### 1.2.3. Small-Signal Model of VSC for Stability Study

Three-phase VSCs are time-variant dynamical systems due to periodically changing operating trajectory and switching functions; and nonlinear because of the control input  $m$  which is dynamically changing with the closed-loop feedback control [35]. By using the averaging technique, the influence of switching functions can be eliminated to a great point. Further, using the RF transformation, the VSC ac variables can be transformed into dc  $dq$  variables in the steady state, thereby, permitting the system linearization and small-signal analysis system similar to the dc-dc PECs [8], [16].

Alternative methods to RF-transformation include dynamic phasors and harmonic linearization [16], [35]. Both methods are based on the truncated Fourier transform of the complex nonlinear systems. While single-phase and unbalanced systems dynamics can be modeled and studied by these methods, however, they are limited with respect to accuracy in some applications like studying system dynamics below the line (fundamental) frequency [16], [33]. Hence, care must be taken when interpreting the results obtained by these methods. Moreover, the corresponding system modeling is

---

<sup>7</sup> The length of transients in the time frame of 0.1 ms to 1 s is classified as electromagnetic time scale in power system [29].

often lengthy and requires relatively complex mathematics. Therefore, to mitigate possible instabilities, the compensator design would be laborious and may not be straightforward [8]. In summary, the application of the latter two methods still demands more investigation [36].

Different methods in the area of power system dynamics and stability can be broadly classified as time-domain state-space approaches and frequency-domain impedance approaches [16]. Both approaches require linear time-invariant (LTI) models of power system components which, as mentioned before, can be obtained by linearizing the developed dynamic models in  $dq$ -RF. In impedance approach, loads and sources are modeled by their input or output impedances. Then, Nyquist stability is used to assess the system stability [16]. Clearly, this method is well-suited for systems with changing structures, namely, distribution ac systems where the connection and disconnection of different loads have a considerable effect on the system overall dynamics and stability. However, the system dynamics in  $d$ - and  $q$ -axis are generally coupled. Therefore, the stability problem cannot be decomposed into study of two decoupled single-input-single-output (SISO) systems where the conventional Nyquist stability criterion [9] can be applied. This complicates the analysis and design [9], [16]. With simplifying assumptions, non-diagonal components of the stability matrix can be set to zero [9], yet, at expense of reducing the system model accuracy.

The state-space approach is the traditional method of studying power system stability in an electromechanical time scale [26]. In this method, loads and sources dynamics are merged to form a total state-space dynamic model that accurately describes the system dynamics. In the state-space approach, the system dynamic modes can be identified and the participation of different variables in the dominant modes can be assessed. These are the superior features of the state-space approach which the impedance approach does not provide [26], [35]. Since the dynamical systems that are studied in the following chapters are not of an excessively high order, the state-space approach is chosen to study these systems in the remainder of this thesis.

#### **1.2.4. Dynamic interaction between VSC control, ac filter, and grid impedance**

At the distribution level,  $LC$  filters usually replace  $L$  filter for interfacing VSC to the ac grid

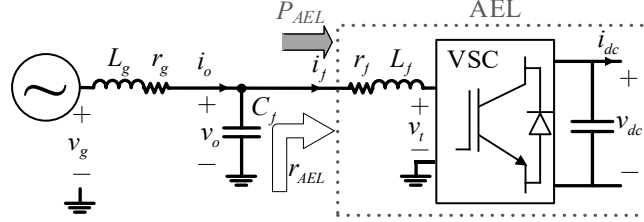


Figure 1.3: VSC controlled as an AEL.

because the grid impedance is not negligible. The capacitance of the filter provides a low-impedance path for the high-frequency components of the current [8], [37]. A resistor is used in series with the capacitance to damp the high-frequency resonance of the  $LC$  filter. Alternatively, an active method can be used to avoid extra power loss in the VSC  $LC$  filter and design difficulty [37], [38]. With this modification in place, dynamic interaction between the tightly regulated VSC and the  $LC$  filter and/or the WG impedance can still induce instability.

Figure 1.3 shows a VSC that works in the rectification mode supplying a dc load. The VSC with the dc-link and  $L$  filter can be considered as an active electronic load (AEL) from the grid point of view. If the CC of the converter has high-bandwidth regulation and the VSC power loss and the effect of harmonics are negligible, then the instantaneous real power  $P_{AEL}$  consumed by the AEL can be assumed constant<sup>8</sup>. If the VSC dynamic model is developed on a  $dq$ -RF that is synched with the output voltage of phase  $a$ , then

$$P_{AEL} = \frac{3}{2}(v_{od}i_{fd} + v_{oq}i_{fq}) = \frac{3}{2}v_{od}i_{fd}. \quad (1-2)$$

In (1-2), the subscript “ $d$ ” denotes the  $d$ -axis component of a variable. Linearizing (1-2), results in

$$\tilde{P}_{AEL} = \left(\frac{3}{2}\right)(\tilde{v}_{od}i_{fd}^{\circ} + v_{od}^{\circ}\tilde{i}_{fd}) = 0 \quad (1-3)$$

where “ $\sim$ ” and “ $^{\circ}$ ” denote small-signal perturbations and the nominal value of a variable, respectively. From (1-3), the output impedance of the AEL can be obtained as follows.

<sup>8</sup> These types of loads are known as constant power loads in power system and power electronics studies.

$$r_{AEL} = -\frac{v_{od}^{\circ}}{i_{fd}^{\circ}} \quad (1-4)$$

where  $r_{AEL}$  is known as the negative incremental resistance (NIR) in the literature [39]. The negative resistance can excite the resonance frequency of the  $LC$  circuit and induce unstable oscillations in the system variables. In the case of nonideal AEL, where the VSC control bandwidth is limited, the DVC closed-loop system represents a nonminimum-phase system in the rectification mode which can become unstable at certain amounts of power [8]. In the inversion mode of operation, increasing the bandwidth of the PLL yields a wider frequency range where the VSC exhibits NIR at the output [28]. Therefore, the interaction between the PLL and the WG impedance can be a source of instability in VSC-WG systems [30]. Further, it is shown in [40] and [41] that the PLL and AVC can contribute to provoking instability in VSC-WG systems mostly when their bandwidths are close to DVC bandwidth.

When the ac grid impedance is not negligible, the PCC voltage can change depending on the power flow condition between the VSC and the grid and any other possible load switching. In this case, the grid is said to be operating under nonstiff conditions [8]. The reasons for nonstiff conditions are detailed in the next chapters. To quantify the strength of the grid, the short-circuit ratio ( $SCR$ ) is defined as the ratio of the grid short circuit power at the PCC to the rated dc power of the VSC [1] as given by

$$SCR = \frac{V_n^2}{P_n |Z_g|} \quad (1-5)$$

where  $V_n$ ,  $P_n$ , and  $Z_g$  are, respectively, the grid nominal voltage, VSC nominal dc power, and the grid impedance; and  $|\cdot|$  is the absolute value function. A grid is considered weak when  $2 < SCR < 3$ , and very weak when  $SCR < 2$ , otherwise it is a stiff grid (SG) [14], [19], [40], [42], [43].

The VOC of VSC has a detrimental effect on the stability of the VSC-to-grid interconnection and can shift the location of the system eigenvalues which might result in poorly damped dynamics and power oscillations [28]. The smaller the  $SCR$  level is, the more prone is the system to instability [44]. A review of the literature reveals five major approaches to improving the stability of VSC-WG systems: (1) designing system parameters considering the possible dynamic interactions in the obtained linear model at different operating conditions [14], [30], [45]; (2) adding passive damping (or equivalent

active damping) to the *LC* filter [38], [46]; (3) shaping the VSC output impedance to avoid dynamic interaction with the grid [20], [47]; (4) removing the PLL by replacing the conventional current-controlled VOC method with the power synchronization method or a nonlinear controller [18], [43]; (5) active compensation method [9], [10], [48], [49].

In the first approach, the VSC parameters need to be designed with excessive design conservatism to avoid possible instabilities. This is usually realized at the cost of VSC limited transient response [21]. The second approach, merely, increases the power conversion loss. Further, as will be shown in the next chapters, the method has a trivial effect on the VSC-WG stability. The third approach often results in changes in the VSC steady-state operation which might have an adverse impact on the system performance including efficiency because usually the VSC control system is designed according to the original nominal operating point. In the fourth approach, the VSC suffers from a lack of overcurrent protection. Therefore, the control design needs to switch back to the current-mode control upon the occurrence of major transients which makes the control design too complicated.

In the fifth method, linear function(s) of system states is dynamically injected into the primary control loops of the VSC control as a form of a feedforward compensation mechanism without changing the system steady-state settings. As a result, the system dominant eigenvalues shift towards the stable region of the complex plane. The application of active compensation has been reported in several works to improve the stability of SGs or microgrids with high penetration of AELs or induction motor loads. Improving stability of a VWG with high integration of current source converter-interfaced RES using active compensation is done in [50].

### **1.3. Summary of Contributions and Outline of the Dissertation**

With the destabilizing effect of dynamic interactions during the connection of the VOC-based VSCs to the WG and the shortcomings of the previous methods, there is still a requirement for active methods that do not change the system steady-state values and can be easily integrated into the conventional VOC of the VSC under very weak conditions. Moreover, their design is independent of the VSC primary control system and totally based on the conventional linear theory tools. To this end, the linear active

compensation method is a promising candidate to improve the mitigate the destabilizing effect of dynamic interactions in weak connections and improve the overall stability of the system in case of high integration of VSC-interfaced loads and DGs. To the best of the author's knowledge, this method with the mentioned qualities has not been tried in VSC-WG systems so far.

Moreover, unlike the WGs which have been the subject of many previous works, the WMG is a novel concept in modern ac power grids and has not been officially reported in the technical literature. Since microgrids, by definition, lack physical inertia and hence are dynamical systems with low damping, the dynamic instabilities in these systems are of major concern. Hence, WMG systems dynamics and stability deserve a thorough study for the future expansion of active power systems. The contributions of this thesis and its outline are summarized as follows.

Based on what is discussed previously, this study is an attempt to find linear active methods to accomplish the stable integration of three-phase dc/ac VSCs in very weak grid or very weak microgrid systems.

### **1.3.1. Chapter 2: Dynamic Model of VSC-WG and Control Design**

This chapter provides the detailed dynamic modeling of the VOC-based VSC including the power circuit and all necessary control dynamics in  $dq$ -RF: CC, DVC, PLL, and AVC. Particularly, an analytical transfer function of the PCC dynamics in WG applications is presented which results in a SISO transfer function plant that accurately describes the PCC dynamics in WG connections. This facilitates the design of AVC controller using linear control methods. The performance of the new analytical model and its superiority over the conventional oversimplified model has been successfully tested and the results are published in [51].

### **1.3.2. Chapter 3: Small-Signal Analysis and Stability Improvements of VSC-WG in Inversion Mode**

In this chapter, the dynamics and stability of VSC-WG systems in the inversion mode are studied under the VWG condition, i.e.,  $SCR = 1$ . To this end, the small-signal model of the system is represented in a state-space form where the influence of all control loops is considered. Next, a linear active compensation is adopted to tackle the instability

issues due to dynamic interaction under VWG conditions. Then the performance comparison is drawn between the compensated and uncompensated models followed by supportive simulation and hardware-in-the-loop (HIL) results which are published in [51].

### **1.3.3. Chapter 4: Small-Signal Analysis and Stability Improvements of VSC-WG in Rectification Mode**

This chapter is a complement to the previous chapter in the sense that the dynamics of VSC-WG are studied under rectification mode. As such, a comparison is drawn between the inversion and rectification modes of operation with respect to system stability of VSC-WG systems with the same VSC parameters at different operating points. It is shown that the system is more prone to instability in the rectification mode than the inversion when the dc power increases and there are more destabilizing modes in the former under the nominal power condition. Based on these observations, a dual active compensation (DAC) method is proposed which improves the system stability and enhances the system dynamics. Small-signal models of the system with and without DAC are developed. Simulation and HIL tests are carried out to verify the analytical analysis. The results are published in [52]–[54].

### **1.3.4. Chapter 5: Dynamic Modeling and Stability Analysis of Converter-Based AC Microgrids**

This chapter investigates the dynamics and stability of an AC microgrid in isolated mode with three VSIs that are locally controlled using the conventional droop method to share active and reactive powers and three PLs and one AEL that are supplied within the microgrid at different locations. The full-dynamic small-signal model of the ac microgrid with and without AEL and considering all operational control loops inside the VSCs is developed and presented in state-space forms. With the help of small-signal analysis, it is shown that the presence of AEL in the ac microgrid negatively affects the overall stability of the system such that the ac microgrid with one of its PLs being replaced by an AEL becomes unstable at some level of power (less than the nominal power) while the original microgrid with three PLs exhibits stable operation. The numerical simulations are also presented to verify the analytical developments. The results are published in [55].

### **1.3.5. Dynamic Modeling and Stability Improvements of Weak AC Microgrid Systems**

In this chapter, the concept of WMG is introduced and studied for the first time. To formulate the weakness of a WMG, the traditional SCR is generalized to include WMG systems. Two WMGs, each with two VSIs, one with an AEL and the other with a PL, are developed for the dynamic study. It is revealed that with the increase of the SCR, instabilities appear due to modes related to VSI droop control and DVC loop of VSR (related to AEL). Two different active compensation methods are utilized to tackle the instability issue. The results show that with the suggested methods, WMGs can stably operate while supplying a nominal load of AEL or PL type and under VWG conditions. A paper that covers the findings of this chapter is in preparation for a journal publication.

### **1.3.6. Chapter 7: Conclusions and Suggestions for Future Works**

The research outcomes and achievements are summarized in this chapter. General conclusions are made based on the theories, simulations, and experiments provided in the thesis. Some ideas that have been generated during the whole project but have not had a chance to be investigated are suggested as future works.

## Chapter 2.

### Dynamic Model of VSC-WG and Control Design

In this chapter, first, multiple control loops of VOC scheme of a VSC-WG system are introduced. The VOC includes inner CC loops; and outer dc-side DVC, PLL, and AVC loops. Then, the linearized dynamic models of control loops are developed and illustrated as SISO systems which establishes a ground to design the VSC controllers. Traditionally, an approximate model is used for the PCC voltage dynamics based on which, the AVC closed-loop dynamics is established. However, as it is shown in this chapter, this oversimplification results in unpredicted oscillatory which can end in unstable system behaviour. To circumvent the shortcoming of this modeling, a detailed modeling of the PCC voltage dynamics is presented. The results of large-signal simulation of the VSC-WG validate the effectiveness of the detailed modeling which can be further used to design the VSC controllers in VSC-WG systems. The organization of this chapter is as follows. In Section 2.1, the mathematical model of the VSC-WG system and the controllers are studied followed by presentation of a detailed model of PCC voltage dynamics which is then compared with the simplified model. In Section 2.2, a discussion of the tuning of the control parameters is briefly presented. Time-domain simulation results are provided in Section 2.3 to validate the dynamic models developed in Section 2.1. Finally, conclusions are presented in Section 2.4.

#### 2.1. VSC-WG Dynamic Model

A VSC-WG system and the corresponding control system VOC, that manages the power flows at the ac- and dc-side of the converter, are shown in Figure 2.1. The dynamic equations relating to the VSC circuit and control parts are described in the synchronous  $dq$ -RF in the following sections. It should be noted that all the equations are written in the  $dq$ -RF in the frequency domain wherein  $s$  represents the Laplace operator, unless stated otherwise. Throughout this chapter, the  $d$ - and  $q$ -axis components of variables are denoted by subscripts “ $d$ ” and “ $q$ ”, respectively; the reference value and steady-state value of variables are denoted by superscript “ $ref$ ” and “ $o$ ”, respectively; and superscript “ $\sim$ ” denotes small-signal perturbations of a variable.

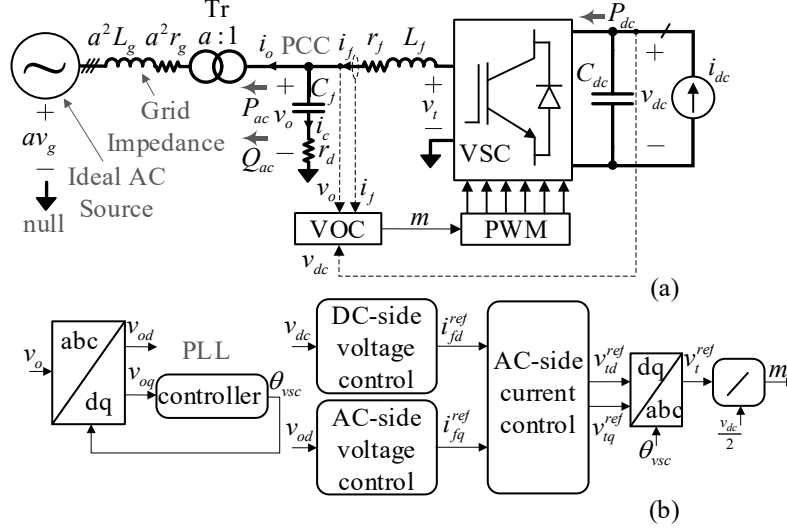


Figure 2.1: VSC-WG system. (a) VSC with LC filter connected to the utility grid through a step-up transformer and the grid impedance. (b) VSC control loops.

### 2.1.1. Power Circuit

A VSC-WG system and the corresponding control system VOC, are shown in Figure 2.1. Based on Figure 2.1(a), the mathematical models of the grid impedance and the LC filter are given as

$$\begin{bmatrix} v_{td} \\ v_{tq} \end{bmatrix} = \begin{bmatrix} v_{od} \\ v_{oq} \end{bmatrix} + Z_f(s) \begin{bmatrix} i_{fd} \\ i_{fq} \end{bmatrix} + \omega_{vsc} L_f \begin{bmatrix} -i_{fq} \\ i_{fd} \end{bmatrix} \quad (2-1)$$

$$\begin{bmatrix} v_{od} \\ v_{oq} \end{bmatrix} = \begin{bmatrix} v_{gd} \\ v_{gq} \end{bmatrix} + Z_g(s) \begin{bmatrix} i_{od} \\ i_{oq} \end{bmatrix} + \omega_{vsc} L_g \begin{bmatrix} -i_{oq} \\ i_{od} \end{bmatrix} \quad (2-2)$$

$$\begin{bmatrix} i_{fd} \\ i_{fq} \end{bmatrix} = \begin{bmatrix} i_{od} \\ i_{oq} \end{bmatrix} + sC_f \begin{bmatrix} v_{cd} \\ v_{cq} \end{bmatrix} + \omega_{vsc} C_f \begin{bmatrix} -v_{cq} \\ v_{cd} \end{bmatrix} \quad (2-3)$$

$$\begin{bmatrix} v_{cd} \\ v_{cq} \end{bmatrix} = \begin{bmatrix} v_{od} \\ v_{oq} \end{bmatrix} - r_d \begin{bmatrix} i_{fd} - i_{od} \\ i_{fq} - i_{oq} \end{bmatrix} \quad (2-4)$$

where  $Z_f(s) = r_f + s\omega_{vsc}L_f$  and  $Z_g(s) = r_g + s\omega_{vsc}L_g$  are the impedances of the filter inductor and grid impedance, respectively, and  $\omega_{vsc}$  is the angular frequency provided by the PLL.

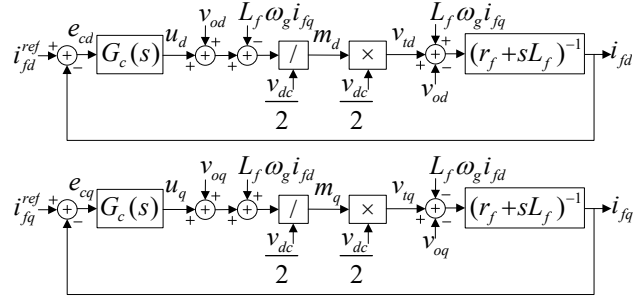


Figure 2.2: Block diagram of the CC loops.

### 2.1.2. Current Control

The block diagram of the CC loops, which is the innermost control loop, is shown in Figure 2.2. As shown, a pair of similar proportional-and-integral (PI) compensators, denoted by  $G_c(s) = K_{pc} + K_{ic}s^{-1}$ , regulate the currents  $i_{fd}$  and  $i_{fq}$  to the corresponding reference values,  $i_{fd}^{ref}$  and  $i_{fq}^{ref}$ , that are assigned by the outer control loops; the DVC and AVC, respectively. Therefore, the following holds.

$$\begin{bmatrix} u_d \\ u_q \end{bmatrix} = G_c(s) \begin{bmatrix} i_{fd}^{ref} - i_{fd} \\ i_{fq}^{ref} - i_{fq} \end{bmatrix} \quad (2-5)$$

where  $u_d$  and  $u_q$  are the control inputs. As shown in Figure 2.2, the modulation indices  $m_d$  and  $m_q$ , that are the input of the VSC PWM block, are defined as

$$\begin{bmatrix} m_d \\ m_q \end{bmatrix} = \left( \begin{bmatrix} u_d \\ u_q \end{bmatrix} + \omega_{vsc} L_f \begin{bmatrix} -i_{fq} \\ i_{fd} \end{bmatrix} + \begin{bmatrix} v_{od} \\ v_{oq} \end{bmatrix} \right) \frac{2}{v_{dc}} \quad (2-6)$$

where the second and third terms are added to decouple the  $d$ - and  $q$ -axis closed-loop dynamics and reject the disturbances, i.e.,  $v_{od}$  and  $v_{oq}$  [8]. If the PWM dynamics are neglected and the fundamental components of the terminal voltage are considered, the following holds [8].

$$\begin{bmatrix} v_{td} \\ v_{tq} \end{bmatrix} = \begin{bmatrix} m_d \\ m_q \end{bmatrix} \frac{v_{dc}}{2} \quad (2-7)$$

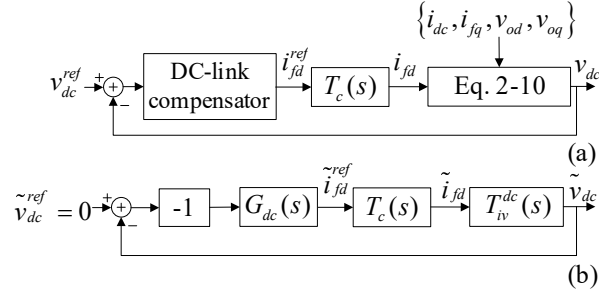


Figure 2.3: Block diagram of the DVC control loop. (a) Large-signal model. (b) Small-signal model

Applying (2-5)–(2-7) into (2-1) results in the following transfer function for the CC loops.

$$T_c(s) = \frac{i_{fd}}{i_{fd}^{ref}} = \frac{i_{fq}}{i_{fq}^{ref}} = \frac{K_{pc}s + K_{ic}}{L_f s^2 + (r_f + K_{pc})s + K_{ic}} \quad (2-8)$$

### 2.1.3. DC-Link Voltage Control

Neglecting the power losses in the VSC switches, the dc power  $P_{dc}$  is equal to the instantaneous active power at the VSC terminals in Figure 1.2(a), which in turn, is the sum of the instantaneous power corresponding to the LC filter and the active power of the VSC injected into the grid,  $P_{ac}$ . Therefore, the following can be written [8].

$$v_{dc} i_{dc} = \frac{1}{2} C_{dc} s v_{dc}^2 + \frac{3}{4} L_f s (i_{fd}^2 + i_{fq}^2) + \frac{3}{2} r_f (i_{fd}^2 + i_{fq}^2) + \frac{3}{2} (v_{od} i_{fd} + v_{oq} i_{fq}) \quad (2-9)$$

Figure 2.3(a) shows the block diagram of the DVC loop based on (2-9). Due to the PLL, discussed in the sequel,  $v_{oq}$  is zero in the steady state. Therefore, (2-9) can be linearized into

$$(C_{dc} v_{dc}^{\circ} s - i_{dc}^{\circ}) \tilde{v}_{dc} = v_{dc}^{\circ} \tilde{i}_{dc} - \frac{3}{2} L_f s (i_{fd}^{\circ} \tilde{i}_{fd} + i_{fq}^{\circ} \tilde{i}_{fq}) - 3r_f (i_{fd}^{\circ} \tilde{i}_{fd} + i_{fq}^{\circ} \tilde{i}_{fq}) - \frac{3}{2} (v_{od}^{\circ} \tilde{i}_{fd} + i_{fd}^{\circ} \tilde{v}_{od} + i_{fq}^{\circ} \tilde{v}_{oq}) \quad (2-10)$$

Rearranging (2-10) to isolate  $\tilde{v}_{dc}$  results in

$$\tilde{v}_{dc} = T_{iv}^{dc}(s) \tilde{i}_{fd} + \Gamma_1(s) \quad (2-11)$$

where

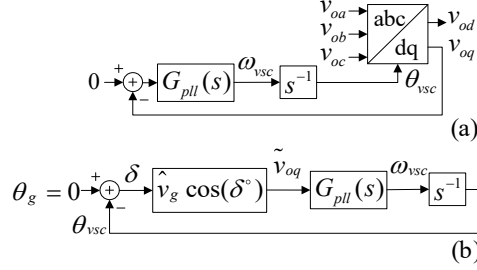


Figure 2.4: Block diagram of the PLL control loop. (a) Large-signal model. (b) Small-signal model.

$$T_{iv}^{dc}(s) = \frac{\tilde{v}_{dc}}{\tilde{i}_{fd}} = -\frac{3L_f \tilde{i}_{fd}^\circ s + 2r_f \tilde{i}_{fd}^\circ + v_{od}^\circ}{C_{dc} v_{dc}^\circ s - i_{dc}^\circ} \quad (2-12)$$

is the transfer function from  $\tilde{i}_{fd}$  to  $\tilde{v}_{dc}$  and  $T_1(s)$  is a linear function showing the effect of the disturbances, i.e.,  $i_{dc}$ ,  $i_{fg}$ ,  $v_{od}$ , and  $v_{oq}$ . As Figure 2.3(b) shows, a PI compensator, i.e.,  $G_{dc}(s) = K_{pdc} + K_{idc}s^{-1}$ , is employed to regulate  $v_{dc}$  to  $v_{dc}^{ref}$  and the output of the compensator  $i_{fd}^{ref}$  is given to the CC block. Also, a negative gain is added to the forward path to preserve the closed-loop stability. According to Figure 2.3, the following relation between  $v_{dc}^{ref}$  and  $i_{fd}^{ref}$  exists.

$$i_{fd}^{ref} = -G_{dc}(s)(v_{dc}^{ref} - v_{dc}) \quad (2-13)$$

#### 2.1.4. Phase-Locked Loop

The PLL, shown in Figure 2.4(a), is based on tracking the angle of the PCC voltage by regulating  $v_{oq}$  to zero as given by

$$\omega_{vsc} = s\theta_{vsc} = G_{pll}v_{oq} \quad (2-14)$$

$$\delta = \theta_g - \theta_{vsc} = (\omega_g - \omega_{vsc})s^{-1} \quad (2-15)$$

where  $\omega_{vsc}$  and  $\theta_{vsc} = \omega_{pll}t + \theta_{vsc0}$  are, the VSC frequency and phase angle generated by the PLL, respectively;  $\omega_g$  and  $\theta_g = \omega_g t + \theta_{g0}$  are the frequency and the phase angle of the grid voltage, respectively;  $\delta$  is the phase angle difference; and  $G_{pll}(s) = K_{p\omega} + K_{i\omega}s^{-1}$  is the PI compensator. The grid voltage  $v_g$  can then be decomposed into  $dq$  components on the  $dq$ -RF as

$$v_{gd} = \hat{v}_g \cos(\delta) \quad (2-16)$$

$$v_{gq} = \hat{v}_g \sin(\delta) \quad (2-17)$$

where  $\hat{v}_g$  is the magnitude of the grid voltage. Substituting for  $v_{oq}$  in (2-14) from (2-2) and then substituting for  $v_{gq}$  from (2-17) in the result gives the nonlinear dynamics of the PLL as

$$\omega_{vsc} = s\theta_{vsc} = G_{pll}(s)(\hat{v}_g \sin(\delta) + (Z_g i_{oq} + \omega_{vsc} L_g i_{od})) \quad (2-18)$$

where the second term in the right-hand-side shows the effect of the grid impedance on the PLL dynamics. If the grid impedance is small, i.e.,  $Z_g(s) \approx 0$ , then  $v_{od} \approx v_{gd}$  and  $\delta \approx 0$  in the steady state. If the grid frequency is constant, then can be linearized as

$$\tilde{\omega}_{vsc} = s\tilde{\theta}_{vsc} = G_{pll}(s)(-\hat{v}_g \cos(\delta^\circ)\tilde{\theta}_{vsc} + \Gamma_2(s)) \quad (2-19)$$

where  $\Gamma_2(s)$  is a linear function showing the effect of the disturbances  $\omega_{vsc}$ ,  $i_{od}$ , and  $i_{oq}$ , which are yielded from the nonzero grid impedance. Ignoring the disturbances in (2-19), the small-signal dynamics of the PLL control can be obtained as shown in Figure 2.4 (b). However, the overall dynamics of the  $\tilde{\theta}_{vsc}$  is significantly affected by the grid disturbances under the WG condition.

## 2.1.5. AC Voltage Control

### ***Detailed Model of PCC Voltage Dynamics***

Since  $v_{oq}$  is regulated to zero by the PLL, the regulation of the PCC voltage is limited to  $v_{od}$ . Similar to the CC loops, AVC loops are introduced in [5] where the feedforward terms are introduced to reject the output current disturbances, i.e.,  $i_{od}$  and  $i_{oq}$  in (2-3), and derive the decoupled SISO outer control loops in the  $dq$ -RF. However, this method cannot be applied to the VSC-WG system since the DVC block regulates the value of  $i_{fd}^{ref}$ . Also,  $v_{oq}$  is set to zero by the PLL. Therefore, a different method is adopted here for the AVC, which is originally used to control the PCC voltage in the static compensator (STATCOM) applications [8], as follows. Linearizing (2-2) results in

$$\begin{bmatrix} \tilde{v}_{od} \\ \tilde{v}_{oq} \end{bmatrix} = \begin{bmatrix} \tilde{v}_{gd} \\ \tilde{v}_{gq} \end{bmatrix} + Z_g(s) \begin{bmatrix} \tilde{i}_{od} \\ \tilde{i}_{oq} \end{bmatrix} + \omega_{vsc}^\circ L_g \begin{bmatrix} -\tilde{i}_{oq} \\ \tilde{i}_{od} \end{bmatrix} + L_g \tilde{\omega}_{vsc} \begin{bmatrix} -i_{oq}^\circ \\ i_{od}^\circ \end{bmatrix} \quad (2-20)$$

where  $\tilde{v}_{gd}$  and  $\tilde{v}_{gq}$  are obtained by replacing  $\delta$  in (2-16) and (2-17) from (2-15) and linearizing the results; and  $\tilde{\omega}_{vsc}$  and  $\tilde{\theta}_{vsc}$  are given in terms of  $\tilde{v}_{oq}$  by perturbing (2-14). Moreover, considering the current of the ac filter capacitor  $i_c$  as a negligible portion of the inductor current  $i_f$  [56], then  $i_{fd} \approx i_{od}$  and  $i_{fq} \approx i_{oq}$ . After some mathematical manipulations,  $\tilde{v}_{od}$  and  $\tilde{v}_{oq}$  are obtained from (2-20) as functions of  $\tilde{i}_{fd}$  and  $\tilde{i}_{fq}$  in the following.

$$\tilde{v}_{od} = (G_1(s)G_2^{-1}(s) + 1)Z_g(s)\tilde{i}_{fd} + (G_1(s)G_2^{-1}(s) - 1)\omega_{vsc}^\circ L_g \tilde{i}_{fq} \quad (2-21)$$

$$\tilde{v}_{oq} = G_2^{-1}(s)(Z_g(s)\tilde{i}_{fq} + \omega_{vsc}^\circ L_g \tilde{i}_{fd}) \quad (2-22)$$

where

$$G_1(s) = G_{pll}(s)(\hat{v}_g \sin(\delta^\circ)s^{-1} - L_g i_{fq}^\circ) \quad (2-23)$$

$$G_2(s) = 1 + G_{pll}(s)(\hat{v}_g \cos(\delta^\circ)s^{-1} - L_g i_{fd}^\circ) \quad (2-24)$$

In [8],  $\tilde{i}_{fd}$  is neglected because the VSC injects zero active power to the grid in the STATCOM applications. Therefore, further treatment is needed to include the effect of  $i_{fd}$  in this chapter. Perturbing (2-13) and rewriting the equation in terms of  $\tilde{i}_{fd}^{ref}$  yields

$$\tilde{v}_{dc} = G_{dc}^{-1}(s)\tilde{i}_{fd}^{ref} \quad (2-25)$$

The AVC is designed to have a much smaller bandwidth compared with the CC loop. Therefore,  $i_{fd} \approx i_{fd}^{ref}$  in the time scale of the voltage dynamics. Thus,  $\tilde{v}_{dc}$  in (2-10) can be replaced by its equivalent in (2-25) as a function of  $i_{fd}$ . Ignoring  $i_{dc}$  as a disturbance, the result can be rearranged to express  $\tilde{i}_{fd}$  as

$$\tilde{i}_{fd} = G_3(s)^{-1}(i_{fd}^\circ \tilde{v}_{od} + i_{fq}^\circ \tilde{v}_{oq} - i_{fq}^\circ (Z_f(s) + r_f)\tilde{i}_{fq}) \quad (2-26)$$

where

$$G_3(s) = -\frac{2 C_{dc} v_{dc}^\circ s^2 - i_{dc}^\circ s}{3 (K_{pdc} s + K_{idc})} - (Z_f(s) i_{fd}^\circ + r_f i_{fd}^\circ + v_{od}^\circ). \quad (2-27)$$

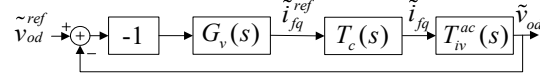


Figure 2.5: Block diagram of the AVC loop.

Using the equivalent expression for  $\tilde{v}_{od}$  and  $\tilde{v}_{oq}$ , given by (2-21) and (2-22), respectively, in (2-26) then  $\tilde{i}_{fd}$  can be expressed in terms of  $\tilde{i}_{fq}$  after a laborious manipulation as

$$\tilde{i}_{fd} = \frac{N_1(s)}{D_1(s)} \tilde{i}_{fq} \quad (2-28)$$

where

$$N_1(s) = (G_1(s) - G_2(s))\omega_{vsc}^\circ L_g + G_3(s)i_{fq}^\circ Z_g(s) - i_{fq}^\circ G_2(s)G_3(s)(Z_f(s) + r_f) \quad (2-29)$$

$$D_1(s) = G_2(s)G_3(s) - (G_1(s) + G_2(s))Z_g(s)i_{fd}^\circ - G_3(s)\omega_{vsc}^\circ L_g i_{fq}^\circ \quad (2-30)$$

Finally, replacing  $\tilde{i}_{fd}$  in (2-21) by its equivalent in (2-28), the current-to-voltage transfer function  $T_{iv}^{ac}(s)$  is deduced as

$$T_{iv}^{ac}(s) = \frac{\tilde{v}_{od}}{\tilde{i}_{fq}} = (G_1(s)G_2^{-1}(s) + 1)Z_g(s)\frac{N_1(s)}{D_1(s)} + (G_1(s)G_2^{-1}(s) - 1)\omega_{vsc}^\circ L_g \quad (2-31)$$

Figure 2.5 shows the control block diagram of the PCC voltage, where  $G_v(s) = K_{pv} + K_{iv}s^{-1}$  is the PI compensator employed to regulate  $v_{od}$ . As shown, a negative gain is added to the forward path to preserve the closed-loop stability. According to Figure 2.5, the AVC set the value of  $i_{fq}^{ref}$  such that

$$i_{fq}^{ref} = -G_v(s)(v_{od}^{ref} - v_{od}) \quad (2-32)$$

### **Simplified Model of PCC Voltage Dynamics**

The simplified model, which is widely used in the literature for the AVC design [8], [50], [57] is presented in this section. According to (2-19),  $\tilde{\theta}_{vsc}$  and  $\tilde{\omega}_{vsc}$  are functions of  $\tilde{i}_{od}$  and  $\tilde{i}_{oq}$ . Therefore, their transient excursion can be ignored if  $\tilde{i}_{od}$  and  $\tilde{i}_{oq}$  change with a sufficiently slow rate [8]. This means that  $\tilde{\omega}_{vsc} \approx \tilde{\theta}_{vsc} \approx 0$  and, since the grid frequency is assumed fixed,  $\tilde{\delta} \approx 0$ . Consequently,  $\tilde{v}_{gd} \approx \tilde{v}_{gq} \approx 0$  according to (2-16) and (2-17). This

condition holds assuming the AVC and DVC dynamics are considerably slower than the CC dynamics. With these assumptions in place, (2-20) simplifies into:

$$\begin{bmatrix} \tilde{v}_{od} \\ \tilde{v}_{oq} \end{bmatrix} = Z_g \begin{bmatrix} \tilde{i}_{fd} \\ \tilde{i}_{fq} \end{bmatrix} + \omega_{vsc}^\circ L_g \begin{bmatrix} -\tilde{i}_{fq} \\ \tilde{i}_{fd} \end{bmatrix} \quad (2-33)$$

Repeating the same procedure in (2-21)–(2-31) results in the following.

$$\tilde{i}_{fd} = \frac{N_2(s)}{D_2(s)} \tilde{i}_{fq} \quad (2-34)$$

$$T_{iv}^{ac}(s) = Z_g(s) \frac{N_2(s)}{D_2(s)} - \omega_{vsc}^\circ L_g \quad (2-35)$$

where

$$N_2(s) = -\omega_{vsc}^\circ L_g + G_3(s) i_{fq}^\circ Z_g(s) - i_{fq}^\circ G_3(s) (Z_f(s) + r_f) \quad (2-36)$$

$$D_2(s) = G_3(s) - Z_g(s) i_{fd}^\circ - G_3(s) \omega_{vsc}^\circ L_g i_{fq}^\circ \quad (2-37)$$

## 2.2. Control Design

The complete system parameters of the VSC-WG system are depicted in Table 2-1. The control gains are designed as explained in the following. As suggested by [8], the bandwidth of the CC loop  $T_c(s)$  is 10% to 20% of the converter switching frequency. The AVC and DVC loops are also considerably slower than the current loop. To this end, the corresponding control gains are selected to assign a bandwidth equal to 17% of the switching frequency to the CC loop and bandwidths equal to 14% and 1.2% of the CC bandwidth to the DVC and AVC loops, respectively. In the latter, the stability of the closed-loop system imposes the maximum permissible degree. The closed-loop bandwidth of the PLL is a trade-off between the filtering characteristics and fast responses [58]. In order to meet a fast tracking and filtering characteristics, the bandwidth of PLL is usually in the range of few tens of Hz [59]. Further, the PLL bandwidth in the grid-connected applications should be smaller than the grid nominal frequency to reject the second and sixth order harmonics [8]. However, it should not be too small so that the PLL tracks fast changes in the PCC voltage following the output power or the grid impedance variations [8].

Table 2-1 Parameters of VSC-WG System

Parameter	Value	Unit
Nominal line-to-line voltage, $V_g$	13.8	kV rms
VSC rated dc power, $P_n$	7.25	MW
Nominal frequency, $\omega_g$	$2\pi \times 60$	rads <sup>-1</sup>
Grid inductance, $L_g$	126.7	$\mu$ H
Grid resistance, $r_g$	4.8	m $\Omega$
Transformer voltage ratio, $a$	13.8/0.6	kV/kV
Filter inductance, $L_f$	100	$\mu$ H
Filter resistance, $r_f$	1.5	m $\Omega$
PCC filter capacitance, $C_f$	500	$\mu$ F
Filter resistance, $r_d$	0.6	$\Omega$
DC-link filter capacitance, $C_{dc}$	15	mF
DC-link nominal voltage, $V_{dc}$	1.6	kV
PLL control gains, $[K_{p\omega}, K_{i\omega}]$	[0.5, 2.5]	[rads <sup>-1</sup> V <sup>-1</sup> , rads <sup>-2</sup> V <sup>-1</sup> ]
CC gains, $[K_{pc}, K_{ic}]$	[0.34, 5]	[ $\Omega$ , $\Omega$ s <sup>-1</sup> ]
AVC gains, $[K_{pv}, K_{iv}]$	[5, 1000]	[ $\Omega^{-1}$ , $\Omega^{-1}$ s <sup>-1</sup> ]
DVC gains, $[K_{pdc}, K_{idc}]$	[14.4, 720]	[ $\Omega^{-1}$ , $\Omega^{-1}$ s <sup>-1</sup> ]
Active damping gain, $K_{cp}$	230	$\Omega^{-1}$
Active damping cut-off frequency, $\omega_{cp}$	15	rads <sup>-1</sup>
VSC switching frequency, $f_s$	3040	Hz
ON-state resistance of VSC switches, $r_{on}$	0.88	m $\Omega$
Forward voltage drop of VSC switches, $V_f$	1	V

### 2.3. Simulation Results

To validate the developed dynamic models, nonlinear time-domain simulations are conducted in MATLAB/Simulink [60] for the system shown in Figure 2.1 and the parameters given in Table 2-1. The average model of the VSC is used for the purpose of dynamic simulation [8]. The dynamic response of the PCC voltage corresponding to the VSC-WG system is presented in this section. The small-signal model is based on the closed-loop system in Figure 2.5 and the values in Table 2-1 whereas the PCC dynamic transfer function  $T_{iv}^{ac}(s)$  is evaluated for the detailed and simplified dynamic models as will be explained in the following. Using (2-31) and the values in Table 2-1, the detailed dynamic model of PCC is given by

$$T_{iv}^{ac}(s) = \frac{N_1(s)}{D_1(s)} \quad (2-38)$$

where  $N_1(s)$  and  $D_1(s)$  are given as follows.

$$\begin{aligned}
N_1(s) &= 8.8 \times 10^{-3}s^{10} + 83.3s^9 + 53.9 \times 10^3s^8 - 3.9 \times 10^8s^7 - 8.5 \times 10^{11}s^6 + 7.1 \times 10^{14}s^5 \\
&\quad - 2.9 \times 10^{17}s^4 - 5.6 \times 10^{19}s^3 - 5.6 \times 10^{21}s^2 - 2.3 \times 10^{23}s - 1 \times 10^{24} \\
D_1(s) &= s^{10} + 7.5 \times 10^3s^9 + 2.2 \times 10^7s^8 + 3.5 \times 10^{10}s^7 + 3.2 \times 10^{13}s^6 + 1.7 \times 10^{16}s^5 \\
&\quad + 4.9 \times 10^{18}s^4 + 6.1 \times 10^{20}s^3 + 7 \times 10^{21}s^2 + 3 \times 10^{23}s + 1.8 \times 10^{24}.
\end{aligned}$$

Using (2-35) and the values in Table 2-1, the simplified dynamic model of PCC is given by

$$T_{iv}^{ac}(s) = \frac{N_2(s)}{D_2(s)} \quad (2-39)$$

where  $N_2(s)$  and  $D_2(s)$  are given as follows.

$$\begin{aligned}
N_2(s) &= -0.05s^6 - 153.5s^5 - 2.6 \times 10^5s^4 - 2.6 \times 10^8s^3 - 1.2 \times 10^{11}s^2 - 1.3 \times 10^{13}s - 8 \times 10^{14} \\
D_2(s) &= s^6 + 5.9 \times 10^3s^5 + 1.2 \times 10^7s^4 + 1.1 \times 10^{10}s^3 + 3.9 \times 10^{12}s^2 + 3.7 \times 10^{14}s + 1.9 \times 10^{16}.
\end{aligned}$$

Figure 2.6 shows the step response of  $v_{od}$  following a 1% step in  $v_{od}^{ref}$  at  $t = 0.5$  s when  $P_{ac} = 0.84$  pu with and without the active compensation. As shown in Figure 2.6(a), where the PLL is slow with a bandwidth of 3.2 Hz, the simplified model is close to a first-order exponential signal whereas the detailed model shows a second-order underdamped behavior with a noticeable overshoot before reaching the steady state. Moreover, the response of the nonlinear large-signal model is shown which closely matches the response of the detailed small-signal model. It is also worth noting that the slow PLL is used for the sake of evaluation only whereas a fast PLL is adopted in this chapter.

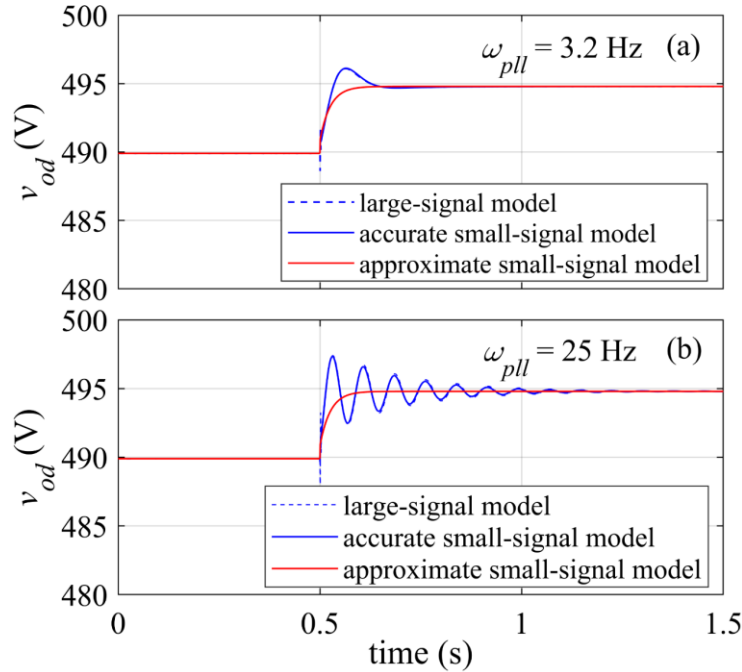


Figure 2.6: Dynamic response of the PCC voltage to 1 percent step variation in the voltage reference at  $t = 0.5$  s under  $P_{ac} = 0.84$  pu. (a) Slow PLL with a bandwidth of 3.2 Hz. (b) Fast PLL with a bandwidth of 25 Hz.

Figure 2.6(b) shows the dynamic responses of the models under the same scenario when a faster PLL with a bandwidth of 25 Hz is implemented. As shown, the response of the simplified model is the same as the case of the slow PLL since the effect of PLL is ignored. However, the responses of the detailed and the large-signal models show a poorly damped oscillatory behavior. Further, the responses of the detailed and large-signal models are closely matched which verifies the development of the small-signal model in (2-20)–(2-32).

## 2.4. Conclusion

In this chapter, it is shown that the small-signal responses yielded from the simplified model of PCC voltage in the VOC-based VSC-WG systems, show a discernable discrepancy between the small- and large-signal transient responses and this difference increases by increasing the PLL bandwidth. This can result in system instability or oscillatory dynamics when the AVC is designed according to the simplified model. On the other hand, using the detailed model of the PCC voltage dynamics results

in a linear model whose response closely matches the large-signal PCC voltage response at different PLL bandwidths. Therefore, it is important to obtain the detailed transfer function of the PCC voltage dynamics if the control design optimization is a main objective.

## Chapter 3.

# Small-Signal Analysis and Stability Improvements of VSC-WG in Inversion Mode

The interfacing of the VOC-based VSCs into WG systems can induce severe instabilities. This is attributed to interactions between the VOC system of the VSCs and the high impedance of the WG. The weak connection limits the amount of active power that can be injected by the VSC to the WG. In this chapter, the small-signal analysis is used to derive the full-order state-space model of the VSC-WG system. A modal analysis is then conducted to develop the participation factors to characterize the influencing states on the dominant modes of the system, followed by a sensitivity analysis to evaluate the influence of the VOC gains and other parameters on the dominant modes. The results of the modal analysis confirm that instabilities at the nominal power are inevitable for VSCs connected to VWGs. Inspired by this shortcoming, a compensation method is devised to mitigate the dynamic instability of VSCs connected to VWGs. Finally, several offline time-domain simulations and HIL real-time experiments are conducted to verify the validity of small-signal analysis, validate the effectiveness of the compensation method; and investigate the performance of the system under challenging scenarios such as sudden variations in the phase angle of the grid.

### 3.1. Introduction

If the equivalent impedance between the power grid and the PCC is negligible, the PCC voltage magnitude and frequency can be assumed to be constant, and hence the control of the VSC can be designed independent of the grid parameters. In this situation, the grid is known as a SG. However, if the equivalent impedance is not small enough, the previous assumption is not valid anymore as the PCC voltage exhibits fluctuations, especially during transient conditions. Moreover, the VSC and the grid dynamics become undesirably coupled [61]. In this case, the grid is known as a WG. The grid impedance is mainly dictated by the long transmission lines and low power transformers [47]. Since wind farms and photovoltaic units are installed in locations far from the load centers [18], [62], even if the main interconnected grid is strong, the integration of DGs

can occur in a WG condition. Moreover, the WG impedance might have a wide range of variations due to faults, loading conditions, and grid reconfigurations by the operator [14], [18], [47], [63].

In the technical literature, several issues are reported due to the interaction dynamics between the VSC and the WG [18]–[22], [28], [30], [40]–[45], [61]–[73]; (1) Low-frequency resonances that interact with the VOC of the VSC which might induce instability under the VWG conditions; (2) Instabilities due to the PLL dynamics especially in the VWG conditions; and (3) Limited active power transfer under the weak conditions. In the literature, many control methods discussed in the following have been proposed to enhance the integration of VSCs to WGs.

The first method is to modify (shape) the PLL control loop used for the VOC method by reducing its bandwidth [30], [40], [41], [45], [65]. The reason is that a high PLL bandwidth increases the negative real-part of the converter output impedance which decreases the overall system damping [22], [28], [65]. Therefore, decreasing the PLL bandwidth improves the stability of the interaction dynamics between the VSC and the WG, which in turn, increases the maximum power capacity of the VSC. However, this method often limits the transient response of the system [21]. Moreover,  $SCR = 1.25$  is the maximum stable condition which is obtained for the VSC-WG system in previous works. However, the instability problem of the VSC-WG systems at  $SCR = 1$ , which is the worst-case scenario [19], does still exist.

The second method, as addressed in [21], [47], [66]–[68], is to change the magnitude or phase angle of the VSC output impedance by adding auxiliary feedforward loop(s) to the current control path of the VOC. However, the minimum  $SCR$  level studied in all these cases equals two. Another common feature in most of these methods is that they change the steady-state response of the VSC by modifying the VSC output impedance as an attempt to enhance the stability of the VSC-WG system.

The third method, as discussed in [18], [43], [62], is to eliminate the conventional PLL instead of dealing with its negative effect on the system stability by replacing the VOC method by the power synchronization control (PSC). The PSC is a new concept in controlling the VSC output power in grid-connected applications, where the VSC is controlled to imitate the characteristics of a synchronous machine. The paramount

advantage of the PSC method is that the VSC does not face any limitation to inject the active power into the VWGs. However, as the ac current is not controlled directly in the PSC, the performance under fault conditions is compromised. Therefore, there is still a great interest to improve the conventional VOC method to adapt to the VWGs and maintain the direct current regulation.

Another variant of the VOC method is introduced in [61] where the inner CC of the VSC is replaced by a voltage controller while the PLL is preserved in the control structure. In this case, the active and reactive power controls are the outer loops of the overall control system. However, similar to the PSC, there is no direct control on the VSC current. Moreover, the stability of the system under study has been verified at  $SCR = 3$  which is not close enough to the worst-case scenario. An improved version of the VOC strategy is suggested in [19], where the classic outer loop is modified by additional four decoupling gains based on the gain-scheduling technique. The VSC shows a stable performance at  $SCR = 1$ . However, the control design requires lookup tables to schedule eight control parameters following the operating point variation. Therefore, there is still a need for a simpler VOC-based method to improve the VSC-WG system stability in the VWG conditions [50].

Inspired by the shortcoming of the previous works to present a simple method to mitigate the instability problem of the VOC-based VSC in the VWG conditions, a simple active compensation method is used in this chapter that can be easily integrated with the existing VOC scheme. The suggested method does not require any change in the VSC control parameters. Also, upon using the compensation method, the steady-state measures of the VSC remain unchanged. Moreover, it is shown that the stability region of the VSC-WG system is increased to  $SCR = 1$  which is the worst-case scenario. The rest of this chapter is organized as follows. Section 3.2 presents the small-signal model of the VSC-WG system followed by extensive modal analysis under the VWG conditions. In Section 3.3, the modeling and design of the active compensation method are discussed. Section 3.4 provides the large-signal simulation results. The real-time verification of the active compensation method is presented in Section 3.5. Finally, Section 3.6 concludes this chapter.

## 3.2. Stability Assessment of Uncompensated System

A small-signal model of the VSC-WG system without active compensation is developed in the form of the state-space equations by linearizing (2-1)–(2-7), (2-9), (2-13)–(2-15), and (2-32) about an equilibrium point which corresponds to the operation of the VSC-WG at the nominal condition according to Table 2-1. The time-domain state-space representation is given by

$$\frac{d}{dt} \tilde{\mathbf{X}}_{\text{uc}}(t) = \mathbf{A}_{\text{uc}} \tilde{\mathbf{X}}_{\text{uc}}(t) \quad (3-1)$$

where superscript “~” denotes small perturbations of a variable and  $\tilde{\mathbf{X}}_{\text{uc}}$  is the state vector as given by

$$\tilde{\mathbf{X}}_{\text{uc}} = [\tilde{\delta} \quad \tilde{v}_{od}^c \quad \tilde{v}_{oq}^c \quad \tilde{i}_{fd}^c \quad \tilde{i}_{fq}^c \quad \tilde{v}_{dc}^c \quad \tilde{i}_{fd} \quad \tilde{i}_{fq} \quad \tilde{v}_{cd} \quad \tilde{v}_{cq} \quad \tilde{i}_{od} \quad \tilde{i}_{oq} \quad \tilde{v}_{dc}]^T \quad (3-2)$$

and  $\mathbf{A}_{\text{uc}}$  is the state matrix as given in Appendix A.

### 3.2.1. Participation Analysis

The relative participation of different states in the dominant eigenvalues (modes) of  $\mathbf{A}_{\text{uc}}$  in (3-1) at the nominal operating point as given in Table 3-1 is evaluated using the participation factor (PF) measure [26]. The relative PFs of the states are calculated for two cases of connection to a SG at  $SCR = 10$ , and a connection to a VWG at  $SCR = 1$ . The PF results are summarized in Table 3-1.

As shown, in the case of the SG, there are two real stable eigenvalues,  $\lambda_1$  and  $\lambda_2$ , which mainly corresponds to the PLL and control states of the PCC voltage, respectively. However, in the case of the WG, there are two real stable eigenvalues,  $\lambda_1$  and  $\lambda_4$ , which are mainly affected by the states of the PLL and the DVC, respectively. Also, there is a pair of unstable complex eigenvalues,  $\lambda_{3-4}$ , which corresponds to the states of the grid impedance, PLL, DVC, and AVC. This shows that the cross-coupling between the states of the VSC control system and the WG impedance is the primary source of instability in the VSC-WG system. In addition, there is a pair of stable complex eigenvalues,  $\lambda_{5-6}$ , which correspond to the states of the PLL, dc-link, and the grid impedance similar to  $\lambda_{3-4}$ . As will be shown, this pair can induce significant progress toward the imaginary axis following variations in the control gains. Therefore, they can be responsible for introducing oscillatory unstable modes to the system dynamics.

Table 3-1 Participation Factor of the VSC-WG States in the Dominant Modes

Subsystem	State	Eigenvalues of $\mathbf{A}_{uc}$ at $P_{ac} = 1$ pu					
		SCR = 10		SCR = 1			
		$\lambda_1 = -5.1$	$\lambda_2 = -4.7$	$\lambda_{5-6} = -69.1 \pm 2362.3j$	$\lambda_2 = -47.4$	$\lambda_1 = -5.1$	$\lambda_{3-4} = 41.1 \pm 60.8j$
AC Network	$\tilde{i}_{od}$	~0	~0	0.25	~0	~0	0.11
	$\tilde{i}_{oq}$	~0	~0	0.42	0.05	~0	0.17
	$\tilde{v}_{cd}$	~0	~0	0.12	~0	~0	~0
	$\tilde{v}_{cq}$	~0	~0	0.21	~0	~0	~0
PLL	$\tilde{\delta}$	0.03	~0	0.12	0.01	0.02	0.12
	$\tilde{v}_{oq}^c$	0.98	0.05	~0	~0	1.02	0.02
DC Network	$\tilde{v}_{dc}$	~0	~0	0.08	0.01	~0	0.16
DVC	$\tilde{v}_{dc}^c$	~0	~0	~0	0.79	~0	0.16
	$\tilde{i}_{fd}$	~0	~0	0.05	~0	~0	0.2
AVC	$\tilde{i}_{fq}$	~0	~0	0.12	~0	~0	0.06
	$\tilde{v}_{od}^c$	0.05	0.95	0.06	0.16	~0	0.54

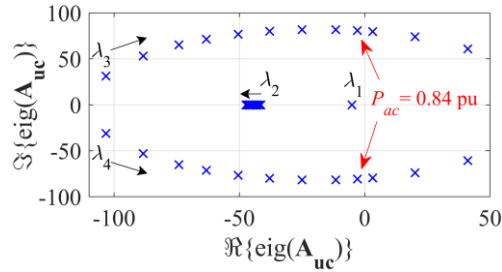


Figure 3.1: Spectrum of the dominant eigenvalues corresponding to  $\mathbf{A}_{uc}$  when  $P_{ac}$  changes between 0.35 to 1 pu.

### 3.2.2. Sensitivity Analysis

#### *Influence of the VSC Power Level*

Figure 3.1 shows the location of the dominant eigenvalues of  $\mathbf{A}_{uc}$  under different values of  $P_{ac}$ . As shown, by changing  $P_{ac}$  from 0.35 to 1 pu,  $\lambda_{3-4}$  have considerable progress toward the imaginary axis while  $\lambda_1$  does not show any noticeable change and  $\lambda_2$  departs slightly from the imaginary axis. Therefore, the stability of the VSC-WG system decreases as the value of  $P_{ac}$  increases. Moreover, the VSC-WG system is not stable for  $P_{ac} > 0.84$  per-unit (pu), which corresponds to  $SCR < 1.2$ .

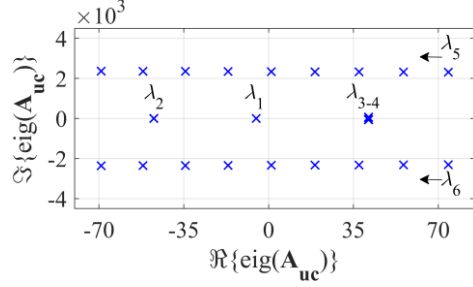


Figure 3.2: Spectrum of the dominant eigenvalues corresponding to  $\mathbf{A}_{uc}$  when  $r_d$  changes between 0.4 to 0.6  $\Omega$  under  $P_{ac} = 1$  pu condition.

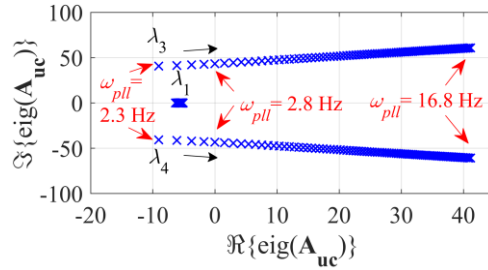


Figure 3.3: Spectrum of the dominant eigenvalues corresponding to  $\mathbf{A}_{uc}$  when  $(K_{p\omega}, K_{i\omega})$  change by a gain of 0.1 to 1 under  $P_{ac} = 1$  pu condition.

### ***Influence of the LC Filter Damping***

Figure 3.2 shows the trajectory of the dominant eigenvalues when the LC filter damping resistance  $r_d$  changes from 0 to 0.6  $\Omega$  under the nominal power condition, i.e.,  $SCR = 1$ . By increasing the passive damping, it is possible to shift  $\lambda_{5-6}$  to the stable region. However,  $\lambda_{3-4}$  is almost unaffected by the passive damping resistance and hence it is not possible to stabilize the system at the nominal power level. Clearly, the origin of the instability is not the ac filter resonance.

### ***Influence of the PLL Controller***

The effect of changing the PLL control gains on the dominant eigenvalues is shown in Figure 3.3. As shown, by multiplying  $(K_{p\omega}, K_{i\omega})$  by a gain of 0.1 to 1, the modes  $\lambda_{3-4}$  progress extensively toward the imaginary axis. Initially, the modes are located in the stable region where the PLL bandwidth  $\omega_{pll}$  is equal to 2.3 Hz. By increasing the PLL gains,  $\lambda_{3-4}$  progress towards the imaginary axis and enter the unstable region at  $\omega_{pll} = 2.8$  Hz which is noticeably smaller than the grid nominal frequency, i.e., 60 Hz. Therefore, for a PLL with extremely limited bandwidth, the VSC-WG system can be

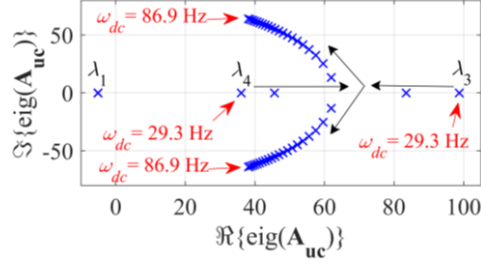


Figure 3.4: Spectrum of the dominant eigenvalues corresponding to  $A_{uc}$  when  $(K_{pdc}, K_{idc})$  change by a gain of 0.28 to 1.23 under  $P_{ac} = 1$  pu condition.

stable. However, limited bandwidth of PLL hinders the excursion of the frequency during transients [8] which, in turn, slows down the response time of the VSC to the variations in the DG power that are typically fast. This effect is also in an agreement with the PF values given in Table 3-1 for  $\lambda_{3-4}$  where  $\tilde{\delta}$  and  $\tilde{v}_{oq}^c$  are the states related to PLL. Therefore, there is a trade-off between the VSC-WG system stability and the fast dynamic response.

### ***Influence of the DC-Link Voltage Controller***

The effect of changing the DVC gains on the dominant eigenvalues is depicted in Figure 3.4. As shown,  $\lambda_3$  and  $\lambda_4$  are initially real with positive values. Then, by multiplying  $(K_{pdc}, K_{idc})$  by a gain of 0.28 to 1.23, the eigenvalues relocate until they merge and turn into the complex pair  $\lambda_{3-4}$ , yet, still in the unstable region. This observation is also in an agreement with the PF values given in Table 3-1 where the states related to the DVC show a considerable participation in  $\lambda_{3-4}$ . Further, the bandwidth of the DVC ( $\omega_{dc}$ ) increases from 29.3 to 86.9 Hz which is equal 6% to 17% of the CC bandwidth. Further increases of the control gains do not show a considerable influence on the system stability.

### ***Influence of the AC Voltage Controller***

The effect of changing the AVC gains on the dominant eigenvalues is depicted in Figure 3.5. According to Figure 3.5(a), similar to changing DVC gains,  $\lambda_3$  and  $\lambda_4$  are initially real values and, by multiplying  $(K_{pv}, K_{iv})$  by a gain of 0.08 to 1.05, a relatively large relocation occurs before merging and turning into a complex pair  $\lambda_{3-4}$ , yet, still in the unstable region. This observation is also in an agreement with the PF values given in

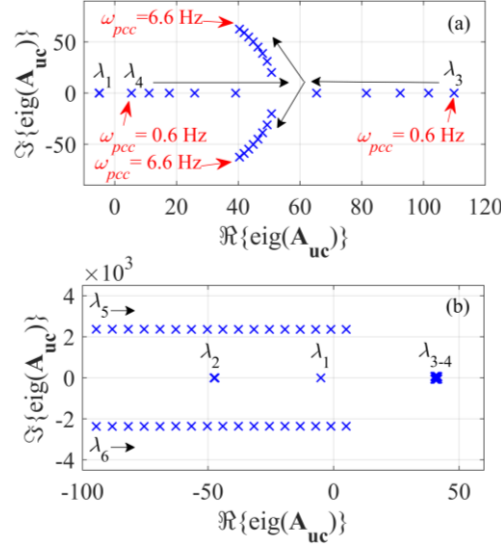


Figure 3.5: Spectrum of the dominant eigenvalues corresponding to  $A_{uc}$  when  $(K_{pv}, K_{iv})$  change by a gain of: (a) 0.08 to 1.05 and (b) 0.98 to 1.05 under  $P_{ac} = 1$  pu.

Table 3-1. Further, the bandwidth of the PCC closed-loop system  $\omega_{pcc}$  increases from 0.6 to 6.6 Hz and so  $\lambda_{5-6}$  progress extensively toward the unstable region as shown in Figure 3.5(b).

### 3.3. Suggested Active Compensation

From Section 3.2.2, it is concluded that without compromising the PLL closed-loop bandwidth, i.e., having the PLL with slow response time, it is not possible to preserve the stability of the VSC-WG system under the worst-case scenario at  $SCR = 1$ . Therefore, an active compensation method is suggested in this chapter to stabilize the VSC-WG system under the same conditions and increase the damping of the system responses under lower levels of  $SCR$ .

Figure 3.6 shows a new feedforward compensation loop (in red) where a perturbed compensation signal  $\tilde{u}_{cp}$  is added to the forward path of the PCC closed-loop control system with a negative sign. Based on this modification, the equation for the  $q$ -axis component of the current reference can be rewritten as

$$i_{fq}^{ref} = -G_v(s)(v_{od}^{ref} - v_{od}) - u_{cp}(s) \quad (3-3)$$

where

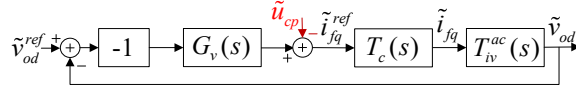


Figure 3.6: Block diagram of the AVC loop with active compensation.

$$u_{cp}(s) = K_{cp} \frac{\omega_{cp}}{s + \omega_{cp}} v_{oq} \quad (3-4)$$

in which,  $K_{cp}$  and  $\omega_{cp}$  are the dc gain and the cut-off frequency of the low-pass filter. In (3-4),  $v_{oq}$  is used for the active compensation because; first, according to Table 3-1,  $v_{oq}$  is the input of the PLL which corresponds to the instability of the dominant modes  $\lambda_{3-4}$ , second,  $v_{oq}$  is zero in the steady-state stable conditions, therefore,  $u_{cp}$  has a zero influence on the steady-state operation of the VSC.

### 3.3.1. Small-Signal Model of Actively Compensated System

To represent the small-signal model of the compensated system, (2-1)–(2-7), (2-9), (2-13)–(2-15), (3-3), and (3-4) are linearized to give the time-domain state-space representation as

$$\frac{d}{dt} \tilde{\mathbf{X}}_{cp} = \mathbf{A}_{cp} \tilde{\mathbf{X}}_{cp} \quad (3-5)$$

where the state vector  $\tilde{\mathbf{X}}_{cp}$  is given by

$$\tilde{\mathbf{X}}_{cp} = [\tilde{\mathbf{X}}_{uc}^T \quad x_{cp}]^T \quad (3-6)$$

where  $x_{cp}$  is the new state variable corresponding to the low-pass filter (LPF) in (3-4); and the state matrix  $\mathbf{A}_{cp}$  is given in Appendix A.

### 3.3.2. Active Compensator Design

According to (3-4), there are two degrees of freedom to design the active compensator. Figure 3.7 shows the eigenvalue spectrum of  $\mathbf{A}_{cp}$  under the nominal conditions when  $K_{cp}$  increases at three different values of the cut-off frequency,  $\omega_{cp} = (15, 20, 25)$  rad/s. As shown, with the different values of  $\omega_{cp}$ , the dominant eigenvalues  $\lambda_{3-4}$  migrate from the unstable to the stable region as  $K_{cp}$  increases. Note that  $\lambda_{3-4}$  move back toward the imaginary axis at higher values of  $K_{cp}$ . Figure 3.7 also shows that with a smaller value of  $\omega_{cp}$ , more improvement in the system stability is obtained. The parameters of the

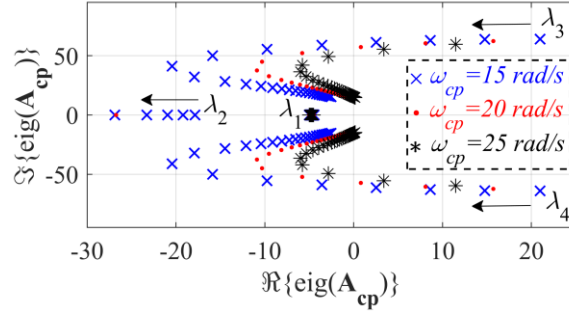


Figure 3.7: Spectrum of the dominant eigenvalues corresponding to  $\mathbf{A}_{cp}$  when  $K_{cp}$  changes by a gain of 0.3 to 3 for  $\omega_{cp} = (15,20,25)$  rad/s under  $P_{ac} = 1$  pu.

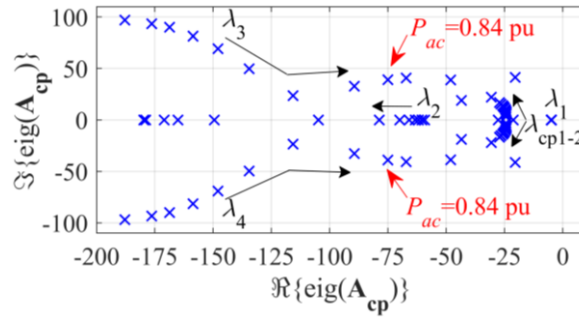


Figure 3.8: Spectrum of the dominant eigenvalues corresponding to  $\mathbf{A}_{cp}$  when  $P_{ac}$  changes from 0.35 pu to 1 pu.

active compensation, as given in Table 3-2, are designed to provide the maximum enhancement in the stability of the VSC-WG system at  $SCR = 1$ .

### 3.3.3. Stability Assessment of Compensated System

Figure 3.8 shows the location of the dominant eigenvalues of  $\mathbf{A}_{cp}$  when  $P_{ac}$  increases from 0.35 to 1 pu. As shown,  $\lambda_{3-4}$  progress toward the imaginary axis while  $\lambda_1$  does not show a visible change whereas  $\lambda_2$  departs slightly away from the imaginary axis. Unlike the uncompensated system in Figure 3.1, it is clear that the dominant eigenvalues are in the stable region for  $0.84 < P_{ac} < 1$  pu. The active compensation loop successfully achieves the full integration of the VSC at  $SCR = 1$ . Figure 3.8 also shows the progress of a pair of complex eigenvalues, denoted by  $\lambda_{cp1-2}$ , which corresponds to the active compensation state. As shown, by increasing  $P_{ac}$ ,  $\lambda_{cp1-2}$  depart slightly from the imaginary axis which does not compromise the system stability.

Table 3-2 Active Compensator Parameters

Parameter	Value	Unit
Active damping gain, $K_{cp}$	230	$\Omega^{-1}$
Active damping cut-off frequency, $\omega_{cp}$	15	$\text{rads}^{-1}$

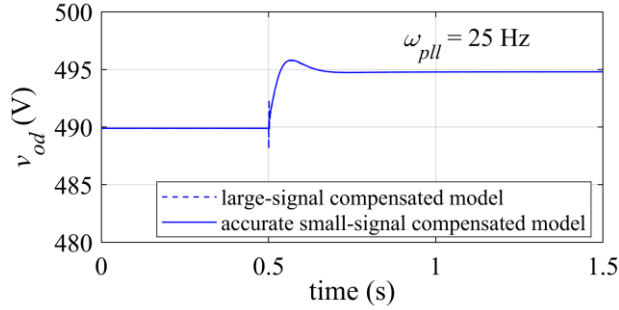


Figure 3.9: Dynamic response of the actively compensated PCC voltage to 1 percent step variation in the voltage reference at  $t = 0.5$  s under  $P_{ac} = 0.84$  pu and fast PLL bandwidth of 25 Hz.

### 3.4. Simulation Results

To validate the developed dynamic models, the small-signal analysis, and the effectiveness of the active compensation method, nonlinear time-domain simulations are conducted in MATLAB/Simulink for the system shown in Figure 2.1 and the parameters given in Table 3-1 and Table 3-2. The average model of the VSC is used for the purpose of dynamic simulation [8].

#### 3.4.1. Influence of AC Voltage Control

According to (3-4), the active compensation modifies the  $q$ -axis current reference  $i_{fq}^{ref}$ . Further, the detailed dynamic modeling of PCC in Section 2.1.5 is carried out without using  $i_{fq}^{ref}$  as an input. Therefore, the active compensation does not affect the PCC dynamics. To verify this remark, the VSC-WG system is tested with active compensation under the same scenario as the uncompensated model in Section 2.3. Figure 3.9 shows the response of the detailed small-signal model as compared to the response of the nonlinear large-signal model. As shown, both responses coincide closely. Moreover, the responses exhibit much less oscillatory behavior as compared to the response of the uncompensated model in Figure 2.6 because the feedforward compensation is included

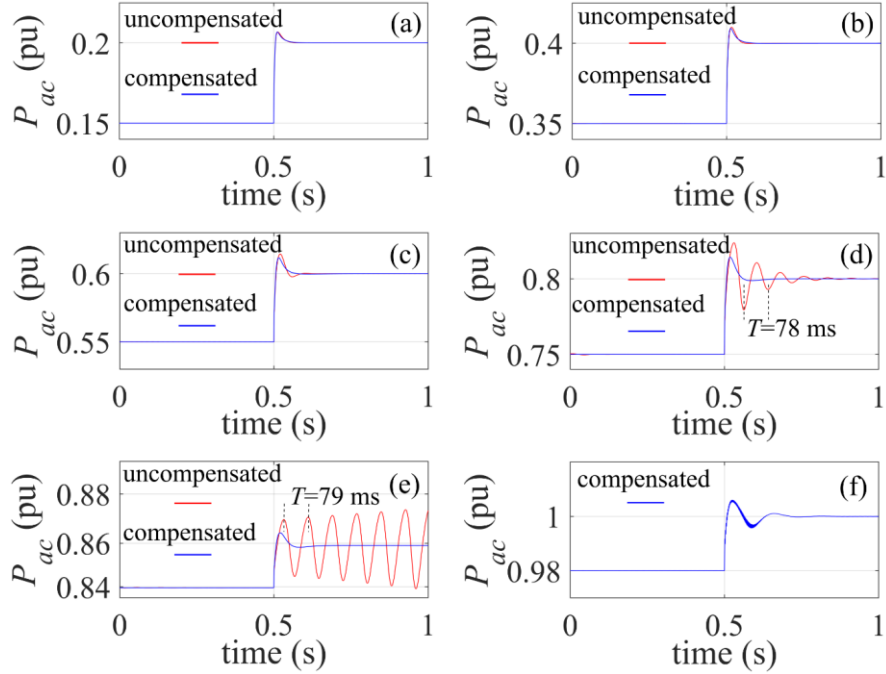


Figure 3.10: Dynamic response of the active power following a step variation in the active power at  $t = 0.5$  s at different power levels.

in the control loop of the PCC voltage.

### 3.4.2. Influence of Power Level

The performance of the VSC-WG system under different active power levels is investigated in Figure 3.10. A small step change in the active power at  $t = 0.5$  s under different levels of power is applied. As shown in Figure 3.10(a)–(c), for  $P_{ac} \leq 0.6$  pu, the responses are similar. However, as shown in Figure 3.10(d), the uncompensated system is oscillatory as the active power increases. These oscillations are related to the relocation of  $\lambda_{3-4}$  with the change in the power according to Figure 3.1. The unstable oscillatory behavior of the uncompensated system is clear at  $P_{ac} = 0.86$  pu as shown in Figure 3.10(e). Note that the frequency of oscillations in Figure 3.10(d)–(e) are 12.8 and 12.7 Hz, respectively, which closely matches the frequency of the corresponding mode  $\lambda_{3-4}$  in Figure 3.1. More importantly, the compensated system exhibits a stable response under the full range of the active power injection including the worst-case scenario at  $SCR = 1$  as shown in Figure 3.10(a)–(f).

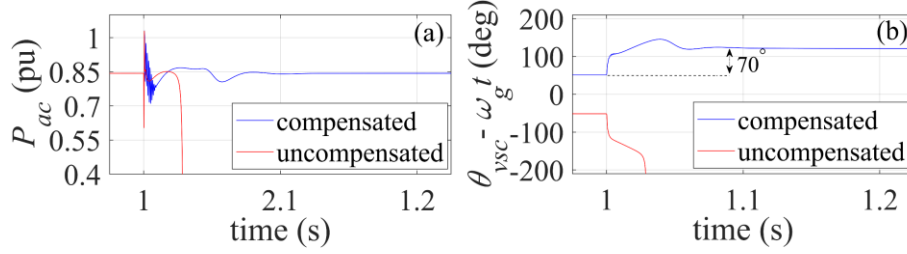


Figure 3.11: Transient responses of the VSC following a  $70^\circ$  step change in the phase angle of the grid voltage at  $t = 1$  s and  $P_{ac} = 0.85$  pu.

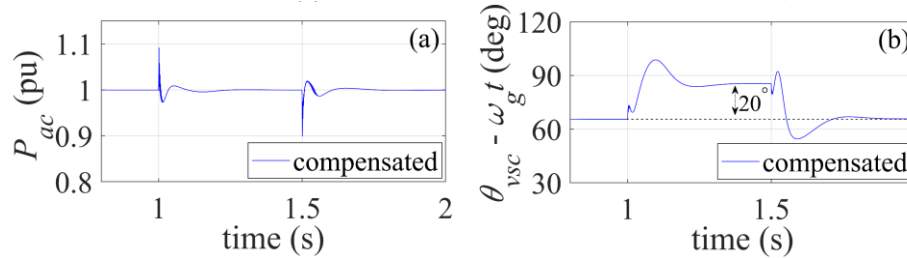


Figure 3.12: Transient responses of the compensated VSC following a  $20^\circ$  step change in the phase angle of the grid voltage at  $t = 1$  s and  $P_{ac} = 1$  pu.

### 3.4.3. Influence of Grid Angle Variation

In this part, another advantage of using the active compensation method is demonstrated. The capability of the compensated VSC-WG system to preserve the stability following a sudden change in the phase angle of the grid voltage  $\theta_g$  is investigated. As an extremely challenging condition, Figure 3.11(a)–(b) show the responses of  $P_{ac}$  and  $v_o$  following a step change of  $70^\circ$  in  $\theta_g$  at  $P_{ac} = 0.85$  pu. Figure 3.11(a) shows that the active power of the compensated system undergoes an overshoot and undershoot of around 0.15 pu, yet, the VSC controller manages to regulate the injected power at the initial value. Therefore, the stability of the system is preserved. As shown in Figure 3.11 (b), the VSC angle relative to the synchronous frame  $\theta_g - \omega_g t$  increases by  $70^\circ$  while its value relative to the grid angle  $\theta_g$  (not shown here) is not changed. The same condition is applied to the uncompensated system. As shown in Figure 3.11(a)–(b), the uncompensated system fails to follow the deviations in the voltage angle and therefore does not reach a stable operating point.

Figure 3.12 (a)–(b) show the active power and angle responses to a  $20^\circ$  increase in  $\theta_g$  between  $t = 1$  s and  $t = 1.5$  s at  $P_{ac} = 1$  pu. As shown, the compensated system

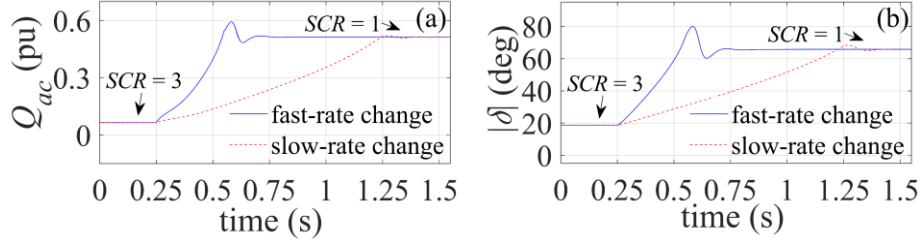


Figure 3.13: Transient responses of the compensated VSC at  $P_{ac} = 1$  pu when  $Z_g$  linearly increases at  $t = 0.25$  s from one-third of the nominal value to the full value in the 0.3 and 1 s corresponding to fast and slow rates, respectively.

stability is preserved under the nominal power condition.

### 3.4.4. Influence of Grid Impedance Variation

Depending on the flow of power, especially in WGs where DGs are integrated, the grid impedance is not constant and might be subject to uncertainties [67], [74]. Online identification methods are suggested to find the real-time values of impedance for the stability assessment [75]. The stability analysis that is conducted in Section 3.3.3 considers the nominal power which corresponds to the worst-case scenario at  $SCR = 1$ , where the suggested active compensation in (41) guarantees the system stability. However, according to (1), the  $SCR$  level is a function of the VSC nominal dc power and the grid impedance. Therefore, in this part, the operation of the VSC-WG system is tested under the nominal power condition and a wide variation range in the grid impedance  $Z_g$ .

Figure 3.13(a)–(b) show the response of the VSC reactive power  $Q_{ac}$  and the magnitude of the phase difference, i.e.,  $|\delta|$ , to the increase in the grid impedance (while the angle of  $Z_g$  is fixed). Since the rate of the change in the grid impedance is not *a priori* knowledge, the simulation is repeated for two periods of 0.3 s and 1 s during which, the grid impedance is changed to assess the effect of the impedance variation on the VSC-WG performance with fast and slow rates, respectively. As shown, the system is initially in the steady-state stable condition at  $SCR = 3$ , i.e., the WG condition, where the grid impedance  $Z_g$  is one-third of the nominal value given in Appendix A. Then, at  $t = 0.25$  s,  $Z_g$  increases linearly until it reaches the nominal value at  $SCR = 1$ , i.e., the VWG condition. In the meantime, according to Figure 3.13(a),  $Q_{ac}$  increases to partially

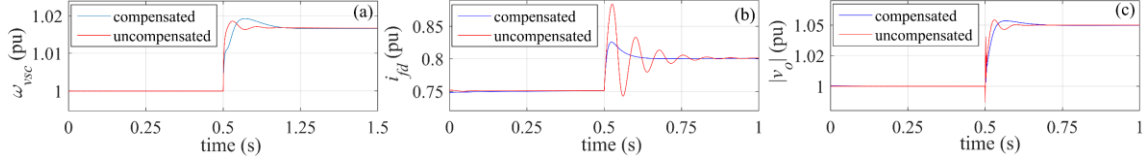


Figure 3.14: Dynamic response of the VSC control loops to a step variation in the reference input at  $t = 0.5$  s and  $P_{ac} = 0.75$  pu. (a) Response of  $\omega_{vsc}$  following a 1 Hz step in the grid frequency. (b) Response of  $i_{fd}$  following a step in the current reference ( $d$ -axis) from 0.75 pu to 0.8 pu. (c) Response of  $v_o$  (magnitude) following a 5% step in the voltage reference.

compensate for the reactive power absorbed by the grid reactance. Since the injected active power is fixed at 1 pu,  $|\delta|$  increases as the grid reactance increases according to Figure 3.13(b). This agrees with the steady-state real power flow equation in inductive lines [26]. Figure 3.13 also shows that there are overshoots and undershoots in the responses corresponding to the fast rate of changes in the grid impedance while they are considerably lessened in the responses of the slow rate of changes. However, the stable operation of the system is maintained during both impedance changes. Therefore, the VSC-WG system with the suggested active compensation method is immune to a wide range of changes in the grid impedance with slow and fast rates.

### 3.4.5. Dynamic Interactions with VSC Primary Controllers

In this part, the dynamic interactions of the active compensation method with the primary controllers of the VSC-WG system are investigated at  $P_{ac} = 0.75$  pu by comparing the compensated and uncompensated responses. Figure 3.14(a) shows the frequency tracking responses of the PLL subsequent to a 1 Hz step change in the frequency of the grid. It is clear that the active compensation loop has an insignificant effect on the PLL bandwidth. Figure 3.14(b) shows the responses of  $i_{fd}$  following a 5% step in the active power at  $t = 0.5$  s. The active compensation method manages to significantly decrease the overshoots and suppress the oscillations before reaching the steady-state operating point.

Figure 3.14(c) shows the variations of the PCC voltage magnitude  $|v_o|$  following a 5% step change in the voltage reference at  $t = 0.5$  s. As shown, the active compensation does not have any noticeable influence on the dynamics of the PCC

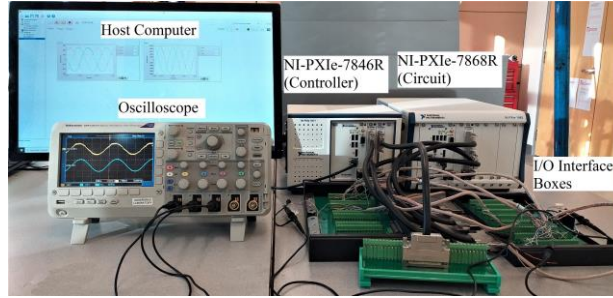


Figure 3.15: VSC-WG experiment platform.

voltage as compared to the uncompensated system. Generally, the design of the VSC controllers is not compromised by the active compensation method.

### 3.5. Real-Time Verification

The feasibility of the suggested compensation method is verified by an FPGA-based HIL platform, as shown in Figure 3.15, where the VSC-WG model is emulated with the same specifications as in Table 2-1. The circuit model of the VSC-WG is developed in the single-FPGA NI-PXIe-7846R real-time simulator with 1  $\mu$ s time step which is interfaced to the host computer by StarSim HIL software. Also, the control model is implemented in the double-FPGA NI-PXIe-7868R simulator which is interfaced to the host computer by StarSim RCP software. The connections between NI-PXIe chassis are realized through three I/O interface boxes.

A series of experiments is performed during which the VSC dc power  $P_{dc}$  increases according to the profile given by  $P_{dc} = [0.4, 0.6, 0.8, 0.9, 0.95, 1]$  pu at  $t = [0, 1, 2, 3, 4, 5]$  s, respectively. Figure 3.16(a) shows the VSC responses  $v_o$ ,  $i_o$ , and the dc-link voltage difference from the nominal value  $\Delta v_{dc}$ . As shown, both  $v_o$  and  $i_o$  are well-damped and regulated under all conditions. Moreover, since  $v_{dc}$  is regulated by the DVC,  $\Delta v_{dc}$  is zero in the steady state as shown in the figure. There are small overshoots in the waveform at the beginning of each step that are less than 0.15 pu at the start-up and less than 0.1 pu for the next steps. Figure 3.16(b) shows a closer view of  $v_o$  and  $i_o$  in the steady state. It should be noted that  $v_o$  has a total harmonic distortion of 5% which is in compliance with the IEEE standard 519 [77].

Figure 3.17(a) shows the increases in the active power injected by the VSC  $P_{ac}$  subjected to the steps in  $P_{dc}$ . There are small overshoots during each step. This regime

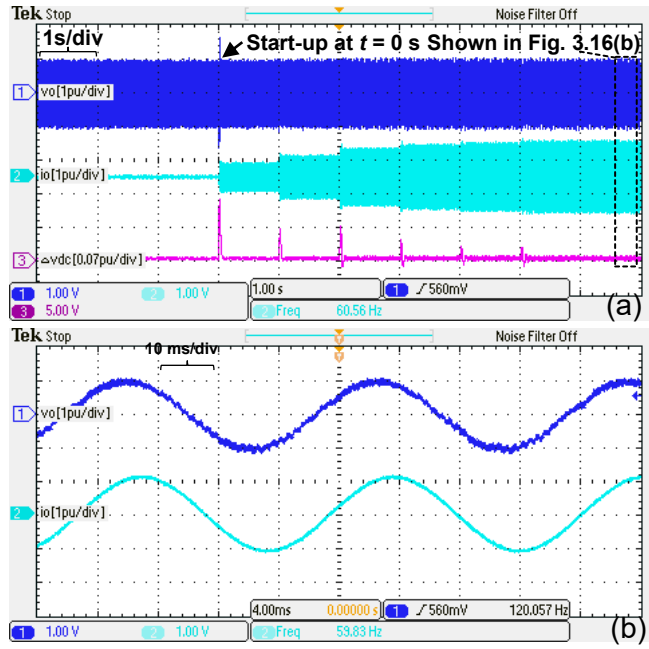


Figure 3.16: Voltages and current responses of the VSC during start-up transients and staircase changes in  $P_{dc}$ . (a) Response of  $v_o$  (phase a),  $i_o$  (phase a), and  $\Delta v_{dc}$ . (b) Zoomed view of  $v_o$  and  $i_o$ .

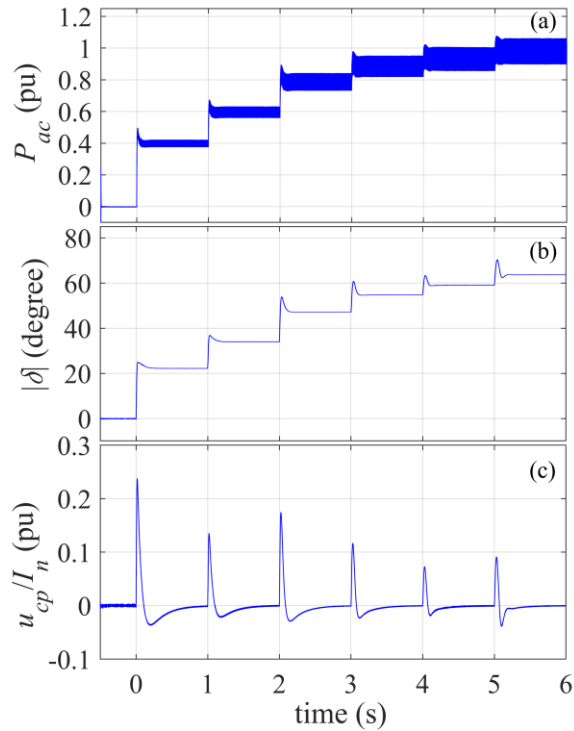


Figure 3.17: VSC Active power, phase angle difference, and compensation signal responses during start-up transients and staircase changes in  $P_{dc}$ .

continues until  $P_{ac}$  reaches the nominal value at  $t > 5$  s. According to Figure 3.17(b), the magnitude of the phase angle difference  $|\delta|$  between the PCC and grid phase voltages increases after each step in  $P_{dc}$ . Figure 3.17(c) shows the variations of the compensation signal  $u_{cp}$ . As shown, the compensation signal is only activated during the transient conditions to mitigate the potential instabilities and has no impact at the steady-state conditions.

### 3.6. Conclusion

In this chapter, the integration of VSCs into the VWG systems has been investigated, and the associated instabilities have been mitigated effectively under the worst-case scenario at  $SCR = 1$ . The active compensator injects a modified version of  $v_{oq}$  into the  $q$ -axis reference of the CC. It is shown that the suggested method contributes successfully to the relocation of the unstable modes into more damped locations on the complex plane. In addition to the stabilization of the compensated system under the VWG conditions, the stability of the system under the grid angle deviations has been improved significantly with the adopted active compensation. The effectiveness of the active compensator has been verified analytically using the small-signal analysis followed by large-signal simulations in MATLAB/Simulink and real-time HIL experiments. The active compensator has the following features; (1) it is simple and can be easily designed using the linear analysis tools; (2) it does not interact with the steady-state performance of the VSC; and (3) it has a minimal influence on the existing VOC structure and so it can be designed independently. Time-domain simulations and experiments of the VSC-WG system are carried out to verify; (1) the stability of the VSC-WG system with the suggested active compensation method under VWG condition at  $SCR = 1$  and its improved damping property at  $SCR > 1$ ; (2) the enhanced capability of the VSC-WG system to withstand sudden grid angle deviations and wide range of variations in the grid impedance.

## Chapter 4.

# Small-Signal Analysis and Stability Improvements of VSC-WG in Rectification Mode

DC subgrids consisting of modern AELs and local DG units are normally interfaced with the main ac grid by utilizing bidirectional VSCs. Under the VWG conditions, the integration of VOC-based VSCs systems in the inversion mode becomes very challenging and therefore undamped oscillations in the power and angle responses are yielded. Most of the existing works address this issue for VSCs in the inversion mode of operation. However, integration of VSCs in the rectification mode with the consideration of the outer loop controllers into the VWGs has not been reported. The rectification mode is practically justified because many modern loads such as battery banks, induction motor drives, LED lighting systems, and data centers, as well as dc microgrids are interfaced to the rest of ac grid through VSCs. To fill up this gap, a state-space model of the bidirectional VSC-WG system is developed in this chapter with an emphasis on the rectification mode of operation. A modal-sensitivity analysis is then utilized to evaluate small-signal stability of the system, identify the dominant modes, and investigate the system states that have a major influence on these modes. The results reveal two pairs of unstable complex modes that are correlated with the dynamic interaction between the VSCs and the VWG impedance. It is also shown that the stability margin of VSCs in the rectification mode is less than that of the inversion mode under the same VWG conditions. To enhance the integration of the VSCs in the rectification mode, a dual-active compensation (DAC) scheme is proposed to mitigate the instabilities under VWG conditions. Several time-domain simulation results are presented to verify the validity of the small-signal model and demonstrate the effectiveness of the DAC scheme under the VWG conditions. Finally, HIL real-time experimental results are presented to validate the simulation results.

### 4.1. Introduction

In certain cases, such as rural areas, islands, and charging stations for electric vehicles, the loads might be far away from the PCC [15]. Similarly, DG systems such as photovoltaic units and wind farms are usually located in distant places with respect to the

center of loads [13], [18], [31], [62]. Moreover, VSC-based HVDC systems and DC MG can be connected to high-impedance ac grids [78]–[80]. All these examples show that there can be long distances between the interfacing VSCs and the main ac grids. Therefore, the grid equivalent series impedance cannot be ignored. In these cases, the grid is known as a WG and the stability of the VSC-WG system becomes very challenging. The voltage at the PCC in WGs features large fluctuations especially during transients because the PCC voltage is a function of the VSC output current and power. In other words, the VSC-based VSC and the grid dynamics are undesirably coupled [61]. Therefore, the design of the VSC control system cannot be achieved without considering the main ac grid parameters. Moreover, the WG impedance might have a wide range of variations due to the loads variations, grid reconfigurations, and faults [14], [15], [18], [47]. However, to realize the plug-and-play characteristics in modern power systems [15], the control design needs to allow seamless integration of the VSC with no prior knowledge of the grid parameters.

The interaction dynamics between the three-phase VSCs in the rectification mode and SGs are studied in [39]. Therein, the rectifier is initially modeled by an ideal constant power load (CPL) and it is shown that the CPL introduces a NIR that becomes prominent at a certain level of power which excites the resonance frequency of the VSC LC filter and as a result, the system becomes unstable. Further investigation of this problem is carried out in [8]. According to [8], the resulting transfer function of the VSC represents a nonminimum-phase zero in the rectification mode which reduces the closed-loop stability margin of the grid-connected VSC whereas the system remains stable in the inversion mode.

Several studies about the VSC-WG systems have shown unstable interaction dynamics. According to [28], even without considering the outer control loops, i.e., the DVC, the AVC, and the PLL, instability can happen due to the interaction of the CC with the VWG impedance. In [22], [30], [57], [61]–[63], [65]–[70], [81], it is shown that the interaction between the PLL unit of VSCs and the WG impedances can be another source of instability. This undesired phenomenon is called the grid synchronization instability [22], [65]. This issue is also another limiting factor for the active power transfer between the WGs and VSCs [65]. Moreover, the instability due to the synchronization is dependent on the operation mode of the VSC, such that the VSC–WG system is stable for a wider range of  $SCR$  in the inversion mode than in the rectification mode. In other

words, a higher power transfer is allowed between the VSC and the WG when the VSC is operating in the inversion mode. Therefore, improving the system stability in the rectification mode is more critical than the inversion mode under VWG conditions; a challenge that has not been widely investigated in the literature.

Since a high-bandwidth PLL decreases the damping of the grid-connected VSC systems [22], [28], [65], several researchers have suggested the idea of reducing the PLL bandwidth as a remedy for fixing the synchronization instability problem and increasing the real power transfer in VSC-WG systems. However, this method often results in a PLL with a very slow dynamic response which is not desirable (see, e.g., [8], [20], [21]). Modifying the structure of the outer control loops, the AVC and PLL, by adding linear functions of output voltage and currents has been proposed to improve the VSC-WG stability [21], [61], [67]. Essentially, these methods change the output impedance of the VSC such that the source-load admittance matching holds between the VSC and WG. Thus, the VSC-WG systems stability is preserved according to the Nyquist criterion. However, most of these methods address the inversion mode of operation whereas the more challenging rectification mode is not considered. Further, the level of improvement in the VSC-WG system stability is limited to  $SCR = 2$ . The compensation of the VWG impedance with a negative virtual impedance that is injected by a front-end VSC has been achieved in an HVDC system assuming that the dc-side voltage is maintained sufficiently high and hence the overmodulation is avoided [20]. Moreover, the dc-side voltage is assumed to be a constant value, and therefore, the DVC is not applied to the VSC. The gain scheduling method is used to design the proposed outer AVC loop of a front-end VSC of an HVDC system [19]. Similar to [20], the VSC-WG system stability is maintained at  $SCR = 1$  in both directions, yet, at the expense of a complicated AVC system that relies on a lookup table to evaluate four pairs of control parameters sets. However, the key disadvantage of the preceding methods is that the steady-state responses of the VSC are affected especially under the VWG conditions.

Emulating the characteristics of synchronous machines has inspired several researchers to develop power synchronization control (PSC) [43], [63], [82], [83]. As a major feature of the PSC, the PLL loop is not required, and the inner CC is replaced by a voltage control loop. Therefore, the integration of VSCs into the VWG can be achieved. While the majority of works about PSC have been done for VSCs in the inversion mode,

the rectification mode of operation is also suggested to improve the stability of the WGs when supplying several VSC-interfaced loads [44]. However, since the current is not directly controlled, the control system must dynamically switch to a current limiting operation under severe transients such as faults which is practically challenging [20]. Therefore, as long as stability issues in the VSC-WG systems can be mitigated, the VOC is still the preferred method [20].

A simple and effective method that can mitigate instabilities due to the interconnection of VOC-based VSCs, in the rectification mode, and ac grids, with extremely low *SCRs*, has not been presented in the literature so far. Motivated by this drawback, a simple and lossless DAC scheme is proposed in this chapter that can be effortlessly integrated into the existing VOC. Upon incorporating the proposed dual-compensation scheme, the dynamic responses of the VOC loops are not negatively affected, and the steady-state values remain unchanged. Therefore, there is no need to redesign the VSC control system.

The rest of the chapter continues as follows. In Section 4.2, the nonlinear model of the VSC-WG system is developed in the *dq*-RF followed by a discussion about the VSC controller design. Section 4.3 discusses the correlation between the power transfer capability of the VSC-WG system and the *SCR* in the rectification mode. In Section 4.4, a small-signal stability analysis of the VSC-WG system in the rectification mode is studied using the linearized model of the system. Then, the modal and sensitivity analyses are carried out under the VWG conditions. In Section 4.5, the proposed DAC scheme is introduced which is followed by a discussion about designing the DAC parameters using the root-locus method. Section 4.6 provides the large-signal simulation results. The real-time verification of the proposed method is presented in Section 4.7. Finally, the chapter is concluded in Section 4.8.

## 4.2. Dynamic Model of VSC-WG System

Figure 4.1, which is the dual of Figure 2.1 with respect to the mode of operation, shows a three-phase VSC in the rectification mode that is supplying a generic dc load at the dc-side with the nominal power  $P_n$ . The dc load is modeled by a current source in parallel with a dc filter capacitor. At the ac-side, the VSC, which is cascaded by an *LC* filter with a passive damping  $r_d$  [76], is connected to the PCC. The role of the *LC* filter in this

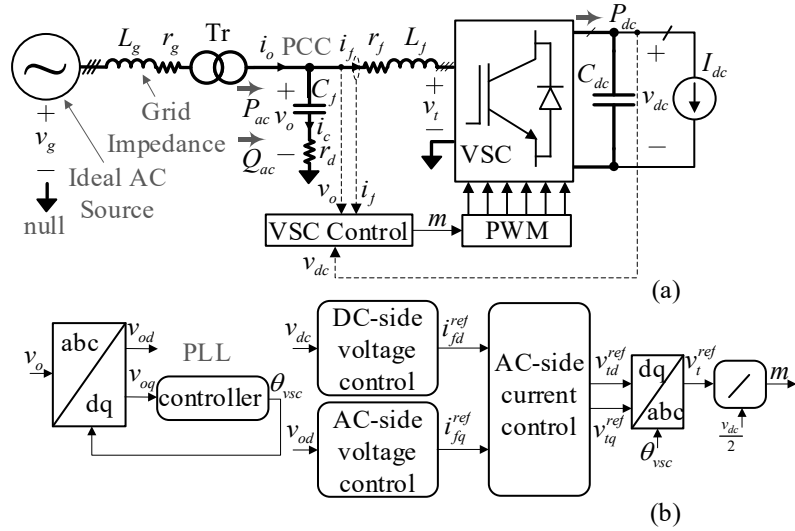


Figure 4.1: VSC-WG system. (a) VSC with LC filter connected to the utility grid through a step-down transformer and the grid impedance. (b) VSC control loops.

Table 4-1 Parameters of VSC-WG System

Parameter	Value	Unit
Nominal line-to-line voltage, $V_g$	13.8	kV rms
VSC rated dc power, $P_n$	7.25	MW
Nominal frequency, $\omega_g$	377	rads <sup>-1</sup>
Grid inductance, $L_g$	111.4	$\mu$ H
Grid resistance, $r_g$	2.8	m $\Omega$
Transformer voltage ratio, $a$	13.8/0.6	kV/kV
Filter inductance, $L_f$	100	$\mu$ H
Filter resistance, $r_f$	1.5	m $\Omega$
PCC filter capacitance, $C_f$	500	$\mu$ F
Filter resistance, $r_d$	0.9	$\Omega$
DC-Side filter capacitance, $C_{dc}$	15	mF
DC-Side nominal voltage, $V_{dc}$	1.9	kV
PLL control gains, $[K_{p\omega}, K_{i\omega}]$	[0.7, 2.5]	[rads <sup>-1</sup> V <sup>-1</sup> , rads <sup>-2</sup> V <sup>-1</sup> ]
CC gains, $[K_{pc}, K_{ic}]$	[0.34, 5]	[ $\Omega$ , $\Omega$ s <sup>-1</sup> ]
AVC gains, $[K_{pv}, K_{iv}]$	[5, 1000]	[ $\Omega^{-1}$ , $\Omega^{-1}$ s <sup>-1</sup> ]
DVC gains, $[K_{pdc}, K_{idc}]$	[9, 450]	[ $\Omega^{-1}$ , $\Omega^{-1}$ s <sup>-1</sup> ]
$d$ -axis active compensator parameters, $[K_{cpd}, \omega_{cpd}, \zeta]$	[3.5, 600, 0.9]	[-, rads <sup>-1</sup> , -]
$q$ -axis compensator parameters, $[K_{cpq}, \omega_{cpq}]$	[225, 10]	[-, rads <sup>-1</sup> ]
VSC switching frequency, $f_s$	3040	Hz
ON-state resistance of VSC switches, $r_{on}$	0.88	m $\Omega$
Forward voltage drop of VSC switches, $V_f$	1	V

arrangement is to reject the switching harmonics from affecting the VSC output voltage  $v_o$ . The PCC is connected to a step-down transformer Tr which, on the high-voltage side, is connected to a WG that is modeled as an ideal voltage source, with constant voltage  $V_g$  and constant frequency  $\omega_g$ , i.e., infinite ac bus, in series with a high-value equivalent impedance. The WG impedance and Tr leakage impedance are lumped together and shown in Figure 4.1(a) as an  $RL$  impedance with  $L_g$  and  $r_g$  as the parameters. The complete system parameters are provided in Table 4-1.

Figure 4.1(b) shows the VOC control system which is established on the synchronous  $dq$ -RF. As shown, the PLL tracks the phase voltage angle at the PCC and generates the required frequency  $\omega_{vsc}$  and the angle  $\theta_{vsc}$  for the transformation of variables between stationary  $abc$ - and  $dq$ -RFs. The dynamic equations corresponding to the VSC-WG circuit and control loops, i.e., CC, PLL, DVC, and AVC, are presented in the following subsections. It should be noted that all equations are in the frequency domain and written in the  $dq$ -RF, wherein  $s$  represents the Laplace operator and the  $d$ - and  $q$ -axis components of variables are denoted by subscripts “ $d$ ” and “ $q$ ”, respectively, unless otherwise stated. In the following equations, all the reference values and steady-state values are denoted by superscript “ $ref$ ” and “ $o$ ”, respectively.

### 4.2.1. Power Circuit

Since the VSC-WG circuit does not change as the mode of operation switches from inversion to rectification (see Figure 4.1(a) and Figure 2.1(a)), the circuit dynamics that are developed in  $dq$ -RF (2-1)–(2-4) are used in this chapter to study the VSC-WG dynamics in the rectification mode.

### 4.2.2. VOC System

The dynamic equations corresponding to the VSC-WG control system in the inversion mode are presented in Chapter 2. Since there is no difference between the inversion and rectification modes of operation (in the uncompensated system cases) as far as the control systems is concerned, the same VSC dynamics as given in Section 2.1 are used in this chapter for the rectification mode with only a minor modification of DVC loop as follows.

## A. DC VOLTAGE CONTROL

The dc-side voltage error  $e_{dc} = v_{dc}^{ref} - v_{dc}$  passes through a PI compensator  $G_{dc}(s) = K_{pdc} + K_{idc}s^{-1}$  and the result is used as a reference for the  $d$  channel of the CC. Therefore, the following relation between  $e_{dc}$  and  $i_{fd}^{ref}$  exists

$$i_{fd}^{ref} = -G_{dc}(s)e_{dc} \quad (4-1)$$

The VSC dc-side power  $P_{dc}$  is equal to the sum of the instantaneous active power at the VSC terminals and in the dc filter capacitor  $C_{dc}$  neglecting the switching loss in the VSC. The dc transfer function from  $i_{fd}$  to  $v_{dc}$ , denoted by  $T_{iv}^{dc}(s)$ , is obtained as follows. First, the following expression is derived based on instantaneous power equilibrium [8].

$$v_{dc}I_{dc} = 1.5(v_{od}i_{fd} + v_{oq}i_{fq}) - 0.75L_f s(i_{fd}^2 + i_{fq}^2) - 1.5r_f(i_{fd}^2 + i_{fq}^2) - 0.5C_{dc}s v_{dc}^2 \quad (4-2)$$

Second, since (4-2) is nonlinear with respect to  $v_{dc}$ , it is linearized at the nominal operating point. The result is given as follows where  $v_{oq}^\circ$  is set to zero due to the PLL action

$$(C_{dc}v_{dc}^\circ s + I_{dc})\tilde{v}_{dc} = 1.5(v_{od}^\circ \tilde{i}_{fd} + i_{fd}^\circ \tilde{v}_{od} + i_{fq}^\circ \tilde{v}_{oq}) - 1.5L_f s(i_{fd}^\circ \tilde{i}_{fd} + i_{fq}^\circ \tilde{i}_{fq}) - 3r_f(i_{fd}^\circ \tilde{i}_{fd} + i_{fq}^\circ \tilde{i}_{fq}) \quad (4-3)$$

where superscript “~” denotes a small-signal perturbation. Rearranging (4-3) to isolate  $\tilde{v}_{dc}$  and considering  $\tilde{i}_{fq}$  and  $\tilde{v}_{od,q}$  as the disturbance inputs result in the dc transfer function as follows

$$T_{iv}^{dc}(s) = -\frac{3L_f i_{fd}^\circ s + 2r_f i_{fd}^\circ - v_{od}^\circ}{2C_{dc}v_{dc}^\circ s + I_{dc}} \quad (4-4)$$

Figure 2.3 shows the DVC closed-loop diagram where  $T_{iv}^{dc}(s)$  is defined by (4-4).

### 4.2.3. Control Design

The bandwidth of the CC loop is usually designed to remain in the range of 10–20% of the converter switching frequency [8]. The bandwidths of AVC and DVC loops are also considerably slower than the CC loop. The control objectives are to design the control loops in Figure 2.2–Figure 2.5 with high bandwidth and small overshoots (enough damping), while the closed-loop stability of the VSC-WG system is preserved at the

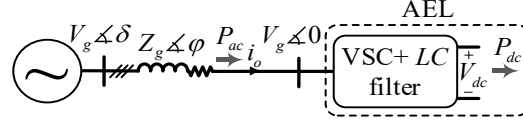


Figure 4.2: Active electronic load connected to the WG through an equivalent series impedance.

nominal operating point. Consequently, the controller gains are obtained as presented in Table 4-1. In summary, the bandwidths of {529, 29, 6} Hz are assigned to the CC, DVC, and AVC loops, respectively. Also, the bandwidth of 26 Hz is assigned to the PLL loop to give reasonably fast-tracking dynamics to the PLL when subjected to fast changes in the operating point and at the same time filter the grid low-frequency harmonics [8], [58], [59].

### 4.3. Power-Angle Limitation at Low SCR Level

The VSC with the  $LC$  filter can be considered as an AEL as seen by the WG. Figure 4.2 shows a VSC with an  $LC$  filter in a compact form that interfaces the dc load to the ac grid. A series  $RL$  impedance  $Z_g \angle \varphi$  is connecting the PCC bus and grid infinite bus with voltage phasors  $V_g \angle 0$  and  $V_o \angle \delta$ , respectively. Since the PCC voltage is regulated at the nominal value  $V_g$ , the steady-state expression for the transferred real power  $P_{ac}$  according to Figure 4.2 can be written as follows

$$P_{ac} = V_g^2 Z_g^{-1} (\cos(\varphi - \delta) - \cos(\varphi)) \quad (4-5)$$

which shows  $P_{ac}$  is a function of the phase angle difference  $\delta$ .

According to the definition of  $SCR$  [42], the following can be written

$$SCR = V_g^2 (Z_g P_n)^{-1} \quad (4-6)$$

Dividing both sides of (1-4) by  $P_n$  and using (1-5) give the per-unit value of the transferred power as follows

$$P_{ac}(pu) = SCR (\cos(\varphi - \delta) - \cos(\varphi)) \quad (4-7)$$

Assuming that the nominal power is transferred to the AEL in Figure 4.2, i.e.,  $P_{ac} = 1$  pu, the critical  $SCR$  ( $SCR^c$ ) which is defined as the smallest  $SCR$  that the system can operate under the nominal condition according to the power-angle limit, is obtained at  $\delta = \varphi$ . Using the result in (4-7) results in the following:

$$SCR^c = (1 - \cos(\varphi))^{-1} \quad (4-8)$$

which shows that  $SCR^c$  depends on the  $X/R$  ratio. Assuming a nonzero line resistance,  $X/R$  ratio is a finite value which results in  $\varphi$  less than  $\frac{\pi}{2}$ . Therefore,  $SCR^c$  for the VSC-WG system in the rectification mode is always more than unity according to (4-8). However, reversing the power to find the limit for  $SCR$  in the inversion mode, i.e.,  $P_{ac} = -1$  pu and  $\delta < 0$ , results in  $SCR^c < 1$ . Consequently, unlike the study of the stability of the VSC-WG system in the inversion mode [51], the VWG condition in the rectification mode is at some  $SCR^c$  which is greater than unity assuming a WG condition.

#### 4.4. Stability Assessment of Uncompensated System

The state-space model of the VSC-WG system without compensation signals is developed by linearizing (2-1)–(2-7), (2-14), (2-15), (2-32), (4-1), and (4-2) at the nominal power level and using the parameters listed in Table 4-1. The time-domain state-space model is represented in the matrix form in the as follows

$$\frac{d}{dt} \tilde{\mathbf{X}}_{uc}(t) = \mathbf{A}_{uc} \tilde{\mathbf{X}}_{uc}(t) \quad (4-9)$$

where  $\mathbf{A}_{uc}$  is the state matrix as given in Appendix B, and  $\tilde{\mathbf{X}}_{uc}$  is the state vector as given by

$$\tilde{\mathbf{X}}_{uc} = [\tilde{\delta} \quad \tilde{v}_{od}^c \quad \tilde{v}_{oq}^c \quad \tilde{i}_{fd}^c \quad \tilde{i}_{fq}^c \quad \tilde{v}_{dc}^c \quad \tilde{i}_{fd} \quad \tilde{i}_{fq} \quad \tilde{v}_{cd} \quad \tilde{v}_{cq} \quad \tilde{i}_{od} \quad \tilde{i}_{oq} \quad \tilde{v}_{dc}]^T. \quad (4-10)$$

##### 4.4.1. Modal Analysis

The nominal values of different states are obtained by solving the algebraic equations of the VSC-WG system at the nominal power operating point and under  $SCR = 1.18$  condition. The algebraic equations can be obtained by setting  $s$  in the VSC-WG dynamic equations to zero. Then,  $\mathbf{A}_{uc}$  in (4-9) is evaluated using the parameter values provided in Table 4-1. Table 4-2 summarizes the results where the relative participation of a state in an eigenvalue (mode) is evaluated using the PF measure [26].

As shown in Table 4-2, the system is highly unstable due to the presence of two unstable complex eigenvalues in the low-frequency and high-frequency ranges,  $\lambda_{2-3}$  and  $\lambda_{4-5}$ , respectively. The presence of these unstable eigenvalues shows that while the

Table 4-2 Participation Factor of the States in the Dominant Modes

Subsystem	State	Dominant Eigenvalues of $\mathbf{A}_{uc}$ at $P_{ac} = 1$ pu and $SCR = 1.18$		
		$\lambda_1 = -4$	$\lambda_{2-3} = 20 \pm 60j$	$\lambda_{4-5} = 681 \pm 942j$
AC Network	$\tilde{i}_{od}$	$\sim 0$	0.2	2.5
	$\tilde{i}_{oq}$	$\sim 0$	0.3	1.1
	$\tilde{i}_{fd}$	$\sim 0$	0.26	1.1
	$\tilde{i}_{fq}$	$\sim 0$	0.2	0.6
	$\tilde{v}_{cd}$	$\sim 0$	$\sim 0$	0.1
	$\tilde{v}_{cq}$	$\sim 0$	$\sim 0$	$\sim 0$
PLL	$\tilde{\delta}$	$\sim 0$	0.8	0.2
	$\tilde{v}_{oq}^c$	1	$\sim 0$	$\sim 0$
DC Network	$\tilde{v}_{dc}$	$\sim 0$	0.4	3.7
DVC	$\tilde{v}_{dc}^c$	$\sim 0$	0.5	0.2
AVC	$\tilde{v}_{od}^c$	$\sim 0$	0.7	0.2

VSC control loops are designed to retain stable dynamics under the nominal condition, the VOC-based VSC and WG interconnection bears highly unstable dynamics. According to the PF analysis in Table 4-2, PLL, AVC, and DVC show strong participation in  $\lambda_{2-3}$  while  $\lambda_{4-5}$  is mostly affected by dc-side and ac network states. Moreover, ac network states have moderate participation in  $\lambda_{2-3}$ . Therefore, the dynamic interaction between the VSC control dynamics and the WG impedance is the primary source of instability in the VSC-WG system. There is also real stable eigenvalue  $\lambda_1$  which corresponds to the PLL states and the WG states do not show any participation in it.

#### 4.4.2. Sensitivity Analysis

##### ***Influence of VSC Power Level***

Figure 4.3 demonstrates how the dominant eigenvalues relocate as the VSC active power  $P_{ac}$  changes from 0.82 to 1 pu. As shown in Figure 4.3(a) for rectification mode, initially both dominant complex eigenvalues  $\lambda_{2-3}$  and  $\lambda_{4-5}$  are in the LHP. As  $P_{ac}$  increases,  $\lambda_{4-5}$  have significant move towards the  $j\omega$  axis while  $\lambda_{2-3}$  exhibit mild movement in the same direction. Therefore, the stability of the VSC-WG system diminishes as the active power increases. Moreover, the VSC-WG system is not stable at  $P_{ac} = 0.86$  pu since  $\lambda_{4-5}$  enter right-half plane (RHP). Eventually,  $\lambda_{2-3}$  enters the RHP at  $P_{ac} = 0.97$  pu as well. Therefore, the VSC-WG system is unstable under the nominal condition due to the movement of two separate pairs of complex eigenvalues into the

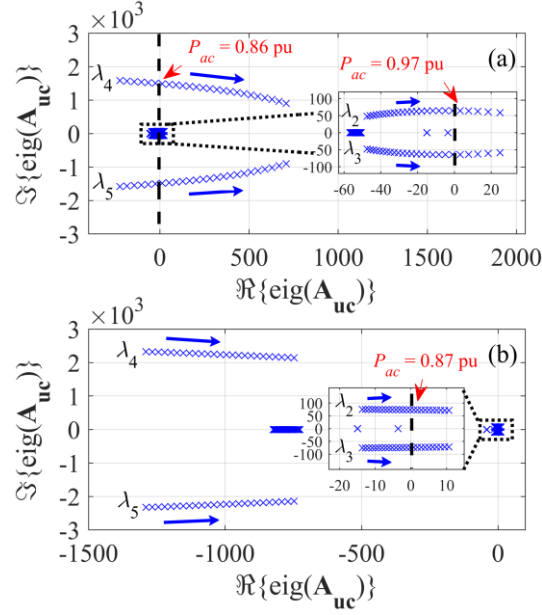


Figure 4.3 Spectrum of the dominant eigenvalues when  $P_{ac}$  changes between 0.82 to 1 pu in the (a) rectification mode and (b) inversion mode.

RHP. Figure 4.3(b) shows the relocation of the dominant eigenvalues as a result of the same changes in the power level in the inversion mode of operation. As shown,  $\lambda_{4-5}$  relocation is limited to the LHP, while  $\lambda_{2-3}$  cross the  $j\omega$  axis and the system becomes unstable at  $P_{ac} = 0.87$  pu. This shows that first, the stability of the VSC-WG system at the nominal ac power is mostly influenced by the dominant low-frequency (range) eigenvalues and high-frequency (range) eigenvalues in the rectification mode and the inversion mode, respectively; second, the stability of the system in the inversion mode is slightly better than the rectification mode.

### ***Influence of Passive Damping***

The effect of adding a series damping resistance  $r_d$  to the VSC LC filter on the dominant eigenvalues of the VSC-WG system is shown in Figure 4.4. According to the figure,  $\lambda_{4-5}$ , that are initially in the RHP, slightly relocate toward the  $j\omega$  axis and then move in the opposite direction as a function of increasing  $r_d$  from zero. As shown, the system remains unstable at the nominal active power. Therefore, passive damping is not able to mitigate the VSC-WG instability problem. However, a value is assigned to  $r_d$  to damp the LC filter resonance peak during light-load conditions and without extra power loss under the VWG condition as given in Table 4-1.

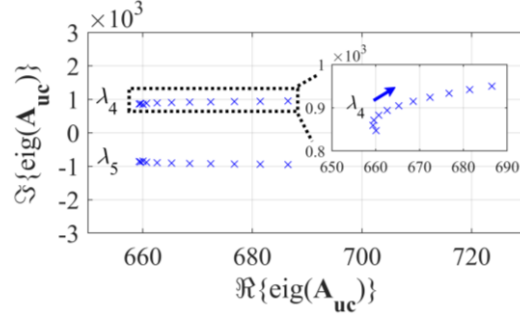


Figure 4.4: Spectrum of the dominant eigenvalues at  $P_{ac} = 1$  pu when  $r_d$  changes between 0 to 1  $\Omega$ .

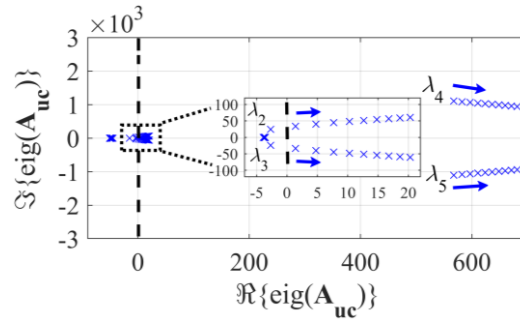


Figure 4.5: Spectrum of the dominant eigenvalues at  $P_{ac} = 1$  pu when  $(K_{p\omega}, K_{i\omega})$  change by a gain of 0.1 to 1.

### ***Influence of PLL***

The effect of changing the PLL bandwidth on the system stability is studied by changing the PLL gains  $(K_{p\omega}, K_{i\omega})$  by a gain of 0.1 to 10. The effect of these changes on the relocation of the dominant eigenvalues is found under the nominal condition and is summarized in Figure 4.5. As demonstrated,  $\lambda_{4-5}$  progress in the RHP in the unstable direction while,  $\lambda_{2-3}$ , which are initially in the LHP, move towards RHP. Figure 4.5 shows that  $\lambda_{2-3}$  are less affected by the changes in the control gains as compared to  $\lambda_{4-5}$ . Moreover, by decreasing the PLL gains by 10 degrees of magnitude, which limits the PLL bandwidth to 3 Hz, the VSC-WG system remains unstable at the nominal active power.

### ***Influence of DC Voltage Control***

DVC gains are changed in this part to investigate their influence on the dominant eigenvalues of the VSC-WG system at the nominal power. Figure 4.6 shows the

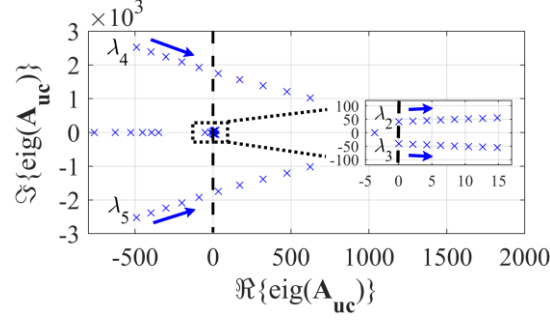


Figure 4.6: Spectrum of the dominant eigenvalues at  $P_{ac} = 1$  pu when  $(K_{pdc}, K_{idc})$  change by a gain of 0.5 to 1.

progress of the eigenvalues towards the imaginary axis as the controller gains  $(K_{pdc}, K_{idc})$  are changed by a gain of 0.5 to 1. As shown, the complex pair  $\lambda_{4-5}$ , that are initially in the LHP, approach the imaginary axis as a result of changes in the control gains until they cross the axis, where the bandwidth of the DVC is 17 Hz. Further increase in the gains results in the relocation of the eigenvalues into the RHP. Meanwhile,  $\lambda_{2-3}$  move in the same direction as  $\lambda_{4-5}$  yet constantly in the RHP. This shows that the instability problem of the VSC-WG system exists within a wide range of variations in the bandwidth of the DVC.

### ***Influence of AC Voltage Control***

The effect of varying the AVC gains on the dominant eigenvalues of the VSC-WG system at the nominal active power is depicted in Figure 4.7. According to the figure, similar to changing DVC gains,  $\lambda_{4-5}$  are initially in the LHP. Then, by multiplying the control gains  $(K_{pv}, K_{iv})$  by a gain of 0.08 to 1, they progress extensively towards the unstable region and enter the RHP, where the bandwidth of the AVC is 2.5 Hz. Meanwhile,  $\lambda_{2-3}$ , that initially have real form, relocate slightly until they merge and turn into a complex pair, still in the RHP, suggesting that the system remains unstable during the whole movement. Parallel to this relocation, the bandwidth of the AVC increases from 0.5 to 5.5 Hz.

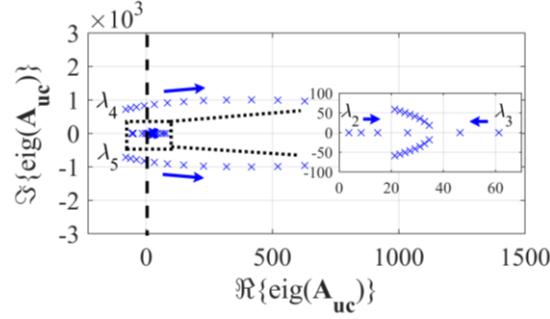


Figure 4.7: Spectrum of the dominant eigenvalues considering the active compensation at  $P_{ac} = 1$  pu when  $(K_{pv}, K_{iv})$  change by a gain of 0.08 to 1.

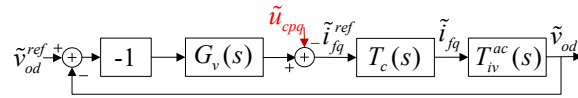


Figure 4.8: Block diagram of the AVC loop with active compensation.

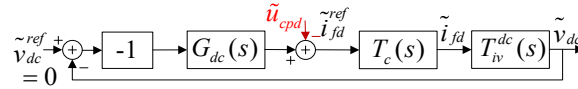


Figure 4.9: Block diagram of the DVC control loop with active compensation.

## 4.5. Proposed Dual Active Compensation

The sensitivity analysis in Section 3.2 shows that the stability of the VSC-WG system is violated at the nominal active power due to the dynamic interaction between the VSC control system and the WG impedance. The instability can be avoided only under the condition that the DVC dynamics are extremely compromised which is not desired. To mitigate this issue, a DAC scheme is proposed by which, two linear functions of the VSC output voltage are added to the AVC and DVC loops, as shown in Figure 4.8 and Figure 4.9, to change the distribution of the system eigenvalues in the complex plane and stabilize the system at the nominal power without compromising the system dynamics. Moreover, the system damping is increased under lower levels of power.

As shown in Figure 4.8 and Figure 4.9 in red, the perturbed feed-forward compensators  $\tilde{u}_{cpd}$  and  $\tilde{u}_{cpq}$  are added to the DVC and AVC closed-loop systems, respectively. Based on these augmentations, the equations for current references can be rewritten as

$$i_{fd}^{ref} = -G_{dc}(s)e_{dc} - u_{cpd}(s) \quad (4-11)$$

$$i_{fq}^{ref} = -G_v(s)e_{od} + u_{cpq}(s) \quad (4-12)$$

The compensators  $u_{cpd}$  and  $u_{cpq}$  in (4-11) and (4-12) are linear transfer functions of the VSC output voltage components in  $d$ - and  $q$ -axis as defined by the following.

$$u_{cpd}(s) = K_{cpd} \frac{2\zeta\omega_{cpd}s}{s^2 + 2\zeta\omega_{cpd}s + \omega_{cpd}^2} v_{od} \quad (4-13)$$

$$u_{cpq}(s) = K_{cpq} \frac{\omega_{cpq}}{s + \omega_{cpq}} v_{oq} \quad (4-14)$$

where  $K_{cpd}$ ,  $\zeta$ , and  $\omega_{cpd}$  are the gain, damping ratio, and center frequency of the band-pass filter (BPF) corresponding to  $u_{cpd}$ ; and  $K_{cpq}$  and  $\omega_{cpq}$  are the dc gain and cut-off frequency of the LPF corresponding to  $u_{cpq}$ . Based on the PFs of  $\tilde{v}_{dc}$  and  $\tilde{v}_{od}^c$  in the dominant eigenvalues of the VSC-WG system as given by Table 4-2, the BPF in (4-13) is selected to affect the unstable modes corresponding to eigenvalues  $\lambda_{4-5}$  in the high-frequency range without any undesired effect on other frequency ranges. Moreover, the LPF in (4-14) is selected to affect the unstable modes corresponding to the low-frequency range dominant eigenvalues  $\lambda_{2-3}$ . Since  $v_{od}$  is constant and  $v_{oq}$  is zero in the steady state, the compensators have zero effects on the steady-state operation of the VSC according to (4-13) and (4-14).

#### 4.5.1. Linear Model of Compensated System

4.5.1The VSC-WG with the DAC is linearized in this part similar to the uncompensated model in Section 4.4 using the same dynamic equations with the exception of considering nonzero compensation signals as given in (4-11) and (4-12). The linearized model of the compensated VSC-WG system is presented in the time-domain state-space representation as follows

$$\frac{d}{dt} \tilde{\mathbf{X}}_{cp}(t) = \mathbf{A}_{cp} \tilde{\mathbf{X}}_{cp}(t) \quad (4-15)$$

where the state matrix  $\mathbf{A}_{cp}$  is shown in Appendix B and the states vector  $\tilde{\mathbf{X}}_{cp}$  is given as

$$\tilde{\mathbf{X}}_{cp} = [\tilde{\mathbf{X}}_{uc}^T \quad x_{cpq} \quad x_{cpd1} \quad x_{cpd2}]^T \quad (4-16)$$

where  $x_{cpd1-2}$  and  $x_{cpq}$ , are the new state variables that are introduced by the BPF and LPF in (4-13) and (4-14).

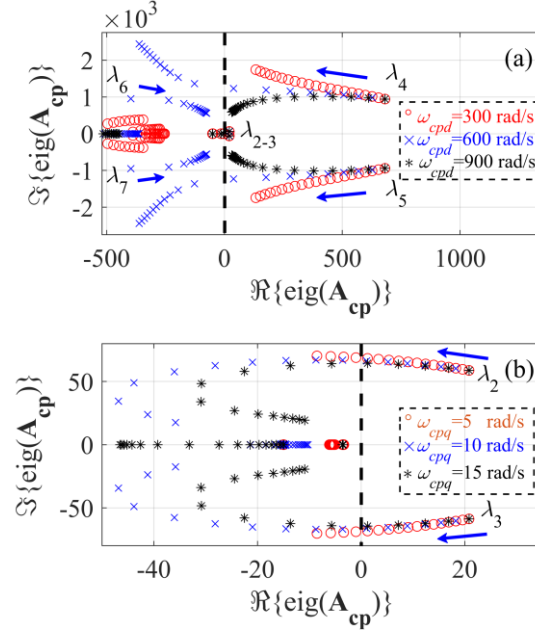


Figure 4.10: Spectrum of the dominant eigenvalues with DAC at  $P_{ac} = 1$  pu and  $SCR = 1.18$ . (a)  $K_{cpd}$  varies from 0 to 5 and  $K_{cpq} = 0$  at  $\omega_{cpd} = (300, 600, 900)$  rad/s. (b)  $K_{cpq}$  varies from 0 to 400 at  $\omega_{cpq} = (5, 10, 15)$  rad/s,  $K_{cpd} = 3.5$ , and  $\omega_{cpd} = 600$  rad/s.

#### 4.5.2. Design of Dual Active Compensators

The DAC compensators presented in (4-13) and (4-14) are three and two degrees of freedom controllers, respectively. The root locus method is used to find the optimum values of the DAC parameters using the state-space model of the compensated VSC-WG system as given in (4-15). The effect of changing different DAC parameters on the dominant eigenvalues of the VSC-WG system is obtained at the nominal power under  $SCR = 1.18$  condition. The summary of the results is shown in Figure 4.10. Figure 4.10(a) shows the migration of  $\lambda_{4-5}$  as a function of the increase in the BPF gain  $K_{cpd}$  at  $\omega_{cpd} = \{300, 600, 900\}$  rad/s while the  $u_{cpq}$  compensator is disabled by setting  $K_{cpq}$  to zero.

As shown,  $\lambda_{4-5}$ , that are initially located in the RHP, move towards the  $j\omega$  axis as  $K_{cpd}$  increases. Moreover, the compensation effectiveness can be boosted by taking larger values of  $\omega_{cpd}$ . As shown, at  $\omega_{cpd} = \{600, 900\}$  rad/s,  $\lambda_{4-5}$  enter the stable region (LHP). According to Figure 4.10(a), the optimum frequency at which  $u_{cpq}$  applies

maximum damping to the overall system dynamics is  $\omega_{cpd} = 600$  rad/s. According to the figure, the effect of increasing  $K_{cpd}$  on the system damping is twofold. On one hand,  $\lambda_{4-5}$  move in the direction of increasing the system stability, on the other hand,  $\lambda_{6-7}$  move in the opposite direction decreasing the system stability. Therefore, a trade-off is considered to find the optimum value for  $K_{cpd}$  where the resulting value is given in Table 4-1. Moreover, increasing the damping ratio  $\zeta$  has a mild positive effect on the system damping (not shown in Figure 4.10). Unlike  $\lambda_{4-5}$ , the low-frequency range eigenvalues  $\lambda_{2-3}$  are not affected by  $u_{cpq}$  compensator and remain in the unstable region (RHP).

Figure 4.10(b) shows the migration of  $\lambda_{2-3}$  as a function of the increases in the  $u_{cpq}$  compensator gain  $K_{cpq}$  at  $\omega_{cpq} = \{5, 10, 15\}$  rad/s while the  $u_{cpd}$  compensator is enabled with the optimum parameters ( $\omega_{cpd} = 600$  Hz and  $K_{cpd} = 3.5$ ). As shown,  $\lambda_{2-3}$ , that are initially in the RHP, relocate and move towards the imaginary axis and enter the stable region. According to Figure 4.10(b), the maximum improvement in the system stability is reached at  $\omega_{cpq} = 10$  rad/s and the optimum value of  $K_{cpd}$  is found at 225 where the dominant modes have the maximum damping. It should be noted that due to the frequency-scale separation between the BPF and LPF, the  $u_{cpd}$  and  $u_{cpq}$  dynamics are decoupled. Therefore, the DAC compensators  $u_{cpd,q}$  can be designed independently. Moreover, the DAC can dynamically mitigate the unstable oscillations in both low-frequency and high-frequency ranges without any unwanted cross-coupling.

### 4.5.3. Stability Assessment of Compensated System

Figure 4.11 shows the trajectory of the dominant eigenvalues of the VSC-WG system with the proposed DAC compensation subject to the increase of  $P_{ac}$  from 0.85 to 1 pu. As shown,  $\lambda_{4-5}$  progress towards the imaginary axis, similar to the uncompensated system in Figure 4.3, nevertheless, constantly in the LHP. Moreover,  $\lambda_{2-3}$ , follow the same pattern as  $\lambda_{4-5}$  in the stable region but with a slower rate. Figure 4.11, shows that the proposed DAC compensation improves the VSC-WG system stability for a wider range of active power (up to 1 pu) in the rectification mode as compared to the uncompensated system under the VWG condition.

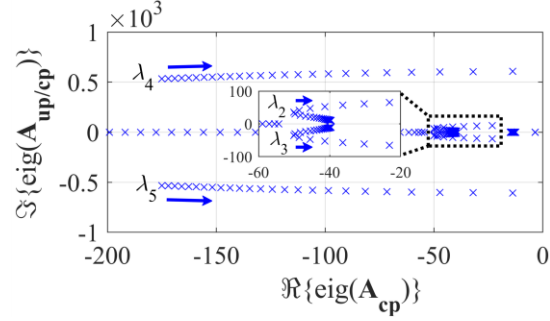


Figure 4.11: Spectrum of the dominant eigenvalues with DAC when  $P_{ac}$  changes from 0.85 pu to 1 pu.

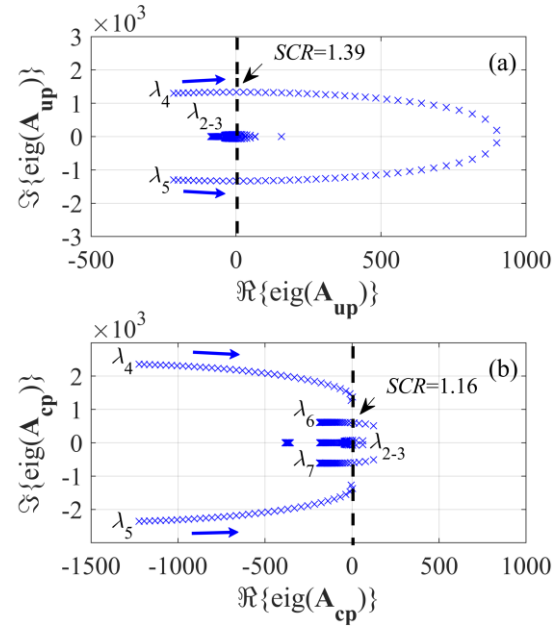


Figure 4.12: Spectrum of the dominant eigenvalues (a) without DAC. (b) with DAC when  $SCR$  changes from 1.5 to 1.1 ( $= SCR^c$ ).

Figure 4.12 shows the progress of the dominant eigenvalues subject to changes in  $SCR$  from 1.5 to 1.1, which corresponds to the  $SCR^c$  level in (4-8) and the  $X/R$  ratio of 15. As shown in Figure 4.12(a),  $\lambda_{4-5}$  move towards the imaginary axis and cross it at  $SCR = 1.39$  as the  $SCR$  is decreased by increasing the grid impedance  $Z_g$ . According to Figure 4.12(b), the dominant modes  $\lambda_{4-5}$  follow a similar trend but cross the imaginary axis at  $SCR = 1.16$ . Therefore, the DAC scheme extends the stability margin of the VSC-WG to a closer vicinity of the theoretical limit as compared to the uncompensated system.

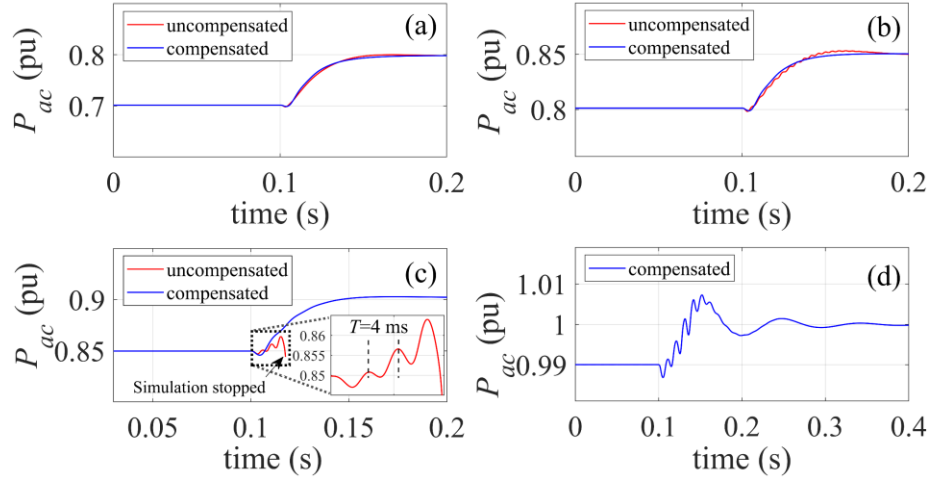


Figure 4.13: Dynamic response of the active power following a step variation in the active power at  $t = 0.1$  s at different power levels in the rectification mode.

## 4.6. Simulation Results

A series of time-domain simulations are carried out on the nonlinear model of the VSC-WG system to verify the results that are obtained based on the small-signal model that is developed in the previous sections. The VSC-WG shown in Figure 4.1 is built in MATLAB/Simulink environment based on the system specifications that are provided in Table 4-1. The average model of the VSC is used for the purpose of dynamic simulation [8].

### 4.6.1. Response to Active Power Step-Up

The active power response of the VSC-WG system subject to the sequential power steps at different power levels is summarized in Figure 4.13. A small step change is applied to the input of the VSC dc-side current source  $I_{dc}$  at  $t = 0.1$  s at different power levels. As shown in Figure 4.13(a)–(b), the responses of the VSC active power with and without DAC are very close up to  $P_{ac} = 0.85$  pu. At higher power levels, the responses begin to diverge. As shown in Figure 4.13(c), the unstable oscillatory behavior is visible in the uncompensated system response  $P_{ac}$  is close to 0.85 pu while the response of the compensated system exhibits well-damped stable dynamics at the same power level. These oscillations relate to the relocation of  $\lambda_{4-5}$  to the RHP with the change in the power as observed in Figure 4.3(a). Note that the period of the oscillations is 4 ms which

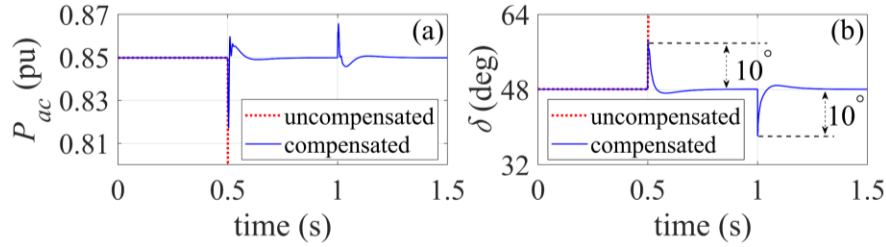


Figure 4.14: Transient responses of the VSC-WG with DAC scheme at  $P_{ac} = 0.85$  pu during  $10^\circ$  step changes in the phase angle of the grid voltage. (a) active power response. (b) angle difference response.

closely matches the frequency of the corresponding eigenvalues  $\lambda_{4-5}$ , i.e., 1494 Hz, as they cross the imaginary axis in Figure 4.3(a). More importantly, the VSC-WG system with enabled DAC demonstrates stable responses under the full range of the active power injection as shown in Figure 4.13(a)–(d).

#### 4.6.2. Response to Grid Angle Change

Another perk of using the proposed DAC scheme is the enhancement in the robustness of the VSC-WG system against the grid angle variations. Figure 4.14 shows the VSC-WG responses where a 10-degree step disturbance happens in the grid voltage angle  $\theta_g$  at the infinite ac bus at  $t = 0.5$  s and is cleared in  $t = 1$  s while the VSC-WG active power is  $P_{ac} = 0.85$  pu. The power response of the compensated system is shown in Figure 4.14(a) in blue. As shown,  $P_{ac}$  undergoes an undershoot and overshoot of about 0.03 and 0.01 pu at  $t = 0.5$  and 1 s, respectively, yet the VSC controller manages to regulate the injected power at the nominal value.

As shown in Figure 4.14(b), there are overshoots and undershoots of 10 degrees in the VSC angle difference response  $\delta$  following the changes in the grid angle. The VSC PLL tracks the actual PCC angle and quickly updates the VSC angle. Since the VSC-WG active power is not changing, the value of  $\delta$  returns to the same value right after changes. Moreover, the VSC-WG system stability is well preserved. The same condition is applied to the uncompensated VSC-WG system. As shown in Fig 16 with the dotted red line, the uncompensated system fails to track the deviations in the angle. Therefore, the VSC-WG does not reach a stable operating point.

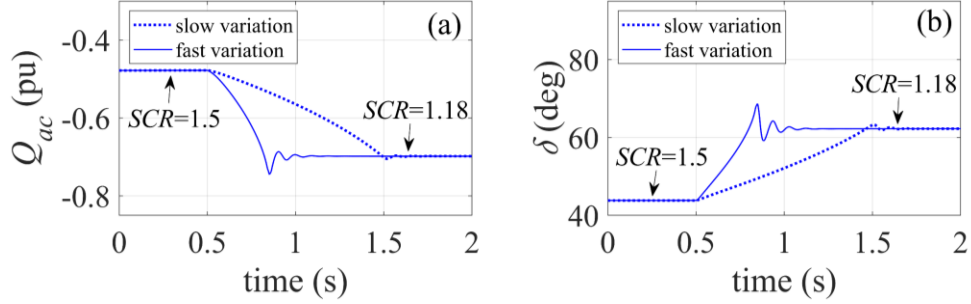


Figure 4.15: Transient responses of the VSC-WG with DAC scheme at  $P_{ac} = 1$  pu when  $Z_g$  linearly increases at slow (0.33 s period) and fast rates (1s period). (a) reactive power response. (b) angle difference response.

### 4.6.3. Response to Grid Impedance Variation

The grid equivalent impedance depends on the power flow especially in grid-connected microgrids where several DGs with plug-and-play capability are accommodated. Moreover, the disconnection of lines in the case of fault occurrence imposes a rapid change in the grid impedance. Therefore, the WG impedance is considered time-varying [18], [67], [74], [84].

Figure 4.15 shows the responses of the VSC-WG system to the increase in the grid impedance  $Z_g$ . Since the rate of the change in the grid impedance is not *a priori* assumption, the simulation is repeated for two periods of 0.33 s and 1 s which represent fast and slow changes in the WG impedance, respectively. The system is initially in the steady-state stable condition at  $SCR = 1.5$ . Then, at  $t = 0.5$  s,  $Z_g$  increases linearly from 0.8 pu to 1 pu and  $SCR$  decreases from 1.5 to 1 consequently while the VSC active power is at the nominal value. In the meantime, according to Figure 4.15(a),  $Q_{ac}$  increases to compensate for the reactive power absorbed by the WG reactance and maintain the so-called voltage stability [26].

As shown in Figure 4.15(b),  $\delta$  increases as the grid reactance increases which is justified according to (1-4) knowing that the VSC-WG active power is not changing. There are overshoots and undershoots in the system responses during the fast-rate changes in the grid impedance. However, the stable operation of the system is maintained during both rates of change. According to Figure 4.15, the stability of the VSC-WG system with DAC enabled is guaranteed under a wide range of fast and slow-

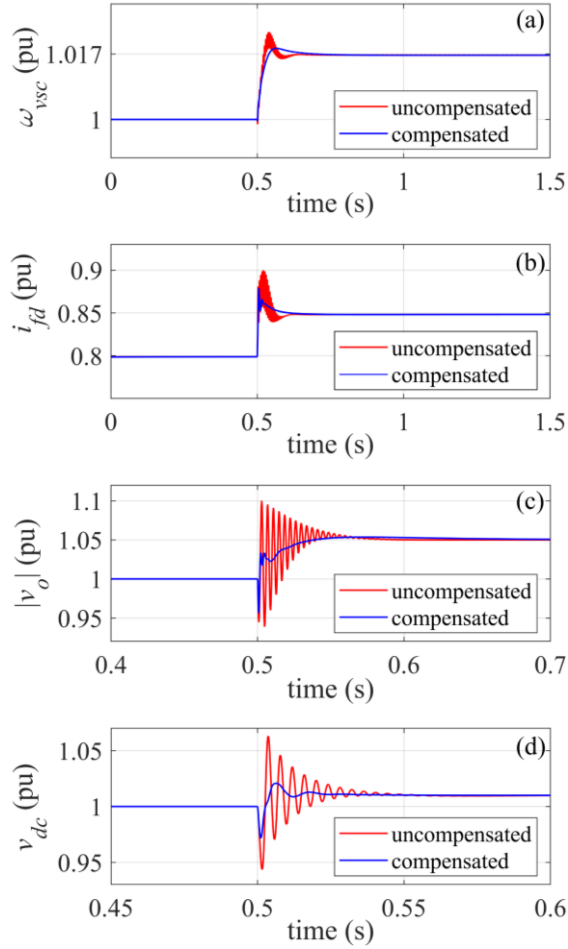


Figure 4.16: Dynamic responses of the VSC control loops subject to a step in the reference inputs at  $t = 0.5$  s and  $P_{ac} = 0.85$  pu. (a) frequency response following a 1 Hz grid frequency step. (b)  $d$  channel current response  $i_{fd}$  following a 5% in the current reference. (c) voltage response following a 5% step in the ac voltage reference. (d) dc voltage response following a 1% step in the dc voltage reference.

rate changes in the grid impedance.

#### 4.6.4. Dynamic Interactions with VSC Primary Controllers

The dynamic interactions of the proposed compensation method with the primary controllers of the VSC-WG control system are investigated at  $P_{ac} = 0.85$  pu, where the system is naturally stable without the active compensation. Figure 4.16(a) shows the frequency tracking responses of the PLL subject to a 1 Hz step in the frequency of the grid at  $t = 0.5$  s. Visibly, the DAC has an insignificant effect on the  $\omega_{vsc}$  response and hence on the PLL dynamics. Figure 4.16(b) shows the responses of  $i_{fd}$  following a 5%

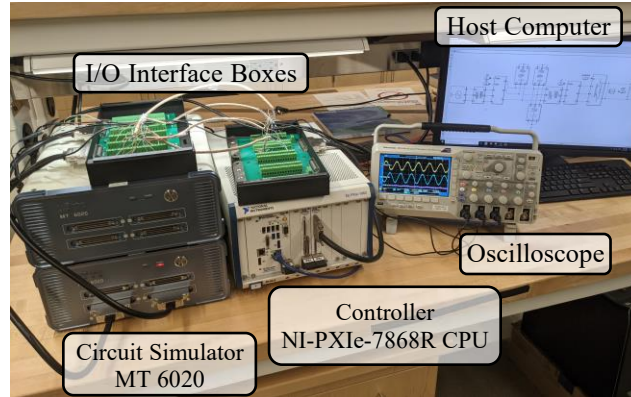


Figure 4.17: VSC-WG FPGA-based experimental set-up.

step in the current reference at  $t = 0.5$  s. As shown, the proposed DAC scheme manages to substantially decrease the overshoots and suppress the oscillations. Fig 18(c) shows the variations in the magnitude of the PCC voltage  $|v_o|$  following a 5% step change at  $t = 0.5$  s. As shown, the proposed DAC scheme suppresses the oscillations in the uncompensated response without making the response sluggish.

The variation of the dc voltage response  $v_{dc}$  is shown in Figure 4.16(d). As shown, when the reference increases by 1% at  $t = 0.5$  s, the compensated system exhibits a much more damped response with smaller over/undershoots as compared to the uncompensated system. Also, the system response speed is not compromised. Therefore, the outer control loop dynamics are not negatively affected by the introduction of the DAC feedforwards while benefiting from the compensators where the undesired oscillations are attenuated.

## 4.7. Real-Time Verification

To verify the simulation results about the effectiveness of the proposed DAC scheme in improving the VSC-WG stability in the rectification mode, the VSC-WG system in Figure 4.1 is developed in the HIL system assuming the switched-model of the VSC as shown in Figure 4.17. The HIL system essentially includes MT 6020 as an FPGA-based real-time circuit simulator and NI-PXIE-7868R CPU on which the VSC-WG controller is developed as shown in Figure 4.17. Two I/O interface boxes are used to allow the physical connection between the circuit simulator and the controller. The emulated VSC-WG and the DAC parameter specifications follow the same values given in Table 4-1.

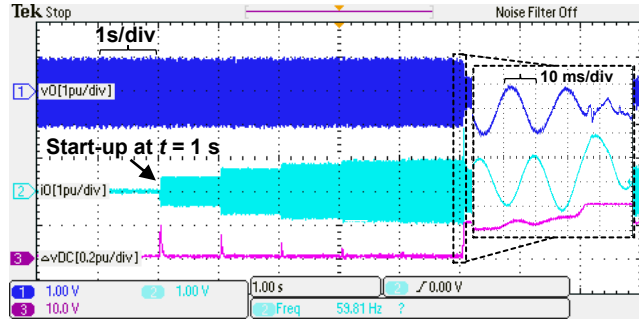


Figure 4.18: Measurement of the VSC-WG responses (DAC disabled) during start-up transients and step-ups in the dc power.

The time-step of the real-time simulation is 1  $\mu$ s while the controller is running at 50  $\mu$ s sampling time.

A series of tests are performed during which the VSC-WG active power is increased with a staircase profile  $P_{ac} = [0.4, 0.6, 0.7, 0.75, 0.8, 0.88]$  pu with increases in the input of the current source  $I_{dc}$  at  $t = [1, 2, 3, 4, 5, 6]$  s. Figure 4.18 shows the responses of the VSC-WG system without DAC compensation. As shown in Figure 4.18(a),  $v_o$  is regulated at 1 pu during the period  $t = [0, 6]$  s due to the AVC action. As shown in Figure 4.18,  $i_o$  increases after each step in the dc power and reaches a new steady-state point each time due to the CC action to maintain the power balance between the dc- and ac-side of the VSC.

The difference of the dc-side voltage from the reference value (dc-side voltage error)  $\Delta v_{dc}$  is depicted in Figure 4.18. According to Figure 4.18, VSC-WG system operation is stable during the period  $t = [0, 6]$  s. However, with further increases in the  $P_{ac}$  at  $t = 6$  s, the  $\Delta v_{dc}$  response shows undamped oscillations as shown in the zoom window superimposed on Figure 4.18. As shown, the VSC-WG system is unstable at  $P_{ac} = 0.88$  pu which agrees with the small-signal result in Figure 4.3(a) where  $\lambda_{4-5}$  are in the unstable region at the same power level. Moreover, the unstable oscillations are more pronounced in the  $\Delta v_{dc}$  response as compared to the other responses in Figure 4.18 since  $v_{dc}$  has the largest participation in the eigenmode related to  $\lambda_{4-5}$  according to Table 4-2.

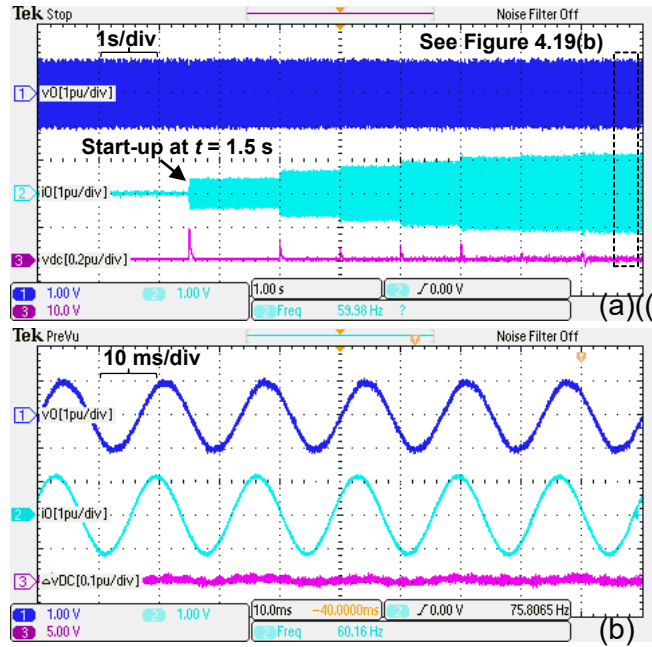


Figure 4.19: Measurement of the VSC-WG responses (DAC enabled) during start-up transients and step-ups in the dc current. (a) VSC output voltage/current (phase a) and dc-side voltage error. (b) zoomed view of the VSC responses in the steady state.

Similar series of tests are repeated for the VSC-WG system with DAC enabled. The active power profile is given as  $P_{ac} = [0.6, 0.8, 0.9, 0.95, 0.97, 0.99, 1]$  pu with the increases in  $I_{dc}$  at  $t = [1.5, 3, 4, 5, 6, 7, 8]$  s. Figure 4.19(a) shows the experimental results. As shown, the system is stable and the  $v_o$ ,  $i_o$ , and  $\Delta v_{dc}$  responses are well-damped and regulated in the steady state during the period  $t = [0, 9]$  s. The undershoots in the  $\Delta v_{dc}$  response in Figure 4.19(a) are less than 0.2 during the start-up and at the beginning of each step. Despite them, the VSC-WG system is stable at the nominal active power under the VWG condition.

Figure 4.19(b) shows a closer view of the VSC-WG responses in the steady-state under the nominal condition where the switching ripple content is pronounced for ac and dc-side voltages. Due to the filtering effect of the WG large inductance, the VSC output current is almost ripple-free as shown in Figure 4.19(b). It should be noted that the total harmonic distortion of  $v_o$  in Figure 4.19(b) is smaller than 5% which complies with the IEEE standard 519 [77]. As shown in Figure 4.19(b), the switching ripples are translated into the dc-side response  $\Delta v_{dc}$  as well. Yet, their content is negligible as compared to the average value of  $v_{dc}$  which is regulated at the nominal value by the DVC.

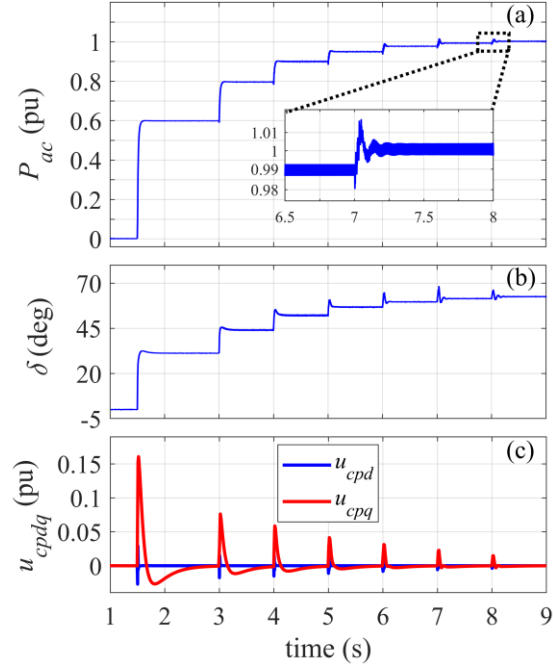


Figure 4.20: The VSC-WG responses (DAC enabled) during start-up transients and step-ups in the dc current (continued). (a) active power. (b) phase angle difference. (c) DAC compensation signals.

Figure 4.20(a) shows the active power response  $P_{ac}$  of the VSC-WG system. The response is well-damped up to  $P_{ac} = 0.95$  pu after which, small oscillations appear in the waveform. Regardless of the small oscillations in the waveform, the system is stable at the nominal power. Moreover, the dynamic response of  $P_{ac}$  around  $t = 7$  s, as magnified by the zoom window in Figure 4.20(a), and the response of the average model in Figure 4.13(d) closely matches. This verifies the development of the small-signal model in Section 4.5.1. Figure 4.20(b) shows the angle difference response  $\delta$ . Initially,  $\delta$  is close to zero since the VSC active power is zero. By increasing  $P_{ac}$  and noting the output voltage is regulated at 1 pu,  $\delta$  increases once the power increases according to (1-4). Figure 4.20(c) shows the variations in the DAC signals  $u_{cpdq}$ . As shown in Figure 4.20(c), the compensation signals are activated during the transient conditions while they have zero impact on the system in the steady state. Moreover, due to the frequency separation of the LPF and BPF function,  $u_{cpdq}$  are visibly separable in terms of dynamic responses.

## 4.8. Conclusion

Throughout this chapter, the integration of VSCs into the VWG systems has been investigated. The instabilities associated with the dynamic interaction between the VOC-based VSC in the rectification mode and the grid impedance have been mitigated effectively using the proposed DAC scheme under the VWG condition. The DAC scheme includes the injection of modified versions of the PCC voltage into the  $dq$  current references of the CC loops. It is shown that the proposed DAC scheme contributes successfully to the relocation of the eigenvalues on the complex plane from the unstable region to more damped locations in the stable region. In addition to the stabilization of the VSC-WG system under the VWG conditions, the stability/robustness of the system subject to the grid angle deviations has been improved with the proposed DAC. The effectiveness of the proposed DAC has been validated analytically using the small-signal analysis and numerically using the large-signal nonlinear model of the VSC-WG system which is developed in MATLAB/Simulink and then tested in real time using a HIL experimental set-up. The proposed DAC has the following features: (1) it is simple and can be easily designed using the linear control tools, (2) it does not impact the steady-state condition of the VSC-WG system, (3) it has a minimal influence on the existing VOC system of the VSC and so it can be designed independently, (4) it requires no extra sensors for practical implementation. Time-domain simulations and experiments of the VSC-WG system are carried out to verify (1), the stability of the VSC-WG system with the proposed DAC scheme under VWG condition, (2) the improved damping property of the compensated VSC-WG system, (3) the enhanced capability of the VSC-WG system to withstand sudden grid angle deviations and wide range of variations in the grid impedance.

## Chapter 5.

# Dynamic Modeling and Stability Analysis of Converter-Based AC Microgrids

The presence of AELs in ac microgrids can induce instabilities due to the interactions between the AEL dynamics with the rest of the microgrid, particularly in the isolated mode of operation. In this chapter, the complete state-space model of an ac microgrid is derived. Then, using small-signal analysis, the influence of integrating an AEL in the ac microgrid on the system stability is investigated under different operating conditions and parameter variations. To verify the small-signal results, a series of large-signal simulations are carried out on an example ac microgrid.

### 5.1. Introduction

Recent global concerns raised over the implications of climate change, primarily due to the overuse of fossil fuels, accompanied by the economical and technical merits of renewable energy resources have given rise to the concept of DG [85]. The emergence of DGs brings the possibility of forming a new entity called ac microgrids [11]. AC microgrids can operate independently from the rest of the power system, i.e., in the isolated mode of operation. The deployment of ac microgrids increases the reliability, efficiency, and quality of the power supply [11]. According to Navigant Research, the capacity of the global microgrids is expecting a 6.2 GW growth from 2015 to 2024, and therefore a widespread interest in microgrid studies is emerging [86].

The dominant power electronic interface for many forms of DGs is the two-level VSC [8]. In ac microgrids, VSCs can operate in the inversion or rectification modes of operations, i.e., as a voltage source inverter (VSI) or a voltage-source rectifier (VSR), respectively, to interface a DG source or a dc load, respectively. In the grid-connected microgrids, VSIs are controlled to provide the active or reactive power to the grid, i.e., a grid-feeding VSI [87], whereas the voltage and the frequency at the PCC are dictated by the main grid. On the contrary, in the isolated mode of operation, some or all the VSIs are responsible for regulating the frequency and the voltage in addition to providing the demanded power [87]. In the hierarchical control strategy, the primary control level

oversees the voltage stability, the frequency stability, and the power sharing among the VSIs in the ac microgrid [88]. The primary control level also offers a plug-and-play capability to DGs and has the dominant bandwidth as compared to the higher control levels. Therefore, the stability of an ac microgrid is primarily associated with this level of control. There is a plethora of power sharing methods in the literature for VSIs in ac microgrids [87]–[92]. The droop-based control method is the most commonly used method due to its simplicity, reliability, and autonomous operation, and hence this method is adopted in this chapter.

In typical distribution systems, PLs include incandescent lamps, and space heaters, whereas AELs include all power electronics-interfaced loads such as LED lamps and energy-efficient appliances. The PLs are modeled as constant impedances in power system studies, while the AELs, depending on the converter dynamics, can be modeled as constant power loads [9], [93], [94]. In the small-signal sense, constant power loads show an NIR which tends to induce instabilities in the system [92]. In [93], a VSR with a regulated dc resistive load is used as an AEL to show the destabilizing effect of AELs in ac microgrids. However, the effect of the PLL is ignored and the paper concludes that the tested ac microgrid is stable under reasonable variations of control parameters. Thus, the VSR design can be done independently. Alternatively, the authors in [9], [94] have implemented motor drive systems as AEL. In addition, the performance of the motor drive loads has been compared to a diode-bridge interfacing a regulated dc-dc converter in [94]. A review of the literature shows that there is a lack of a study that analyses the stability of an ac microgrid when a PL is replaced by an AEL of the same power level, including all system dynamics such as the PLL. Despite the claim made in [93], it is shown in this chapter that the integration of AEL in ac microgrids can introduce dynamic instabilities to the system.

In this chapter, an ac microgrid with three VSIs, PLs, and a VSR is studied. The full-order state-space model of the microgrid including all control dynamics is derived. The small-signal analysis shows that the states of the VSI power controller, and PLL and DVC modules of VSR have the highest impact on the dominant eigenvalues, and hence the overall system stability. The large-signal time-domain simulation results confirm the small-signal findings.

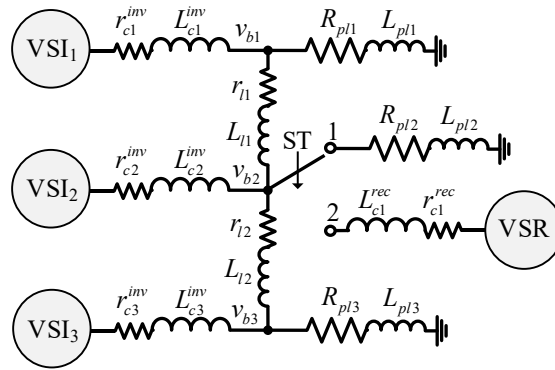


Figure 5.1: Single-line diagram of the ac microgrid with  $VSI_{1-3}$ ,  $PL_{1,3}$  at nodes 1 and 3, and a selector switch ST to switch between  $PL_2$  and AEL at node 2.

## 5.2. Small-Signal Dynamic Modeling of AC Microgrid

The diagram of the microgrid under study is shown in Figure 5.1 which consists of  $VSI_{1-3}$ , three  $RL$ -type PLs, denoted by  $PL_{1-3}$ , and VSR that interfaces a dc resistive load to the ac microgrid. The ac microgrid is in the islanded mode of operation, also called stand-alone, isolated mode, or autonomous mode, which means the upstream network becomes disconnected from the host ac grid and an island is formed [5]. In the islanded ac microgrid,  $VSI_{1-3}$  inject active and reactive power based on the load demand. Also, it is assumed that all three of VSIs are operating in grid-supporting mode, i.e., they are regulating the output ac voltages and frequency as well as sharing active and reactive power with the rest of the microgrid [87]. A selector switch (ST) is used to choose between an VSR (case I) and  $PL_2$  (case II) for the connection to node 2 to investigate the influence of integrating an VSR on the stability of the ac microgrid. All VSCs are controlled by the VOC scheme.

### 5.2.1. Multiple Reference Frames and Dynamical Transform

In the steady-state stable condition, the synchronization is preserved between  $VSI_{1-3}$  output voltage frequency. However, this is not the case during the transients since the VSIs are sharing active power under the droop control scheme, which is introduced in the next subsection, where their output frequency is set according to droop gains which are necessarily the same. Therefore, the angle differences between  $VSI_{1-3}$  output voltages are changing during the transients. While the VSR is not participating in the

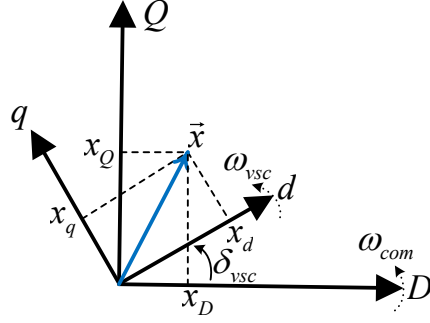


Figure 5.2: RF transformation.

power sharing, the synchronization mechanism embedded in the corresponding VOC results in the frequency difference between the VSR control and the rest of the AC microgrid during the transients.

As discussed in Chapter 2 and Chapter 3, the dynamic equations of VSCs are derived in the  $dq$ -RF which is synchronous with the output voltage phasor of the same converter module. Therefore,  $dq$ -RFs used by VSC modules for control purposes are asynchronous and varying during transients in the ac microgrid. Since the dynamic equations of different elements of the ac microgrid are mathematically coupled, to study the ac microgrid overall dynamics and stability, the set of variables that are defined in the corresponding  $dq$ -RF of each module needs to be translated into their equivalent in a common RF, symbolically denoted by  $DQ$ -RF, and vice versa. Therefore, the transformation tools that are required for this purpose are explained in the following.

Figure 5.2 shows a vector  $\vec{x}$  (in blue) with components (coordinates)  $x_d$  and  $x_q$  on an arbitrary  $dq$ -RF which rotates with the angular frequency  $\omega_{vsc}$ . The equivalent coordinates on the common  $DQ$ -RF, which rotates with the frequency  $\omega_{com}$ , may be obtained in time domain as follows [92].

$$\begin{bmatrix} x_D \\ x_Q \end{bmatrix} = \mathbf{T}(\delta_{vsc}) \begin{bmatrix} x_d \\ x_q \end{bmatrix} \quad (5-1)$$

$$\mathbf{T}(\delta_{vsc}) = \begin{bmatrix} \cos \delta_{vsc} & -\sin \delta_{vsc} \\ \sin \delta_{vsc} & \cos \delta_{vsc} \end{bmatrix} \quad (5-2)$$

where  $\mathbf{T}(\delta_{vsc})$  is the RF transform matrix function and  $\delta_{vsc}$  is the  $dq$ -RF angle (difference) with respect to the common  $DQ$ -RF. Perturbing the variables in (5-1) and (5-2) results in the following small-signal equivalent of the transformation in (5-1).

$$\begin{bmatrix} \tilde{x}_D \\ \tilde{x}_Q \end{bmatrix} = \mathbf{T}(\delta_{vsc}^\circ) \begin{bmatrix} \tilde{x}_d \\ \tilde{x}_q \end{bmatrix} + \mathbf{T}_d(\delta_{vsc}^\circ) \begin{bmatrix} x_d^\circ \\ x_q^\circ \end{bmatrix} \tilde{\delta}_{vsc} \quad (5-3)$$

where

$$\mathbf{T}_d(\delta_{vsc}) = \begin{bmatrix} -\sin \delta_{vsc} & -\cos \delta_{vsc} \\ \cos \delta_{vsc} & -\sin \delta_{vsc} \end{bmatrix} \quad (5-4)$$

and “~” and “°” denote small-signal perturbations and the nominal value of a variable, respectively. The corresponding equations for the reverse transformation from  $DQ$ - to  $dq$ -RF are presented time domain as follows.

$$\begin{bmatrix} x_d \\ x_q \end{bmatrix} = \mathbf{T}_{rev}(\delta_{vsc}) \begin{bmatrix} x_D \\ x_Q \end{bmatrix} \quad (5-5)$$

$$\begin{bmatrix} \tilde{x}_d \\ \tilde{x}_q \end{bmatrix} = \mathbf{T}_{rev}(\delta_{vsc}^\circ) \begin{bmatrix} \tilde{x}_D \\ \tilde{x}_Q \end{bmatrix} + \mathbf{T}_{rev,d}(\delta_{vsc}^\circ) \begin{bmatrix} x_D^\circ \\ x_Q^\circ \end{bmatrix} \tilde{\delta}_{vsc} \quad (5-6)$$

where

$$\mathbf{T}_{rev}(\delta_{vsc}) = \begin{bmatrix} \cos \delta_{vsc} & \sin \delta_{vsc} \\ -\sin \delta_{vsc} & \cos \delta_{vsc} \end{bmatrix} \quad (5-7)$$

$$\mathbf{T}_{rev,d}(\delta_{vsc}) = \begin{bmatrix} -\sin \delta_{vsc} & \cos \delta_{vsc} \\ -\cos \delta_{vsc} & -\sin \delta_{vsc} \end{bmatrix} \quad (5-8)$$

It should be noted that all equations in the following subsections are in the frequency domain and written in the  $dq$ -RF, wherein  $s$  represents the Laplace operator, unless otherwise stated.

### 5.2.2. Dynamic Model of VSI

The block diagram of a VSI interfacing an ideal dc source with an  $LC$  filter and control loops is shown in Figure 5.3. The averaged model of a three-phase two-level ideal VSC topology [8] is assumed in this chapter. The control functions of the VSI are implemented in the synchronous  $dq$ -RF. The definition of the system parameters is given in Table 5-1.



Table 5-1 continued

DC-Link nominal voltage, $v_{dc}^{vsr,ref}$	1.2	kV
DC-Link filter capacitance, $C_{dc}^{vsr}$	300	$\mu\text{F}$
PLL control gains, $[K_{p\omega}^{vsr}, K_{i\omega}^{vsr}]$	[307, 202]	$[\text{rads}^{-1}\text{V}^{-1}, \text{rads}^{-2}\text{V}^{-1}]$
DVC gains, $[K_{pdc}^{vsr}, K_{idc}^{vsr}]$	[1.8, 20]	$[\Omega^{-1}, \Omega^{-1}\text{s}^{-1}]$
AVC gains, $[K_{pv}^{vsr}, K_{iv}^{vsr}]$	[0, 0]	$[\Omega^{-1}, \Omega^{-1}\text{s}^{-1}]$
CC gains, $[K_{pc}^{vsr}, K_{ic}^{vsr}, F_c^{vsr}]$	[0.63, 63, 1]	$[\Omega, \Omega\text{s}^{-1}, -]$
PL <sub>1-3</sub>	Value	Unit
Nominal power, $S_{n1-3}^{pl}$	[10, 17, 15]	kVA
Power factor	[0.95, 1, 0.95]	—

### Power Circuit

The dynamic equations for the LC filter and the interfacing inductance shown in Figure 5.3 can be described as follows.

$$v_{td}^{vsi} - v_{od}^{vsi} = (r_f^{vsi} + sL_f^{vsi})i_{fd}^{vsi} - \omega_{vsi}L_f^{vsi}i_{fq}^{vsi} \quad (5-9)$$

$$v_{tq}^{vsi} - v_{oq}^{vsi} = (r_f^{vsi} + sL_f^{vsi})i_{fq}^{vsi} + \omega_{vsi}L_f^{vsi}i_{fd}^{vsi} \quad (5-10)$$

$$i_{fd}^{vsi} - i_{od}^{vsi} = sC_f^{vsi}v_{od}^{vsi} - \omega_{vsi}C_f^{vsi}v_{oq}^{vsi} \quad (5-11)$$

$$i_{fq}^{vsi} - i_{oq}^{vsi} = sC_f^{vsi}v_{oq}^{vsi} + \omega_{vsi}C_f^{vsi}v_{od}^{vsi} \quad (5-12)$$

$$v_{od}^{vsi} - v_{bd}^{vsi} = (r_c^{vsi} + sL_c^{vsi})i_{od}^{vsi} - \omega_{vsi}L_c^{vsi}i_{oq}^{vsi} \quad (5-13)$$

$$v_{oq}^{vsi} - v_{bq}^{vsi} = (r_c^{vsi} + sL_c^{vsi})i_{oq}^{vsi} + \omega_{vsi}L_c^{vsi}i_{od}^{vsi} \quad (5-14)$$

### Power Sharing Control

The power control loop in Figure 5.3 introduces a virtual droop in the VSI output voltage frequency and amplitude to control the active and reactive output power of the VSI. The related expressions are given by

$$\omega_{vsi} = \omega_{nl} - mP_{vsi} \quad (5-15)$$

$$v_{od}^{vsi,ref} = v_{nl} - nQ_{vsi} \quad (5-16)$$

where  $m$  and  $n$  are static droop gains [92], and  $\omega_{nl}$ , and  $v_{nl}$  are the nominal frequency and voltage set points, respectively. The choice of droop gains in different cases is

discussed in [92], [95]. Since the VOC scheme is adopted for VSIs, the  $q$ -axis component of the output reference voltage is set to zero [7]. Therefore,

$$v_{oq}^{vsi,ref} = 0 \quad (5-17)$$

The instantaneous values of the active and reactive power are filtered by LPFs, and so the VSI power expressions can be written as

$$P_{vsi} = \frac{3}{2} \left( \frac{\omega_c}{s+\omega_c} \right) (v_{od}^{vsi} i_{od}^{vsi} + v_{oq}^{vsi} i_{oq}^{vsi}) \quad (5-18)$$

$$Q_{vsi} = -\frac{3}{2} \left( \frac{\omega_c}{s+\omega_c} \right) (v_{od}^{vsi} i_{oq}^{vsi} - v_{oq}^{vsi} i_{od}^{vsi}) \quad (5-19)$$

where  $\omega_c$  is the LPF cut-off frequency and  $s$  is the Laplace operator.

The RF of VSI<sub>1</sub> is arbitrarily selected as the common  $dq$ -RF. To facilitate the integration of a VSI model into the microgrid model, the variables from the inverter  $dq$ -RF need to be transformed into the common  $DQ$ -RF. To this end, the difference between a VSI  $dq$ -RF angle and the  $DQ$ -RF angle is defined as

$$\delta_{vsi} = \frac{1}{s} (\omega_{vsi} - \omega_{com}) \quad (5-20)$$

### **Voltage and Current Control**

The cascaded outer AVC and inner CC loops are shown in Figure 5.3. The following dynamic equations represent the VSI control system.

$$i_{fd}^{vsi,ref} = (K_{pv}^{vsi} + K_{iv}^{vsi} s^{-1})(v_{od}^{vsi,ref} - v_{od}^{vsi}) - \omega_n C_f^{vsi} v_{oq}^{vsi} + F_v^{vsi} i_{od}^{vsi} \quad (5-21)$$

$$i_{fq}^{vsi,ref} = (K_{pv}^{vsi} + K_{iv}^{vsi} s^{-1})(v_{oq}^{vsi,ref} - v_{oq}^{vsi}) + \omega_n C_f^{vsi} v_{od}^{vsi} + F_v^{vsi} i_{oq}^{vsi} \quad (5-22)$$

$$v_{td}^{vsi} = (K_{pc}^{vsi} + K_{ic}^{vsi} s^{-1})(i_{fd}^{vsi,ref} - i_{fd}^{vsi}) - \omega_n L_f^{vsi} i_{fq}^{vsi} + F_c^{vsi} v_{od}^{vsi} \quad (5-23)$$

$$v_{tq}^{vsi} = (K_{pc}^{vsi} + K_{ic}^{vsi} s^{-1})(i_{fq}^{vsi,ref} - i_{fq}^{vsi}) + \omega_n L_f^{vsi} i_{fd}^{vsi} + F_c^{vsi} v_{oq}^{vsi} \quad (5-24)$$

where  $K_{px}^{vsi}$  and  $K_{ix}^{vsi}$  are the proportional and integral gains of a VSI-related PI compensator, and  $F_v^{vsi}$  and  $F_c^{vsi}$  are the gains of feedforward terms in the AVC and CC loops, respectively [8].

### State-Space Model of VSI

The state-space representation of the VSI can be obtained by linearizing (5-9)–(5-24) and using (5-3) and (5-6). This results in the state-space representation given by the following equations in the time domain.

$$\frac{d}{dt} \tilde{\mathbf{X}}_{vsi}(t) = \mathbf{A}_{vsi} \tilde{\mathbf{X}}_{vsi} + \mathbf{B}_{1vsi} \tilde{\mathbf{U}}_{vsi} + \mathbf{B}_{2vsi} \tilde{\omega}_{com} \quad (5-25)$$

$$\tilde{\mathbf{Y}}_{vsi} = \mathbf{C}_{vsi} \tilde{\mathbf{X}}_{vsi} \quad (5-26)$$

where the states, input, and output vectors of the VSI state-space model are as follows and the expanded forms of  $\mathbf{A}_{vsi}$ ,  $\mathbf{B}_{1vsi}$ ,  $\mathbf{B}_{2vsi}$ , and  $\mathbf{C}_{vsi}$  are presented in Appendix C.

$$\tilde{\mathbf{X}}_{vsi} = [\tilde{\delta}_{vsi} \quad \tilde{P}_{vsi} \quad \tilde{Q}_{vsi} \quad \tilde{\mathbf{V}}_{dq}^{vsi,c} \quad \tilde{\mathbf{I}}_{dq}^{vsi,c} \quad \tilde{\mathbf{I}}_{fdq}^{vsi} \quad \tilde{\mathbf{V}}_{odq}^{vsi} \quad \tilde{\mathbf{I}}_{odq}^{vsi}]^T \quad (5-27)$$

$$\tilde{\mathbf{U}}_{vsi} = [\tilde{v}_{bD}^{vsi} \quad \tilde{v}_{bQ}^{vsi}]^T \quad (5-28)$$

$$\tilde{\mathbf{Y}}_{vsi} = [\tilde{\omega}_{vsi} \quad \tilde{v}_{oD}^{vsi} \quad \tilde{v}_{oQ}^{vsi}]^T \quad (5-29)$$

where  $\{\tilde{\mathbf{V}}_{dq}^{vsi,c}, \tilde{\mathbf{I}}_{dq}^{vsi,c}\}$  are row vectors of the states related to the AVC and CC integrators in (5-21)–(5-24), respectively;  $\{\tilde{\mathbf{I}}_{fdq}^{vsi}, \tilde{\mathbf{V}}_{odq}^{vsi}, \tilde{\mathbf{I}}_{odq}^{vsi}\}$  are row vectors of the corresponding state variables (in lowercase) in  $d$ - and  $q$ -axis; and  $\{v_{bD}^{vsi}, v_{bQ}^{vsi}\}$ , are the  $D$ - and  $Q$ -axis components of the ac node that interfaces the VSI to the ac microgrid. For VSI<sub>1</sub>, since the angle of the output voltage phasor is taken as the common RF, thus,  $\delta_{vsi1} = \tilde{\delta}_{vsi1} = 0$ .

### 5.2.3. The Dynamic Model of VSR

The block diagram of a VSR with the  $LC$  filter and control loops interfacing a regulated dc load is shown in Figure 5.4. A PLL control block is used to generate the required angle for the  $abc$ - to  $dq$ -RF transformation. The dynamic equations in the following sections represent the AEL control system in Figure 5.4.

#### Power Circuit

The dynamic equations for the  $LC$  filter and the interfacing inductance shown in Figure 5.4 are presented as follows.

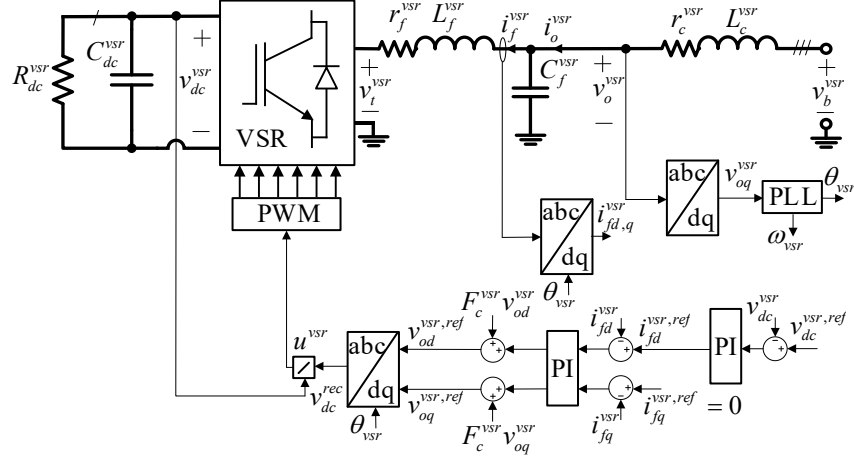


Figure 5.4: VSR with cascaded control loops, LC filter, and interface inductance interfacing dc load to the ac microgrid.

$$v_{od}^{vsr} - v_{td}^{vsr} = (r_f^{vsr} + sL_f^{vsr})i_{fd}^{vsr} - \omega_{vsr}L_f^{vsr}i_{fq}^{vsr} \quad (5-30)$$

$$v_{oq}^{vsr} - v_{tq}^{vsr} = (r_f^{vsr} + sL_f^{vsr})i_{fq}^{vsr} + \omega_{vsr}L_f^{vsr}i_{fd}^{vsr} \quad (5-31)$$

$$i_{od}^{vsr} - i_{fd}^{vsr} = sC_f^{vsr}v_{od}^{vsr} - \omega_{vsr}C_f^{vsr}v_{oq}^{vsr} \quad (5-32)$$

$$i_{oq}^{vsr} - i_{fq}^{vsr} = sC_f^{vsr}v_{oq}^{vsr} + \omega_{vsr}C_f^{vsr}v_{od}^{vsr} \quad (5-33)$$

$$v_{bd}^{vsr} - v_{od}^{vsr} = (r_c^{vsr} + sL_c^{vsr})i_{od}^{vsr} - \omega_{vsr}L_c^{vsr}i_{oq}^{vsr} \quad (5-34)$$

$$v_{bq}^{vsr} - v_{oq}^{vsr} = (r_c^{vsr} + sL_c^{vsr})i_{oq}^{vsr} + \omega_{vsr}L_c^{vsr}i_{od}^{vsr} \quad (5-35)$$

The dynamics of the VSR dc-side filter capacitance is integrated into the VSR dynamics using the instantaneous power balance between the ac- and dc-side as follows.

$$v_{dc}^{vsr2} R_{dc}^{-1} + \frac{1}{2} C_{dc}^{vsr} s(v_{dc}^{vsr}) = \frac{3}{2} (v_{td}^{vsr} i_{fd}^{vsr} + v_{tq}^{vsr} i_{fq}^{vsr}) \quad (5-36)$$

## PLL

The dynamics of the PLL is given by [94]

$$\omega_{vsr} = (K_{p\omega}^{vsr} + K_{i\omega}^{vsr} s^{-1})(0 - v_{oq}^{vsr}) \quad (5-37)$$

where the  $q$ -axis component of the VSR input voltage is set to zero and  $K_{px}^{vsr}$  and  $K_{ix}^{vsr}$  are the proportional and integral gains of a VSR-related PI compensator. The angle difference between the VSR rotating RF and the common  $DQ$ -RF is given by

$$\delta_{vsr} = \frac{1}{s} (\omega_{vsr} - \omega_{com}) \quad (5-38)$$

which is used to facilitate the integration of the AEL in the microgrid linearized model.

### **Voltage and Current Control**

The dynamics of the outer AVC and DVC loops in Figure 5.4 are represented by

$$i_{fd}^{vsr,ref} = -(K_{pdc}^{vsr} + K_{idc}^{vsr} s^{-1})(v_{dc}^{vsr,ref} - v_{dc}^{vsr}) \quad (5-39)$$

$$i_{fq}^{vsr,ref} = -(K_{pv}^{vsr} + K_{iv}^{vsr} s^{-1})(v_{od}^{vsr,ref} - v_{od}^{vsr}) \quad (5-40)$$

The dynamics of the CC inner loops are expressed by

$$v_{td}^{vsr,ref} = -(K_{pc}^{vsr} + K_{ic}^{vsr} s^{-1})(i_{fd}^{vsr,ref} - i_{fd}^{vsr}) + \omega_n L_f^{vsr} i_{fq}^{vsr} + F_c^{vsr} v_{od}^{vsr} \quad (5-41)$$

$$v_{tq}^{vsr,ref} = -(K_{pc}^{vsr} + K_{ic}^{vsr} s^{-1})(0 - i_{fq}^{vsr}) - \omega_n L_f^{vsr} i_{fd}^{vsr} + F_c^{vsr} v_{oq}^{vsr} \quad (5-42)$$

where  $F_c^{vsr}$  is the gain of feedforward terms in the CC loops [8].

### **State-Space Model of VSR**

The state-space representation of the VSR can be obtained in the time domain by linearizing (5-30)–(5-42) as

$$\frac{d}{dt} \tilde{\mathbf{X}}_{vsr}(t) = \mathbf{A}_{vsr} \tilde{\mathbf{X}}_{vsr} + \mathbf{B}_{1vsr} \tilde{\mathbf{U}}_{vsr} + \mathbf{B}_{2vsr} \tilde{\omega}_{com} \quad (5-43)$$

$$\tilde{\mathbf{Y}}_{vsr} = \mathbf{C}_{vsr} \tilde{\mathbf{X}}_{vsr} \quad (5-44)$$

where the states, input, and output vectors of the VSR state-space model are as follows and the expanded forms of  $\mathbf{A}_{vsr}$ ,  $\mathbf{B}_{1vsr}$ ,  $\mathbf{B}_{2vsr}$ , and  $\mathbf{C}_{vsr}$  are presented in Appendix C.

$$\tilde{\mathbf{X}}_{vsr} = [\tilde{\delta}_{vsr} \quad \tilde{\mathbf{v}}_{odq}^{vsr,c} \quad \tilde{\mathbf{I}}_{dq}^{vsr,c} \quad \tilde{v}_{dc}^{vsr,c} \quad \tilde{\mathbf{I}}_{fdq}^{vsr} \quad \tilde{\mathbf{V}}_{odq}^{vsr} \quad \tilde{\mathbf{I}}_{odq}^{vsr} \quad \tilde{v}_{dc}^{vsr}]^T \quad (5-45)$$

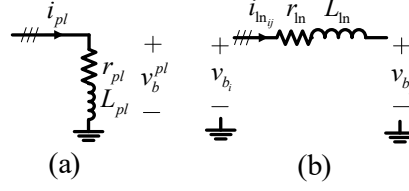


Figure 5.5: (a) PL interfaced directly to the AC microgrid, (b) Network line connecting  $i^{\text{th}}$  and  $j^{\text{th}}$  nodes of the ac microgrid.

$$\tilde{\mathbf{U}}_{\text{vsr}} = [\tilde{v}_{bD}^{\text{vsr}} \quad \tilde{v}_{bQ}^{\text{vsr}}]^T \quad (5-46)$$

$$\tilde{\mathbf{Y}}_{\text{vsr}} = [\tilde{i}_{oD}^{\text{vsr}} \quad \tilde{i}_{oQ}^{\text{vsr}}]^T \quad (5-47)$$

where  $\tilde{\mathbf{I}}_{\text{dq}}^{\text{vsr},c}$  is related to the CC integrators in (5-41) and (5-42);  $\tilde{\mathbf{v}}_{\text{odq}}^{\text{vsr},c}$  is a row vector of the states related to AVC integrator in (5-40) and PLL integrator in (5-37);  $\tilde{v}_{ac}^{\text{vsr},c}$  is the state related to the DVC integrator in (5-39);  $\{\tilde{\mathbf{I}}_{\text{fdq}}^{\text{vsr}}, \tilde{\mathbf{V}}_{\text{odq}}^{\text{vsr}}, \tilde{\mathbf{I}}_{\text{odq}}^{\text{vsr}}\}$  are row vectors of the corresponding state variables (in lowercase) in  $d$ - and  $q$ -axis; and,  $\{v_{bD}^{\text{vsr}}, v_{bQ}^{\text{vsr}}\}$  are the  $D$ - and  $Q$ -axis components of the ac node that interfaces the VSR to the ac microgrid.

#### 5.2.4. Dynamic Model of PL

Figure 5.5(a) shows a single-line diagram of a  $RL$ -type PL which is realized by a grounded three-phase series resistor  $r_{pl}$  and inductor  $L_{pl}$  circuit. The  $RL$ -type PL dynamics in  $DQ$ -RF is presented as follows.

$$v_{bD}^{pl} = (r_{pl} + sL_{pl})i_{plD} - \omega_{com}L_{pl}i_{plQ} \quad (5-48)$$

$$v_{bQ}^{pl} = (r_{pl} + sL_{pl})i_{plQ} + \omega_{com}L_{pl}i_{plD} \quad (5-49)$$

where  $v_{bD}^{pl}$  and  $v_{bQ}^{pl}$  are the  $D$ - and  $Q$ -axis components of the ac node voltage that interfaces the  $RL$ -type PL to the ac microgrid. The dynamics represented by (5-48) and (5-49) can be reformulated into the time-domain state-space representation of the  $RL$  load as follows.

$$\frac{d}{dt}\tilde{\mathbf{X}}_{\text{pl}}(t) = \mathbf{A}_{\text{pl}}\tilde{\mathbf{X}}_{\text{pl}} + \mathbf{B}_{1\text{pl}}\tilde{\mathbf{U}}_{\text{pl}} + \mathbf{B}_{2\text{pl}}\tilde{\omega}_{com} \quad (5-50)$$

where the expanded forms of the  $\mathbf{A}_{pl}$ ,  $\mathbf{B}_{1pl}$ , and  $\mathbf{B}_{2pl}$  are presented in Appendix C and the state, input, output vectors are as follows.

$$\tilde{\mathbf{X}}_{pl} = [\tilde{i}_{plD} \quad \tilde{i}_{plQ}]^T \quad (5-51)$$

$$\tilde{\mathbf{U}}_{pl} = [\tilde{v}_{bD}^{pl} \quad \tilde{v}_{bQ}^{pl}]^T \quad (5-52)$$

$$\tilde{\mathbf{Y}}_{pl} = \tilde{\mathbf{X}}_{pl} \quad (5-53)$$

### 5.2.5. Dynamic Model of Network Line

Figure 5.5(b) shows a single-line diagram of a network line of the ac microgrid that connects the  $i^{th}$  and  $j^{th}$  nodes of the microgrid network with the line current  $i_{lnij}$  flowing through it. The line is realized by a three-phase series inductor  $L_{ln}$  and resistor  $r_{ln}$  circuit. The line dynamics in  $DQ$ -RF is presented as follows.

$$v_{bD_i} - v_{bD_j} = (r_{ln} + sL_{ln})i_{lnDij} - \omega_{com}L_{ln}i_{lnQij} \quad (5-54)$$

$$v_{bQ_i} - v_{bQ_j} = (r_{ln} + sL_{ln})i_{lnQij} - \omega_{com}L_{ln}i_{lnDij} \quad (5-55)$$

where  $\{v_{bD_i}, v_{bQ_i}\}$  and  $\{v_{bD_j}, v_{bQ_j}\}$  are the  $D$ - and  $Q$ -axis voltage components of the  $i^{th}$  and  $j^{th}$  ac nodes, respectively. The dynamics presented by (5-54) and (5-55) can be reformulated into the time-domain state-space representation of the line as follows.

$$\frac{d}{dt}\tilde{\mathbf{X}}_{lnij}(t) = \mathbf{A}_{lnij}\tilde{\mathbf{X}}_{lnij} + \mathbf{B}_{1lnij}\tilde{\mathbf{U}}_{lnij} + \mathbf{B}_{2lnij}\tilde{\omega}_{com} \quad (5-56)$$

$$\tilde{\mathbf{X}}_{lnij} = [\tilde{i}_{lnDij} \quad \tilde{i}_{lnQij}]^T \quad (5-57)$$

$$\tilde{\mathbf{U}}_{lnij} = [\tilde{v}_{bD_i} \quad \tilde{v}_{bQ_i} \quad \tilde{v}_{bD_j} \quad \tilde{v}_{bQ_j}]^T \quad (5-58)$$

$$\tilde{\mathbf{Y}}_{lnij} = \tilde{\mathbf{X}}_{lnij} \quad (5-59)$$

where the expanded forms of the  $\mathbf{A}_{lnij}$ ,  $\mathbf{B}_{1lnij}$ , and  $\mathbf{B}_{2lnij}$  are presented in Appendix C.

## 5.2.6. State-Space Model of AC Microgrid

Combining the state-space models developed for the ac microgrid submodules in (5-25), (5-43), and (5-56), the state-space model of the ac microgrid can be obtained where the node voltages are the (exogenous) inputs of the state-space representation. To develop the autonomous state-space representation of the microgrid, as suggested by [92], a nodal equation for each microgrid node can be written using the currents entering (with a positive sign) or leaving (with a negative sign) the node. With this technique, the node voltages are defined as functions of the currents which in turn are the outputs of the state-space models. Performing a similar manipulation leads to the microgrid complete state-space representation in the time domain as

$$\frac{d}{dt} \tilde{\mathbf{X}}_{\text{mg}}(t) = \mathbf{A}_{\text{mg}} \tilde{\mathbf{X}}_{\text{mg}} \quad (5-60)$$

where

$$\tilde{\mathbf{X}}_{\text{mg}} = [\tilde{\mathbf{X}}_{\text{VSI}}^T \quad \tilde{\mathbf{X}}_{\text{LN}}^T \quad \tilde{\mathbf{X}}_{\text{PL}}^T \quad \tilde{\mathbf{X}}_{\text{vsr}}^T]^T \quad (5-61)$$

and  $\{\tilde{\mathbf{X}}_{\text{VSI}}, \tilde{\mathbf{X}}_{\text{LN}}, \tilde{\mathbf{X}}_{\text{PL}}\}$  are the combined states of VSI<sub>1-3</sub>, network lines, and PL<sub>1-3</sub>, respectively. The details of deriving (5-60) are presented in Appendix C.

## 5.3. Small-signal Stability Analysis

A small-signal analysis is conducted in this section using the parameters presented in Table 5-1. The nominal frequency droop is 0.87% at the maximum real power output and the nominal voltage droop is 13% [92] at the maximum reactive power output.

### 5.3.1. Case I: Microgrid with Three PLs

The eigenvalue spectrum of  $\mathbf{A}_{\text{mg}}$  is obtained and shown in Figure 5.6(a). As shown, the eigenvalues are distributed in a wide stable region of the complex plane. The eigenvalues can be divided into three groups: low-frequency ( $\text{Re}\{\lambda\} > -103$ ), mid-frequency ( $-2 \times 103 < \text{Re}\{\lambda\} < -103$ ), and high-frequency ( $\text{Re}\{\lambda\} < -2 \times 103$ ).

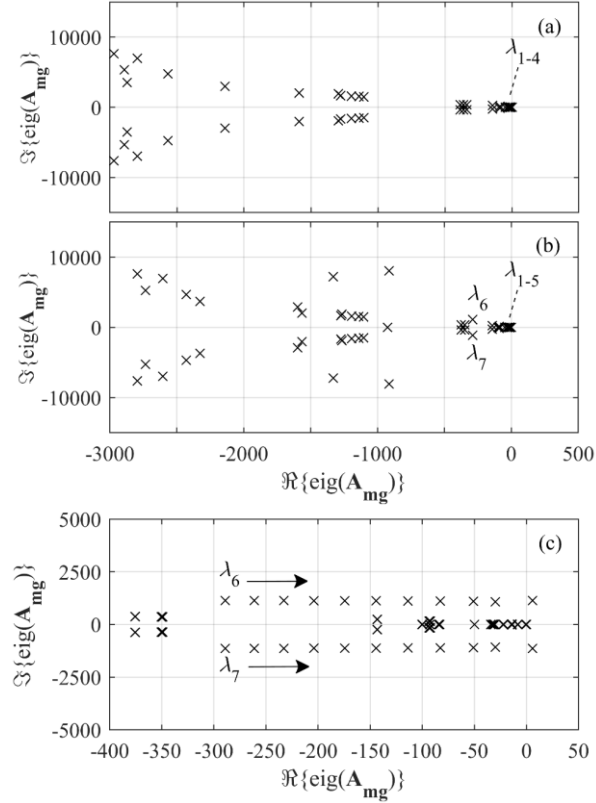


Figure 5.6: Eigenvalue spectrum of the ac microgrid when ST is at (a) position 1; (b) position 2 and  $P_{dc} = 15$  kW; (c) position 2 and  $P_{dc}$  is varied from 15 kW to 25 kW (only the eigenvalues with  $\text{Re}\{\lambda\} \geq -400$  are shown).

### 5.3.2. Case II: Microgrid with Two PLs and an AEL

In this case, the PL at node 2 is replaced by the AEL with the dc power  $P_{dc}$  equal to 15 kW. Compared to the eigenvalue spectrum of Case I in Figure 5.6(a), there are less-damped eigenvalues added to Case II in Figure 5.6(b). More importantly, a pair of complex eigenvalues denoted by  $\lambda_{6-7}$  is added which clearly shows the effect of replacing the PL with the AEL. Next,  $P_{dc}$  has been increased and the results are summarized in Figure 5.6(c), where the trace of the dominant eigenvalues including  $\lambda_{6-7}$  is shown. Clearly, increasing the  $P_{dc}$  relocates  $\lambda_{6-7}$  closer to the imaginary axis until the pair enters the unstable region at  $P_{dc} = 25$  kW. Therefore, the introduction of the AEL to the ac microgrid decreases the system stability (damping) and might induce instabilities. A similar analysis in Case I did not show any significant change in the pattern of eigenvalues of AMG in the complex plane.

Table 5-2 Participation Factors of AC Microgrid State Variables on Dominant Modes

State	Eigenvalues of $A_{mg}$							
	Case I			Case II; $P_{dc} = 15$ kW				
	$\lambda_{1-2} = -14 \pm 19j$	$\lambda_3 = -8.4$	$\lambda_4 = 0$	$\lambda_{1-2} = -14 \pm 19j$	$\lambda_3 = -8.5$	$\lambda_5 = -0.66$	$\lambda_4 = 0$	$\lambda_{6-7}^*$
$\delta_1^{vsi}$	0	0	1	0	0	0	1	0
$\tilde{P}_1^{vsi}$	0.26	0.15	~0	0.27	0.15	~0	~0	~0
$\delta_2^{vsi}$	0.72	0.1	~0	0.72	0.1	~0	~0	~0
$\tilde{P}_2^{vsi}$	0.36	0.06	~0	0.34	0.06	~0	~0	~0
$\delta_3^{vsi}$	0.04	1.8	~0	0.04	1.81	~0	~0	~0
$\tilde{P}_3^{vsi}$	~0	0.42	~0	~0	0.42	~0	~0	~0
$\tilde{v}_{dc}^{vsr,c}$				~0	~0	1	~0	~0
$\tilde{i}_{fd}^{vsr}$				~0	~0	~0	~0	0.6
$\tilde{i}_{od}^{vsr}$				~0	~0	~0	~0	0.11
$\tilde{v}_{dc}^{vsr}$				~0	~0	~0	~0	0.72
				~0	~0	~0	~0	

\* $\lambda_{6-7} = 289 \pm 1131j$

### 5.3.3. Participation Factor Analysis

To find the most influencing parameters on the microgrid stability, the PF analysis is conducted [92]. The system PFs are calculated for the microgrid states in Case I and II and the results are summarized in Table 5-2. As shown, the dominant eigenvalues in Case I with damping more than  $-16 s^{-1}$  include two real and a complex pair of eigenvalues. According to Table 5-2, the eigenvalues are mainly affected by the states of the power controller of VSI<sub>1-3</sub>. Therefore, the dynamics of the power controller (that is affected by the droop gains) has a significant effect on the location of the dominant eigenvalues.

In Case II, and according to Table 5-2, the most dominant eigenvalues with a damping more than  $-16 s^{-1}$  include three real and a complex pair of eigenvalues. As compared to Case I, the eigenvalues  $\lambda_{1-4}$  closely match in both cases. According to Table 5-2, all the dominant eigenvalues are mainly affected by the states of power sharing controllers except for  $\lambda_5$  which is only influenced by the PLL integrator state  $\mu q$ . This shows that the PLL controller must be designed carefully since it can easily impose an oscillatory or unstable mode to the system.

As shown in Figure 5.6(b), eigenvalues  $\lambda_{6-7}$  with a damping of  $-289 s^{-1}$  are relatively far from the imaginary axis. However, as shown in Figure 5.6(c), they have

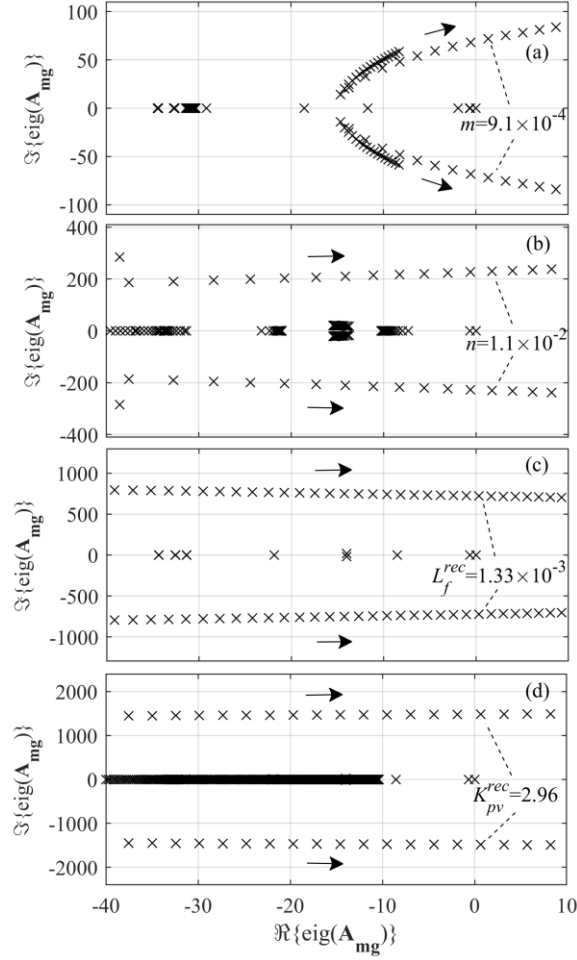


Figure 5.7: Progress of the dominant eigenvalue of the ac microgrid as a function of (a)  $9.4 \times 10^{-6} \leq n \leq 1.8 \times 10^{-3}$ ; (b)  $1.3 \times 10^{-4} \leq n \leq 1.9 \times 10^{-2}$ ; (c)  $1 \times 10^{-4} \leq L_f^{vsr} \leq 1 \times 10^{-3}$ ; (d)  $0.5 \leq K_{pv}^{vsr} \leq 6$ .

noticeable progress towards the imaginary axis as the AEL power increases. As shown in Table 5-2, the PF for  $\lambda_{6-7}$  is strongly related to the VSR input current, the inductor current, and the dc-side voltage. It is concluded that the dynamics of the ac microgrid can be prone to instabilities due to the high penetration of AELs.

### 5.3.4. Sensitivity Analysis

Based on the identified state variables that are effective on the microgrid stability, the influence of the variations of the parameters on the system stability is investigated. The most significant results are shown in Figure 5.7(a)–(d). As shown, a pair of complex

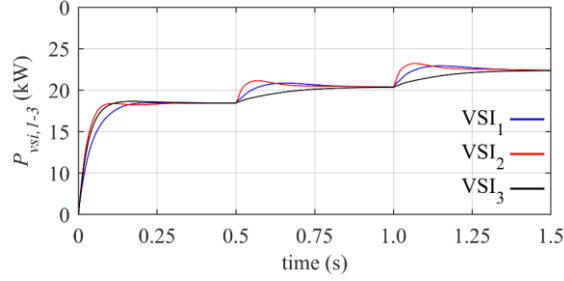


Figure 5.8: Active power of VSI<sub>1-3</sub> with step changes in the PL at node 2.

eigenvalues tend to move toward the imaginary axis as a function of the variation in the power droop gains, the VSR filter inductor, and the proportional gain of the VSR voltage controller, respectively. The complex pair eventually enter the unstable region at different points. The coordinated control design and system parameterization are crucial to preserving the system stability.

## 5.4. Time-Domain Simulation Results

To validate the effectiveness of the small-signal analysis, large-signal simulations of the microgrid are conducted in MATLAB/Simulink using the system parameters depicted in Table 5-1. Two series of simulations are conducted to compare the responses of the microgrid in cases I and II. During the simulation of case II, the dc power level of the AEL at node 2 is stepped from zero to 15 kW at  $t = 0$  s, then the power is increased to 20 kW at  $t = 0.5$  s, and finally increased to 25 kW at  $t = 1$  s. For each loading condition, the ac power fed at node 2 is calculated to determine the equivalent AEL.

Figure 5.8 shows the output power responses of VSI<sub>1-3</sub> in case I. As shown, the system is stable and the output active powers of VSI<sub>1-3</sub> converge to the same steady-state value following the step load change due to the same droop coefficients. Also, it can be observed that the responses of VSI<sub>2</sub> (in red) exhibit higher overshoots after each load change as compared to the responses of VSI<sub>1,3</sub>. This is attributed to the proximity of VSI<sub>2</sub> to the load changes at node 2.

Figure 5.9 shows the output power responses of VSI<sub>1-3</sub> following the step changes in the AEL power in case II. The changes in the power level of AEL are made by decreasing the VSR dc-side resistor while the dc-link voltage is regulated at 1.2 kV. As shown, the system is stable after the first load step and the responses are well-

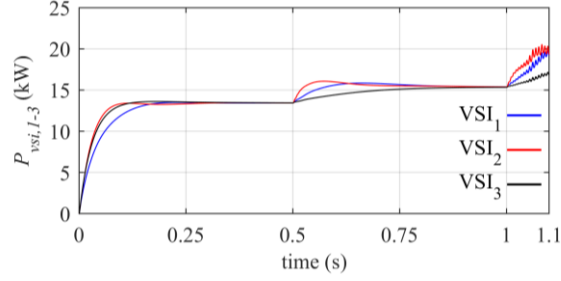


Figure 5.9: Active power of VSI<sub>1-3</sub> with step changes in the AEL at node 2.

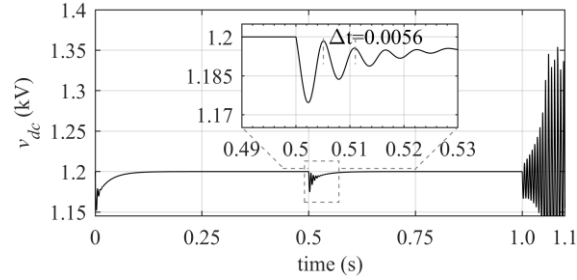


Figure 5.10: DC-Side voltage of VSR with step changes in the AEL at node 2.

damped similar to the case I. However, the system becomes unstable after the second load step at  $t = 1$  s. This confirms the small-signal analysis results in Figure 5.6(c), where it is shown that the AEL introduces a pair of complex eigenvalues that are sensitive to the AEL power level and tend to destabilize the system at 25 kW.

Figure 5.10 illustrates the dc-link voltage (as a response of the VSR) to the step changes in the power. As shown, the voltage is regulated by the voltage controller at 1.2 kV level before the instability occurs. However, as the system becomes unstable, the voltage controller fails to regulate the voltage. A closer look into Figure 5.10 reveals that during the first load change, the voltage shows oscillatory behavior while the responses of VSI<sub>1-3</sub> in Figure 5.8 are well-damped. The magnified versions of the VSR dc voltage response around  $t = 0.5$  s in Figure 5.10 shows that the period of oscillation is about 5.6 ms which coincides closely with the frequency of  $\lambda_{6-7} = -144 \pm 1123j$  at  $P_{dc} = 20$  kW. According to the mode participation analysis results in Table 5-2, the participation of  $\lambda_{6-7}$  in the VSI states is zero, hence the oscillation is not reflected in VSI power and angle responses, while it has its highest participation in the states of VSR.

## 5.5. Conclusion

In this chapter, an attempt is made to evaluate the effect of integrating AELs in a typical converter-based ac microgrid on the system stability. Using the average model of the VSCs and considering the dynamics of the control loops, lines, and PLs, the complete state-space model of a microgrid with three VSIs, three PLs, and AEL is derived. According to the small-signal analyses, eigenvalues of the microgrid with PLs are distributed in three groups, namely, the low-frequency, the mid-frequency, and the high-frequency. The stability of the microgrid is essentially associated with eigenvalues of the low-frequency which are close to the imaginary axis. It is shown that replacing PL<sub>2</sub> with the AEL induces more eigenvalues to the spectrum of the microgrid in the complex plane. While the dominant eigenvalues are strongly coupled with the states of VSI<sub>1-3</sub> power controllers, VSR voltage controller, and PLL, it is shown the AEL power level highly affects the microgrid stability. Moreover, the power droop control gains, the VSR filter inductance, and the proportional gain of the VSR voltage controller are the parameters that significantly affect the system stability. The results of the large-signal time-domain simulations of the microgrid verify the predictions of small-signal analysis; the penetration of AEL can destabilize the ac microgrid. The complete system dynamics needs to be studied for an ac microgrid stability especially when AELs are integrated.

## Chapter 6.

# Dynamic Modeling and Stability Improvements of Weak AC Microgrid Systems

In this chapter, the concept of ac weak microgrid (WMG) is introduced and *SCR* is generalized to include WMG systems. Then two simple cases of weak ac microgrids with two VSIs and either a PL or an AEL are considered for the dynamic study. The eigenvalue study of both systems shows instability due to droop control in lower levels of *SCR* as well as a dynamic interaction between the DVC loop of the AEL and WMG impedance. Linear active compensation methods are suggested to mitigate the instabilities followed by extensive small-signal analysis and supportive time-domain simulations.

### 6.1. Introduction

In Chapter 4 and Chapter 5, the conditions where a front-end VSC is connected to a weak ac grid are studied. As explained in these chapters, regardless of the VSC mode of operation (inversion or rectification mode), the dynamic interaction between the VSC (control) and the ac grid impedance can give rise to oscillations in the system variables like active power exchanged, output voltage angle, and PLL frequency and eventually instability can occur. For the same reasons discussed in those chapters, a weak connection can form when a VSC is connected to an ac microgrid. For example, subsequent to a fault, the microgrid disconnects from the upstream network where the resources and loads are located far away from each other. Another example is the outage of a line within an isolated ac microgrid that results in a large increase in the equivalent impedance between the sources and loads. In these cases, the sources of power are VSIs with dynamics that are mostly shaped by the power sharing scheme adopted within VSIs control system, particularly the commonly used droop control technique. Therefore, the isolated ac microgrid, called WMG henceforth, cannot be modeled by a strong voltage source in series with an *RL* impedance that interfaces a VSC to the grid as was the case in the previous chapters. Therefore, the causes of disrupting dynamic interactions between VSCs and the grid impedance in WMG cases

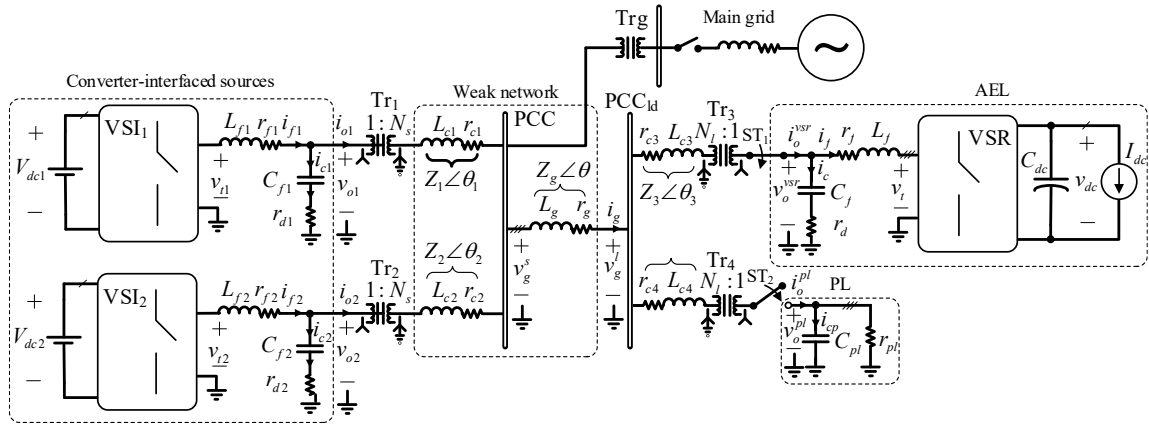


Figure 6.1: Single-line diagram of an islanded ac microgrid with a network of high-impedance lines that hosts two converter-interfaced sources, an AEL, and a PL.

are more complicated than the grid-connected applications and need separate treatment. To the best of the author's knowledge, the concept of WMG is not mentioned in current literature. Yet, its presence in the modern grids cannot be overseen as the power electronics application in the future (micro)grids, particularly PEC-interfaced DGs and electronic loads, grows. Consequently, a study about the dynamics and stability of this new emerging concept seems necessary which is the subject matter of this chapter. The remainder of this chapter is organized as follows. In Section 6.2 the structure of the WMG under study is introduced. Next, in Section 6.3 the notion of SCR is generalized to WMG applications. In Section 6.4 the dynamics of the WMG in the form of PL-WMG and VSC-WMG systems are developed. The static power transfer capability of WMGs is discussed in Section 6.5. In Section 6.6, state-space models of PL-WMG and VSC-WMG systems are created by linearizing the WMGs dynamics. Then, with the help of state-space models, the small-signal stability of WMG is thoroughly investigated. In Sections 6.7 and 6.8, respectively, active compensation strategies of the PL-WMG and VSC-WMG systems are examined. In Section 6.9, large-signal nonlinear simulations of both systems are carried out. Finally, the chapter is concluded in Section 5.5.

## 6.2. Weak AC Microgrid Structure

The diagram of the WMG is shown in Figure 6.1. As shown, on the source-side,  $VSI_{1-2}$  interface two DGs to the ac microgrid.  $VSI_{1-2}$  are cascaded by LC filters and are connected to the microgrid by similar low-to-high interface transformers  $Tr_1$  and  $Tr_2$ , respectively, with high-to-low voltage ratio  $N_s$ . It is assumed that the DGs are supported

by distributed energy storage system so they can be considered as dispatchable sources of energy [5]. A pair of lines connect the interface transformers to the PCC. The leakage impedances of the transformers, which are referred to the high-voltage side, are effectively lumped into the line impedances  $Z_1\angle\theta_1$  and  $Z_2\angle\theta_2$ , respectively, as shown in Figure 6.1. The VSI corresponding lines are connected to the PCC at the microgrid-side. The conventional droop control given in (5-15) and (5-16) is utilized in this chapter such that  $m_2 = 1.5m_1$  and  $n_2 = 1.5n_1$  according to their corresponding DGs capacity.

As shown on the load-side of the ac microgrid in Figure 6.1, an AEL and an RC-type PL, as an example of a passive load whose voltage can be maintained at 1 pu using its parallel capacitance, are interfaced to the ac microgrid through switches  $ST_1$  and  $ST_2$  and similar high-to-low interface transformers  $Tr_3$  and  $Tr_4$  with high-to-low voltage ratio  $N_l$  which, in turn, are connected to the  $PCC_{id}$  by connecting lines with impedances  $Z_3\angle\theta_3$  and  $Z_4\angle\theta_4$ , respectively. A long line with the impedance  $Z_g\angle\theta_g$  links PCC and  $PCC_{id}$  to each other. The leakage impedance of the interface transformer is referred to the high-voltage side and lumped with the connecting line impedances.  $ST_1$  and  $ST_2$  are operating complementary to let either VSR or PL be energized by the ac microgrid at a time.

When  $ST_1$  is closed (and  $ST_2$  is open), the VSR is effectively connected to a high-impedance grid from its point of view because the line between PCC and  $PCC_{id}$  (or equivalently the  $VSI_{1-2}$  connecting lines) is assumed to be long. Therefore, a VSC-WMG connection is formed. Similarly, when  $ST_2$  is closed, a PL-WMG connection is formed. In this chapter, the dynamics and stability of these systems are studied assuming that the microgrid is in the islanded mode of operation.

### 6.3. Definition of Short-Circuit Ratio in Weak AC Microgrid Systems

In the steady-state stable condition,  $VSI_{1-2}$  can be regarded as equal ac voltage sources. Ignoring the circulating current that can flow from one VSI to another, the simplified steady-state model of the VSC- and PL-WMG systems can be obtained as represented in Figure 6.2 where  $V_{nl}$  is the nominal voltage of  $VSI_{1-2}$  and  $Z_{mg}$  is the WMG equivalent impedance as seen from the ac microgrid load-side and is given by

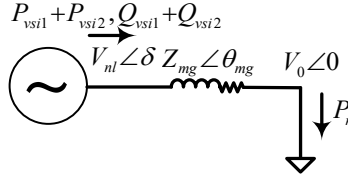


Figure 6.2: Thevenin equivalent circuit of the WMG.

$$Z_{mg} \angle \theta_{mg} = Z_{vsi} \angle \theta_{vsi} + Z_g \angle \theta_g + Z_{ld} \angle \theta_{ld} \quad (6-1)$$

where  $ld \in \{3,4\}$  and  $Z_{vsi} \angle \theta_{vsi}$  is the parallel combination of the VSI<sub>1-2</sub> connecting impedances such that

$$Z_{vsi} \angle \theta_{vsi} = Z_1 \angle \theta_1 \parallel Z_2 \angle \theta_2 = \frac{Z_1 Z_2 \angle \theta_1 + \theta_2}{Z_1 \angle \theta_1 + Z_2 \angle \theta_2} \quad (6-2)$$

The short circuit ratio of a WMG is defined as

$$SCR^{mg} = \frac{V_{nl}^2}{P_n Z_{mg}} \quad (6-3)$$

where  $V_{nl}$  is the ac microgrid nominal voltage, and  $P_n$  is the VSR nominal dc power. It is worth mentioning that the secondary control of the ac microgrids, as a centralized controller, restores the microgrid voltage and frequency and compensates for the deviations caused by the primary control [88]. Therefore, the choice of  $V_{nl}$  for VSI<sub>1-2</sub> is justified in the steady state.

## 6.4. Weak Microgrid Dynamics

For comparing the effect of the AEL on the WMG modes with the effect of the PL in Figure 6.1, it is assumed that only one type of the loads is energized at a time, i.e., ST<sub>1</sub> and ST<sub>2</sub> are operating complementary. In the following, the dynamics of the weak microgrid in Figure 6.1 are studied in two separate cases of VSC-WMG and PL-WMG systems. The dynamics and state-space of the weak microgrid submodules are studied in the following. It should be noted that all equations in the following are in the frequency domain, wherein  $s$  represents the Laplace operator unless otherwise, mentioned.

### 6.4.1. Dynamic Model of VSI

The structure and control systems of VSI<sub>1-2</sub> hosted in the VSC-WMG system are similar to that of the VSI studied in Section 5.2.2 by comparing Figure 6.1 and Figure 5.3; with the exception of presence of passive damping in the  $LC$  filter of VSI<sub>1-2</sub>. Therefore, repeating the same small-signal modeling on (5-9)–(5-24) where (5-11) and (5-12) are replaced by (2-3) to include the effect the passive damping, then the state-space models of the VSI<sub>1-2</sub> are fully represented by (5-25) where the  $D$ - and  $Q$ -axis components of the PCC voltage  $v_g$  are the voltage inputs of the state-space model as represented by

$$\tilde{\mathbf{U}}_{\text{vsi}} = [\tilde{v}_{gD}^s \quad \tilde{v}_{gQ}^s]^T \quad (6-4)$$

$$\tilde{\mathbf{Y}}_{\text{vsi}} = [\tilde{\omega}_{\text{vsi}} \quad \tilde{i}_{oD}^{\text{vsi}} \quad \tilde{i}_{oQ}^{\text{vsi}}]^T \quad (6-5)$$

where “ $\sim$ ” denotes small-signal perturbations of a variable, and the subscripts “ $D$ ” and “ $Q$ ” denote the  $D$ - and  $Q$ -axis components of a variable in the  $DQ$ -RF. It shall be noted that the connecting impedances of VSIs are referred to the low-voltage side, i.e.,  $N_s^{-2}L_c$ ,  $N_s^{-2}r_c$ . Further, the VSI<sub>1</sub> corresponding  $dq$ -RF is taken as the common  $DQ$ -RF. Hence, the frequency input of any submodule state-space model is given by

$$\omega_{\text{com}} = \omega_{\text{vsi1}} \quad (6-6)$$

### 6.4.2. Dynamic Model of VSR

The dynamics of the VSR in the ac microgrids are studied in Section 5.2.3 in the VSR  $dq$ -RF. Therein, since there is no control on the VSR output voltage, the AVC is disabled, i.e.,  $i_{fq}^{\text{vsr,ref}} = 0$ . However, when ST<sub>1</sub> is closed (and ST<sub>2</sub> is open), the VSR is connected to a high-impedance line according to Figure 6.1. Therefore, the AVC is adopted in the VOC of the VSR to regulate the output voltage  $v_o^{\text{ref}}$  at the nominal value, allowing for reactive power compensation. Then, the state-space representation of the AEL is governed by (5-30)–(5-42) where (5-32) and (5-33) are replaced by (2-3) to include the effect the passive damping according to Figure 6.1, and assuming the parameters of the connecting impedance are referred to the low-voltage side, i.e.,  $N_l^{-2}L_{c3}$ ,  $N_l^{-2}r_{c3}$ . With this arrangement, the input and output vectors of the VSR state-space representation are given by

$$\tilde{\mathbf{U}}_{\text{vsr}} = [\tilde{v}_{ldD}^{vsr} \quad \tilde{v}_{ldQ}^{vsr}]^T \quad (6-7)$$

$$\tilde{\mathbf{Y}}_{\text{vsr}} = [\tilde{i}_{oD}^{vsr} \quad \tilde{i}_{oQ}^{vsr}]^T \quad (6-8)$$

### 6.4.3. Dynamic Model of PL

The single-line diagram of an  $RC$ -type PL is shown in Figure 6.1 which is realized by a grounded three-phase series resistor  $r_{pl}$  and inductor  $C_{pl}$  circuit. Similar to the VSR, the PL is connected to a high-impedance network. Therefore, the capacitor bank  $C_{pl}$  is connected in parallel with the PL resistance  $r_{pl}$  to regulate the output voltage at the nominal value. When  $ST_2$  is closed (and  $ST_1$  is open), the PL is energized by the weak microgrid and its dynamics in  $DQ$ -RF are governed by

$$i_{oD}^{pl} = (r_{pl}^{-1} + sC_{pl})v_{oD}^{pl} - \omega_{com}C_{pl}v_{oQ}^{pl} \quad (6-9)$$

$$i_{oQ}^{pl} = (r_{pl}^{-1} + sC_{pl})v_{oQ}^{pl} + \omega_{com}C_{pl}v_{oD}^{pl} \quad (6-10)$$

$$N_l^{-1}v_{gD}^l - v_{oD}^{pl} = (r_{c4} + sL_{c4})i_{oD}^{pl} - \omega_{com}L_{c4}i_{oQ}^{pl} \quad (6-11)$$

$$N_l^{-1}v_{gQ}^l - v_{oQ}^{pl} = (r_{c4} + sL_{c4})i_{oQ}^{pl} + \omega_{com}L_{c4}i_{oD}^{pl} \quad (6-12)$$

The time-domain state-space model of the PL is obtained by linearizing (6-9)–(6-12) as follows.

$$\frac{d}{dt}\tilde{\mathbf{X}}_{\text{pl}}(t) = \mathbf{A}_{\text{pl}}\tilde{\mathbf{X}}_{\text{pl}} + \mathbf{B}_{1\text{pl}}\tilde{\mathbf{U}}_{\text{pl}} + \mathbf{B}_{2\text{pl}}\tilde{\omega}_{com} \quad (6-13)$$

$$\tilde{\mathbf{Y}}_{\text{pl}} = \mathbf{C}_{\text{pl}}\tilde{\mathbf{X}}_{\text{pl}} \quad (6-14)$$

where the corresponding state-space vectors are as follows and the state, input, and output matrices of the PL state-space model are presented in Appendix D.

$$\tilde{\mathbf{X}}_{\text{pl}} = [\tilde{v}_{oD}^{pl} \quad \tilde{v}_{oQ}^{pl} \quad \tilde{i}_{oD}^{pl} \quad \tilde{i}_{oQ}^{pl}]^T \quad (6-15)$$

$$\tilde{\mathbf{U}}_{\text{pl}} = [v_{gD}^l \quad v_{gQ}^l]^T \quad (6-16)$$

$$\tilde{\mathbf{Y}}_{\text{pl}} = [i_{oD}^{pl} \quad i_{oQ}^{pl}]^T \quad (6-17)$$

#### 6.4.4. Weak Microgrid State-Space Model

The state-space representation of the WMG in Figure 6.1 is developed for two cases of VSC-WMG and PL-WMG systems in a similar way that the state-space model of a generic ac microgrid is derived in Section 5.2. Two network nodes associated with the PCC and PCC<sub>ld</sub> are considered. The state-space models developed in previous subsections are used to build the total state-space model. Two nodal equations are written at the PCC and PCC<sub>ld</sub> nodes assuming adequately large virtual resistances  $r_n$  between the nodes and the ground [92] and considering the algebraic sum of the currents entering or leaving the nodes including VSI<sub>1-2</sub> and the load output currents referred to the high-voltage side and the long line current.

The WMG state-space representation is obtained in the time domain as follows.

$$\frac{d}{dt} \tilde{\mathbf{X}}_{\text{wmg}}(t) = \mathbf{A}_{\text{wmg}} \tilde{\mathbf{X}}_{\text{wmg}} \quad (6-18)$$

where  $\mathbf{A}_{\text{wmg}}$  is the state matrix of the weak microgrid whose expanded form is represented in Appendix D and the state vector is given by

$$\tilde{\mathbf{X}}_{\text{wmg}}^{\text{vsr}} = [\tilde{\mathbf{X}}_{\text{VSI}}^T \quad \tilde{\mathbf{X}}_{\text{In}}^T \quad \tilde{\mathbf{X}}_{\text{PL}}^T \quad \tilde{\mathbf{X}}_{\text{vsr}}^T]^T \quad (6-19)$$

where  $\tilde{\mathbf{X}}_{\text{In}}$  is the states of the line between PCC and PCC<sub>ld</sub> whose state-space model is presented in Section 5.2.5.

### 6.5. Static Capability of Weak AC Microgrid

Figure 6.3 demonstrates the single-line diagram of the WMG hosting VSI<sub>1-2</sub> and AEL/PL. The static transfer capability of the WMG is carried out in this section to find the maximum power delivered to the AEL or PL by VSI<sub>1-2</sub> in steady-state stable conditions. To this end, the nonlinear dynamic model of the VSC- and PL-WG systems in Section 6.4 are first evaluated using the parameters presented in Table 6-1 where the values of the nominal frequency and voltage droop gains of VSI<sub>1-2</sub> are 0.2% and 0.8% at the maximum real power and output reactive power, respectively [92]. Then, the nonlinear problem is solved to find the steady-state values for different loading conditions, i.e., dc power values of VSR. The following relations must hold in the steady-state condition for nonlinear models of the systems shown in Figure 6.3.

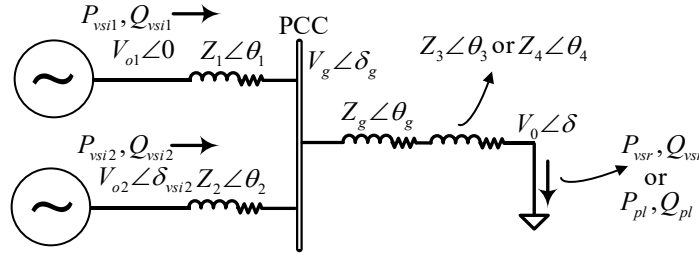


Figure 6.3: Single-line diagram of the WMG.

Table 6-1 Parameters of WMG System

AC Network	Value	Unit
Nominal line-to-line voltage, $v_n$	13.8	kV rms
Nominal frequency, $\omega_n$	$2\pi \times 60$	rad/s
Transformer high-to-low voltage ratio, $N_s/N_l$	13.8/0.69	kV/kV
Equivalent impedance, $Z_{mg}$ <sup>9</sup>	16.42	$\Omega$
$X/R$ ratio	10	—
VSI <sub>1-2</sub>	Value	Unit
Nominal power, $S_n^{vsi}$	7.25	MVA
Nominal frequency setpoint, $\omega_{nl}$	$2\pi \times 60$	rad/s
Nominal voltage setpoint, $v_{nl}$	690	Vrms
AC filter, $[L_f^{vsi}, r_f^{vsi}, C_f^{vsi}, r_d^{vsi}]$	[100, 1.5, 50, 0.3]	[ $\mu\text{H}$ , m $\Omega$ , $\mu\text{H}$ , $\Omega$ ]
DC-Link nominal voltage, $v_{dc}^{vsi,ref}$	1.9	kV
Droop gains, $[m_1, n_1, m_2, n_2]$	[0.13, 12.7, 0.19, 19.1]	[rad/MW/s, V/MVAR]
AVC gains, $[K_{pv}^{vsi}, K_{iv}^{vsi}, F_v^{vsi}]$	[3.6, 60, 0.9]	[ $\Omega^{-1}$ , $\Omega^{-1}\text{s}^{-1}$ , —]
CC gains, $[K_{pc}^{vsi}, K_{ic}^{vsi}, F_c^{vsi}]$	[0.4, 4.76, 1]	[ $\Omega$ , $\Omega\text{s}^{-1}$ , —]
Low-frequency compensator parameters, $[m_{d1}, n_{d1}, m_{d2}, n_{d2}]$	PL: [0.8, 0, 1.2, 0] AEL: [0.5, 0, 0.75, 0]	[Rad/MW, Vs/MVAR]
VSR	Value	Unit
Nominal power, $S_n^{vsr}$	7.25	MVA
AC filter, $[L_f^{vsr}, r_f^{vsr}, C_f^{vsr}, r_d^{vsr}]$	[100, 1.5, 500, 0.9]	[ $\mu\text{H}$ , m $\Omega$ , $\mu\text{H}$ , $\Omega$ ]
DC-Link nominal voltage, $v_{dc}^{vsr,ref}$	1.9	kV
DC-Link filter capacitance, $C_{dc}^{vsr}$	15	mF
PLL control gains, $[K_{p\omega}^{vsr}, K_{i\omega}^{vsr}]$	[0.7, 2.5]	[ $\text{rads}^{-1}\text{V}^{-1}$ , $\text{rads}^{-2}\text{V}^{-1}$ ]
AVC gains, $[K_{pv}^{vsr}, K_{iv}^{vsr}]$	[5, $10^3$ ]	[ $\Omega^{-1}$ , $\Omega^{-1}\text{s}^{-1}$ ]
CC gains, $[K_{pc}^{vsr}, K_{ic}^{vsr}, F_c^{vsr}]$	[0.34, 5, 1]	[ $\Omega$ , $\Omega\text{s}^{-1}$ , —]
DVC gains, $[K_{pac}^{vsr}, K_{idc}^{vsr}]$	[11.9, 593.5]	[ $\Omega$ , $\Omega^{-1}\text{s}^{-1}$ ]
Mid-frequency compensator parameters, $[K_{cpd}, \omega_{cpd}, \zeta]$	[15, 300, 0.9]	[—, $\text{rads}^{-1}$ , —]
PL	Value	Unit
Nominal power, $S_{pl}$	7.25	MVA

<sup>9</sup> According to IEEE standard 242-2001 [99], this equates 40.3 km of a medium voltage (RL type) single-line copper conductor.

$$\omega_{com} = \omega_{vsi,i} = \omega_n - m_i P_{vsi,i}, i = 1 - 2 \quad (6-20)$$

$$v_{oi} = v_n - n_i Q_{vsi,i}, i = 1 - 2 \quad (6-21)$$

$$v_o^{vsr} = v_o^{pl} = v_n \quad (6-22)$$

$$P_{vsr} = P_{pl} = P_n \quad (6-23)$$

where  $P$  and  $Q$  stand for the active and reactive power generated, with “vsi” subscript, or received, with “vsr” or “pl” subscripts, by different modules of the WMG, respectively. In the case of VSC-WG system, the steady-state relations between the dc and ac sides of the VSR and upper limits on the value of the VSR modulation index, i.e.,  $m \leq 1$ , are considered as additional conditions that are not shown here. Further, in the case of PL-WG system, the value of  $C_{pl}$  is found numerically so that  $v_o^{pl} = v_n$  holds for all loading conditions. In both cases,  $SCR^{mg}$  is decreased until the lowest value at which the system has a numerical solution, called static critical value and denoted by  $SCR^{mg,cr}$ , is found. The results reveal that  $SCR^{mg,cr}$  is equal to 1.15 and 1.13 for VSC- and PL-WG cases, respectively. This shows that with the same ac WG parameters and equal loading  $P_{vsr} = P_{pl}$ , the VSC-WG system has lower power transfer capability if the ac voltage compensation is enabled.

## 6.6. Small-Signal Stability of Weak AC Microgrid

### 6.6.1. Case 1: PL-WMG System

#### ***Influence of Power Level***

The PL power is changed in this part to see its effect on the PL-WMG stability.  $SCR^{mg} = 1.6$  is taken to impose the very weak condition on the WMG and the impedance ratio  $Z_g/Z_{vsi}$  is equal to 1.5. The state matrix of the system in (6-18) is evaluated at different loading levels  $P_{pl}$  using the parameters given in Table 6-1 and the dominant eigenvalues

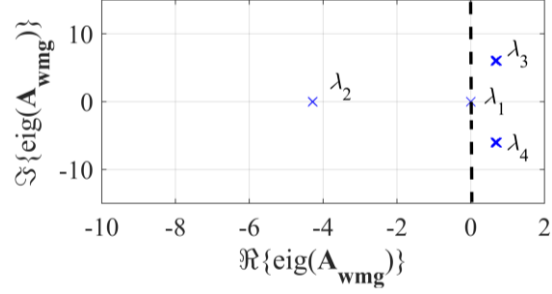


Figure 6.4: Spectrum of the dominant eigenvalues of PL-WMG when  $P_{pl}$  changes between 0.42 to 1 pu at  $SCR^{mg} = 1.6$  and the impedance ratio is equal to 9.

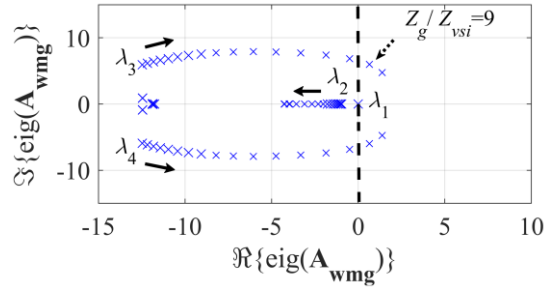


Figure 6.5: Spectrum of the dominant eigenvalues of PL-WMG when impedance ratio changes between 0.2 to 19 at the nominal loading power and  $SCR^{mg} = 1.6$ .

are obtained accordingly. The results are summarized in Figure 6.4. As shown, there are two real eigenvalues  $\lambda_{1-2}$  in the stable region and a pair of complex eigenvalues  $\lambda_{3-4}$  in the RHP which indicates dominant unstable modes of the system. The spectrum of the dominant modes does not show a visible change as the power level increases from 0.42 pu to 1 pu. Therefore, the ac microgrid with the impedance ratio equal to 9 is unstable with the high integration of PLs in the very weak condition. It should be noted that the impedance ratio can impact the results as discussed in the next part.

### ***Influence of Impedance Ratio***

Assuming  $Z_{ld}$  is negligible in (6-1), then  $Z_{mg}$  is equal to the series combination of  $Z_{vsi}$  and  $Z_g$ . Therefore, the impedance ratio is changed in this part to find its effect on the PL-WMG stability while the  $Z_{mg}$  (or  $SCR^{mg}$ ) is fixed. Figure 6.5 shows the result of changing the ratio from 0.2 to 19 at nominal loading power and under very weak condition  $SCR^{mg} = 1.6$ . According to the figure,  $\lambda_{3-4}$  are initially on the LHF and the system is stable at

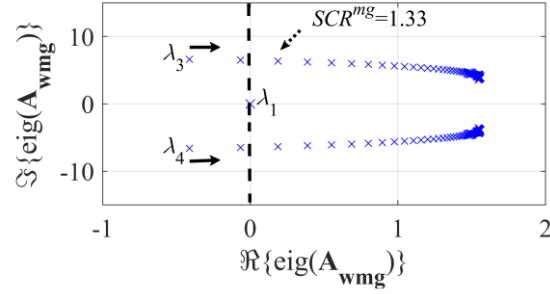


Figure 6.6: Spectrum of the dominant eigenvalues of PL-WMG at the nominal loading power when  $SCR^{mg}$  changes between 1.13 to 10 and the impedance ratio is equal to 9.

Table 6-2 Participation factor of PL-WMG variables on dominant modes at  $SCR^{mg} = 1.6$ , impedance ratio equal to 1.5, and under nominal loading power condition.

State	Eigenvalues of $A_{wmg}$		
	$\lambda_2 = -4.3$	$\lambda_1 = 0$	$\lambda_{3-4} = 0.65 \pm 6j$
$\tilde{\delta}_1^{vsi}, \tilde{\delta}_2^{vsi}$	0, 0.39	1, $\sim 0$	0, 0.32
$\tilde{v}_{od1}^{vsi,c}, \tilde{v}_{od2}^{vsi,c}$	0.15, 0.14	$\sim 0, \sim 0$	0.17, 0.18
$\tilde{v}_{og1}^{vsi,c}, \tilde{v}_{og2}^{vsi,c}$	0.21, 0.18	$\sim 0, \sim 0$	0.15, 0.16

the impedance ratio where the  $Z_{mg}$  value is dominated by  $Z_{vsi}$ . Then, by the increase of the proportion of the long line impedance  $Z_g$  in  $Z_{mg}$ , or equivalently decrease of  $Z_{vsi}$ ,  $\lambda_{3-4}$  approach the imaginary axis. Ultimately, the system exhibits unstable dynamics once the impedance ratio is equal to 9.

### ***Influence of Short Circuit Ratio***

The equivalent impedance  $Z_{mg}$  is changed in this part to evaluate the system stability as a function of  $SCR^{mg}$ . Figure 6.6 shows the spectrum of the dominant eigenvalues subjected to the variation of  $SCR^{mg}$  between the critical value 1.13 (very weak condition) and 10 (stiff condition). According to Figure 6.6,  $\lambda_{3-4}$  progress toward the imaginary axis which means that the PL-WMG stability is reduced as a function of increasing the  $SCR^{mg}$ . At  $SCR^{mg} = 1.33$ ,  $\lambda_{3-4}$  enter the RHP which means the PL-WMG system is unstable at this value of  $SCR^{mg}$  and higher.

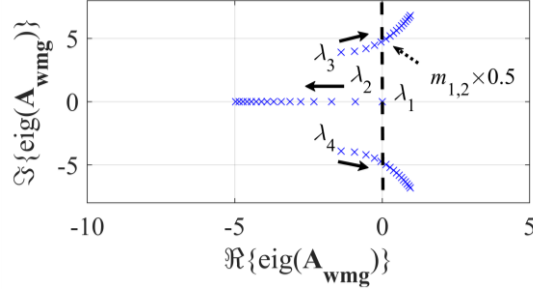


Figure 6.7: Spectrum of the dominant eigenvalues of PL-WMG when  $m_{1-2}$  vary between 0–1.5 times the nominal values at the nominal power,  $SCR^{mg} = 1.6$ , and the impedance ratio is equal to 9.

### **Participation Factor of Dominant Modes**

Participation of different state variables in the dominant modes of the PL-WMG state-space model is presented in Table 6-2. The system is operating under nominal condition and  $SCR^{mg} = 1.6$  is taken at which the system exhibits unstable behavior according to Figure 6.6. According to Table 6-2,  $\lambda_1$  is exclusively associated with the VSI<sub>1</sub> angle which is constantly zero since it is taken as the common *DQ*-RF angle. This is why  $\lambda_1$  is not affected by the changes in the system parameters according to Figure 6.4–Figure 6.6.  $\lambda_2$  is mainly influenced by VSI<sub>2</sub> angle perturbations and slightly by the AVC submodules of VSI<sub>1-2</sub>. However, it does not impose any instability concern according to Figure 6.4–Figure 6.5.

As shown in Table 6-2,  $\lambda_{3-4}$  are mainly influenced by the VSI<sub>2</sub> angle perturbations and slightly by the AVC submodules of VSI<sub>1-2</sub>. Further, the results in Figure 6.5 about the effect of the impedance ratio can be intuitively justified as follows. Assuming a large  $X/R$  ratio, the active power is a function of the angle difference between each VSI output voltage phasor and the PCC voltage phasor, as well as the amplitude of the impedance between them as described by (4-5). Hence, in the linearized model of (4-5), the perturbed value of the angle difference is affected by the impedance value at the same operating point. Since the VSIs output angles are strongly coupled with the dominant modes of  $\lambda_{3-4}$  according to Table 6-2, the impedance ratio, in turn, can affect the location of  $\lambda_{3-4}$  in the complex plane.

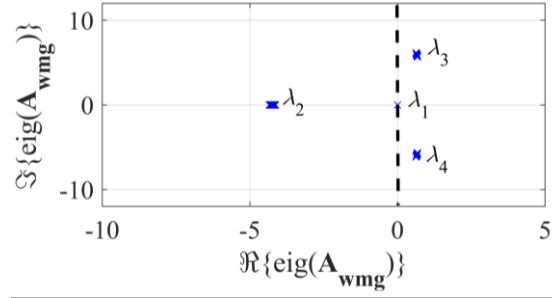


Figure 6.8: Spectrum of the dominant eigenvalues of PL-WMG when  $n_{1-2}$  vary 0–1.5 times the nominal values at the nominal power,  $SCR^{mg} = 1.6$ , and the impedance ratio is equal to 9.

### **Sensitivity Analysis of Control Parameters**

Sensitivity analysis of the PL-WMG system is conducted in this part to find the effect of changing control gains on the system stability under the same condition as the PFs are obtained in Table 6-2. As depicted in Figure 6.7, the dominant unstable modes related to  $\lambda_{3-4}$  are located in the stable region at very small values of static droop gains  $m_{1-2}$  and they enter the unstable region as the gains retrieve the original values. However, this is done at the cost of having VSIs with the output power responses that are extremely slow which is not desirable, especially in the MG application where the power demand is provided solely by PEC-interfaced resources. Further, the droop gain values might be enforced according to the economic interest of the system operator [92].

As depicted in Figure 6.8, the dominant unstable modes are hardly affected by the variations in the droop gains  $n_{1-2}$  and tend to remain in the unstable region. Comparing the results in Figure 6.7 and Figure 6.8 shows that the droop gains associated with the active power sharing affect the stability by relocating the dominant modes. However, the droop gain related to the reactive power sharing does not reshape the distribution of the dominant eigenvalues much. This is in agreement with the results presented in Table 6-2 where it is shown that  $\lambda_{3-4}$  are mainly influenced by the angle variable and not by the output voltage amplitude.

Figure 6.9 shows the relocation of the dominant eigenvalues as a function of changes in the AVC gains  $\{K_{pv1-2}, K_{iv1-2}\}$  at  $SCR^{mg}$ . As shown, at  $SCR^{mg} = 1.6$ , the dominant unstable modes related to  $\lambda_{3-4}$  eventually enter the stable region as the control gains increase while according to the same figure, at  $SCR^{mg} = 2$  and higher

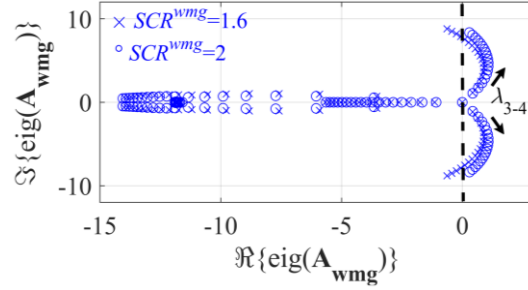


Figure 6.9: Spectrums of the dominant eigenvalues of PL-WMG when  $(K_{pv1}^{vsi}, K_{iv1}^{vsi})$  and  $(K_{pv2}^{vsi}, K_{iv2}^{vsi})$  vary between 0.1–1.6 times the nominal values at the nominal power,  $SCR^{mg} = \{1.6, 2\}$ , and the impedance ratio is equal to 9.

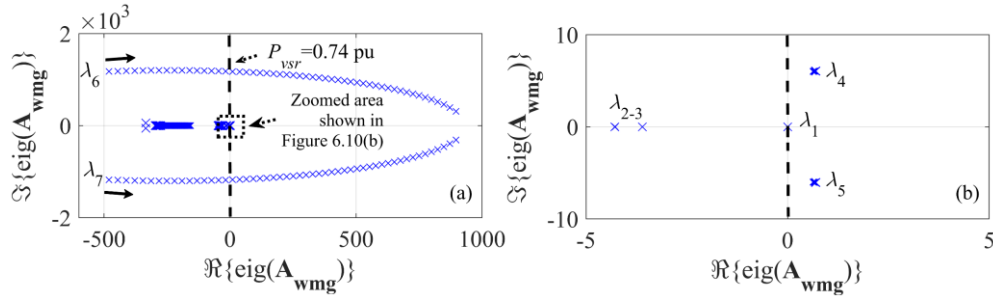


Figure 6.10: Spectrums of the dominant eigenvalues of VSC-WMG when  $P_{vsr}$  changes between 0.42 to 1 pu,  $SCR^{mg} = 1.6$ , and the impedance ratio is equal to 9.

levels, the unstable modes tend to remain in the unstable region. Further investigation, which is not reflected in the figure, shows that to shift all the dominant modes into the stable region, the BW of AVC loops within the VOC of VSI<sub>1-2</sub> needs to increase above half of the BW of CC loops at  $SCR^{mg} = 1.6$ . Therefore, under very weak conditions and with taking high-value AVC compensator gains, it is possible to make PL-WMG stable, while the system with the same control design still shows unstable behavior under stiffer conditions.

## 6.6.2. Case II: VSC-WMG System

### ***Influence of Power Level***

The AEL power  $P_{vsr}$  is changed in this part to find its effect on the VSC-WMG stability. The results are summarized in Figure 6.10 where  $SCR^{mg} = 1.6$ , the impedance ratio is equal to 9, and the rest of the parameters are presented in Table 6-1. As shown in

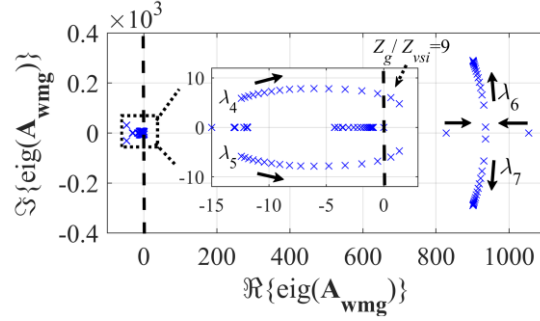


Figure 6.11: Spectrum of the dominant eigenvalues of VSC-WMG at the nominal loading power when impedance ratio changes between 0.2 to 19 at  $SCR^{mg} = 1.6$ .

Figure 6.10(a), there is a pair of complex eigenvalues  $\lambda_{6-7}$  that are initially in the RHP and migrate towards the imaginary axis. They finally enter the stable region at  $P_{vsr} = 0.74$  pu. Meanwhile, as focused on them in Figure 6.10(b), the other pair of eigenvalues labeled by  $\lambda_{4-5}$  tend to remain in the unstable region.

### ***Influence of Impedance Ratio***

The impact of the impedance ratio on the system stability is studied in this part at  $SCR^{mg} = 1.6$  and under the nominal load condition. Figure 6.11 shows the results of changing the ratio from 0.2 to 19. According to the figure,  $\lambda_{4-5}$  are initially on the LHF. Then, by increasing the impedance ratio or equivalently decreasing the proportion of  $Z_{vsi}$ , the dominant modes approach the imaginary axis and eventually enter the RHP once the impedance ratio is equal to 9. However, the system is unstable due to the persistent presence of  $\lambda_{6-7}$  in the RHP according to Figure 6.11.

### ***Influence of Short Circuit Ratio***

The microgrid equivalent impedance  $Z_{mg}$  is changed to evaluate the stability of the VSC-WMG system as a function of  $SCR^{mg}$ . Figure 6.12 shows the spectrum of the dominant eigenvalues subjected to the variation of  $SCR^{mg}$  between the critical value 1.15 (very weak condition) to 10 (stiff condition). According to Figure 6.12(a),  $\lambda_{6-7}$  that are initially real and in the RHP move across the real axis in the opposite direction until they meet and then split into a complex pair approaching the imaginary axis. They eventually enter the LHP at  $SCR^{mg} = 2.9$ . As shown in Figure 6.12(b),  $\lambda_{4-5}$ , that are initially in the LHP, leave the LHP at  $SCR^{mg} = 1.3$  and enter the unstable region as the  $SCR^{mg}$  increases.

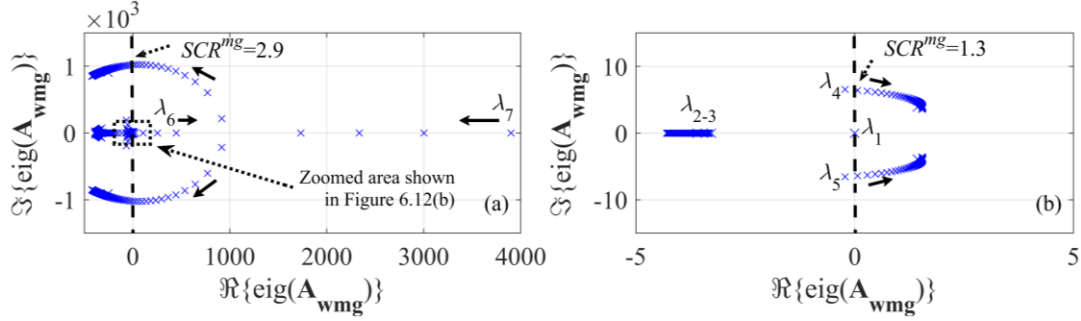


Figure 6.12: Spectrum of the dominant eigenvalues of VSC-WMG at the nominal loading power when  $SCR^{mg}$  changes between 1.15 to 10 and the impedance ratio equal to 9.

Table 6-3 Participation factor of VSC-WMG variables on dominant modes at  $SCR^{mg} = 1.6$ , impedance ratio equal to 1.5, and under nominal loading power condition.

State	Eigenvalues of $A_{wmg}$				
	$\lambda_3 = -4.3$	$\lambda_2 = -3.6$	$\lambda_1 = 0$	$\lambda_{4-5} = 0.63 \pm 6j$	$\lambda_{6-7} = 901.8 \pm 288.7j$
$\tilde{\delta}_1^{vsi}, \tilde{\delta}_2^{vsi}$	0, 0.4	0, ~0	1, ~0	0, 0.32	0, ~0
$\tilde{v}_{od1}^{vsi,c}, \tilde{v}_{od2}^{vsi,c}$	0.14, 0.15	~0, ~0	~0, ~0	0.18, 0.17	~0, ~0
$\tilde{v}_{oq1}^{vsi,c}, \tilde{v}_{oq2}^{vsi,c}$	0.21, 0.18	~0, ~0	~0, ~0	0.15, 0.16	~0, ~0
$\tilde{i}_{od1}^{vsi}, \tilde{i}_{od2}^{vsi}$	~0, ~0	~0, ~0	~0, ~0	~0, ~0	0.27, 0.27
$\tilde{v}_{cd1}^{vsi}, \tilde{v}_{cd2}^{vsi}$	~0, ~0	~0, ~0	~0, ~0	~0, ~0	0.18, 0.19
$\tilde{i}_{fd1}^{vsi}, \tilde{i}_{fd2}^{vsi}$	~0, ~0	~0, ~0	~0, ~0	~0, ~0	0.54, 0.55
$\tilde{i}_{fq1}^{vsi}, \tilde{i}_{fq2}^{vsi}$	~0, ~0	~0, ~0	~0, ~0	~0, ~0	0.12, 0.11
$\tilde{\delta}^{vsr}$	~0	~0	~0	~0	0.11
$\tilde{i}_{od}^{vsr}$	~0	~0	~0	~0	3.93
$\tilde{i}_{oq}^{vsr}$	~0	~0	~0	~0	1.51
$\tilde{v}_{od}^{vsr,c}$	~0	~0	~0	~0	0.34
$\tilde{v}_{cd}^{vsr}$	~0	~0	~0	~0	0.25
$\tilde{i}_{fd}^{vsr}$	~0	~0	~0	~0	1.59
$\tilde{i}_{fq}^{vsr}$	~0	~0	~0	~0	0.41
$\tilde{v}_{oq}^{vsr,c}$	~0	1.01	~0	~0	~0
$\tilde{v}_{dc}^{vsr}$	~0	~0	~0	~0	7.74
$\tilde{v}_{dc}^{vsr,c}$	~0	~0	~0	~0	0.44

### Participation Factor of Dominant Modes

Participation of different state variables in the dominant modes of the VSC-WMG state-space model under the nominal condition is presented in Table 6-3.  $SCR^{mg} = 1.6$  is selected at which the system exhibits unstable dynamics as already shown in

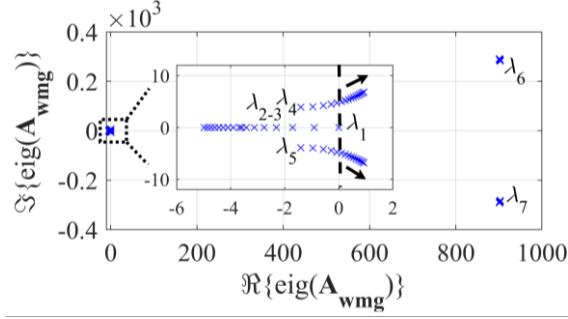


Figure 6.13: Spectrum of the dominant eigenvalues of VSC-WMG when  $m_{1-2}$  vary between 0–1.5 times the nominal values at the nominal power,  $SCR^{mg} = 1.6$ , and the impedance ratio equal to 9.

Figure 6.10. According to Table 6-3,  $\lambda_1$  is associated with the VSI<sub>1</sub> angle perturbations and  $\lambda_2$  is merely influenced by the PLL compensator of the VSR. Further,  $\lambda_3$  and  $\lambda_{4-5}$  are mainly influenced by VSI<sub>2</sub> angle perturbations (hence related to the active power droop control gains) and slightly by the AVC submodules of VSI<sub>1-2</sub>.

According to Table 6-3,  $\lambda_{6-7}$  are mainly influenced by the dc-side voltage of the VSR and to a lesser extent associated with  $\tilde{v}_{od}^{vsr}$ . This means that the interaction dynamics between the VOC of the VSR and the ac microgrid impedance can induce unstable modes under very weak conditions.

### **Sensitivity Analysis of Control Parameters**

Sensitivity analysis of the VSC-WMG system is conducted in this part to find the effect of changing control gains on the system stability under the same condition as the PFs are obtained. As depicted in Figure 6.13, the dominant unstable modes related to  $\lambda_{4-5}$  are shifted to the stable region by taking very small values of static droop gains  $m_{1-2}$ . However,  $\lambda_{6-7}$  remain in the unstable region which agrees with the results presented in Table 6-3. Moreover, as depicted in Figure 6.14, the dominant unstable modes are barely affected by the variations in the droop gains  $n_{1-2}$ .

Figure 6.15 shows the relocation of the dominant eigenvalues as a function of changes in the AVC gains  $\{K_{pv1-2}, K_{iv1-2}\}$  at  $SCR^{mg} = 1.6$ . As shown, the dominant eigenvalues are constantly in RHP as the compensator gains increase from 0.1–1.6 times the nominal values.

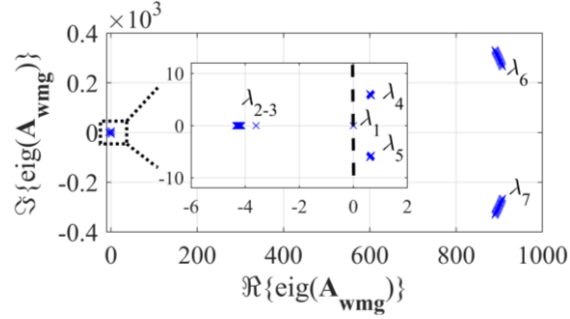


Figure 6.14: Spectrum of the dominant eigenvalues of VSC-WMG when  $n_{1-2}$  vary 0–1.5 times the nominal values at the nominal power,  $SCR^{mg} = 1.6$ , and the impedance ratio equal to 9.

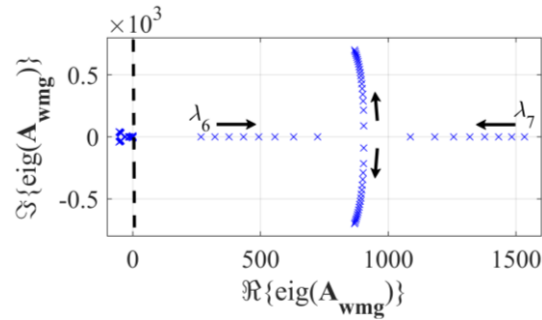


Figure 6.15: Spectrum of the dominant eigenvalues of VSC-WMG when  $(K_{pv1}^{vsi}, K_{iv1}^{vsi})$  and  $(K_{pv2}^{vsi}, K_{iv2}^{vsi})$  vary between 0.1–1.6 times the nominal values at the nominal power,  $SCR^{mg} = 1.6$ , and the impedance ratio equal to 9.

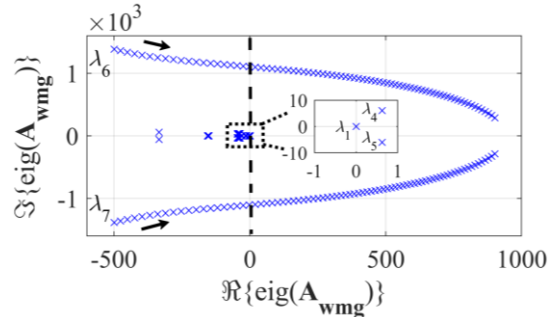


Figure 6.16: Spectrum of the dominant eigenvalues of VSC-WMG when  $(K_{pdc}^{vsr}, K_{idc}^{vsr})$  vary between 0.6–1 times of the nominal values at the nominal power,  $SCR^{mg} = 1.6$ , and the impedance ratio equal to 9.

As shown in Figure 6.16, the gains of the DVC compensator  $\{K_{pdc}^{vsr}, K_{idc}^{vsr}\}$  in the VOC of the VSR are changed to investigate its effect on the stability of VSC-VWG under the very weak condition at  $SCR^{mg} = 1.6$  where  $\lambda_{6-7}$  induce unstable modes. As shown,

$\lambda_{6-7}$  migrate towards the imaginary axis in the LHP and eventually enter the RHP where the BW of the DVC is less than half of the BW of the original system with the parameters given in Table 6-1 (not highlighted in Figure 6.16). However, as shown in the zoomed window in Figure 6.16,  $\lambda_{4-5}$  tend to stay on the RHP while the DVC gains increases from 0.6–1 times the nominal values.

## 6.7. Active Compensation of PL-WMG System

The dynamic study of PL-WMG in Section 6.6.1 reveals that the system stability is affected by a pair of complex unstable modes for a wide range of  $SCR^{mg}$  values at the nominal power. According to Table 6-2, the unstable modes are primarily affected by the active power droop control of VSI<sub>1-2</sub> and secondarily by the reactive power droop gains. Further, the instability can be mitigated only by compromising the VSIs droop dynamics which is not desired nor frequently permitted. Therefore, the following modifications of the droop control is proposed accordingly to mitigate the instability issue in the PL-WMG system.

$$\omega_{vsi} = \omega_{nl} - mP_{vsi} - m_d \frac{dP_{vsi}}{dt} \quad (6-24)$$

$$v_{od}^{vsi,ref} = v_{nl} - nQ_{vsi} - n_d \frac{dQ_{vsi}}{dt} \quad (6-25)$$

where  $m_d$  and  $n_d$  are the dynamic droop gains, as opposed to the static droop gains  $m$  and  $n$ . As can be understood from the dynamic droop expression in (6-24) and (6-25), these modifications are effective during the transients and have no influence on the steady-state performance of the system.

### 6.7.1. Compensation Design

The state-space model of the compensated PL-WMG system is obtained similar to the uncompensated version of PL-WMG in (6-18) where the expressions for the droop control in (5-15) and (5-16) are replaced by (6-24) and (6-25). For simplicity, the following ratio is kept between the control gains of VSI<sub>1</sub> and VSI<sub>2</sub> throughout the compensator design procedure:  $m_{d2} = 1.5m_{d1}$  and  $n_{d2} = 1.5n_{d1}$ . Then, the design of the dynamic droop gains under the nominal condition with the parameters given in Table 6-1 based on the state-space method as follows.

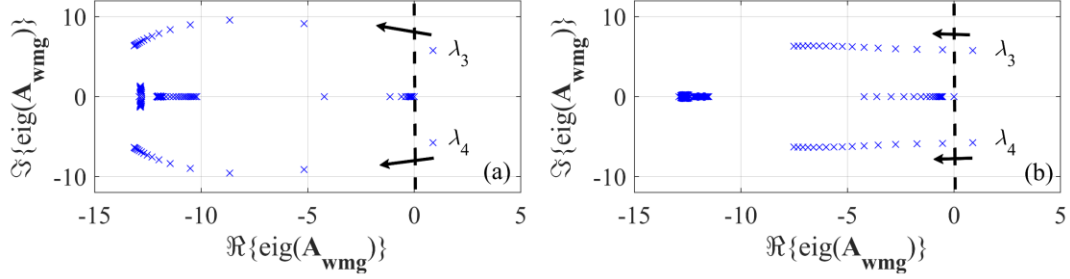


Figure 6.17: Spectrums of the dominant eigenvalues of compensated PL-WMG system at the nominal power,  $SCR^{mg} = 1.6$ , and impedance ratio equal to 9. (a)  $m_{d1}$  changes between  $0-15 \times 10^{-7}$  and  $n_{d1} = 0$ . (b)  $n_{d1}$  changes from  $0-15 \times 10^{-6}$  and  $m_{d1} = 0$ .

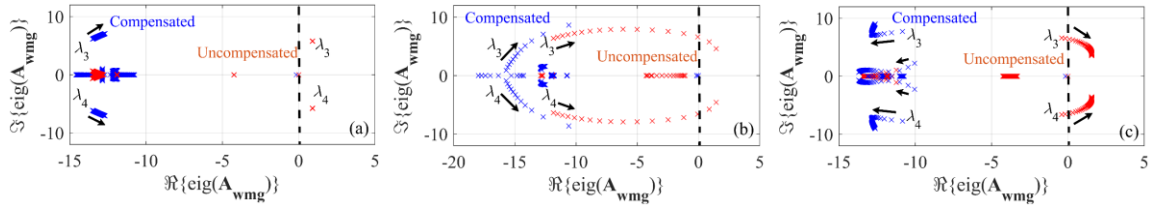


Figure 6.18: Spectrums of the dominant eigenvalues of uncompensated PL-WMG system (in red) versus compensated PL-WMG system assuming  $m_{d1} = 8 \times 10^{-7}$  and  $n_{d1} = 0 \times 10^{-7}$  (in blue) subjected to variations of (a)  $P_{pl}$  between 0.42 to 1 pu at  $SCR^{mg} = 1.6$  and impedance ratio equal to 9, (b) impedance ratio between 0.2 to 19 at the nominal loading power and  $SCR^{mg} = 1.6$ , (c)  $SCR^{mg}$  value between 1.13–10 at the nominal loading power and impedance ratio equal to 9.

The movement of  $\lambda_{3-4}$  is shown in Figure 6.17(a) subjected to an increase in  $m_{d1}$  from 0 to  $15 \times 10^{-7}$  while  $n_{d1}$  is kept at zero. The flipped situation is shown in Figure 6.17(b) where  $n_{d1}$  changes from 0 to  $15 \times 10^{-7}$  and  $m_{d1}$  is kept at zero. Comparing Figure 6.17(a) with Figure 6.17(b) shows that changing  $m_{d1}$  results in more damping in the eigenvalue spectrum of the compensated system than changing  $n_{d1}$ . This confirms the results in Table 6-2 about the states that have significant influence the dominant modes related to  $\lambda_{3-4}$ . Further investigation that is not reflected in Figure 6.17(a)–Figure 6.17(b) reveals that maximum damping is obtained at  $m_{d1} = 8 \times 10^{-7}$  and  $n_{d1} = 0$ .

### Analysis of Active Compensation

The traces of dominant eigenvalues of the PL-WMG system with and without active compensation under different conditions are compared in Figure 6.18(a)–Figure 6.18(c) in red and blue, respectively. According to Figure 6.18(a),  $\lambda_{3-4}$  related to the compensated system are constantly in the LHP and the system is well-damped as the

$P_{ld}$  varies from 0.42 to 1 pu. Meanwhile, the uncompensated system is unstable as the dominant eigenvalues are in RHP. Figure 6.18(b) shows that  $\lambda_{3-4}$  of the compensated system are in the LHP and the system stability is preserved under wide variations of the impedance ratio. However, according to the same figure, while the eigenvalues of the uncompensated system are initially in the LHP, they eventually enter the RHP and the system stability is violated under the nominal condition.

As shown in Figure 6.18(c), the compensated system is stable and well-damped under a wide range of changes in  $SCR^{mg}$  between 1.13–10 while the stability of the uncompensated system is preserved only for a small portion of the same range, the uncompensated system becomes unstable for the rest of the range as  $SCR^{mg}$  increases (see Figure 6.4–Figure 6.6 for further details about the uncompensated version).

## 6.8. Active Compensation of VSC-WMG System

The dynamic study of VSC-WMG in Section 6.6.2 reveals that the system stability issue occurs under the nominal condition. In particular, according to Table 6-3, there are low-frequency unstable modes that are primarily influenced by the active power droop control of VSI<sub>1-2</sub> similar to the case of PL-WMG while there are mid-frequency unstable modes that are due to the dynamic interaction between the VOC of VSR the equivalent impedance of the ac microgrid. Further investigation shows that the instability cannot be avoided even with wide range of changes in the primary control designs of VSIs and VSR. Therefore, in addition to the low-frequency compensation in (6-24) and (6-25), that are concerned with affecting the low-frequency unstable modes, the DVC dynamics in (5-39) is modified into the following expression to affect the mid-frequency unstable modes:

$$i_{fd}^{vsr,ref} = -(K_{pdc}^{vsr} + K_{idc}^{vsr} s^{-1})(v_{dc}^{vsr,ref} - v_{dc}^{vsr}) - K_{cpd} \frac{2\zeta\omega_{cpd}s}{s^2 + 2\zeta\omega_{cpd}s + \omega_{cpd}^2} v_{od} \quad (6-26)$$

where  $K_{cpd}$ ,  $\zeta$ , and  $\omega_{cpd}$  are the gain, damping ratio, and center frequency of the BPF expression.

### 6.8.1. Compensation Design

The state-space model of the compensated VSC-WMG system is obtained similar to the compensated PL-WMG counterpart in which the expressions for the droop control in

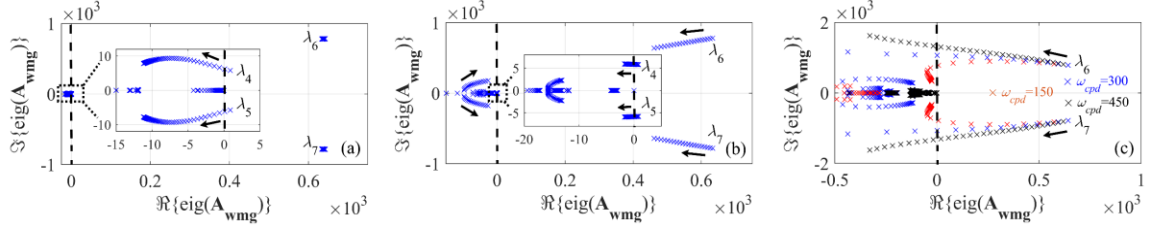


Figure 6.19: Spectrums of the dominant eigenvalues of compensated VSC-WMG system at the nominal power,  $SCR^{mg} = 1.6$ , and impedance ratio equal to 9. (a)  $0 \leq m_{d1} \leq 5 \times 10^{-7}$ ,  $n_{d1} = 0$ , and  $K_{cpd} = 0$ . (b)  $m_{d1} = 0$ ,  $0 \leq n_{d1} \leq 2 \times 10^{-6}$  and  $K_{cpd} = 0$ . (c)  $m_{d1} = 5 \times 10^{-7}$ ,  $n_{d1} = 0$ ,  $0 \leq K_{cpd} \leq 15$ ,  $\omega_{cpd} = \{150, 300, 450\}$  rad/s, and  $\zeta = 0.9$ .

(5-15) and (5-16) are replaced by (6-24) and (6-25) and the DVC dynamics is replaced by (6-26). Further details are provided in Section 4.5.1 in which an active compensation based on LPF is integrated into the system state-space model. Assuming  $m_{d2} = 1.5m_{d1}$  and  $n_{d2} = 1.5n_{d1}$ , the compensation design of VSC-WMG system is conducted under the nominal condition with the parameters given in Table 6-1 using the root-locus method as follows.

The migration of dominant eigenvalues of the VSC-WMG system with active compensation under the nominal load condition is shown in Figure 6.19(a)–Figure 6.19(c). According to Figure 6.19(a)–Figure 6.19(b), increasing either of the dynamic droop gains while the mid-frequency compensator is disabled, i.e.,  $K_{cpd} = 0$ , results in the relocation of low-frequency eigenvalues  $\lambda_{4-5}$  into the LHP while these compensatory augmentations are ineffective in shifting high-frequency eigenvalues  $\lambda_{6-7}$ . The optimal setting where the eigenvalue spectrum demonstrate maximum damping is found to be at  $m_{d1} = 5 \times 10^{-7}$  and  $n_{d1} = 0$ .

Next, keeping the dynamic droop gains at the optimal values,  $K_{cpd}$  is increased from 0 to 15 at different values of  $\omega_{cpd}$  to shift  $\lambda_{6-7}$ . According to Figure 6.19(c), the mid-frequency compensator manages to relocate  $\lambda_{6-7}$  to the LHP while the low-frequency compensation is not disrupted. Further, the maximum damping is found to be at  $K_{cpd} = 15$ ,  $\omega_{cpd} = 300$  rad/s and  $\zeta = 0.9$ . Therefore, the combination of low-frequency and mid-frequency compensations successfully resolves the instability problem of VSC-WMG at the nominal power.

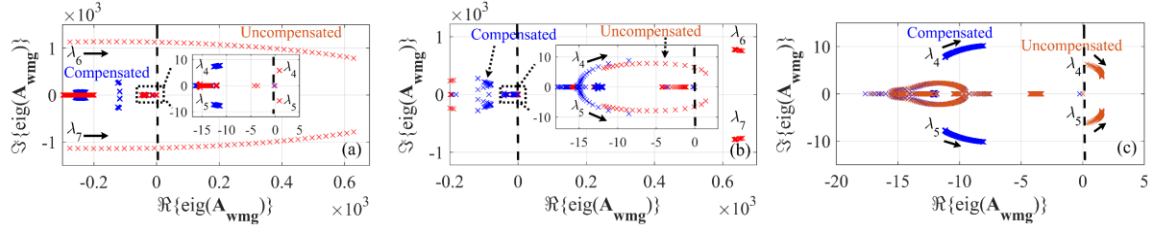


Figure 6.20: Spectrums of the dominant eigenvalues of uncompensated VSC-WMG system (in red) versus compensated VSC-WMG system assuming  $m_{d1} = 5 \times 10^{-7}$  and  $n_{d1} = 0 \times 10^{-7}$  (in blue) subjected to variations of (a)  $P_{vsr}$  between 0.42 to 1 pu at  $SCR^{mg} = 1.6$  and impedance ratio equal to 9, (b) impedance ratio between 0.2 to 19 at the nominal loading power and  $SCR^{mg} = 1.6$ , (c)  $SCR^{mg}$  between 1.42–10 at the nominal loading power and impedance ratio equal to 9.

### 6.8.2. Analysis of Active Compensation

The traces of dominant eigenvalues of the PL-WMG system with and without active compensation under different conditions are compared in Figure 6.20(a)–Figure 6.20(c) in red and blue, respectively. According to Figure 6.20(a),  $\lambda_{3-4}$  related to the compensated system are constantly in the LHP and the system is well-damped as the  $P_{vsr}$  varies from 0.42 to 1 pu. Meanwhile, the uncompensated system is unstable as corresponding  $\lambda_{3-4}$  are in the RHP. As shown in Figure 6.20(b),  $\lambda_{3-4}$  related to the compensated system are progressing towards the imaginary axis while constantly in the LHP. Therefore, the system stability is preserved under wide variations of the impedance ratio using the active compensation. However, according to the same figure,  $\lambda_{6-7}$  related to the uncompensated system are constantly in the RHP and  $\lambda_{3-4}$  of the same system, while initially in the LHP, eventually enter the RHP. Therefore, the uncompensated system is unstable for the same range of changes in the impedance ratio.

Figure 6.20(c) demonstrates the trace of low-frequency eigenvalues of the uncompensated and compensated systems subsequent to changes in the value of  $SCR^{mg}$ . As shown, the compensated system is stable and well-damped under a wide range of changes in  $SCR^{mg}$  between 1.42–10 while the stability of the uncompensated system is violated for the same range of changes (see Figure 6.10 and Figure 6.11 for further details about the uncompensated version).

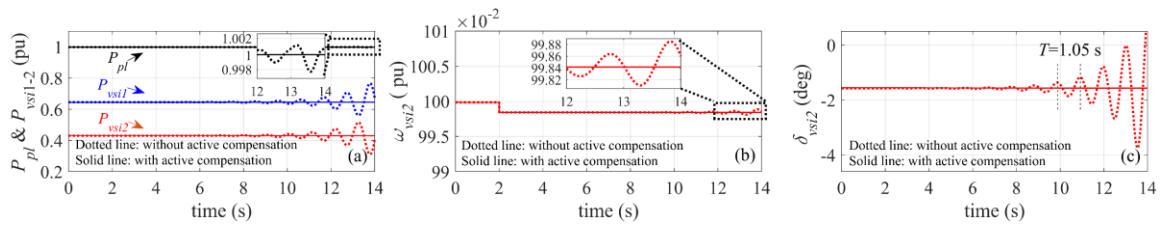


Figure 6.21: Responses of PL-WMG system with and without active compensation with  $m_{1-2}$  initially set at one-tenth of the original values and stepped to the designated values at  $t = 2$  s under the nominal loading power condition at  $SCR^{mg} = 1.6$  and impedance ratio equal to 9. (a) active power of VSI<sub>1-2</sub> and PL (in blue, red, and black respectively). (b) VSI<sub>2</sub> frequency. (c) VSI<sub>2</sub> voltage angle.

## 6.9. Time-Domain Simulation Results

To validate the small-signal analysis, large-signal simulations of the microgrid are conducted in MATLAB/Simulink using the system parameters presented in Table 6-1. A series of simulations are conducted to compare the responses of the weak ac microgrid in Cases I and II with and without active compensation. In the first part of the simulations, the responses of the systems are found subjected step disturbance in the frequency droop gains and the microgrid loading (in the case of the VSC-WMG system). In the second part, the responses of the system are found as continuous functions of stairstep increases in the microgrid loading to find the feasibility of the active compensations during all loading levels including start-up transients. The results are discussed in the following.

### 6.9.1. PL-WMG System Responses

Figure 6.21 shows the step responses of the PL-WMG system under the nominal loading power. According to the Figure 6.21(a), initially, when the frequency droop gains are one-tenth of the original values, the nominal loading power (1 pu) is shared by VSI<sub>1-2</sub>, proportionally according to the frequency droop gains (1.5), and the responses are stable and similar in both uncompensated and compensated cases. Then, at  $t = 2$  s, the responses of the uncompensated system (identified by dashed lines) slowly exhibit increasing oscillations in their amplitudes since the droop gains return to the original values. However, the responses of the compensated system (identified by solid lines) remain stable and unchanged over the entire operating range of the system in spite of the introduction of the step change in the droop gains.

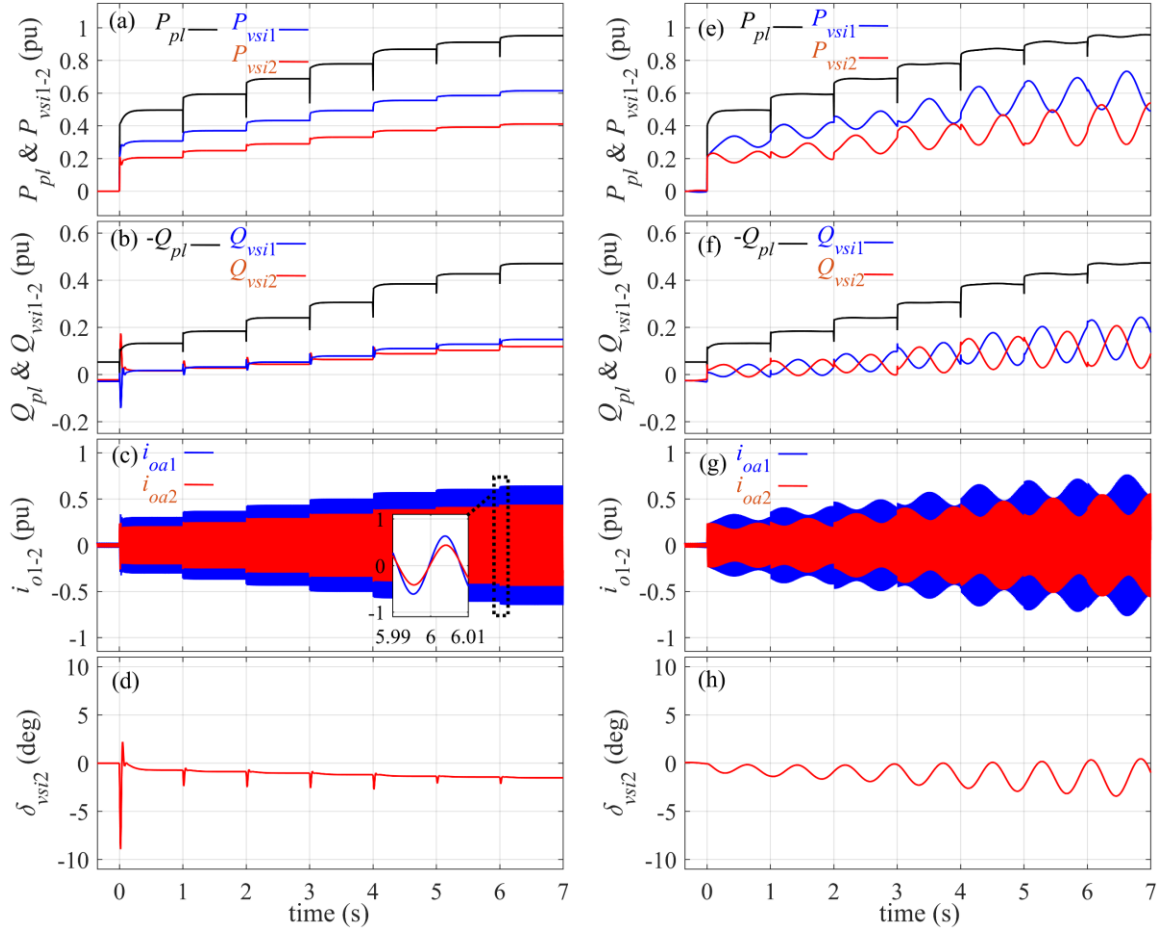


Figure 6.22: Responses of PL-WMG system during start-up transient and staircase changes in  $P_{pl}$ . (a)–(d) with active compensation. (e)–(h) without active compensation.

The angle and frequency responses of VSI<sub>2</sub> follow the same pattern as the power responses according to Figure 6.21(b)–Figure 6.21(c). As shown, the active compensation does not change the steady-state value of the frequency. Moreover, the period of oscillations in Figure 6.21(c) is equal to 1.05 s which closely matches the frequency of  $\lambda_{3-4}$  in Table 6-2. This confirms the small-signal development of PL-WMG system in Section 6.6.1.

Figure 6.22(a)–Figure 6.22(d) represents the responses of the compensated PL-WMG system for the time span of  $t = [0-7]$  s subject to changes in the PL power from the no-load condition to full-load condition. The load active power is changed by changing  $r_{pl}$ . As shown, the stability of the compensated system is maintained during the transients and the responses, namely the VSI<sub>1-2</sub> output currents, are well-damped. According to Figure 6.22(a), during each step, load active power  $P_{pl}$  is picked by VSI<sub>1-2</sub>

output powers  $P_{vsi1}$  and  $P_{vsi2}$  according to the frequency droop gain relation  $m_2/m_1$  which is equal to 1.5. As Figure 6.22(b) shows, parallel to the increases in the PL active power, the reactive power that is injected from the load-side is increased in the magnitude to maintain the output voltage  $v_o^{pl}$  at 1 pu. This is done by adjusting the value of  $c_{pl}$  accordingly.

Figure 6.22(b) demonstrates the reactive power responses of the VSCs. As shown, the reactive power sharing between VSI<sub>1-2</sub> at lower levels of power is poor which is a typical drawback of the droop control method [92]. The reactive power sharing between VSI<sub>1-2</sub> can be improved by taking higher values of voltage droop gains at the expense of poor voltage quality [92]. However, as discussed in Section 6.6.1, the system stability is not significantly affected by the voltage droop gains. Therefore, no effort is done to fix this issue of droop control. Moreover, as shown, the PL reactive power has a negative value which shows the PL is participating in the voltage regulation of the connecting ac bus (PCC<sub>ld</sub> in Figure 6.1).

According to Figure 6.22(e), there are relatively high overshoots in the angle response of VSI<sub>2</sub> at  $t = 0$  s due to the system start-up from 0 pu to 0.5 pu of PL power which is a large transient. Yet, the responses are dynamically damped and stable following steps in the PL power. On the other hand, Figure 6.22(e)–Figure 6.22(h) represents the responses of the uncompensated system for the time span of  $t = [0-7]$  s. As shown, the uncompensated system is not stable, and oscillations are visible in the system responses which shows the presence of the low-frequency unstable modes that are discussed in Section 6.6.1.

### 6.9.2. VSC-WMG System Responses

The step responses of the VSC-WMG system are found in this subsection at  $P_{ac} = 0.5$  pu subject to step changes in  $m_{1-2}$ . At this loading level, the mid-frequency eigenvalues  $\lambda_{6-7}$  are in the LHP. Thus, they do not impose any instability issue on the dynamic performance of the system. Figure 6.23 shows the responses with and without low-frequency active compensation. As shown, initially, when the frequency droop gains are one-tenth of the original values, the system is stable, and the responses are similar in both uncompensated and compensated cases. Later, at  $t = 2$  s, when the values of the

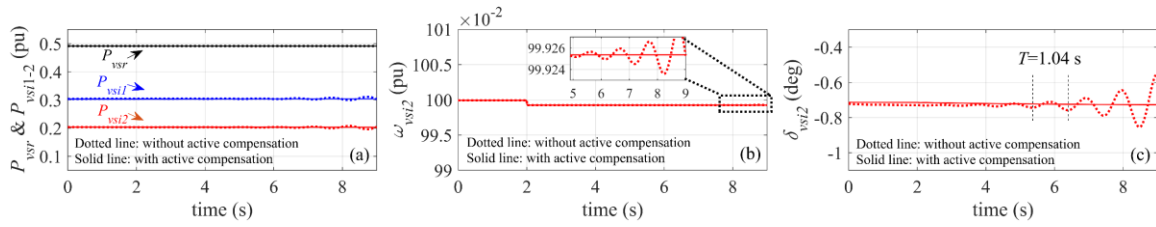


Figure 6.23: Responses of VSC-WMG system with and without active compensation with  $m_{1-2}$  initially set at one-tenth of the original values and stepped to the designated values at  $t = 2$  s under 0.5 pu loading power condition at  $SCR^{mg} = 1.6$  and impedance ratio equal to 9. (a) active power of VSI<sub>1-2</sub> and AEL (in blue, red, and black respectively). (b) VSI<sub>2</sub> frequency. (c) VSI<sub>2</sub> voltage angle.

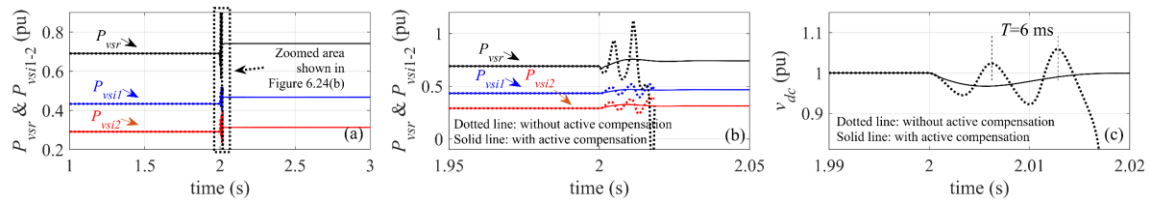


Figure 6.24: Responses of VSC-WMG system with and without mid-frequency active compensation while low-frequency compensation is enabled subject to step change of 0.69–0.74 times pu power in  $P_{vsr}$  at  $t = 2$  s,  $SCR^{mg} = 1.6$ , and impedance ratio equal to 9. (a) active power of VSI<sub>1-2</sub> and AEL. (b) zoomed view of active power responses. (c) VSR dc-link voltage.

gains are stepped back to the original values, the responses of the uncompensated system (identified by dashed lines) slowly exhibit unstable variations while the responses of the compensated system remain unchanged (identified by solid lines in Figure 6.23). Moreover, the period of oscillations in Figure 6.23(c) closely matches with the frequency of  $\lambda_{4-5}$  in Table 6-2. This confirms the small-signal development of VSC-WMG system in Section 6.6.2.

The step responses of the VSC-WMG system are found in this part subject to a step change in the VSR active power. To find the exclusive influence of the mid-frequency active compensation on the system stability, the low-frequency compensation is enabled, and hence,  $m_{1-2}$  take their designated values from the beginning. Figure 6.24 shows the responses of VSC-WG with and without mid-frequency active compensation where,  $P_{vsr}$  value steps from 0.69 pu to 0.74 pu at  $t = 2$  s. As shown in Figure 6.24(a), the power responses of the compensated system (identified by solid lines) reach the new stable steady-state values while the dc-link voltage response is

regulated at the nominal value according to Figure 6.24(c). Therefore, the VSC-WMG system is stable at the 0.74 pu level of AEL power.

As illustrated in Figure 6.24, the responses of the uncompensated system (identified by dashed lines), completely overlap with the compensated system responses before  $t = 2$  s. However, after the introduction of the disturbance at  $t = 2$  s, the uncompensated responses exhibit unstable behavior. A closer look at the power responses in the vicinity of the disturbance moment is shown in Figure 6.24(b). As illustrated, while the responses of the compensated system begin to reach the new stable values, those of the uncompensated system oscillate increasingly. The unstable dynamics are also reflected in the dc-link voltage response of the VSR according to Figure 6.24(c). Further, as annotated on the same figure, the period of the oscillation is 6 ms which matches the frequency of  $\lambda_{6-7}$  at 0.74 pu power level in Figure 6.10. This confirms the small-signal development of the VSC-WMG in Section 6.6.2.

Figure 6.25(a)–Figure 6.25(e) represents the responses of the compensated VSC-WMG system for the time span of  $t = [0-4.5]$  s subject to changes in the AEL power from no-load condition to full-load condition. The change of power is done by changing the VSR dc-side current source value (see Figure 2.1(a)). As shown, the compensated system is stable for different levels of power including the nominal load power and the system responses are well-damped during transients while converging to their corresponding reference values. According to Figure 6.25(a), during each step, load active power  $P_{vsr}$  is picked by VSI<sub>1-2</sub> output powers  $P_{vsi1}$  and  $P_{vsi2}$  according to the frequency droop gain relation  $m_2/m_1$  (that is equal to 1.5). Figure 6.25(b) shows that parallel to the step increases in the AEL active power, the reactive power that the VSR injects into the WMG increases to regulate the output voltage  $v_o^{vsr}$  at 1 pu. According to Figure 6.25(e), the maximum overshoots on  $v_{dc}$  is around 10% of the nominal value (1900 V), yet it is damped quickly. Moreover, as compared to the response of the uncompensated counterpart in Figure 6.25(j), the active compensation does not deteriorate the  $v_{dc}$  transients.

Figure 6.25(f)–Figure 6.25(j) represents the responses of the uncompensated VSC-WMG system under the same condition as the compensated system. According to Figure 6.25(f)–Figure 6.25(g),  $P_{vsi,1-2}$  and  $Q_{vsi,1-2}$  responses exhibit relatively slow oscillations at lower levels of power (before  $t = 2.5$  s) while the VSR responses, namely

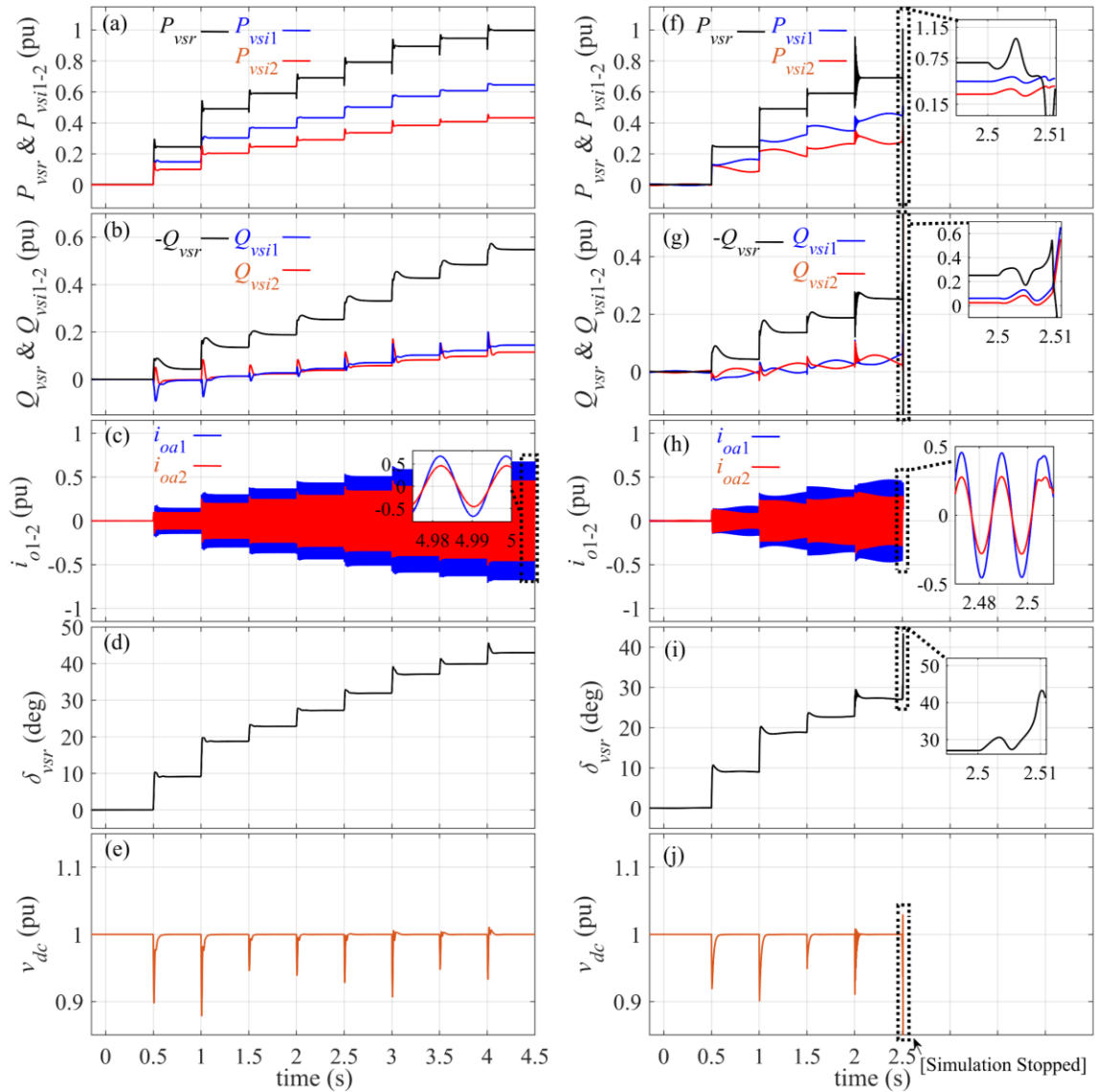


Figure 6.25: Responses of VSC-WMG system during start-up transient and staircase changes in  $P_{dc}$ . (a)–(e) with active compensation. (f)–(j) without active compensation.

$\delta_{vsr}$  and  $v_{dc}$ , seem to be free of this type of distortion. However, at  $t = 2.5$  s, where  $P_{vsr}$  steps to 0.74 pu, the VSR responses exhibit unstable oscillations which are relatively

faster than those of the VSI<sub>1-2</sub> responses. Overall, the uncompensated system is unstable due to low-frequency and mid-frequency responses, particularly at the nominal load power.

It should be noted that the low-frequency oscillations in the VSI<sub>1-2</sub> (instantaneous) power responses are damped by the LPFs, which are introduced in (5-18) and (5-19). Therefore, the states of the real and reactive power do not show any

considerable participation in the dominant low-frequency modes according to the corresponding participation table.

## 6.10. Conclusion

In this chapter, the concept of WMG is introduced. To measure the strength of WMGs in islanded mode,  $SCR^{mg}$  is defined which is a generalization of the measure of the traditional ac grids' strength to WMG applications. A WMG with two VSIs and a VSR that integrate two DG sources and dc load/microgrid into WMG, respectively, is assumed. A network of long  $RL$ -type lines that have high-impedance characteristics interconnects the sources and loads inside the WMG. A parallel  $RC$  circuit and a VSR that interfaces a dc current represent the PL and AEL within the WMG respectively. Complementary switches are considered that connect the PL or AEL one at a time to the WMG ac bus. Therefore, the study of the WMG is boiled down to investigate two possible configurations: the PL-WMG system and the VSC-WMG system.

Using the average model of the VSC; and considering the detailed VOC system of the VSCs and  $RL$  line dynamics, the dynamic model of WMG for each of the aforementioned configurations is derived. Then, the static power transfer capability of the WMG systems is studied to find the minimum  $SCR^{mg}$  of each system at which, the system operates stably. Next, the complete state-space model of WMG is derived by linearizing the dynamic models of PL-WMG and VSC-WMG systems. Then, the small-signal analyses show that there are two complex low-frequency unstable modes associated with the droop control of VSIs in PL-WMG and VSC-WMG systems under the nominal load power condition. Moreover, there are mid-frequency complex unstable modes that are the result of the dynamic interaction between the DVC module of the VSR and the WMG impedance in the case of the VSC-WMG system.

The sensitivity analyses show that the small-signal stability of both systems under nominal conditions is not within reach or, if possible, at the expense of having systems with extremely poor dynamics. Therefore, low-frequency and mid-frequency active compensations are employed to improve the stability of the systems. Since the introduced compensators are linear, the widely accepted linear control tools can be used to design the parameters.

The design of active compensation parameters is done using the state-space method to ensure the system stability at different loading conditions and a wide range of  $SCR^{mg}$  variations and also to maximize the system damping. Large-signal time-domain simulations of PL-WMG and VSC-WMG systems are carried out to verify the small-signal developments. The results show that the compensated versions of the mentioned systems are stable under a wide range of load changes without changing the steady-state values and compromising the operation of the VSCs' primary control systems while the uncompensated versions fail to reach the same stable operating conditions.

## Chapter 7.

# Summary, Conclusions, and Suggestions for Future Work

### 7.1. Summary and Conclusion

In this thesis, the dynamics and instability of WGs and WMGs are studied. Using eigenvalue analysis, the sources of instabilities and parameters that mainly influence them are found. These findings provide insight into potential linear methods to confront the destabilizing effects without compromising the primary designs of these dynamical systems. The key contributions of the present dissertation may be summarized as:

1. Stability analysis and assessment of the operation of the VSCs in the inversion and rectification modes under the VWG condition.
2. Development of an actively compensated VSC-WG system in the inversion mode to achieve stable performance at  $SCR = 1$ , i.e., worst-case scenario.
3. Development of an actively compensated VSC-WG system in the rectification mode to achieve stable performance under the VWG conditions, i.e.,  $SCR = 1.16$ .
4. Derivation of a small-signal state-space full-order model of the VOC-based VSC-WG system augmented by the compensation methods where the influence of the AVC, the PLL, the CC, and the DVC is considered.
5. Development of an actively compensated PL-WMG and VSC-WMG systems to achieve stable performances under the VWG conditions, i.e.,  $SCR = 1.13$  and  $SCR = 1.42$ , respectively.
6. Stability analysis and assessment of weak ac microgrids with integration of PLs and AELs.
7. Derivation of a detailed analytical transfer function of the PCC dynamics, which can be used for designing the PCC control system using SISO control tools.

In summary, considering the major contributions of this research, the integration of three-phase VSC into the very weak ac grids and microgrids is effectively realized.

## **7.2. Suggestions for Future Research**

Based on the experience gained throughout this research, the following research directions can be followed extensions out of this thesis.

### **7.2.1. Other Load Configurations**

Other types of dynamic loads and the stability challenges they impose on the WG and WMGs under very weak conditions need separate attention. As an example, induction motors incorporate a load share of 60% and 80% in residential and industrial sectors, respectively [48]. Among this share, online motors are of interest because they introduce low- to medium-frequency dominant modes to system stability [48], [96]. Therefore, their impact on the stability of WGs and WMG in Chapter 3–Chapter 6 shall be interesting. Moreover, in VSC-WG configuration, the PCC is not shared by any other types of loads. Hence, the VSC-WG systems in Chapter 3 and Chapter 4 can be augmented by a parallel large load of a different type, e.g., PL, whose connection or disconnection (as a large disturbance) can challenge the system stability. Therefore, this can complicate the design of the active compensation for the primary system under study.

### **7.2.2. Impedance-based modeling**

As the dimension of WMG grows, the mathematical states of the WMG dynamic model grow exponentially in number. Therefore, time-domain state-space approach which is a great method for well-defined systems may not be suitable in systems where loads play an important role in stability because the system model needs to be reformulated after each change in the loads or system structure [16], [97]. This makes the state-space approach inefficient for low- to medium- voltage complex power systems. Compared to state-space approaches, the frequency-domain impedance-based approach has the advantage of scalability. As such, adding or removing a source or a load, or changing the operation mode of a load only affects one impedance element in the system impedance network [16], [98]. Hence, another direction would be studying the dynamics and stability of the systems in this work through the impedance modeling point of view.

### **7.2.3. Robust Control Design**

Unpredicted connection and disconnection of loads, unscheduled line outage due to fault, and unmodelled load dynamics are among reasons that add some degree of uncertainty the stability problem in WGs and microgrids in general. To evaluate the performance of active compensation in presence of uncertainty in WG impedance, two series of slow and fast ramp-wise variations are introduced in the WG impedance of VSC-WG systems in Chapter 3 and Chapter 4. However, to officially treat this topic and ensure the system stability mathematically, Robust Control tools need to be used. Several works have suggested robust control strategies in grid-connected VSC and microgrid applications [71], [100]–[104]. Therefore, the other direction is to design active compensation methods that are robustly stable against the variations in WGs and WMG parameters (like impedance) within (a) certain range(s).

## References

- [1] K. R. Padiyar and A. M. Kulkarni, *Dynamics and Control of Electric Transmission and Microgrids*, Hoboken, NJ, USA: Wiley, 2019.
- [2] N. Hatziargyriou, *Microgrids: Architectures and Control*, Chichester, U.K.:Wiley, pp. 1–24, 2014.
- [3] D. Boroyevich, I. Cvetković, D. Dong, R. Burgos, F. Wang and F. Lee, “Future electronic power distribution systems a contemplative view,” 2010 12th International Conference on Optimization of Electrical and Electronic Equipment, Basov, 2010, pp. 1369–1380.
- [4] S. Chakraborty, B. Kramer, B. Kroposki, “A review of power electronics interfaces for distributed energy systems toward achieving low-cost modular design,” in *Renewable and Sustainable Energy Reviews* 13, 2009, pp. 2323–2335.
- [5] A. Yazdani, “Control of an islanded Distributed Energy Resource unit with load compensating feed-forward,” 2008 IEEE Power and Energy Society General Meeting - Conversion and Delivery of Electrical Energy in the 21st Century, Pittsburgh, PA, 2008, pp. 1–7.
- [6] F. Blaabjerg, R. Teodorescu, M. Liserre, and A. V. Timbus, “Overview of control and grid synchronization for distributed power generation systems,” *IEEE Trans. Ind. Electron.*, vol. 53, no. 5, pp. 1398–1409, Oct. 2006.
- [7] Y. Mohamed and E. El-Saadany, “Adaptive decentralized droop controller to preserve power sharing stability of paralleled inverters in distributed generation microgrids,” *IEEE Trans. Power Electron.*, vol. 23, no. 6, pp. 2806–2816, 2008.
- [8] A. Yazdani and R. Iravani, *Voltage-Sourced Converters in Power Systems: Modeling Control and Applications*, Wiley-IEEE press, 2010.
- [9] A. A. A. Radwan and Y. A. I. Mohamed, “Analysis and Active-Impedance-Based Stabilization of Voltage-Source-Rectifier Loads in Grid-Connected and Isolated Microgrid Applications,” *IEEE Trans. Sustain. Energy*, vol. 4, no. 3, pp. 563–576, July 2013.
- [10] A. A. A. Radwan and Y. A. I. Mohamed, “Modeling, Analysis, and Stabilization of Converter-Fed AC Microgrids With High Penetration of Converter-Interfaced Loads,” *IEEE Trans. Smart Grid*, vol. 3, no. 3, pp. 1213–1225, Sept. 2012.
- [11] R. H. Lasseter, “Microgrids,” in *Proc. Power Eng. Soc. Winter Meeting*, Jan. 2002, vol. 1, pp. 305–308.

- [12] S. Lu, Z. Xu, L. Xiao, W. Jiang and X. Bie, "Evaluation and Enhancement of Control Strategies for VSC Stations Under Weak Grid Strengths," *IEEE Trans. Power Syst.*, vol. 33, no. 2, pp. 1836–1847, March 2018.
- [13] M. Liserre, R. Teodorescu and F. Blaabjerg, "Stability of photovoltaic and wind turbine grid-connected inverters for a large set of grid impedance values," *IEEE Trans. Power Electron.*, vol. 21, no. 1, pp. 263–272, Jan. 2006.
- [14] Z. Xie et al., "Modeling and Control Parameters Design for Grid-Connected Inverter System Considering the Effect of PLL and Grid Impedance," *IEEE Access*, vol. 8, pp. 40474–40484, 2020.
- [15] W. Rui et al., "Line Inductance Stability Operation Domain Assessment for Weak Grids With Multiple Constant Power Loads," *IEEE Trans. Energy Convers.*, vol. 36, no. 2, pp. 1045-1055, June 2021.
- [16] J. Sun, "Small-Signal Methods for AC Distributed Power Systems—A Review," *IEEE Trans. Power Electron.*, vol. 24, no. 11, pp. 2545–2554, Nov. 2009.
- [17] B. Wu, M. Narimani, *High-Power Converters and AC Drives*, Wiley-IEEE IEEE Press, 2017.
- [18] M. Ashabani and Y. A. I. Mohamed, "Integrating VSCs to Weak Grids by Nonlinear Power Damping Controller With Self-Synchronization Capability," *IEEE Trans. Power Syst.*, vol. 29, no. 2, pp. 805–814, March 2014.
- [19] A. Egea-Alvarez, S. Fekriasl, F. Hassan and O. Gomis-Bellmunt, "Advanced Vector Control for Voltage Source Converters Connected to Weak Grids," *IEEE Trans. Power Syst.*, vol. 30, no. 6, pp. 3072–3081, Nov. 2015.
- [20] J. A. Suul, S. D'Arco, P. Rodríguez and M. Molinas, "Impedance-compensated grid synchronisation for extending the stability range of weak grids with voltage source converters", *IET Gener. Transm. Distrib.*, vol. 10, no. 6, pp. 1315-1326, Apr. 2016.
- [21] X. Zhang, D. Xia, Z. Fu, G. Wang, and D. Xu, "An improved feedforward control method considering PLL dynamics to improve weak grid stability of grid-connected inverters," *IEEE Trans. Ind. Appl.*, vol. 54, no. 5, pp. 5143–5151, Sep. 2018.
- [22] B. Wen, D. Boroyevich, R. Burgos, P. Mattavelli and Z. Shen, "Analysis of D-Q Small-Signal Impedance of Grid-Tied Inverters," *IEEE Trans. Power Electron.*, vol. 31, no. 1, pp. 675–687, Jan. 2016.
- [23] M. P. Kazmierkowski and L. Malesani, "Current control techniques for three-phase voltage source PWM converters: A survey", *IEEE Trans. Ind. Electron.*, vol. 45, no. 5, pp. 691–703, 1998.

- [24] V. Venkatasubramanian, H. Schattler and J. Zaborszky, "Fast timevarying phasor analysis in the balanced three-phase large electric power system", *IEEE Trans. Autom. Control*, vol. 40, no. 11, pp. 1975–1982, 1995.
- [25] R. Wang, Q. Sun, D. Ma, and Z. Liu, "The Small-Signal Stability Analysis of the Droop-Controlled Converter in Electromagnetic Timescale," *IEEE Trans. Sustain. Energy*, vol. 10, no. 3, pp. 1459–1469, July 2019.
- [26] P. Kundur, *Power System Stability and Control*. New York: McGrawHill, 1994.
- [27] E. A. A. Coelho, P. C. Cortizo and P. F. D. Garcia, "Small-signal stability for parallel-connected inverters in stand-alone AC supply systems," *IEEE Trans. Ind. Electron.*, vol. 38, no. 2, pp. 533-542, March–April 2002.
- [28] L. Harnefors, M. Bongiorno and S. Lundberg, "Input-Admittance Calculation and Shaping for Controlled Voltage-Source Converters," *IEEE Trans. Ind. Electron.*, vol. 54, no. 6, pp. 3323–3334, Dec. 2007.
- [29] J. Machowski, J. W. Bialek and J. R. Bumby, *Power System Dynamics*, Hoboken, NJ, USA: Wiley, 2008.
- [30] G. Wu et al., "Parameter Design Oriented Analysis of the Current Control Stability of the Weak-Grid-Tied VSC," *IEEE Trans. Power Del.*, vol. 36, no. 3, pp. 1458–1470, June 2021.
- [31] W. Rui, S. Qiuye, M. Dazhong and H. Xuguang, "Line Impedance Cooperative Stability Region Identification Method for Grid-Tied Inverters Under Weak Grids," *IEEE Trans. Smart Grid*, vol. 11, no. 4, pp. 2856–2866, July 2020.
- [32] X. Wang, F. Blaabjerg and W. Wu, "Modeling and Analysis of Harmonic Stability in an AC Power-Electronics-Based Power System," *IEEE Trans. Power Electron.*, vol. 29, no. 12, pp. 6421–6432, Dec. 2014.
- [33] X. Guo, Z. Lu, B. Wang, X. Sun, L. Wang and J. M. Guerrero, "Dynamic Phasors-Based Modeling and Stability Analysis of Droop-Controlled Inverters for Microgrid Applications," *IEEE Trans. Smart Grid*, vol. 5, no. 6, pp. 2980–2987, Nov. 2014.
- [34] S. V. Iyer, M. N. Belur, and M. C. Chandorkar, "A generalized computational method to determine stability of a multi-inverter microgrid," *IEEE Trans. Power Electron.*, vol. 25, no. 9, pp. 2420–2432, Sep. 2010.
- [35] X. Wang and F. Blaabjerg, "Harmonic Stability in Power Electronic-Based Power Systems: Concept, Modeling, and Analysis," *IEEE Trans. Smart Grid*, vol. 10, no. 3, pp. 2858–2870, May 2019.
- [36] A. Radwan, "Modeling, analysis and stabilization of converter-dominated power distribution grids," M.Sc. thesis, Dept. Electr. Comput. Eng., Univ. Alberta, Edmonton, AB, Canada, 2012.

- [37] V. Blasko and V. Kaura, "A novel control to actively damp resonance in input LC filter of a three-phase voltage source converter," *IEEE Trans. Ind. Appl.*, vol. 33, no. 2, pp. 542–550, Mar.-Apr. 1997.
- [38] J. Dannehl, C. Wessels and F. W. Fuchs, "Limitations of Voltage-Oriented PI Current Control of Grid-Connected PWM Rectifiers With LCL Filters," *IEEE Trans. Ind. Electron.*, vol. 56, no. 2, pp. 380–388, Feb. 2009.
- [39] M. Belkhat, "Stability criteria for AC power systems with regulated loads," PhD thesis, Purdue Univ., West Lafayette, IN, USA, 1997.
- [40] Y. Huang, X. Yuan, J. Hu and P. Zhou, "Modeling of VSC Connected to Weak Grid for Stability Analysis of DC-Link Voltage Control," *IEEE Trans. Emerg. Sel. Topics Power Electron.*, vol. 3, no. 4, pp. 1193–1204, Dec. 2015.
- [41] Y. Huang, X. Yuan, J. Hu, P. Zhou and D. Wang, "DC-Bus Voltage Control Stability Affected by AC-Bus Voltage Control in VSCs Connected to Weak AC Grids," *IEEE Trans. Emerg. Sel. Topics Power Electron.*, vol. 4, no. 2, pp. 445–458, June 2016.
- [42] "IEEE Guide for Planning DC Links Terminating at AC Locations Having Low Short-Circuit Capacities," in *IEEE Std 1204-1997*, vol., no., pp.1–216, 21 Jan. 1997.
- [43] L. Zhang, L. Harnefors, and H.-P. Nee, "Power-synchronization control of grid-connected voltage-source converters," *IEEE Trans. Power Syst.*, vol. 25, no. 2, pp. 809–820, May 2010.
- [44] J. Guo et al., "Wideband dq-Frame Impedance Modeling of Load-Side Virtual Synchronous Machine and Its Stability Analysis in Comparison With Conventional PWM Rectifier in Weak Grid," *IEEE Trans. Emerg. Sel. Topics Circuits Syst*, vol. 9, no. 2, pp. 2440–2451, April 2021.
- [45] J. Z. Zhou, et al., "Impact of Short-Circuit Ratio and Phase-Locked-Loop Parameters on the Small-Signal Behavior of a VSC-HVDC Converter," *IEEE Trans. Power Del.*, vol. 29, no. 5, pp. 2287–2296, Oct. 2014.
- [46] M. Cespedes, L. Xing and J. Sun, "Constant-Power Load System Stabilization by Passive Damping," *IEEE Trans. Power Electron.*, vol. 26, no. 7, pp. 1832–1836, July 2011.
- [47] D. Yang, X. Ruan, and H. Wu, "Impedance shaping of the grid-connected inverter with LCL filter to improve its adaptability to the weak grid condition," *IEEE Trans. Power Electron.*, vol. 29, no. 11, pp. 5795–5805, Nov. 2014.
- [48] A. A. A. Radwan and Y. A. I. Mohamed, "Stabilization of Medium-Frequency Modes in Isolated Microgrids Supplying Direct Online Induction Motor Loads," *IEEE Trans. Smart Grid*, vol. 5, no. 1, pp. 358–370, Jan. 2014.

- [49] A. A. A. Radwan Y. A. R. I. Mohamed E. F. El-Saadany "Assessment and performance evaluation of DC-side interactions of voltage-source inverters interfacing renewable energy systems" in *Sustainable Energy, Grids and Networks*, vol. 1 pp. 28–44 2015.
- [50] A. A. A. Radwan and Y. A. I. Mohamed, "Improved Vector Control Strategy for Current-Source Converters Connected to Very Weak Grids," *IEEE Trans. Power Syst.*, vol. 31, no. 4, pp. 3238–3248, July 2016.
- [51] S. Rezaee, A. Radwan, M. Moallem and J. Wang, "Voltage Source Converters Connected to Very Weak Grids: Accurate Dynamic Modeling, Small-Signal Analysis, and Stability Improvement," *IEEE Access*, vol. 8, pp. 201120–201133, 2020.
- [52] S. Rezaee, M. Moallem, J. Wang and A. A. A. Radwan, "Assessment of Dynamic Instabilities in Weak Grids with High Penetration of Power Electronic Loads," 2020 IEEE 8th International Conference on Smart Energy Grid Engineering (SEGE), 2020, pp. 13–17.
- [53] S. Rezaee, A. Radwan, M. Moallem and J. Wang, "Dual Active Compensation for Voltage Source Rectifiers Under Very Weak Grid Conditions," *IEEE Access*, vol. 9, pp. 160446–160460, 2021.
- [54] S. Rezaee, A. Radwan, M. Moallem and J. Wang, "Stability Analysis of a Remote DC Subgrid/Microgrid Connected to a Very Weak AC Grid," 2021 IEEE 9th International Conference on Smart Energy Grid Engineering (SEGE), 2021, pp. 1–6.
- [55] S. Rezaee, M. Moallem, J. Wang and A. A. A. Radwan, "Dynamic Modeling and Stability Analysis of Converter-based Three-phase AC Microgrids with Active Loads," 2019 IEEE 28th International Symposium on Industrial Electronics (ISIE), 2019, pp. 81–86.
- [56] P. P. Dash and M. Kazerani, "Dynamic Modeling and Performance Analysis of a Grid-Connected Current-Source Inverter-Based Photovoltaic System," *IEEE Trans. Sustain. Energy*, vol. 2, no. 4, pp. 443–450, Oct. 2011.
- [57] D. Wang, L. Liang, L. Shi, J. Hu and Y. Hou, "Analysis of Modal Resonance Between PLL and DC-Link Voltage Control in Weak-Grid Tied VSCs," *IEEE Trans. Power Syst.*, vol. 34, no. 2, pp. 1127–1138, March 2019.
- [58] Se-Kyo Chung, "A phase tracking system for three phase utility interface inverters," *IEEE Trans. Power Electron.*, vol. 15, no. 3, pp. 431–438, May 2000.
- [59] Q. Hu, L. Fu, F. Ma and F. Ji, "Large Signal Synchronizing Instability of PLL-Based VSC Connected to Weak AC Grid," *IEEE Trans. Power Syst.*, vol. 34, no. 4, pp. 3220–3229, July 2019.

- [60] (2018). Simulink Dynamic System Simulation Software Users Manual (MathWorks Inc.). [Online]. Available: <http://www.mathworks.com>.
- [61] S. Sang, N. Gao, X. Cai and R. Li, "A Novel Power-Voltage Control Strategy for the Grid-Tied Inverter to Raise the Rated Power Injection Level in a Weak Grid," *IEEE Trans. Emerg. Sel. Topics Power Electron.*, vol. 6, no. 1, pp. 219–232, March 2018.
- [62] M. Ashabani, Y. A. R. I. Mohamed, M. Mirsalim and M. Aghashabani, "Multivariable Droop Control of Synchronous Current Converters in Weak Grids/Microgrids With Decoupled dq-Axes Currents," *IEEE Trans. Smart Grid*, vol. 6, no. 4, pp. 1610–1620, July 2015.
- [63] H. Wu and X. Wang, "Design-Oriented Transient Stability Analysis of PLL-Synchronized Voltage-Source Converters," *IEEE Trans. Power Electron.*, vol. 35, no. 4, pp. 3573–3589, April 2020.
- [64] A. Adib, B. Mirafzal, X. Wang and F. Blaabjerg, "On Stability of Voltage Source Inverters in Weak Grids," *IEEE Access*, vol. 6, pp. 4427–4439, 2018.
- [65] L. Huang et al., "Grid-Synchronization Stability Analysis and Loop Shaping for PLL-Based Power Converters With Different Reactive Power Control," *IEEE Trans. Smart Grid*, vol. 11, no. 1, pp. 501–516, Jan. 2020.
- [66] J. Xu, S. Xie, and T. Tang, "Improved control strategy with grid-voltage feedforward for LCL-filter-based inverter connected to weak grid," *IET Power Electron.*, vol. 7, no. 10, pp. 2660–2671, 2014.
- [67] X. Chen, Y. Zhang, S. Wang, J. Chen, and C. Gong, "Impedance-phased dynamic control method for grid-connected inverters in a weak grid," *IEEE Trans. Power Electron.*, vol. 32, no. 1, pp. 274–283, Jan. 2017.
- [68] D. Zhu, et al., "Small-Signal Disturbance Compensation Control for LCL-Type Grid-Connected Converter in Weak Grid," *IEEE Trans. Ind Appl.*, vol. 56, no. 3, pp. 2852–2861, May–June 2020.
- [69] T. Midtsund, J. A. Suul and T. Undeland, "Evaluation of current controller performance and stability for voltage source converters connected to a weak grid," The 2nd International Symposium on Power Electronics for Distributed Generation Systems, Hefei, 2010, pp. 382–388.
- [70] X. Wang, J. Yao, J. Pei, P. Sun, H. Zhang and R. Liu, "Analysis and Damping Control of Small-Signal Oscillations for VSC Connected to Weak AC Grid During LVRT," *IEEE Trans. Energy Convers.*, vol. 34, no. 3, pp. 1667–1676, Sept. 2019.
- [71] M. Davari and Y. A. I. Mohamed, "Robust Vector Control of a Very Weak-Grid-Connected Voltage-Source Converter Considering the Phase-Locked Loop Dynamics," *IEEE Trans. Power Electron.*, vol. 32, no. 2, pp. 977–994, Feb. 2017.

- [72] M. Durrant, H. Werner and K. Abbott, "Model of a VSC HVDC terminal attached to a weak AC system," Proceedings of 2003 IEEE Conference on Control Applications, 2003. CCA 2003., Istanbul, Turkey, 2003, pp. 178–182, vol. 1.
- [73] D. Dong, B. Wen, D. Boroyevich, P. Mattavelli, and Y. Xue, "Analysis of phase-locked loop low-frequency stability in three-phase grid-connected power converters considering impedance interactions," *IEEE Trans. Ind. Electron.*, vol. 62, no. 1, pp. 310–321, Jan. 2015.
- [74] R. Luhtala, T. Roinila and T. Messo, "Implementation of Real-Time Impedance-Based Stability Assessment of Grid-Connected Systems Using MIMO-Identification Techniques," *IEEE Trans. Ind. Appl.*, vol. 54, no. 5, pp. 5054–5063, Sept.–Oct. 2018.
- [75] M. Berg, A. Aapro, R. Luhtala and T. Messo, "Small-Signal Analysis of Photovoltaic Inverter With Impedance-Compensated Phase-Locked Loop in Weak Grid," *IEEE Trans. Energy Convers.*, vol. 35, no. 1, pp. 347–355, March 2020.
- [76] R. Peña-Alzola, M. Liserre, F. Blaabjerg, R. Sebastián, J. Dannehl and F. W. Fuchs, "Analysis of the Passive Damping Losses in LCL-Filter-Based Grid Converters," *IEEE Trans. Power Electron.*, vol. 28, no. 6, pp. 2642–2646, June 2013.
- [77] IEEE Recommended Practice and Requirements for Harmonic Control in Electric Power Systems, in IEEE Std 519-2014 (Revision of IEEE Std 519-1992) , vol., no., pp. 1–29, 11 June 2014.
- [78] M. F. M. Arani and Y. A. I. Mohamed, "Analysis and Performance Enhancement of Vector-Controlled VSC in HVDC Links Connected to Very Weak Grids," *IEEE Trans. Power Syst.*, vol. 32, no. 1, pp. 684–693, Jan. 2017.
- [79] L. Huang, H. Xin, H. Yang, Z. Wang and H. Xie, "Interconnecting Very Weak AC Systems by Multiterminal VSC-HVDC Links With a Unified Virtual Synchronous Control," *IEEE Trans. Emerg. Sel. Topics Circuits Syst.*, vol. 6, no. 3, pp. 1041–1053, Sept. 2018.
- [80] P. Mitra, L. Zhang, and L. Harnefors, "Offshore wind integration to a weak grid by VSC-HVDC links using power-synchronization control: A Case Study," *IEEE Trans. Power Del.*, vol. 29, no. 1, pp. 453–461, Feb. 2014.
- [81] H. Wu and X. Wang, "Design-Oriented Transient Stability Analysis of Grid-Connected Converters With Power Synchronization Control," *IEEE Trans. Ind. Electron.*, vol. 66, no. 8, pp. 6473–6482, Aug. 2019.
- [82] J. Guo et al., "Impedance Analysis and Stabilization of Virtual Synchronous Generators With Different DC-Link Voltage Controllers Under Weak Grid," *IEEE Trans. Power Electron.*, vol. 36, no. 10, pp. 11397–11408, Oct. 2021.

- [83] A. Asrari, M. Mustafa, M. Ansari and J. Khazaei, "Impedance Analysis of Virtual Synchronous Generator-Based Vector Controlled Converters for Weak AC Grid Integration," *IEEE Trans. Sustain. Energy.*, vol. 10, no. 3, pp. 1481–1490, July 2019.
- [84] R. Luhtala et al., "Identification of Three-Phase Grid Impedance in the Presence of Parallel Converters," *Energies*, vol. 12, no. 14, p. 2674, Jul. 2019.
- [85] H. L. Willis and W. G. Scott, *Distributed Power Generation: Planning and Evaluation*. New York: Marcel Dekker, 2000.
- [86] Market Data: Microgrids, Navigant Research, Boulder, CO, USA. 2016.[Online]. Available: <https://www.navigantresearch.com/reports/market-data-microgrids>
- [87] J. Rocabert, A. Luna, F. Blaabjerg, P. Rodriguez, "Control of power converters in AC microgrids," *IEEE Trans. Power Electron.*, vol. 27, no. 11, pp. 4734–4749, Nov. 2012.
- [88] A. Bidram and A. Davoudi, "Hierarchical structure of microgrids control system," *IEEE Trans. Smart Grid*, vol. 3, no. 4, pp. 1963–1976, Dec. 2012.
- [89] H. Han et al., "Review of power sharing control strategies for islanding operation of AC microgrids," *IEEE Trans. Smart Grid.*, vol. 7, no. 1, pp. 200–215, Jan. 2016.
- [90] Y. Han, et al., "Review of active and reactive power sharing strategies in hierarchical controlled microgrids," *IEEE Trans. Power Electron.*, vol. 32, no. 3, pp. 2427–2451, Mar. 2017.
- [91] T. Morstyn, B. Hredzak, and V. G. Agelidis, "Control strategies for microgrids with distributed energy storage systems: An overview," *IEEE Trans. Smart Grid.*, vol. 9, no. 4, pp. 3652–3666, July. 2018.
- [92] N. Pogaku, M. Prodanovic, and T. C. Green, "Modeling, analysis and testing of autonomous operation of an inverter-based microgrid," *IEEE Trans. Power Electron.*, vol. 22, no. 2, pp. 613–625, Mar. 2007.
- [93] N. Bottrell, M. Prodanovic, T. C. Green, "Dynamic stability of a microgrid with an active load," *IEEE Trans. Power Electron.*, vol. 28, no. 11, pp. 5107–5119, Nov. 2013.
- [94] J. Chen and J. Chen, "Stability Analysis and Parameters Optimization of Islanded Microgrid With Both Ideal and Dynamic Constant Power Loads," *IEEE Trans. Inds. Electron.*, vol. 65, no. 4, pp. 3263–3274, April 2018.
- [95] C. A. Hernandez-Aramburo, T. C. Green, and N. Mugniot, "Fuel consumption minimization of a microgrid," *IEEE Trans. Ind. Appl.*, vol. 41, no. 3, pp. 673–681, May/Jun. 2005.

- [96] A. Kahrobaeian and Y. A. I. Mohamed, "Analysis and Mitigation of Low-Frequency Instabilities in Autonomous Medium-Voltage Converter-Based Microgrids with Dynamic Loads," *IEEE Trans. Ind. Electron.*, vol. 61, no. 4, pp. 1643–1658, April 2014.
- [97] S. D. Sudhoff et al., "Admittance space stability analysis of power electronic systems," in *IEEE Transactions on Aerospace and Electronic Systems*, vol. 36, no. 3, pp. 965–973, July 2000.
- [98] M. Cespedes and J. Sun, "Impedance Modeling and Analysis of Grid-Connected Voltage-Source Converters," *IEEE Trans. Power Electron.*, vol. 29, no. 3, pp. 1254–1261, March 2014.
- [99] IEEE Recommended Practice for Protection and Coordination of Industrial and Commercial Power Systems, pp. 242–2001, 2001.
- [100] A. H. Etemadi, E. J. Davison and R. Iravani, "A Decentralized Robust Control Strategy for Multi-DER Microgrids—Part I: Fundamental Concepts," *IEEE Trans. Power Del.*, vol. 27, no. 4, pp. 1843–1853, Oct. 2012.
- [101] A. H. Etemadi, E. J. Davison and R. Iravani, "A Decentralized Robust Control Strategy for Multi-DER Microgrids—Part II: Performance Evaluation," *IEEE Trans. Power Del.*, vol. 27, no. 4, pp. 1854–1861, Oct. 2012.
- [102] M. Babazadeh and H. Karimi, "A Robust Two-Degree-of-Freedom Control Strategy for an Islanded Microgrid," *IEEE Trans. Power Del.*, vol. 28, no. 3, pp. 1339–1347, July 2013.
- [103] A. Kahrobaeian and Y. A. I. Mohamed, "Robust Single-Loop Direct Current Control of LCL-Filtered Converter-Based DG Units in Grid-Connected and Autonomous Microgrid Modes," *IEEE Trans. Power Electron.*, vol. 29, no. 10, pp. 5605–5619, Oct. 2014.
- [104] M. S. Sadabadi, A. Haddadi, H. Karimi and A. Karimi, "A Robust Active Damping Control Strategy for an LCL-Based Grid-Connected DG Unit," *IEEE Trans. Ind. Electron.*, vol. 64, no. 10, pp. 8055–8065, Oct. 2017.

## Appendix A.

### State Matrices of VSC-WG System in Inversion Mode

The state matrices introduced in Chapter 3 are as follows.  $\mathbf{A}_{uc} = \mathbf{A}_{cp}(i, j)$  for  $1 \leq i, j \leq 13$  and  $\mathbf{A}_{cp}$  is given as follows.

$$\mathbf{A}_{cp} = \begin{bmatrix} 0 & 0 & -K_{i\omega} & 0 & 0 & 0 & 0 & K_{p\omega}r_d & 0 & -K_{p\omega}r_d & 0 & -K_{p\omega} & 0 & 0 \\ 0 & 0 & 0 & 0 & 0 & 0 & r_d & 0 & -r_d & 0 & -1 & 0 & 0 & 0 \\ 0 & 0 & 0 & 0 & 0 & 0 & 0 & -r_d & 0 & r_d & 0 & 1 & 0 & 0 \\ 0 & 0 & 0 & 0 & 0 & 0 & -K_{idc} & 0 & 0 & -1 & 0 & 0 & 0 & K_{pdc} \\ 0 & -K_{iv} & 0 & 0 & 0 & 0 & 0 & -K_{pv}r_d & 0 & K_{pv}r_d & -1 & K_{pv} & 0 & 0 & -1 \\ 0 & 0 & 0 & 0 & 0 & 0 & 0 & 0 & 0 & 0 & 0 & 0 & 0 & -1 & 0 \\ \frac{v_{gq}^0}{L_g} & 0 & K_{i\omega}i_{oq}^0 & 0 & 0 & 0 & -\frac{r_d + r_g}{L_g} & \Lambda_9 & \frac{r_d}{L_g} & K_{p\omega}r_d i_{oq}^0 & \frac{1}{L_g} & K_{p\omega}i_{oq}^0 & 0 & 0 & 0 \\ -\frac{v_{gd}^0}{L_g} & 0 & -K_{i\omega}i_{od}^0 & 0 & 0 & 0 & -\omega_{vsc}^0 & \Lambda_4 & 0 & \Lambda_{11} & 0 & \Lambda_{12} & 0 & 0 & 0 \\ 0 & 0 & K_{i\omega}i_{fq}^0 & \frac{K_{ic}}{L_f} & 0 & -\frac{K_{pc}K_{idc}}{L_f} & 0 & -K_{p\omega}r_d i_{fq}^0 & -\frac{K_{pc} + r_f}{L_f} & \Lambda_6 & 0 & K_{p\omega}i_{fq}^0 & \frac{K_{pc}K_{pdc}}{L_f} & 0 & 0 \\ 0 & -\frac{K_{iv}K_{pc}}{L_f} & -K_{i\omega}i_{fd}^0 & \frac{K_{ic}}{L_f} & 0 & -\frac{K_{pc}K_{pv}r_d}{L_f} & K_{p\omega}r_d i_{fd}^0 & \Lambda_5 & \Lambda_7 & \frac{K_{pc}K_{pv}}{L_f} & -K_{p\omega}i_{fd}^0 & 0 & -\frac{K_{pc}}{L_f} & 0 & 0 \\ 0 & 0 & K_{i\omega}v_{cq}^0 & 0 & 0 & 0 & -C_f^{-1} & -K_{p\omega}r_d v_{cq}^0 & C_f^{-1} & K_{p\omega}r_d v_{cq}^0 & 0 & \Lambda_{13} & 0 & 0 & 0 \\ 0 & 0 & -K_{i\omega}v_{cd}^0 & 0 & 0 & 0 & 0 & \Lambda_{10} & 0 & -\Lambda_{10} & -\omega_{vsc}^0 & -K_{p\omega}v_{cd}^0 & 0 & 0 & 0 \\ 0 & \sigma K_{pc}K_{iv}i_{fq}^0 & 0 & -\sigma K_{ic}i_{fd}^0 & -\sigma K_{ic}i_{fq}^0 & \sigma K_{pc}K_{idc}i_{fd}^0 & \sigma r_d \Lambda_1 & \sigma r_d i_{fq}^0 & \sigma \Lambda_2 & \sigma \Lambda_2 & -\sigma \Lambda_1 & -\sigma i_{fq}^0 & \sigma \Lambda_8 & \sigma K_{pc}i_{fq}^0 & 0 \\ 0 & 0 & 0 & 0 & 0 & 0 & 0 & -r_d K_{cp}\omega_{cp} & 0 & r_d K_{cp}\omega_{cp} & 0 & K_{cp}\omega_{cp} & 0 & 0 & -\omega_{cp} \end{bmatrix} \quad (\text{A-1})$$

where  $\Lambda_1 = i_{fd}^0 + K_{pc}K_{pv}i_{fq}^0$ ,  $\Lambda_2 = -v_{td}^0 + (K_{pc} - r_d)i_{fd}^0 - (L_f\omega_g + K_{pc}K_{pv}r_d)i_{fq}^0$ ,  $\Lambda_3 = -v_{tq}^0 + (K_{pc} - r_d)i_{fq}^0 + L_f\omega_g i_{fd}^0$ ,  $\Lambda_4 = K_{p\omega}r_d i_{od}^0 - (r_d + r_g)L_g^{-1}$ ,  $\Lambda_5 = K_{pc}K_{pc}r_d L_f^{-1} + \omega_g - \omega_{vsc}^0$ ,  $\Lambda_6 = \omega_{vsc}^0 - \omega_g + K_{p\omega}r_d i_{fq}^0$ ,  $\Lambda_7 = -(r_f + K_{pc})L_f^{-1} - K_{p\omega}r_d i_{fd}^0$ ,  $\Lambda_8 = (\frac{2}{3})i_{dc}^0 - K_{pc}K_{pdc}i_{fd}^0$ ,  $\Lambda_9 = \omega_{vsc}^0 - K_{p\omega}r_d i_{oq}^0$ ,  $\Lambda_{10} = K_{p\omega}r_d v_{cd}^0 - C_f^{-1}$ ,  $\Lambda_{11} = r_d(L_g^{-1} - K_{p\omega}i_{od}^0)$ ,  $\Lambda_{12} = L_g^{-1} - K_{p\omega}i_{od}^0$ ,  $\Lambda_{13} = \omega_{vsc}^0 + K_{p\omega}v_{cq}^0$ ,  $\sigma = \frac{3}{2}(C_{dc}v_{dc}^0)^{-1}$ .

## Appendix B.

### State Matrices of VSC-WG System in Rectification Mode

The state matrices introduced in Chapter 4 are as follows.  $\mathbf{A}_{uc} = \mathbf{A}_{cp}(i, j)$  for  $1 \leq i, j \leq 16$  and  $\mathbf{A}_{cp}$  is given as follows.

$$\mathbf{A}_{cp} = \begin{pmatrix} 0 & 0 & -K_{i\omega} & 0 & 0 & 0 & 0 & K_{p\omega}r_d & 0 & -K_{p\omega}r_d & 0 & -K_{p\omega} & 0 & 0 & 0 & 0 \\ 0 & 0 & 0 & 0 & 0 & 0 & r_d & 0 & -r_d & 0 & -1 & 0 & 0 & 0 & 0 & 0 \\ 0 & 0 & 0 & 0 & 0 & 0 & 0 & -r_d & 0 & r_d & 0 & 1 & 0 & 0 & 0 & 0 \\ 0 & 0 & 0 & 0 & 0 & -K_{idc} & 0 & 0 & 0 & 0 & 0 & 0 & K_{pdc} & 0 & -1 & 0 \\ 0 & -K_{iv} & 0 & 0 & 0 & 0 & -K_{pv}r_d & 0 & K_{pv}r_d & -1 & K_{pv} & 0 & 0 & -1 & 0 & 0 \\ 0 & 0 & 0 & 0 & 0 & 0 & 0 & 0 & 0 & 0 & 0 & 0 & -1 & 0 & 0 & 0 \\ \frac{v_{gq}^o}{L_g} & 0 & K_{i\omega}i_{oq}^o & 0 & 0 & 0 & \frac{r_d + r_g}{-L_g} & \Lambda_9 & \frac{r_d}{L_g} & K_{p\omega}r_d i_{oq}^o & \frac{1}{L_g} & K_{p\omega}i_{oq}^o & 0 & 0 & 0 & 0 \\ \frac{v_{gd}^o}{-L_g} & 0 & -K_{i\omega}i_{od}^o & 0 & 0 & 0 & -\omega_{vsc}^o & \Lambda_4 & 0 & \Lambda_{11} & 0 & \Lambda_{12} & 0 & 0 & 0 & 0 \\ 0 & 0 & K_{i\omega}i_{fq}^o & \frac{K_{ic}}{L_f} & 0 & \frac{K_{pc}K_{idc}}{-L_f} & 0 & -K_{p\omega}r_d i_{fq}^o & \frac{K_{pc} + r_f}{-L_f} & \Lambda_6 & 0 & K_{p\omega}i_{fq}^o & \frac{K_{pc}K_{pdc}}{L_f} & 0 & \frac{K_{pc}}{-L_f} & 0 \\ 0 & \frac{K_{i\omega}K_{pc}}{-L_f} & -K_{i\omega}i_{fd}^o & 0 & \frac{K_{ic}}{L_f} & 0 & \frac{K_{pc}K_{pv}r_d}{-L_f} & K_{p\omega}r_d i_{fd}^o & \Lambda_5 & \Lambda_7 & \frac{K_{pc}K_{pv}}{L_f} & -K_{p\omega}i_{fd}^o & 0 & \frac{K_{pc}}{-L_f} & 0 & 0 \\ 0 & 0 & K_{i\omega}v_{cq}^o & 0 & 0 & 0 & -C_f^{-1} & -K_{p\omega}r_d v_{cq}^o & C_f^{-1} & K_{p\omega}r_d v_{cq}^o & 0 & \Lambda_{13} & 0 & 0 & 0 & 0 \\ 0 & 0 & -K_{i\omega}v_{cd}^o & 0 & 0 & 0 & 0 & \Lambda_{10} & 0 & -\Lambda_{10} & -\omega_{vsc}^o & -K_{p\omega}v_{cd}^o & 0 & 0 & 0 & 0 \\ 0 & \sigma K_{pc}K_{iv}i_{fq}^o & 0 & -\sigma K_{ic}i_{fd}^o & -\sigma K_{ic}i_{fq}^o & \sigma K_{pc}K_{idc}i_{fd}^o & \sigma r_d \Lambda_1 & \sigma r_d i_{fq}^o & \sigma \Lambda_2 & \sigma \Lambda_3 & -\sigma \Lambda_1 & -\sigma i_{fq}^o & \sigma \Lambda_8 & \sigma K_{pc}i_{fq}^o & \sigma K_{pc}i_{fd}^o & 0 \\ 0 & 0 & 0 & 0 & 0 & 0 & 0 & -r_d K_{cpq} \omega_{cpq} & 0 & r_d K_{cpq} \omega_{cpq} & 0 & K_{cpq} \omega_{cpq} & 0 & -\omega_{cpq} & 0 & 0 \\ 0 & 0 & 0 & 0 & 0 & 0 & 0 & 0 & 0 & 0 & 0 & 0 & 0 & 0 & 0 & 1 \\ \Lambda_{14} & 0 & \Lambda_{15} & \Lambda_{16} & 0 & \Lambda_{17} & \Lambda_{18} & \Lambda_{19} & \Lambda_{20} & \Lambda_{21} & \Lambda_{22} & \Lambda_{23} & \Lambda_{24} & 0 & \Lambda_{25} & -2\omega_{cpd}\xi \end{pmatrix} \quad (\text{B-1})$$

where ,  $\Lambda_1 = i_{fd}^o + K_{pc}K_{pv}i_{fq}^o$ ,  $\Lambda_2 = -v_{td}^o + (K_{pc} - r_d)i_{fd}^o - (L_f\omega_g + K_{pc}K_{pv}r_d)i_{fq}^o$ ,  $\Lambda_3 = -v_{tq}^o + (K_{pc} - r_d)i_{fq}^o S + L_f\omega_g i_{fd}^o$ ,  $\Lambda_4 = K_{p\omega}r_d i_{od}^o - (r_d + r_g)L_g^{-1}$ ,  $\Lambda_5 = K_{pc}K_{pc}r_d L_f^{-1} + \omega_g - \omega_{vsc}^o$ ,  $\Lambda_6 = \omega_{vsc}^o - \omega_g + K_{p\omega}r_d i_{fq}^o$ ,  $\Lambda_7 = -(r_f + K_{pc})L_f^{-1} - K_{p\omega}r_d i_{fd}^o$ ,  $\Lambda_8 = \left(\frac{2}{3}\right)i_{dc}^o - K_{pc}K_{pdc}i_{fd}^o$ ,  $\Lambda_9 = \omega_{vsc}^o - K_{p\omega}r_d i_{oq}^o$ ,  $\Lambda_{10} = K_{p\omega}r_d v_{cd}^o - C_f^{-1}$ ,  $\Lambda_{11} = r_d(L_g^{-1} - K_{p\omega}i_{od}^o)$ ,  $\Lambda_{12} = L_g^{-1} - K_{p\omega}i_{od}^o$ ,  $\Lambda_{13} = \omega_{vsc}^o + K_{p\omega}v_{cq}^o$ ,  $\sigma = \frac{3}{2}(C_{dc}v_{dc}^o)^{-1}$ ,  $\rho = 2K_{cpd}r_d\omega_{cpd}\xi$ ,  $\Lambda_{14} = -\rho V_g \sin(\delta_0)L_f^{-1}$ ,  $\Lambda_{15} = \rho K_{i\omega}(v_{cq}^o r_d^{-1} + i_{fq}^o - i_{oq}^o)$ ,  $\Lambda_{16} = \rho K_{ic}L_f^{-1}$ ,  $\Lambda_{17} = -\rho K_{idc}K_{pc}L_f^{-1}$ ,  $\Lambda_{18} = -\rho(r_d^{-1}C_f^{-1} - (r_d + r_g))$ ,  $\Lambda_{19} = -\rho(\omega_{vsc}^o + K_{p\omega}r_d i_{fq}^o L_g^{-1} + K_{p\omega}v_{cq}^o - K_{p\omega}r_d i_{oq}^o)$ ,  $\Lambda_{20} = \rho(r_d^{-1}C_f^{-1} - (K_{pc} + r_f)L_f^{-1} + L_g^{-1})$ ,  $\Lambda_{21} = \rho(\omega_{vsc}^o - \omega_g + K_{p\omega}r_d i_{fq}^o + K_{p\omega}v_{cq}^o - K_{p\omega}r_d i_{oq}^o)$ ,  $\Lambda_{22} = -\rho L_g^{-1}$ ,  $\Lambda_{23} = \rho((\omega_{vsc}^o + K_{p\omega}v_{cq}^o)r_d^{-1} + K_{p\omega}i_{fq}^o - K_{p\omega}i_{oq}^o)$ ,  $\Lambda_{24} = \rho K_{pdc}K_{pc}L_f^{-1}$ ,  $\Lambda_{25} = -\omega_{cpd}^2 - \rho K_{pdc}K_{pc}L_f^{-1}$ .

## Appendix C.

### State Matrices of AC Microgrid System

The state-space matrices used in Chapter 5 are introduced as follows.

#### VSI's state-space matrices

The following matrices correspond to the VSI state-space model developed in Section 5.2.2. The superscript "vsi" is dropped for the sake of compactness.

$$\mathbf{A}_{\text{vsi}} = \begin{bmatrix} 0 & -m & 0 & 0 & 0 & 0 & 0 & 0 & 0 & 0 & 0 & 0 & 0 & 0 \\ 0 & -\omega_c & 0 & 0 & 0 & 0 & 0 & 0 & 0 & \Lambda_1 & \Lambda_2 & \Lambda_3 & \Lambda_4 & 0 \\ 0 & 0 & -\omega_c & 0 & 0 & 0 & 0 & 0 & 0 & -\Lambda_2 & \Lambda_1 & \Lambda_4 & -\Lambda_3 & 0 \\ 0 & 0 & -n & 0 & 0 & 0 & 0 & 0 & 0 & -1 & 0 & 0 & 0 & 0 \\ 0 & 0 & 0 & 0 & 0 & 0 & 0 & 0 & 0 & 0 & -1 & 0 & 0 & 0 \\ 0 & 0 & -K_{pv}n & K_{iv} & 0 & 0 & 0 & -1 & 0 & -K_{pv} & \omega_{nl}C_f & F_v & 0 & 0 \\ 0 & 0 & 0 & 0 & K_{iv} & 0 & 0 & 0 & -1 & \omega_{nl}C_f & -K_{pv} & 0 & 0 & F_v \\ 0 & -mi_{fq}^\circ & -K_{pc}K_{pv}L_f^{-1}n & K_{pc}K_{iv}L_f^{-1} & 0 & K_{ic}L_f^{-1} & 0 & \Lambda_5 & \omega^\circ - \omega_{nl} & \Lambda_6 & -\Lambda_7 & F_vK_{pc}L_f^{-1} & 0 & 0 \\ 0 & mi_{fd}^\circ & 0 & 0 & K_{pc}K_{iv}L_f^{-1} & 0 & K_{ic}L_f^{-1} & \omega^\circ - \omega_{nl} & \Lambda_5 & \Lambda_7 & \Lambda_6 & 0 & F_vK_{pc}L_f^{-1} & 0 \\ 0 & -mv_{oq}^\circ & 0 & 0 & 0 & 0 & 0 & C_f^{-1} & 0 & 0 & \omega^\circ & -C_f^{-1} & 0 & 0 \\ 0 & mv_{od}^\circ & 0 & 0 & 0 & 0 & 0 & 0 & C_f^{-1} & -\omega^\circ & 0 & 0 & 0 & -C_f^{-1} \\ \Lambda_8 & -mi_{oq}^\circ & 0 & 0 & 0 & 0 & 0 & 0 & 0 & L_c^{-1} & 0 & -r_cL_c^{-1} & \omega^\circ & 0 \\ \Lambda_9 & -mi_{od}^\circ & 0 & 0 & 0 & 0 & 0 & 0 & 0 & 0 & L_c^{-1} & -\omega^\circ & -r_cL_c^{-1} & 0 \end{bmatrix} \quad (\text{C-1})$$

$$\mathbf{B}_{1\text{vsi}} = [\mathbf{0}_{2 \times 11} \quad -\mathbf{T}(\delta_{\text{vsi}}^\circ)]^T L_c^{-1} \quad (\text{C-2})$$

$$\mathbf{B}_{2\text{vsi}} = [-\mathbf{1} \quad \mathbf{0}_{1 \times 12}]^T \quad (\text{C-3})$$

$$\mathbf{C}_{\text{vsi}} = \begin{bmatrix} -i_{oq}^\circ \cos(\delta_{\text{vsi}}^\circ) - i_{od}^\circ \sin(\delta_{\text{vsi}}^\circ) & \mathbf{0}_{1 \times 10} & \mathbf{T}(\delta_{\text{vsi}}^\circ) \\ i_{od}^\circ \cos(\delta_{\text{vsi}}^\circ) - i_{oq}^\circ \sin(\delta_{\text{vsi}}^\circ) & & \end{bmatrix} \quad (\text{C-4})$$

where  $\Lambda_1 = \frac{3}{2}i_{od}^\circ\omega_c$ ,  $\Lambda_2 = \frac{3}{2}i_{oq}^\circ\omega_c$ ,  $\Lambda_3 = \frac{3}{2}v_{od}^\circ\omega_c$ ,  $\Lambda_4 = \frac{3}{2}v_{oq}^\circ\omega_c$ ,  $\Lambda_5 = -(K_{pc} + r_f)L_f^{-1}$ ,  $\Lambda_6 = -(K_{pc}K_{pv} - F_c + 1)L_f^{-1}$ ,  $\Lambda_7 = K_{pc}\omega_{nl}C_fL_f^{-1}$ ,  $\Lambda_8 = (v_{bd}^\circ \sin(\delta_{\text{vsi}}^\circ) - v_{bq}^\circ \cos(\delta_{\text{vsi}}^\circ))L_c^{-1}$ ,  $\Lambda_9 = (v_{bd}^\circ \cos(\delta_{\text{vsi}}^\circ) + v_{bq}^\circ \sin(\delta_{\text{vsi}}^\circ))L_c^{-1}$ , and  $\mathbf{0}_{i \times j}$  is a matrix of zero entries with  $i$  rows and  $j$  columns. Taking the VSI<sub>1</sub> corresponding  $dq$ -RF as the common  $DQ$ -RF, the combined state-space model of VSI<sub>1-3</sub> can be derived as follows.

$$\frac{d}{dt} \tilde{\mathbf{X}}_{\text{VSI}}(t) = \mathbf{A}_{\text{VSI}} \tilde{\mathbf{X}}_{\text{VSI}} + \mathbf{B}_{\text{VSI}} \tilde{\mathbf{U}}_{\text{vsi}} \quad (\text{C-5})$$

$$\tilde{\mathbf{X}}_{\text{VSI}} = [\tilde{\mathbf{X}}_{\text{vsi1}}^T \quad \tilde{\mathbf{X}}_{\text{vsi2}}^T \quad \tilde{\mathbf{X}}_{\text{vsi3}}^T]^T \quad (\text{C-6})$$

$$\tilde{\mathbf{U}}_{\text{VSI}} = [\tilde{\mathbf{U}}_{\text{vsi1}}^T \quad \tilde{\mathbf{U}}_{\text{vsi2}}^T \quad \tilde{\mathbf{U}}_{\text{vsi3}}^T]^T \quad (\text{C-7})$$

$$\tilde{\mathbf{Y}}_{\text{VSI}} = [\tilde{i}_{oD_1}^{vsi} \quad \tilde{i}_{oQ_1}^{vsi} \quad \tilde{i}_{oD_2}^{vsi} \quad \tilde{i}_{oQ_2}^{vsi} \quad \tilde{i}_{oD_3}^{vsi} \quad \tilde{i}_{oQ_3}^{vsi}]^T \quad (\text{C-8})$$

where

$$\mathbf{A}_{\text{VSI}} = \begin{bmatrix} \mathbf{A}_{\text{vsi1}} + \mathbf{B}_{2\text{vsi}}\mathbf{C}_{\text{com}} & \mathbf{0}_{13 \times 13} & \mathbf{0}_{13 \times 13} \\ \mathbf{B}_{2\text{vsi}}\mathbf{C}_{\text{com}} & \mathbf{A}_{\text{vsi2}} & \mathbf{0}_{13 \times 13} \\ \mathbf{B}_{2\text{vsi}}\mathbf{C}_{\text{com}} & \mathbf{0}_{13 \times 13} & \mathbf{A}_{\text{vsi3}} \end{bmatrix} \quad (\text{C-9})$$

$$\mathbf{B}_{\text{VSI}} = \begin{bmatrix} \mathbf{B}_{1\text{vsi1}} & \mathbf{0}_{13 \times 2} & \mathbf{0}_{13 \times 2} \\ \mathbf{0}_{13 \times 2} & \mathbf{B}_{1\text{vsi2}} & \mathbf{0}_{13 \times 2} \\ \mathbf{0}_{13 \times 2} & \mathbf{0}_{13 \times 2} & \mathbf{B}_{1\text{vsi3}} \end{bmatrix} \quad (\text{C-10})$$

$$\mathbf{C}_{\text{VSI}} = \begin{bmatrix} \mathbf{C}_{\text{vsi1}} & \mathbf{0}_{2 \times 13} & \mathbf{0}_{2 \times 13} \\ \mathbf{0}_{2 \times 13} & \mathbf{C}_{\text{vsi2}} & \mathbf{0}_{2 \times 13} \\ \mathbf{0}_{2 \times 13} & \mathbf{0}_{2 \times 13} & \mathbf{C}_{\text{vsi3}} \end{bmatrix} \quad (\text{C-11})$$

$$\mathbf{C}_{\text{com}} = [0 \quad m_1 \quad \mathbf{0}_{1 \times 11}] \quad (\text{C-12})$$

In (C-9),  $\mathbf{C}_{\text{com}}$  is used to integrate the second input of each VSI state-space model, i.e.,  $\tilde{\omega}_{\text{com}} = \tilde{\omega}_{\text{vsi1}}$ , into VSI<sub>1-3</sub> combined state-space model.

### VSR state-space matrices

The following matrices correspond to the VSR state-space model developed in Section 5.2.3. The superscript “vsr” is dropped for the sake of compactness.

$\mathbf{A}_{\text{vsr}} =$

$$\begin{bmatrix} 0 & 0 & K_{i\omega} & 0 & 0 & 0 & 0 & 0 & 0 & K_{p\omega} & 0 & 0 & 0 \\ 0 & 0 & 0 & 0 & 0 & 0 & 0 & 0 & 0 & -1 & 0 & 0 & 0 \\ 0 & 0 & 0 & 0 & 0 & 0 & 0 & 0 & 0 & 1 & 0 & 0 & 0 \\ 0 & 0 & 0 & 0 & 0 & K_{idc} & -1 & 0 & 0 & 0 & 0 & 0 & -K_{pdc} \\ 0 & -K_{iv} & 0 & 0 & 0 & 0 & 0 & -1 & -K_{pv} & 0 & 0 & 0 & 0 \\ 0 & 0 & 0 & 0 & 0 & 0 & 0 & -1 & 0 & 0 & 0 & 0 & 0 \\ 0 & 0 & 0 & 0 & 0 & 0 & 0 & 0 & 0 & 0 & 0 & 0 & -1 \\ 0 & 0 & K_{i\omega}i_{fq}^* & K_{ic}L_f^{-1} & 0 & K_{pc}K_{idc}L_f^{-1} & -(K_{pc} + r_f)L_f^{-1} & \omega^\circ - \omega_{nl} & 0 & K_{p\omega}i_{fq}^* & 0 & 0 & -K_{pc}K_{pdc}L_f^{-1} \\ 0 & 0 & -K_{i\omega}i_{fd}^* & 0 & K_{ic}L_f^{-1} & 0 & \omega_{nl} - \omega^\circ & -(K_{pc} + r_f)L_f^{-1} & 0 & -K_{p\omega}i_{fd}^* & 0 & 0 & 0 \\ 0 & 0 & K_{i\omega}v_{oq}^* & 0 & 0 & 0 & -C_f^{-1} & 0 & 0 & \omega^\circ + K_{p\omega}v_{oq}^* & C_f^{-1} & 0 & 0 \\ 0 & 0 & -K_{i\omega}v_{od}^* & 0 & 0 & 0 & 0 & -C_f^{-1} & -\omega^\circ & -K_{p\omega}v_{od}^* & 0 & C_f^{-1} & 0 \\ \Lambda_1 & 0 & K_{i\omega}i_{oq}^* & 0 & 0 & 0 & 0 & 0 & 0 & -L_c^{-1} & K_{p\omega}i_{oq}^* & -r_cL_c^{-1} & \omega^\circ \\ \Lambda_2 & 0 & -K_{i\omega}i_{od}^* & 0 & 0 & 0 & 0 & 0 & 0 & -K_{p\omega}i_{od}^* - L_c^{-1} & -\omega^\circ & -r_cL_c^{-1} & 0 \\ 0 & 0 & 0 & -\rho K_{ic}i_{fd}^* & -\rho K_{ic}i_{fq}^* & -\rho K_{pc}K_{idc}i_{fd}^* & \Lambda_3 & \Lambda_4 & \rho i_{fd}^* & \rho i_{fq}^* & 0 & 0 & \Lambda_5 \end{bmatrix} \quad (\text{C-13})$$

$$\mathbf{B}_{1\text{vsr}} = [\mathbf{0}_{2 \times 9} \quad -\mathbf{T}(\delta_{\text{vsr}}^\circ) \quad \mathbf{0}_{2 \times 1}]^T L_c^{-1} \quad (\text{C-14})$$

$$\mathbf{B}_{2\text{vsr}} = [-\mathbf{1} \quad \mathbf{0}_{1 \times 11}]^T \quad (\text{C-15})$$

$$\mathbf{C}_{\text{vsr}} = \begin{bmatrix} -i_{oq}^\circ \cos(\delta_{\text{vsr}}^\circ) - i_{od}^\circ \sin(\delta_{\text{vsr}}^\circ) & \mathbf{0}_{1 \times 8} & \mathbf{T}(\delta_{\text{vsr}}^\circ) & \mathbf{0}_{2 \times 1} \\ i_{od}^\circ \cos(\delta_{\text{vsr}}^\circ) - i_{oq}^\circ \sin(\delta_{\text{vsr}}^\circ) & & & \end{bmatrix} \quad (\text{C-16})$$

where  $\Lambda_1 = (v_{bD}^\circ \cos(\delta_{\text{vsr}}^\circ) + v_{bQ}^\circ \sin(\delta_{\text{vsr}}^\circ)) L_c^{-1}$ ,  $\Lambda_2 = (v_{bD}^\circ \cos(\delta_{\text{vsr}}^\circ) + v_{bQ}^\circ \sin(\delta_{\text{vsr}}^\circ)) L_c^{-1}$ ,  
 $\Lambda_3 = \rho(v_{td}^\circ + K_{pc} i_{fd}^\circ - \omega_{nl} L_f i_{fq}^\circ)$ ,  $\Lambda_4 = \rho(v_{tq}^\circ + K_{pc} i_{fd}^\circ + \omega_{nl} L_f i_{fq}^\circ)$ ,  $\Lambda_5 = -\rho \left( \frac{4v_{dc}^\circ}{3R_{dc}} - K_{pc} K_{pv} i_{fd}^\circ \right)$ ,  $\rho = \frac{3}{2C_{dc} v_{dc}^\circ}$ .

### **RL-Type PLs state-space matrices**

The following matrices correspond to the RL-type PL state-space model developed in Section 5.2.4.

$$\mathbf{A}_{\text{pl}} = \begin{bmatrix} -r_{pl} L_{pl}^{-1} & \omega_{com}^\circ \\ -\omega_{com}^\circ & -r_{pl} L_{pl}^{-1} \end{bmatrix} \quad (\text{C-17})$$

$$\mathbf{A}_{\text{pl}} = \begin{bmatrix} -r_{pl} L_{pl}^{-1} & \omega_{com}^\circ \\ -\omega_{com}^\circ & -r_{pl} L_{pl}^{-1} \end{bmatrix} \quad (\text{C-18})$$

$$\mathbf{B}_{1\text{pl}} = \begin{bmatrix} L_{pl}^{-1} & 0 \\ 0 & L_{pl}^{-1} \end{bmatrix} \quad (\text{C-19})$$

$$\mathbf{B}_{2\text{pl}} = \begin{bmatrix} i_{plQ}^\circ \\ -i_{plD}^\circ \end{bmatrix} \quad (\text{C-20})$$

The combined state-space model of the PL<sub>1-2</sub> can be derived as follows.

$$\frac{d}{dt} \tilde{\mathbf{X}}_{\text{PL}}(t) = \mathbf{A}_{\text{PL}} \tilde{\mathbf{X}}_{\text{VSI}} + \mathbf{B}_{1\text{PL}} \tilde{\mathbf{U}}_{\text{PL}} + \mathbf{B}_{2\text{PL}} \tilde{\omega}_{com} \quad (\text{C-21})$$

$$\tilde{\mathbf{Y}}_{\text{PL}} = \tilde{\mathbf{X}}_{\text{PL}} \quad (\text{C-22})$$

where

$$\tilde{\mathbf{X}}_{\text{PL}} = [\tilde{\mathbf{X}}_{\text{pl1}}^T \quad \tilde{\mathbf{X}}_{\text{pl2}}^T \quad \tilde{\mathbf{X}}_{\text{pl3}}^T]^T \quad (\text{C-23})$$

$$\tilde{\mathbf{U}}_{\text{PL}} = [\tilde{\mathbf{U}}_{\text{pl1}}^T \quad \tilde{\mathbf{U}}_{\text{pl2}}^T \quad \tilde{\mathbf{U}}_{\text{pl3}}^T]^T \quad (\text{C-24})$$

$$\mathbf{A}_{\text{PL}} = \begin{bmatrix} \mathbf{A}_{\text{PL1}} & \mathbf{0}_{2 \times 2} & \mathbf{0}_{2 \times 2} \\ \mathbf{0}_{2 \times 2} & \mathbf{A}_{\text{PL2}} & \mathbf{0}_{2 \times 2} \\ \mathbf{0}_{2 \times 2} & \mathbf{0}_{2 \times 2} & \mathbf{A}_{\text{PL3}} \end{bmatrix} \quad (\text{C-25})$$

$$\mathbf{B}_{1\text{PL}} = \begin{bmatrix} \mathbf{B}_{1\text{pl1}} & \mathbf{0}_{2 \times 2} & \mathbf{0}_{2 \times 2} \\ \mathbf{0}_{2 \times 2} & \mathbf{B}_{1\text{pl2}} & \mathbf{0}_{2 \times 2} \\ \mathbf{0}_{2 \times 2} & \mathbf{0}_{2 \times 2} & \mathbf{B}_{1\text{pl3}} \end{bmatrix} \quad (\text{C-26})$$

$$\mathbf{B}_{2\text{PL}} = [\mathbf{B}_{2\text{pl1}}^T \quad \mathbf{B}_{2\text{pl3}}^T \quad \mathbf{B}_{2\text{pl3}}^T]^T \quad (\text{C-27})$$

It should be noted that if PL<sub>2</sub> is disconnected from the ac microgrid by the selector switch ST, the corresponding rows and columns are deleted in matrices introduced in (C-23)–(C-27).

### **Network lines state-space matrices**

The following matrices correspond to the line state-space model that is developed in Section 5.2.5.

$$\mathbf{A}_{\text{ln}ij} = \begin{bmatrix} -r_{\text{ln}} L_{\text{ln}}^{-1} & \omega_{\text{com}}^\circ \\ -\omega_{\text{com}}^\circ & -r_{\text{ln}} L_{\text{ln}}^{-1} \end{bmatrix} \quad (\text{C-28})$$

$$\mathbf{B}_{1\text{ln}ij} = \begin{bmatrix} L_{\text{ln}}^{-1} & 0 & -L_{\text{ln}}^{-1} & 0 \\ 0 & L_{\text{ln}}^{-1} & 0 & -L_{\text{ln}}^{-1} \end{bmatrix} \quad (\text{C-29})$$

$$\mathbf{B}_{2\text{ln}ij} = \begin{bmatrix} i_{\text{ln}Q}^\circ \\ -i_{\text{ln}D}^\circ \end{bmatrix} \quad (\text{C-30})$$

The combined state-space model of the lines can be derived as follows.

$$\frac{d}{dt} \tilde{\mathbf{X}}_{\text{LN}}(t) = \mathbf{A}_{\text{LN}} \tilde{\mathbf{X}}_{\text{LN}} + \mathbf{B}_{1\text{LN}} \tilde{\mathbf{U}}_{\text{LN}} + \mathbf{B}_{2\text{LN}} \tilde{\omega}_{\text{com}} \quad (\text{C-31})$$

$$\tilde{\mathbf{Y}}_{\text{LN}} = \tilde{\mathbf{X}}_{\text{LN}} \quad (\text{C-32})$$

where

$$\tilde{\mathbf{X}}_{\text{LN}} = [\tilde{\mathbf{X}}_{\text{LN1}}^T \quad \tilde{\mathbf{X}}_{\text{LN2}}^T]^T \quad (\text{C-33})$$

$$\tilde{\mathbf{U}}_{LN} = [\tilde{\mathbf{U}}_{LN1}^T \quad \tilde{\mathbf{U}}_{LN2}^T]^T \quad (\text{C-34})$$

$$\mathbf{A}_{LN} = \begin{bmatrix} \mathbf{A}_{LN1} & \mathbf{0}_{2 \times 2} \\ \mathbf{0}_{2 \times 2} & \mathbf{A}_{LN2} \end{bmatrix} \quad (\text{C-35})$$

$$\mathbf{B}_{1LN} = \begin{bmatrix} \mathbf{B}_{1LN1} & \mathbf{0}_{2 \times 2} \\ \mathbf{0}_{2 \times 2} & \mathbf{B}_{1LN2} \end{bmatrix} \quad (\text{C-36})$$

$$\mathbf{B}_{2LN} = [\mathbf{B}_{2Ln1}^T \quad \mathbf{B}_{2Ln2}^T]^T \quad (\text{C-37})$$

### Microgrid state-space matrices

If a large resistance  $r_n$  is added to all nodes of the ac microgrid, then each node voltage is a function of the algebraic sum of all currents meeting at the same node multiplied by the virtual resistance added to the node. Therefore, the voltages can be written as functions of the ac microgrid states. With this systematic method, the state matrix of the ac microgrid autonomous state-space model, which is introduced in Section 5.2.6, is derived as follows.

$$\mathbf{A}_{mg} = \begin{bmatrix} \mathbf{A}_{VSI} + \mathbf{B}_{VSI} \mathbf{R}_N \mathbf{M}_{VSI} \mathbf{C}_{VSI} & \mathbf{B}_{VSI} \mathbf{R}_N \mathbf{M}_{LN} & \mathbf{B}_{VSI} \mathbf{R}_N \mathbf{M}_{PL} & \mathbf{B}_{VSI} \mathbf{R}_N \mathbf{M}_{vsr} \mathbf{C}_{vsr} \\ \mathbf{B}_{1LN} \mathbf{R}_N \mathbf{M}_{VSI} \mathbf{C}_{VSI} + \mathbf{B}_{2LN} \mathbf{C}_{COM} & \mathbf{A}_{net} + \mathbf{B}_{1LN} \mathbf{R}_N \mathbf{M}_{LN} & \mathbf{B}_{1LN} \mathbf{R}_N \mathbf{M}_{PL} & \mathbf{B}_{1LN} \mathbf{R}_N \mathbf{M}_{vsr} \mathbf{C}_{vsr} \\ \mathbf{B}_{1PL} \mathbf{R}_N \mathbf{M}_{VSI} \mathbf{C}_{VSI} + \mathbf{B}_{2PL} \mathbf{C}_{COM} & \mathbf{B}_{1PL} \mathbf{R}_N \mathbf{M}_{LN} & \mathbf{A}_{pl} + \mathbf{B}_{1PL} \mathbf{R}_N \mathbf{M}_{PL} & \mathbf{B}_{1PL} \mathbf{R}_N \mathbf{M}_{vsr} \mathbf{C}_{vsr} \\ \mathbf{B}_{1vsr} \mathbf{T}_{vsr} \mathbf{R}_N \mathbf{M}_{VSI} \mathbf{C}_{VSI} + \mathbf{B}_{2vsr} \mathbf{C}_{COM} & \mathbf{B}_{1vsr} \mathbf{T}_{vsr} \mathbf{R}_N \mathbf{M}_{LN} & \mathbf{B}_{1vsr} \mathbf{T}_{vsr} \mathbf{R}_N \mathbf{M}_{PL} & \mathbf{A}_{vsr} + \mathbf{B}_{1vsr} \mathbf{T}_{vsr} \mathbf{R}_N \mathbf{M}_{vsr} \mathbf{C}_{vsr} \end{bmatrix} \quad (\text{C-38})$$

where

$$\mathbf{C}_{COM} = [\mathbf{C}_{com} \quad \mathbf{0}_{1 \times 26}] \quad (\text{C-39})$$

$$\mathbf{C}_{com} = [0 \quad -m_1 \quad \mathbf{0}_{1 \times 11}] \quad (\text{C-40})$$

$$\mathbf{R}_N = r_n \mathbf{I}_{6 \times 6} \quad (\text{C-41})$$

$$\mathbf{M}_{VSI} = \mathbf{I}_{6 \times 6} \quad (\text{C-42})$$

$$\mathbf{M}_{LN} = \begin{bmatrix} -1 & 0 & 1 & 0 & 0 & 0 \\ 0 & -1 & 0 & 1 & 0 & 0 \\ 0 & 0 & -1 & 0 & 1 & 0 \\ 0 & 0 & 0 & -1 & 0 & 1 \end{bmatrix}^T \quad (\text{C-43})$$

$$\mathbf{M}_{PL} = -\mathbf{I}_{6 \times 6} \quad (\text{C-44})$$

$$\mathbf{M}_{vsr} = \begin{bmatrix} 0 & 0 \\ 0 & 0 \\ -1 & 0 \\ 0 & -1 \end{bmatrix} \quad (\text{C-45})$$

$$\mathbf{T}_{vsr} = \begin{bmatrix} 0 & 0 & 1 & 0 & 0 & 0 \\ 0 & 0 & 0 & 1 & 0 & 0 \end{bmatrix} \quad (\text{C-46})$$

where,  $\mathbf{1}_{i \times j}$  is a matrix of ones with  $i$  rows and  $j$  columns;  $\mathbf{I}_{i \times i}$  is an identity matrix;  $\mathbf{M}_x$  matrices are used to integrate the currents of each microgrid module in the virtual nodal

equation;  $\mathbf{C}_{COM}$  is used to integrate the second input of the modules state-space models, i.e.,  $\tilde{\omega}_{com} = \tilde{\omega}_{vsi1}$ , into the ac microgrid state-space model; and  $\mathbf{T}_{VSR}$  is used to integrate the voltage components of node 2 into the VSR state-space model. Since VSI<sub>1-3</sub> are connected to nodes 1-3, respectively,  $\mathbf{M}_{vsi}$  is an identity matrix. It should be noted that if AEL is disconnected from the ac microgrid by the selector switch ST, the corresponding rows and columns are deleted from  $\mathbf{A}_{mg}$ . On the other hand, if PL<sub>2</sub> is disconnected then

$$\mathbf{M}_{PL} = \begin{bmatrix} -1 & 0 & 0 & 0 & 0 & 0 \\ 0 & -1 & 0 & 0 & 0 & 0 \\ 0 & 0 & 0 & 0 & -1 & 0 \\ 0 & 0 & 0 & 0 & 0 & -1 \end{bmatrix}^T \quad (\text{C-47})$$

## Appendix D.

### State Matrices of Weak AC Microgrid

The state-space matrices used in Chapter 6 are introduced as follows.

#### RC-Type PL state-space matrices

$$\mathbf{A}_{pl} = \begin{bmatrix} -r_{pl}C_{pl}^{-1} & \omega_{com}^{\circ} & C_{pl}^{-1} & 0 \\ -\omega_{com}^{\circ} & -r_{pl}C_{pl}^{-1} & 0 & C_{pl}^{-1} \\ -L_{c4}^{-1} & 0 & -r_{c4}L_{c4}^{-1} & \omega_{com}^{\circ} \\ 0 & -L_{c4}^{-1} & -\omega_{com}^{\circ} & -r_{c4}L_{c4}^{-1} \end{bmatrix}^T \quad (D-1)$$

$$\mathbf{B}_{1pl} = \begin{bmatrix} 0 & 0 & 1 & 0 \\ 0 & 0 & 0 & 1 \end{bmatrix}^T L_{c4}^{-1} N_l^{-1} \quad (D-2)$$

$$\mathbf{B}_{2pl} = [v_{oQ}^{pl^{\circ}} \quad -v_{oD}^{pl^{\circ}} \quad i_{oQ}^{pl^{\circ}} \quad -i_{oD}^{pl^{\circ}}]^T \quad (D-3)$$

$$\mathbf{C}_{pl} = \begin{bmatrix} 0 & 0 & 1 & 0 \\ 0 & 0 & 0 & 1 \end{bmatrix} N_l^{-1} \quad (D-4)$$

#### Weak microgrid state-space matrices

With this systematic method introduced in Appendix C, the state matrix of the WMG state space model introduced in Section 6.4.4 is derived as follows.

$$\mathbf{A}_{wmg} = \begin{bmatrix} \mathbf{A}_{VSI} + \mathbf{B}_{VSI} \mathbf{T}_{VSI} \mathbf{R}_N \mathbf{M}_{VSI} \mathbf{C}_{VSI} & \mathbf{B}_{VSI} \mathbf{T}_{VSI} \mathbf{R}_N \mathbf{M}_{in} & \mathbf{B}_{VSI} \mathbf{T}_{VSI} \mathbf{R}_N \mathbf{M}_{pl} \mathbf{C}_{pl} & \mathbf{B}_{VSI} \mathbf{T}_{VSI} \mathbf{R}_N \mathbf{M}_{vsr} \mathbf{C}_{vsr} \\ \mathbf{B}_{1in} \mathbf{R}_N \mathbf{M}_{VSI} \mathbf{C}_{VSI} + \mathbf{B}_{2in} \mathbf{C}_{COM} & \mathbf{A}_{in} + \mathbf{B}_{1in} \mathbf{R}_N \mathbf{M}_{in} & \mathbf{B}_{1in} \mathbf{R}_N \mathbf{M}_{pl} \mathbf{C}_{pl} & \mathbf{B}_{1in} \mathbf{R}_N \mathbf{M}_{vsr} \mathbf{C}_{vsr} \\ \mathbf{B}_{1pl} \mathbf{T}_{pl} \mathbf{R}_N \mathbf{M}_{VSI} \mathbf{C}_{VSI} + \mathbf{B}_{2pl} \mathbf{C}_{COM} & \mathbf{B}_{1pl} \mathbf{T}_{pl} \mathbf{R}_N \mathbf{M}_{in} & \mathbf{A}_{pl} + \mathbf{B}_{1pl} \mathbf{T}_{pl} \mathbf{R}_N \mathbf{M}_{pl} \mathbf{C}_{pl} & \mathbf{B}_{1pl} \mathbf{T}_{pl} \mathbf{R}_N \mathbf{M}_{vsr} \mathbf{C}_{vsr} \\ \mathbf{B}_{1vsr} \mathbf{T}_{vsr} \mathbf{R}_N \mathbf{M}_{VSI} \mathbf{C}_{VSI} + \mathbf{B}_{2vsr} \mathbf{C}_{COM} & \mathbf{B}_{1vsr} \mathbf{T}_{vsr} \mathbf{R}_N \mathbf{M}_{in} & \mathbf{B}_{1vsr} \mathbf{T}_{vsr} \mathbf{R}_N \mathbf{M}_{pl} \mathbf{C}_{pl} & \mathbf{A}_{vsr} + \mathbf{B}_{1vsr} \mathbf{T}_{vsr} \mathbf{R}_N \mathbf{M}_{vsr} \mathbf{C}_{vsr} \end{bmatrix} \quad (D-5)$$

where

$$\mathbf{C}_{COM} = [\mathbf{C}_{com} \quad \mathbf{0}_{1 \times 13}] \quad (D-6)$$

$$\mathbf{C}_{com} = [0 \quad -m_1 \quad \mathbf{0}_{1 \times 11}] \quad (D-7)$$

$$\mathbf{R}_N = r_n \mathbf{I}_{4 \times 4} \quad (D-8)$$

$$\mathbf{M}_{VSI} = \begin{bmatrix} 1 & 0 & 1 & 0 \\ 0 & 1 & 0 & 1 \\ 0 & 0 & 0 & 0 \\ 0 & 0 & 0 & 0 \end{bmatrix} \quad (D-9)$$

$$\mathbf{M}_{\text{In}} = \begin{bmatrix} -1 & 0 \\ 0 & -1 \\ 1 & 0 \\ 0 & 1 \end{bmatrix} \quad (\text{D-10})$$

$$\mathbf{M}_{\text{pl}} = \mathbf{M}_{\text{vsr}} = \begin{bmatrix} 0 & 0 \\ 0 & 0 \\ -1 & 0 \\ 0 & -1 \end{bmatrix} \quad (\text{D-11})$$

$$\mathbf{T}_{\text{vSI}} = \begin{bmatrix} 1 & 0 & 0 & 0 \\ 0 & 1 & 0 & 0 \\ 1 & 0 & 0 & 0 \\ 0 & 1 & 0 & 0 \end{bmatrix} \quad (\text{D-12})$$

$$\mathbf{T}_{\text{pl}} = \mathbf{T}_{\text{vsr}} = \begin{bmatrix} 0 & 0 & 1 & 0 \\ 0 & 0 & 0 & 1 \end{bmatrix} \quad (\text{D-13})$$

where  $\mathbf{I}$  is an identity matrix;  $\mathbf{0}$  is a matrix of zeros;  $\mathbf{M}_{\mathbf{x}}$  are used to integrate the currents of each weak microgrid module into the virtual nodal equations; and  $\mathbf{T}_{\mathbf{x}}$  is used to integrate the voltage components of either node 1 or 2 into the corresponding matrix expressions of a submodule of the WMG.